Bhattacharyya, Aneesh (2026) *Tunable dispersion and energy harvesting characteristics in nonlinear periodic structures.* PhD thesis.

https://theses.gla.ac.uk/86321/

Copyright and moral rights for this work are retained by the author

A copy can be downloaded for personal non-commercial research or study, without prior permission or charge

This work cannot be reproduced or quoted extensively from without first obtaining permission from the author

The content must not be changed in any way or sold commercially in any format or medium without the formal permission of the author

When referring to this work, full bibliographic details including the author, title, awarding institution and date of the thesis must be given

Enlighten: Theses
https://theses.gla.ac.uk/
research-enlighten@glasgow.ac.uk



TUNABLE DISPERSION AND ENERGY HARVESTING CHARACTERISTICS IN NONLINEAR PERIODIC STRUCTURES

A Thesis

Submitted to

The University of Glasgow

by

Aneesh Bhattacharyya

In Partial Fulfilment

of the Requirements for the Degree

Doctor of Philosophy in Civil Engineering

in the

James Watt School of Engineering, University of Glasgow

July, 2026.

To my brother, Aabesh Bhattacharyya,
my mother, Chandrima Bandyopadhyay,
my father, Barun Bhattacharyya,
and Isha Roy Chowdhuri

ACKNOWLEDGEMENTS

I would like to express my sincere gratitude and deepest appreciation to my Ph.D. supervisor, Professor Sondipon Adhikari, for his guidance, support, and encouragement throughout my doctoral journey. Pursuing a doctorate has always been an aspiration of mine, and his supervision has been central to making this work possible. I am especially thankful for his generous availability, his technical guidance at every stage of my research, and his continued confidence in me during difficult periods. His persistent guidance, moral support, and willingness to help in every possible way have meant more to me than I can adequately express. I could not have hoped for a better supervisor. He gave me the independence to develop and pursue my own research ideas, while also providing exactly the right balance of technical direction, critical feedback, and personal encouragement.

I am also deeply grateful to my secondary supervisor, Professor Lukasz Kaczmarczyk, for his support and technical guidance, particularly during a period when I was struggling to resolve a challenging research problem. His expertise and insight were extremely valuable in helping me bring that problem to a satisfactory conclusion. I sincerely appreciate the time and effort he devoted to detailed and fruitful discussions when I had been stuck for weeks. I would also like to thank Dr. Chun Hean Lee, who supported me through my annual progression reviews and served as my panel convenor. His motivation, questions, and constructive inputs during the review meetings helped me refine the direction of my work and shape the final form of this Thesis.

I would like to express my heartfelt thanks to my brother, Aabesh Bhattacharyya, who recently passed his Ph.D. defense in Statistics at the University of Chicago, for his constant support, encouragement, and inspiration throughout my doctoral journey. Whenever I faced difficult situations in my personal or professional life, he was always there to support me, advise me, and help me find a way forward. He is, by far, one of the most intelligent and compassionate people I have ever known, and I feel fortunate to have him as my brother. I am also profoundly grateful to my parents, Chandrima Bandyopadhyay and Barun Bhattacharyya, for their continuous moral support during my Ph.D. and during my earlier Master's studies. They were the first people to encourage me to pursue doctoral research and higher education, rather than moving directly into an industry job after my Bachelor's degree. I would also like to thank the beautiful woman who I love Isha Roy Chowdhuri for her continuous support and belief in my potential during my difficult times.

A doctoral journey without friends and colleagues would have been incomplete and, in many ways, far less meaningful. I would therefore like to thank my friends and colleagues for their support, companionship, and help in many different ways throughout my doctoral life. In particular, Alan, Sudip, Andrew, Shiting, Dewangga, Turkay, Tadas, Huy, Alfredo, Tanzib, Samarth, Cleison and Professor Eric were especially helpful and formed

an important part of my time at the University of Glasgow. I have shared many wonderful and memorable moments with them, and I will always value their presence during this stage of my life.

Finally, I am grateful to all the Thesis committee members, panel convener Dr. Peter Grassl, internal examiner Dr. Ankush Aggarwal, and external examiner Professor David Wagg, for devoting their time and effort to evaluating my doctoral research work.

Contents

ACKNOWLEDGEMENTS iii

List of Tables ix

List of Figures x

Summary xiv

1 Introduction 1
- 1.1 Overview . . . 1
- 1.2 Periodic structures, wave filtering, and mechanical metamaterials . . . 2
- 1.3 Nonlinear periodic structures and amplitude-dependent dispersion . . . 3
- 1.4 Passive tunability through bi-stability and inertial coupling . . . 4
- 1.5 Practical motivation for wave-based energy harvesting . . . 6
- 1.6 Energy harvesting potential of multistable periodic media . . . 7
- 1.7 Motivations . . . 8
- 1.8 Research Objectives . . . 9
- 1.9 Organization of the work . . . 10

2 A review of vibration energy harvesting, periodic systems, and nonlinear wave dynamics 12
- 2.1 Scope of the review . . . 12
- 2.2 Vibration energy harvesting and engineering need . . . 12
- 2.3 Effectiveness of periodic structures in energy harvesting . . . 14
- 2.4 Nonlinear and multistable energy harvesting . . . 15
- 2.5 Analysis of nonlinear periodic structures . . . 16
- 2.6 Inertial coupling, diatomicity, and nonlinear transition fronts . . . 17
- 2.7 Literature gap and position of the present work . . . 19

3 Bandgap manipulation through a bi-stable inertially coupled strongly nonlinear periodic chain 21
- 3.1 A bi-stable-inertial unit cell underpinning nonlinear metamaterials . . . 21
  - 3.1.1 The mechanical model . . . 21
  - 3.1.2 Dynamic analysis in the phase plane . . . 23
- 3.2 A generalized, consolidated framework for discrete nonlinear periodic structures . . . 28

3.2.1 Notation and unit-cell modeling 29
3.2.2 Linear baseline and weakly nonlinear perturbations 29
3.2.3 Generalized harmonic balance for strongly nonlinear responses . . . 29
3.2.4 Inverse (time-domain) method for independent validation 30
3.2.5 Handling non-integrable, non-polynomial nonlinearities 31
3.2.6 From weak to strong nonlinearity: one workflow 32
3.3 Specific problem formulation: An inertially coupled strongly nonlinear periodic chain 33
3.4 Asymptotic analysis 34
3.4.1 Proximity to global energy minima and perturbation expansion . . 34
3.4.2 Linear dispersion analysis at first level of approximation 35
3.4.3 Positive definiteness of the unit cell mass matrix (Sylvester's criterion) 36
3.4.4 Second-order correction to the Dispersion Profiles 38
3.4.5 Dispersion diagrams from asymptotic analysis 39
3.4.6 Bandgap variation with the mass ratios 40
3.4.7 Dispersion profile by the direct method in the linearized domain . . 44
3.5 Generalized harmonic balance (HB) method for strongly nonlinear regime . 45
3.5.1 Generalized harmonic approximation 45
3.5.2 Dispersion profiles obtained using the generalized harmonic balance method 46
3.5.3 Comparison of HB results with results from asymptotic analysis . . 52
3.6 Time-domain simulation of the finite chain and comparison with HB results 53
3.6.1 Inverse Method (IM) 53
3.6.2 Dispersion plots showing comparison between harmonic balance and IM results, an error quantification and computational speedup . . . 55
3.6.3 Discussion of the comparison between time-domain simulation and HB results, possible chaos and nonlinear modal interactions 56
3.7 Concluding remarks 58

4 Energy harvesting from transient free waves in a piezoelectric periodic chain: a settling-time approach 61
4.1 Introducing the baseline model for free-wave energy harvesting 61
4.1.1 Linear piezoelectric harvester 61
4.1.2 Equations of motion 62
4.2 Dispersion characteristics in the regime of free wave propagation 65
4.2.1 Band structure behavior with the electrical and structural parameters 66
4.3 Energy harvested through free wave propagation 69
4.3.1 Dependence of maximum steady-state power on non-dimensional free wave frequency ω 71
4.3.2 Dependence of maximum steady-state power on structural and electrical parameters 73
4.4 An analytical approach to characterize harvested power through free wave propagation 75
4.4.1 Time-domain 75
4.4.2 Laplace domain 77
4.4.3 Settling time 78

4.4.4 Comparison of theoretical power with numerical time-domain integration . . . 80
4.5 Concluding remarks . . . 81

5 Energy harvesting potential of inertially coupled nonlinear piezomagnetoelastic chains 83
5.1 Extending free-wave harvesting framework to nonlinear periodic systems . 83
5.2 A piezomagnetoelastic unit-cell model . . . 84
5.3 The periodic chain . . . 89
5.4 Dispersion characteristics in the linearized regime . . . 92
5.4.1 Dispersion relation . . . 92
5.4.2 Band structure behavior in the linearized regime . . . 95
5.4.3 Summary of dispersion behavior in the linearized regime . . . 99
5.5 Energy harvested in the linearized regime through free wave propagation . 100
5.6 Dependence of maximum steady-state power on free wave frequency . . . 102
5.7 Analytical approach . . . 104
5.7.1 Time-domain . . . 104
5.7.2 Laplace domain . . . 108
5.7.3 Optimum time . . . 112
5.7.4 Comparison of theoretical power with numerical time-domain integration . . . 116
5.8 General strongly nonlinear regime – Intrawell motions of the tip mass . . . 117
5.8.1 Amplitude-dependent dispersion relation within a potential well . . 118
5.8.2 Time-domain response and energy harvested in the strongly nonlinear regime. . . . 120
5.9 General strongly nonlinear regime – Interwell motions of the tip mass, related wave profile and localized energy harvesting . . . 124
5.9.1 Quantitative justification for single-mode reduction to study interwell fronts and associated harvesting within the parameter space considered . . . 124
5.9.2 Continuum limit of the discrete piezomagnetoelastic chain . . . 125
5.9.3 Parametric plotting to compare with numerical results . . . 133
5.9.4 Advantages over a linear model with no magnets or inerters . . . 141
5.9.5 Discussion of interwell energy harvesting . . . 144
5.10 Concluding remarks . . . 144

6 Energy harvesting capacity of diatomic inertially coupled nonlinear piezomagnetoelastic chains 147
6.1 The mass-diatomic unit-cell model . . . 147
6.1.1 Equations of motion . . . 147
6.1.2 Phase plane behavior . . . 149
6.2 Linearized dispersion behavior for the mass-diatomic chain . . . 152
6.2.1 Dispersion relation . . . 152
6.2.2 Bandstructure behavior with system parameters . . . 157
6.3 Energy harvesting in the linearized regime . . . 159
6.3.1 Harvesting formulation . . . 159

6.3.2 Power variation with wavenumber . . . 163
6.4 General strongly nonlinear regime . . . 167
6.4.1 Long-wavelength continuum limit of the diatomic chain for studying snap-through transition fronts . . . 167
6.4.2 Analytical leading-order transition fronts . . . 168
6.4.3 Comparison of theoretical leading-order wavefronts with numerical simulations . . . 172
6.4.4 Bloch-consistent Harmonic Balance Method . . . 173
6.4.5 Nonlinear dispersion branches . . . 175
6.4.6 Energy harvested in the general nonlinear regime . . . 177
6.5 Enhanced energy harvesting potential of the strongly nonlinear model . . . 180
6.5.1 Nonlinear model advantages . . . 180
6.5.2 Numerical validation . . . 181
6.6 Concluding remarks . . . 182

7 Conclusion and future outlook 185
7.1 Summary . . . 185
7.2 How the Thesis fills the literature gap . . . 188
7.3 Research contributions . . . 189
7.4 Novelty and impact . . . 190
7.5 Recommendations for future work . . . 191
7.5.1 Experimental realization and validation . . . 191
7.5.2 Improved nonlinear time-domain validation . . . 191
7.5.3 Multimode beam and higher-dimensional electromechanical models 191
7.5.4 Two and three-dimensional nonlinear harvesting lattices . . . 191
7.5.5 Circuit design and adaptive electrical interfaces . . . 192
7.5.6 Optimization, uncertainty, and design maps . . . 192
7.5.7 General transient and stochastic excitation environments . . . 192
7.6 Final remarks . . . 192

REFERENCES 194

List of Tables

3.1 Summary of bandgap behavior in weakly nonlinear regime 44
3.2 Summary of bandgap behavior in strongly nonlinear regime 51
3.3 HB convergence study 51
3.4 Relative error metrics between the Harmonic Balance (HB) dispersion predictions and the Inverse Method (IM) time-domain validation. 56

4.1 Dimensional parameters chosen for the electromechanical model. 66

5.1 Parameters used for the piezomagnetoelastic chain model. 94

List of Figures

3.1 Three-DOF bi-stable-inertial unit-cell model. 22
3.2 Bi-stable mass phase-space behavior for $\xi(0) = 0.1$. 26
3.3 Bi-stable mass phase-space behavior for $\xi(0) = 0.7$. 27
3.4 The ALIGN nonlinear-dispersion workflow. 32
3.5 Periodic chain and its repeating nonlinear unit cell. 34
3.6 Asymptotic dispersion branches with varying r_1. 40
3.7 Asymptotic dispersion branches with varying r_2. 41
3.8 Asymptotic dispersion branches with varying r_a. 42
3.9 Bandgap and midpoint frequency difference variation with the mass ratio r_1 keeping all the other parameters fixed. 42
3.10 Bandgap and midpoint frequency difference variation with the mass ratio r_2 keeping all the other parameters fixed. 43
3.11 Bandgap and midpoint frequency difference variation with the mass ratio r_a keeping all the other parameters fixed. 43
3.12 Dispersion profile showing the real and imaginary parts of the wavenumber for a range of varying frequency 45
3.13 Dispersion diagrams obtained from the generalized harmonic balance method for varying mass ratio r_1 with the values of the other parameters kept fixed 47
3.14 Dispersion diagrams obtained from the generalized harmonic balance method for varying mass ratio r_2 with the values of the other parameters kept fixed. 48
3.15 Dispersion diagrams obtained from the generalized harmonic balance method for varying mass ratio r_a with the values of the other parameters kept fixed. 49
3.16 Modal participation fractions along the HB dispersion branches for a representative set of mass ratios. 50
3.17 Branch-wise and global convergence metrics for HB dispersion with increasing HB truncation N_h. 52
3.18 Comparison of dispersion profiles obtained using HB method and asymptotic analysis. 53
3.19 Comparison of harmonic balance (HB) results with direct time-domain (IM) simulations (wavenumber μ vs frequency ω). 55
3.20 Relative error $\left|\frac{\omega_{\mathrm{IM}}(\mu)-\omega_{\mathrm{HB}}(\mu)}{\omega_{\mathrm{HB}}(\mu)}\right|$ plotted against the wavenumber μ 57
3.21 Nonlinear Floquet stability of the harmonic balance (HB) periodic Bloch orbits. 58
3.22 A Generalized Framework for Discrete Nonlinear Periodic Structures. . . . 59

4.1 The repeating piezoelectric unit cell with tip masses and beams of adjacent cells shown. 62
4.2 Dispersion profiles obtained with and without the piezoelectric energy harvester for varying load resistance R_l 67
4.3 Dispersion profiles obtained with and without the piezoelectric energy harvester for varying coupling-spring stiffness k 68
4.4 Representative free-response histories of $\tilde{Y}_n(\tau)$ and $\tilde{V}_n(\tau)$ for $\tilde{Y}_n(0) = 0.104$, $\tilde{Y}_n'(0) = 0$, $\omega = 1$ and the parameters in Table 4.1. 71
4.5 Variation of maximum steady-state harvested power with free-wave frequency ω for $\tilde{Y}_n(0) = 0.104$ and $\tilde{Y}_n'(0) = 0$. 72
4.6 Variation of maximum steady-state power with the non-dimensional stiffness parameter $\tilde{k}$ for $\omega = \omega_e \approx 1$ for four different chosen representative values of load resistance R_l 73
4.7 Variation of maximum steady-state power with the non-dimensional electrical time constant $\hat{\tau}_e$ at $\omega = \omega_e \approx 1$ for four different representative values of the stiffness parameter $\tilde{k}$ 74
4.8 Comparison of analytical, numerical, and Laplace-axis power predictions using $\tau_s(\omega)$ from Eq. (4.46), for the chosen parameter set, $\tau_s(\omega)$ varies from 115.39 to 142.73 over the plotted frequency range. 80

5.1 The repeating piezomagnetoelastic unit-cell model. 84
5.2 Phase-plane behavior of tip mass $Y(t)$ and voltage $V(t)$ for small intrawell oscillations of the tip mass about its stable equilibrium position and large interwell motions of the tip mass resulting in crossing the unstable saddle. 88
5.3 The periodic piezomagnetoelastic chain. 89
5.4 Dispersion profiles for the nonlinear piezomagnetoelastic chain obtained in the linearized regime with and without the piezoelectric energy harvester for varying load resistance R_l. 96
5.5 Dispersion profiles for the nonlinear piezomagnetoelastic chain obtained in the linearized regime with and without the piezoelectric energy harvester for varying coupling-spring stiffness k. 97
5.6 Dispersion profiles for the nonlinear piezomagnetoelastic chain obtained in the linearized regime with and without the piezoelectric energy harvester for varying inerter mass-ratio m_a/M_t. 99
5.7 Time-domain responses in the linearized regime showing the tip mass displacement $Y_n(t)$ from the stable equilibrium point and voltage generated in the piezoelectric patch $V_n(t)$ for a representative n-th unit cell. 101
5.8 Power harvested in the linearized regime over the cycle of maximum steady-state voltage amplitude plotted with free wave frequency ω. 103
5.9 Comparison of analytical time-domain estimate, numerical integration, and Laplace-axis power prediction using analytically derived settling-time formula in Eq. (5.110). 116
5.10 Time-domain responses and phase portraits showing the tip mass displacement $Y_n(t)$ and voltage generated $V_n(t)$ for intrawell oscillations in the strongly nonlinear regime for a representative n-th unit cell. 121

5.11 Comparison between power harvested in the general strongly nonlinear regime and in the linearized regime for intrawell oscillations within the stable potential well at $Y_n = +Y_s$. 123
5.12 Comparison of the theoretically predicted wavefront with numerically determined wave profile in strongly nonlinear interwell regime. 135
5.13 Transition-front position vs time, extracted from the numerical $Y = 0$ crossing. The red line shows the least-squares fit used to estimate the representative averaged propagation speed. 136
5.14 Comparison of the theoretically predicted voltage model with numerically determined voltage envelope in strongly nonlinear interwell regime. 137
5.15 Comparison of theoretically predicted average power with numerically obtained power profile in strongly nonlinear interwell regime 139
5.16 Comparison of the theoretically predicted voltage model with numerically determined voltage envelope for different inerter mass-parameters and coupling spring stiffness values in strongly nonlinear interwell regime. 140
5.17 Comparison of the theoretically predicted voltage model with numerically determined voltage envelope for varying values of load resistance R_l in strongly nonlinear interwell regime. 140
5.18 Comparison of power harvested vs mass index n of the nonlinear, inertially coupled piezomagnetoelastic chain with a linear piezoelectric chain with no inerters and magnets. 142
5.19 Comparison of power harvested vs mass index n of the nonlinear, inertially coupled piezomagnetoelastic chain with a linear piezoelectric chain with inerters and without magnets. 143
5.20 Comparison of power harvested vs mass index n of the bi-stable, inertially coupled piezomagnetoelastic chain with a bi-stable piezomagnetoelastic chain without inerters. 143

6.1 The repeating diatomic piezomagnetoelastic unit-cell model. 148
6.2 Phase-plane behavior of tip mass $Y(t)$ and voltage $V(t)$ of the diatomic unit-cell model for principal mass ratio $M_2/M_1 = 0.5$. 150
6.3 Phase-plane behavior of tip mass $Y(t)$ and voltage $V(t)$ of the diatomic unit-cell model for principal mass ratio $M_2/M_1 = 1$. 151
6.4 The periodic diatomic chain. 152
6.5 Linearized dispersion branches plotted with varying mass ratios m_a/M_1 and M_2/M_1, solid curves represent lower acoustic-like branch and dotted curves represent upper optical-like branch. 158
6.6 Linearized dispersion branches plotted with varying coupling spring stiffness k, solid curves represent lower acoustic-like branch and dotted curves represent upper optical-like branch. 159
6.7 Power vs wavenumber μ in the linearized regime plotted with varying mass ratios m_a/M_1 and M_2/M_1, solid curves represent lower branch and dashed curves represent upper branch. 164
6.8 Power vs wavenumber μ in the linearized regime plotted with varying coupling spring stiffness k, solid curves represent lower branch and dashed curves represent upper branch. 166

6.9 Comparison of the theoretically predicted wavefront with numerically determined wave profile in strongly nonlinear snap-through regime. 172
6.10 Nonlinear dispersion branches plotted with varying mass ratios m_a/M_1 and M_2/M_1. 176
6.11 Nonlinear dispersion branches plotted with varying coupling spring stiffness k. 176
6.12 Power vs wavenumber μ in the general strongly nonlinear regime plotted with varying mass ratios m_a/M_1 and M_2/M_1, coupling spring stiffness is kept fixed. 178
6.13 Power vs wavenumber μ in the general strongly nonlinear regime plotted with varying coupling spring stiffness k, with mass ratios m_a/M_1 and M_2/M_1 kept fixed. 179
6.14 Comparison of energy harvested using the exact nonlinear diatomic model against the linearized diatomic model. 180
6.15 Comparison of the harvested power upper branch between the nonlinear HB model and direct numerical simulations of a finite periodic chain. . . . 182

Summary

This Thesis investigates tunable bandgap behavior and energy harvesting characteristics in nonlinear periodic structures, motivated by the need for passive wave-control strategies that remain effective when disturbances are transient, spatially distributed, and amplitude dependent. Whereas classical periodic structures and conventional resonant harvesters offer limited tunability and typically rely on fixed band structures or sustained external excitation, the work pursued here shows that geometric and magnetic bi-stability, inerter-effects, and electromechanical coupling can be used to reshape dispersion, attenuation, and energy-transfer mechanisms in a systematic manner. The thesis therefore develops a unified research arc that connects nonlinear wave propagation with practical energy conversion, moving from bandgap engineering in strongly nonlinear lattices to broadband and spatially localized harvesting from free waves generated solely by initial conditions.

The first part of the Thesis (Chapter 3) focuses on tunable dispersion characteristics in a bi-stable periodic chain with coupled horizontal–vertical dynamics and stable negative-inerter mechanism. A new semi-analytical framework, ALIGN, is developed to bridge weakly and strongly nonlinear regimes through asymptotic analysis, multi-harmonic harmonic balance, robust branch tracking, and amplitude-locked inverse time-domain validation. This framework enables the computation and verification of amplitude-dependent Bloch dispersion in systems with non-polynomial geometric nonlinearities, while also identifying well-defined mass-ratio thresholds, branch-merging behavior, and systematic routes for bandgap manipulation. In this sense, the work demonstrates that combining bi-stability with appropriately chosen inertial coupling produces a richer and more tunable wave environment than classical linear periodic chains or simpler nonlinear lattices and simultaneously enables the exploitation of inexpensive analytical/semi-analytical models to capture this environment adequately without relying solely on computationally heavy numerical simulations.

The second part of the Thesis (Chapter 4, Chapter 5) exploits these wave phenomena for energy harvesting in periodic piezoelectric and piezomagnetoelastic chains under free or unforced propagation. First, a linear piezoelectric baseline is established in which Bloch-reduced electromechanical dynamics is combined with the concept of settling time to define and optimize the maximum steady-state harvested power under unforced transient motion. This idea is then extended to inertially coupled nonlinear piezomagnetoelastic chains, where magnetic bi-stability is shown to transform a sharply tuned linear optimum into a broad quasi-saturated band of near-optimal intrawell performance, while interwell dynamics is shown to give rise to spatially localized harvesting through slowly modulated ϕ^4-type transition fronts rather than exact conservative solitons. The final work (Chapter 6) then introduces mass-diatomicity in the nonlinear piezomagnetoelastic chain, where richer branch and bandgap behavior in the large-amplitude nonlinear regime

intrinsically gives rise to almost 10^2 times higher harvesting performance favoring shorter wavelength components of the transient free wave.

Taken together, the results establish a physically realizable and analytically informed design framework for multifunctional nonlinear metamaterials that can simultaneously tailor bandgaps, guide and attenuate waves, and harvest useful energy from transient disturbances relevant to self-powered sensing and vibration-control applications.

Chapter 1

Introduction

1.1 Overview

Periodic structures have long provided a natural route for controlling mechanical and elastic waves. Their repeated unit-cell architecture allows the designer to determine which frequencies propagate, which frequencies attenuate, and how energy is distributed in space. In the classical linear setting, this wave-control capability is usually expressed through dispersion diagrams, pass bands, stop bands, attenuation zones, and bandgaps. Such features make periodic media useful as filters, vibration isolators, waveguides, resonators, and mechanical metamaterials. However, a linear periodic structure has an important limitation: once the geometry, material constants, and unit-cell topology are fixed, the band structure is also fixed. Thus, the same structure cannot easily adapt its wave-propagation characteristics to changing disturbance amplitudes, transient excitation conditions, or multiple design tasks.

This Thesis investigates how this limitation can be overcome by using nonlinear periodic structures in which the propagation characteristics are not fixed once and for all, but depend on amplitude, internal state, electromechanical coupling, and unit-cell architecture. The central theme is that nonlinearity should not be regarded only as a complication to be avoided. Instead, it can be used as a design mechanism for tunable bandgap behavior, broadband energy transfer, and localized energy harvesting. The work therefore develops a systematic arc from nonlinear wave propagation to practical energy conversion. It begins with a geometrically bi-stable, inertially coupled periodic lattice; establishes a free-wave harvesting baseline through a settling-time-aware piezoelectric chain; extends this baseline to an inertially coupled nonlinear piezomagnetoelastic chain; and finally introduces mass diatomicity to obtain richer branch behavior and enhanced harvesting capacity. Here, mass-diatomic means that each representative n-th unit cell contains two principal mechanical degrees of freedom with unequal associated masses M_1 and M_2. Repetition of this two-mass cell produces the two sublattices studied in Chapter 6.

The main literature gap addressed in this Thesis is the absence of a unified framework that connects nonlinear dispersion engineering with transient electromechanical energy harvesting. Existing studies have separately developed linear and nonlinear wave propagation in periodic media, inertial-amplification-based attenuation, multistable and piezoelectric harvesting, and transition-front dynamics. What is still missing is a design pathway that proceeds continuously from bandgap manipulation, to prediction of

power harvested from free waves, to nonlinear broadening of useful harvesting regimes, and finally to intrinsic localization through interwell fronts. This Thesis fills that gap by treating wave propagation and harvesting as one coupled problem in nonlinear periodic electromechanical media.

1.2 Periodic structures, wave filtering, and mechanical metamaterials

A periodic structure consists of a repeated arrangement of unit cells. Depending on the length scale and physical context, these unit cells may represent atoms in a lattice, inclusions in a phononic crystal, resonators embedded in an elastic host, or lumped mechanical elements connected by springs and constraints. The essential feature is that the spatial repetition imposes phase relations between neighboring cells, allowing Bloch–Floquet ideas to reduce the analysis of an extended medium to the behavior of a representative cell. The intellectual foundations of wave propagation in periodic media were established through classical studies of dispersion, lattice waves, and band formation [1, 2, 3, 4]. These ideas remain central to modern acoustic and elastic metamaterials, where geometry, periodicity, internal resonators, and material contrast are used to design targeted wave properties [5, 6, 7].

The most familiar feature of a periodic medium is the occurrence of frequency intervals in which propagating wave solutions are suppressed. In such bandgaps, energy is not primarily attenuated because of material damping; rather, the periodic structure creates destructive interference, Bragg scattering, local resonance, or effective inertia mechanisms that prevent wave transmission. This gives periodic structures the ability to function as frequency-selective mechanical filters. At the same time, dispersion surfaces and group-velocity fields can be shaped to control the direction in which energy moves through the structure. Thus, periodic media are not only frequency filters but also spatial filters.

The modern field of mechanical metamaterials has broadened this classical viewpoint. Mechanical metamaterials are engineered structures whose effective dynamic behavior is governed more by architecture than by constituent material alone. Recent developments emphasize flexible, nonlinear, active, and multifunctional designs, rather than only fixed linear bandgaps [8, 9, 10, 11]. Related work on metadamping shows that architected media can also tailor the distribution and dissipation of vibrational energy across modes and length scales [12]. Active, adaptive, and intrinsically nonlinear structures further extend the design space by allowing transport, switching, and attenuation to depend on the state of the system rather than only on fixed geometry [13, 14, 15].

This transition from fixed linear band structures to adaptive and amplitude-dependent wave behavior motivates the present Thesis. The structures considered here are periodic, but their useful behavior arises from a combination of periodicity and nonlinearity. The repeated cell sets the spatial wave framework, while nonlinear mechanisms such as bistability, magnetic potentials, inertial coupling, and piezoelectric dissipation modify how energy is transported, attenuated, converted, and localized.

1.3 Nonlinear periodic structures and amplitude-dependent dispersion

Nonlinear periodic structures arise when the restoring force, inertia, constraint geometry, or electromechanical coupling cannot be described by a purely linear relation. In weakly nonlinear systems, the nonlinear terms may be treated as perturbations to a linear periodic structure. In strongly nonlinear systems, however, the nonlinear forces can dominate the response, and the wave behavior may no longer be described as a small correction to a linear band diagram. This distinction is important because the methods, physical interpretation, and design opportunities differ substantially between the two regimes.

Weakly nonlinear periodic structures can often be analyzed using perturbation methods, multiple-scales analysis, or asymptotic corrections to linear dispersion branches [16, 17, 18, 19]. These methods are valuable because they provide analytical insight into how amplitude modifies cut-off frequencies, band edges, group velocities, and modal interactions. They also clarify when a periodic structure can behave as an amplitude-dependent filter. Nevertheless, such approaches are restricted by the assumption that nonlinear terms remain sufficiently small and that the response remains close to the corresponding linear wave mode.

Strongly nonlinear periodic structures present a more difficult problem. Geometric constraints, snap-through mechanisms, Hertzian contacts, magnetic forces, and nonlinear inertial couplings can generate non-polynomial, non-integrable, or non-smooth force laws. In such cases, wave branches may shift substantially with amplitude, merge, exchange modal content, or lose stability across the Brillouin zone [20, 21, 22, 23]. The concepts of nonlinear normal modes, normal-form transformations, and nonlinear-vibration analysis provide powerful ways to interpret nonlinear modal behavior in finite-dimensional mechanical systems [24, 25, 26]. Backbone curve and spectral-submanifold approaches further provide reduced-order descriptions of nonlinear forced responses and high-dimensional mechanical systems [27, 28, 29]. For periodic media, however, these ideas must be combined with Bloch-type spatial phase relations, branch continuation, and validation against finite-chain time-domain simulations. NOFRF-based, harmonic, and spectral-element formulations have each contributed important tools for treating nonlinear response features in periodic structures [30, 31, 32]. Nonlinear dispersion analysis, large-strain homogenization, and data-driven modeling have further expanded the available methodology for nonlinear structured media beyond simple lumped-parameter chains [33, 34, 35]. Recent adaptive harmonic balance formulations, including asymptotic harmonic selection strategies, also provide useful methodological context for strongly nonlinear response calculations where the relevant harmonic content is not known a priori [36].

A recurring difficulty in strongly nonlinear periodic structures is that the existence of a computed periodic Bloch orbit does not automatically imply that the corresponding wave will be robustly realized in a finite chain under realistic initial conditions. Nonlinear periodic orbits may be unstable, nearby branches may coexist, and finite-chain boundary effects may distort the response. Therefore, a useful analysis framework must do more than compute nonlinear dispersion curves. It must also track branches reliably, handle high-harmonic content, identify physically admissible parameter regimes, and compare the semi-analytical prediction with direct time-domain simulations. These requirements motivate the development of the ALIGN framework in this Thesis.

1.4 Passive tunability through bi-stability and inertial coupling

Two passive mechanisms are especially useful for low-frequency nonlinear wave control: bi-stability and inertial coupling. Bi-stability introduces a double-well potential landscape. A mass or structural element can then undergo small intrawell oscillations about a stable equilibrium, or large interwell transitions that cross an energy barrier. This creates amplitude-dependent behavior that is absent in purely linear periodic structures. Snap-through and double-well mechanisms can support nonlinear transport, interwell switching, transition waves, and modal redistribution [37, 38, 39, 40]. Closely related ideas have also been developed in the adaptive-structures literature on bi-stable composite plates, where reduced-order modelling, dynamic snap-through, and cross-well dynamics have been used to describe large-amplitude transitions between stable configurations [41, 42, 43]. This body of work is relevant here because the present Thesis also exploits the distinction between intrawell oscillations and interwell transitions, but embeds these mechanisms within a periodically coupled lattice for wave tailoring and energy harvesting. In periodic media, this means that the same unit cell can support qualitatively different wave regimes depending on the initial energy.

A closely related class of passive low frequency nonlinear systems is provided by quasi-zero-stiffness and geometrically nonlinear isolator–harvester designs. Recent studies have shown that QZS-based systems can exhibit monostable, zero-linear-stiffness and bi-stable oscillation regimes, retain performance under mass-load deviation, suppress subharmonic responses, and move between quasi-zero-stiffness and zero-stiffness behavior for broadband low-frequency isolation [44, 45, 46, 47]. Bio-inspired X-shaped and multilayer nonlinear isolators further demonstrate how layered geometry and internal resonance can be exploited for low-frequency vibration control [48, 49]. These works reinforce the broader idea that geometric nonlinearity and tunable stiffness can be powerful passive design mechanisms; however, they are primarily concerned with forced-response vibration isolation or device-level nonlinear dynamics, whereas the present Thesis embeds related passive nonlinear ideas within periodically coupled lattices for amplitude-dependent wave propagation, bandgap manipulation, and free-wave energy harvesting.

Besides bi-stability, inertial coupling through conventional inertial amplifiers provides a different but complementary mechanism. Instead of adding large resonator masses, an inertial-amplifier linkage magnifies the effective inertia associated with selected relative motions. This can open or enlarge low-frequency attenuation regions and reshape dispersion without requiring impractically heavy attachments [50, 51, 52, 53]. This viewpoint is closely aligned with the broader literature on inerter-based vibration mitigation, in which a mechanical network element is used to generate an effective inertial force that can greatly exceed the physical mass of the device and thereby provide a compact route to vibration suppression [54, 55]. Nonlinear inertial devices, negative-stiffness mechanisms, and resonator-enhanced configurations further show that inertial amplification can be used beyond conventional linear vibration-isolation settings [56, 57, 58, 59]. In the present Thesis, inerter is not used as an isolated absorber, but as a unit-cell mechanism that modifies the dispersion, stability thresholds, broadening of useful energy-harvesting regime and spatial localization properties of nonlinear periodic chains.

Although bi-stability and inertial coupling have each been studied as powerful design

mechanisms, their combination in a single nonlinear periodic architecture is less developed. This is the first major technical opportunity addressed in the present work. A hybrid unit cell containing coupled horizontal–vertical motion, geometric bi-stability, and inertial coupling can produce richer behavior than either ingredient alone. The bi-stable degree of freedom stores and redistributes energy within the unit cell, while the inerter modifies the effective relative motion between coupled degrees of freedom. This combination creates a platform in which mass ratios, amplitudes, and coupling geometry can tune bandgap behavior, branch merging, and stability thresholds. Design parameters specify the physical model, such as masses, stiffnesses and reference geometry. Tuning parameters are selected design or circuit parameters, such as the load resistance, varied to modify dispersion or harvesting performance; the two categories therefore overlap. Here, parametric tuning generally means comparing fixed parameter choices, not varying them during a free-response simulation.

The problem is also methodologically significant. The governing equations of such a hybrid chain contain non-polynomial square-root terms from geometric constraints and a non-diagonal effective mass matrix from inertial coupling. These features prevent a purely closed-form treatment in the strongly nonlinear regime. They also make the system a useful test case for a general analysis pipeline for nonlinear periodic structures. In this Thesis, the resulting framework is used to bridge weakly nonlinear asymptotic dispersion, strongly nonlinear multi-harmonic harmonic balance, and inverse time-domain validation. In this way, the work extends the study of nonlinear lattices beyond simpler monoatomic, diatomic, or local-resonator examples [60].

Conventional inertial amplification and the inertial coupling adopted in the present work are deliberately distinguished. A conventional inerter has positive inertance, $b_a > 0$, and generates a two-terminal force proportional to the relative acceleration, thereby increasing the kinetic-energy contribution associated with relative motion [61, 55]. In contrast, the present work employs an architected stable negative inertial coupling, represented at reduced-order level by $b_a = -r_a < 0$, with the initial inclination angle α retained conventionally as a geometric parameter controlling the coupling magnitude. This choice reduces the effective inertia of selected non-uniform wave modes while the complete lattice mass matrix is constrained to remain positive definite. It is adopted specifically because the resulting inertial-reduction regime provides the well-defined admissibility thresholds directly in terms of design parameters of the inerters, and simultaneously provides desirable dispersion and energy-harvesting characteristics such as enhanced bandgap tunability which is captured/predicted adequately via inexpensive analytical/semi-analytical algorithms, nonlinear broadening of the useful free-wave harvesting range, nonlinear front-mediated localization of voltage and power, and enhanced nonlinear mass-diatomicity-induced harvested power through the nonlinear periodic models proposed in this work. Such a coupling is not a negative-mass assumption: passive architected realization principles based on elastically supported masses and moment-free rigid-link mechanisms have been shown to generate dynamically stable negative inertial coupling [62]. Related scissor-like electromechanical metamaterials further demonstrate that architected inertial mechanisms can be integrated with piezoelectric elements to enhance voltage generation and electrical dissipation [63]. The negative coupling itself is conservative and reshapes the modal kinetic-energy distribution; irreversible energy extraction is still supplied by the resistive piezoelectric loads.

1.5 Practical motivation for wave-based energy harvesting

Energy harvesting from structural vibration is not intended to replace large-scale power generation; rather, its practical role is to supply small but useful amounts of electrical energy to distributed sensors, embedded electronics, and low-power monitoring devices. This is especially relevant in structural health monitoring, civil infrastructure, aerospace panels, rotating machinery, pipelines, rail systems, and other engineering systems where wiring can be expensive, intrusive, or impractical, and where periodic battery replacement can limit long-term deployment [64, 65, 66]. Piezoelectric transduction is particularly attractive in this setting because it directly converts strain-induced mechanical deformation into electrical output, can be integrated into slender beams and plate-like members, and has a relatively high energy density compared with many alternative small-scale transduction mechanisms [67, 68, 69]. Classical vibration harvesters therefore provide a natural route to self-powered sensing, but their most efficient operation is usually tied to a narrow resonance band and to the availability of sustained excitation near a known frequency [70, 71, 72].

This narrowband resonant character is a major practical limitation. Real structural vibrations are rarely ideal steady harmonic inputs: they may arise from impacts, traffic loads, human motion, machinery start-up and shut-down, wind loading, wave loading, or localized transient disturbances. Various tuning and bandwidth-extension strategies have been proposed, including tuned auxiliary structures, axial preload, and bidirectionally tunable harvesters [73, 74, 75]. Closed-loop mechanical tuning and electrically assisted interface circuits can further enlarge the effective operating range of piezoelectric harvesters [76, 77, 78]. However, such approaches still primarily focus on improving the performance of a local resonant device, whereas many engineering disturbances propagate through the host structure as waves before reaching a transducer.

Periodic structures are useful for energy harvesting precisely because they allow this wave-propagation stage to be engineered. Instead of treating the harvester as a single local oscillator attached to a vibrating host, a periodic electromechanical structure can shape how mechanical energy travels, slows down, localizes, or attenuates before it is converted into electricity. Sonic crystals, resonator arrays, and acoustic mirrors have shown that spatial organization can increase the amount of wave energy available to a transducer by exploiting reflection, resonance, and wave concentration [79, 80, 81]. Metamaterial-inspired harvesters, granular-chain arrays, and graded metasurfaces further demonstrate that periodic or nearly periodic architectures can redistribute vibrational energy over space and concentrate it in regions where electrical conversion is most effective [82, 83, 84]. Defect states, tunable sub-wavelength plates, and elastic metasurfaces also show that band-structure design can be used to place large deformation, high strain, or strong wave localization near selected harvesting elements [85, 86, 87].

Thus, the use of periodic structures in this Thesis is not only motivated by bandgap physics. It is also motivated by an engineering need, which is, to convert spatially distributed and transient mechanical disturbances into usable electrical output in a predictable way. Periodicity provides the analytical structure needed for Bloch-based design, while piezoelectric coupling provides the energy-conversion mechanism. Nonlinearity then adds the possibility of amplitude-dependent dispersion, broadband near-optimal harvest-

ing, and localized interwell-front-based energy extraction. In this sense, the present research work treats a nonlinear periodic harvester as a multifunctional structural component which can guide and attenuate waves, redistribute transient mechanical energy, and convert part of that energy into electrical power for self-powered sensing and monitoring applications.

1.6 Energy harvesting potential of multistable periodic media

Once wave propagation can be controlled, a natural next question is whether the transported mechanical energy can be harvested. Classical vibration energy harvesting has often relied on piezoelectric devices tuned to operate near resonance under sustained harmonic excitation. Such devices can produce useful output, but their performance is typically narrowband and sensitive to the match between the forcing frequency and the harvester dynamics [70, 71, 69, 72]. This limitation has motivated extensive work on nonlinear and multistable harvesters, where the aim is to widen the operating bandwidth, exploit large-amplitude motion, or use interwell dynamics for enhanced energy conversion [88, 89, 90, 91]. Recent nonlinear harvesting studies have also emphasized bi-stability, magnetic plucking, and frequency up-conversion as practical routes to low-frequency and broadband operation; for example, rotational bi-stable harvesters with frequency up-conversion have been experimentally validated for low-power sensing, while magnetic plucking mechanisms have been enhanced by engineering the magnetic interaction itself [92, 93]. For nonlinear vibration energy harvesters, the electrical load cannot be chosen independently of the nonlinear mechanical response. For example, Cammarano et al. studied optimum resistive loading for electromagnetic harvesters with stiffening nonlinearities and showed how numerical continuation can be used to determine load choices in nonlinear harvesting systems [94]. This is consistent with the perspective adopted in the present Thesis, where the harvested power depends jointly on the structural dynamics, electrical time scale, and post-transient response envelope.

Several strategies have been proposed to address the narrowband nature of conventional harvesters. These include electrical tuning, multistable potentials, nonlinear energy sinks, and broadband or frequency-up-conversion mechanisms [95, 96, 78, 97]. Preloaded and mechanically tuned designs provide additional flexibility, although they often still rely on sustained excitation or carefully selected operating conditions [98]. Similarly, recent QZS-based piezoelectric harvesters with RL electrical loading have shown that intrawell and interwell oscillations under internal resonance can be exploited for nonlinear electromechanical conversion [99]. This is closely related in physical motivation to the present work, but it remains primarily a forced-response oscillator-level framework, whereas the present Thesis formulates harvesting through transient free-wave propagation in periodically coupled electromechanical chains.

In parallel, phononic and metamaterial concepts have shown that the host structure itself can be designed to guide, trap, focus, or redistribute vibrational energy before it is converted electrically [100, 80, 81, 82]. Defect state-based harvesting and tunable phononic structures show that localized modes can concentrate mechanical energy before transduction [85, 86, 101]. Multifunctional piezoelectric metastructures and elastic meta-

surfaces further demonstrate how engineered wave fields can enhance electromechanical conversion through integrated wave manipulation and harvesting [102, 87]. Topological trapping and coupled metamaterial–harvester architectures extend this idea by using protected or deliberately tailored localization mechanisms for targeted energy concentration [103, 104, 105].

Despite this progress, an important gap remains. Many harvesting studies assume persistent forcing, while many periodic-structure studies focus on dispersion and attenuation without defining a harvesting metric for transient free propagation. Real disturbances in engineering structures are often intermittent, impulsive, or generated by initial conditions rather than by a prescribed harmonic load. A bridge is therefore needed between free-wave propagation in periodic structures and post-transient energy extraction in piezoelectric circuits. This Thesis addresses that need by introducing a settling-time-aware power metric for a piezoelectric periodic chain. The metric identifies when the decaying voltage response has entered a smooth post-transient regime and then evaluates the one-period average harvested power. This converts transient free-wave decay into a design variable and provides an internally consistent way to identify an optimum free-wave harvesting frequency.

Magnetoelastic and piezomagnetoelastic systems provide a natural physical realization of this idea in the nonlinear regime. A cantilever beam with a tip mass, piezoelectric patch, and magnetic interaction can realize a double-well electromechanical potential while retaining a compact structural architecture. Magnetoelastic and piezomagnetoelastic oscillators have long served as canonical models for nonlinear double-well dynamics and energy harvesting [106, 107, 108, 109]. Beam-type unit cells and nonlinear periodic electromechanical media further show how structural wave transport and electrical conversion can be coupled at the lattice level [110, 111, 112, 113]. Recent reviews of multistable harvesting and work on inertial amplification confirm that these ingredients are individually promising for broadband and low-frequency operation [114, 115]. The present Thesis combines them in a single periodic framework for free-wave harvesting.

The multistable setting also creates a second harvesting mechanism based on transition fronts. In bi-stable lattices and related nonlinear media, interwell fronts can connect wave propagation, topological switching, energy transfer, and localization [116, 117, 118, 119]. This connects the harvesting problem to a broader literature on nonlinear front dynamics, kinks, solitary waves, and transition-wave control [120, 121, 122, 123]. Recent studies have shown that such fronts can be guided, graded, and used as carriers of concentrated mechanical energy [124, 125, 126, 127]. Domain-wall and transition-wave formation in multistable metamaterials further emphasizes the importance of this regime [128]. In the present Thesis, this idea is extended to dissipative piezomagnetoelastic chains, where the relevant propagating object is a slowly modulated ϕ^4-type front whose voltage and power envelopes are directly connected to localized energy harvesting.

1.7 Motivations

The work in this Thesis is motivated by the need for passive structures that can control and harvest energy from realistic disturbances. In many engineering settings, vibrations are not steady sinusoidal inputs supplied at a known frequency. They may arise from impacts, start-up transients, moving loads, broadband disturbances, environmental fluctuations,

or localized initial perturbations. A design framework based only on forced resonance is therefore incomplete. What is needed is a framework that can predict how a transient wave travels through a periodic structure, how its amplitude and nonlinear state affect the available propagation paths, and how much of the transported energy can be converted into electrical output.

The first motivation is to exploit nonlinearity as a source of tunability. In a linear periodic medium, bandgaps and pass bands are fixed by the unit-cell design. In a nonlinear periodic medium, the wave amplitude and internal state can alter the effective dispersion relation. This creates the possibility of bandgap manipulation without redesigning the entire structure.

The second motivation is to combine bi-stability and suitably chosen inertial coupling in a physically meaningful way. Bi-stability provides amplitude-dependent intrawell and interwell dynamics, while positive/stable-negative inertial coupling offers a route to low/high-frequency attenuation respectively and effective inertia control. Hence, the combination of bi-stability and inertial coupling can produce tunable wave behavior in parameter regimes that are not accessible to either mechanism alone.

The third motivation is to formulate energy harvesting directly in the free-wave setting. A transient disturbance generates a decaying electromechanical response, not a steady forced oscillation. Therefore, harvesting performance should be evaluated after the initial transient has settled, using a criterion tied to the actual voltage envelope and circuit dynamics. This motivates the settling-time-aware power metric developed in the Thesis.

The fourth motivation is to use nonlinear wave phenomena with appropriately chosen inertial-coupling effects to broaden the useful harvesting regime and spatially localize harvesting. Intrawell nonlinear dynamics can convert a sharply tuned harvesting optimum into a wider region of near-optimal performance. Interwell dynamics can generate transition fronts that concentrate energy spatially. Both mechanisms are attractive for self-powered sensing and vibration-control applications where the location and frequency content of disturbances may vary.

The fifth motivation is to extend these ideas beyond monoatomic chains. Mass diatomicity introduces acoustic-like and optical-like branches, branch separation, and mass-contrast effects. When combined with piezomagnetoelastic nonlinearity, this creates additional design freedom for tuning both band structure and harvested power.

1.8 Research Objectives

Guided by the motivations above, the main objectives of this Thesis are as follows.

1. To develop a semi-analytical framework for studying weakly and strongly nonlinear wave propagation in discrete periodic structures with non-polynomial geometric nonlinearities.

2. To design and analyze a geometrically bi-stable, inertially coupled unit cell capable of supporting coupled horizontal–vertical dynamics, intrawell oscillations, interwell motion, and tunable bandgap behavior.

3. To characterize how mass ratios, inertial-mechanism parameters, and nonlinear amplitude affect dispersion branches, bandgaps, branch merging, and set physically ad-

missible stability thresholds for embedding a general negative-inerter before proposing the same for obtaining desirable energy harvesting characteristics in nonlinear periodic structures.

4. To introduce a free-wave energy-harvesting metric for piezoelectric periodic chains based on settling time, post-transient voltage response, and one-period averaged harvested power.

5. To extend the free-wave harvesting theory to inertially coupled nonlinear piezomagnetoelastic chains and determine how magnetic bi-stability and inertance magnitude alter the optimum harvesting frequency, harvested-power magnitude, and useful bandwidth in the intrawell regime.

6. To analyze interwell transition-front propagation in dissipative piezomagnetoelastic chains and determine how such fronts generate spatially localized voltage and power profiles.

7. To introduce mass diatomicity into the nonlinear piezomagnetoelastic chain and investigate how acoustic-like and optical-like branches, mass contrast, nonlinear backbone curves, and transition fronts affect harvested power.

8. To validate analytical and semi-analytical predictions using direct numerical simulations of finite chains, thereby connecting infinite-chain Bloch descriptions to practically realizable transient dynamics.

1.9 Organization of the work

The remainder of the Thesis is organized as follows:

Chapter 2 gives a brief review of energy harvesting through structural vibrations and how the present research fits into the state of the art of energy harvesting through nonlinear periodic structures and what gaps it fills in the existing literature.

Chapter 3 presents the bi-stable, inertially coupled periodic chain and develops the ALIGN framework for bandgap manipulation in weakly and strongly nonlinear regimes. The chapter begins with the phase-plane behavior of the isolated unit cell, then derives weakly nonlinear dispersion relations, computes strongly nonlinear harmonic-balance Bloch branches, and validates the results using amplitude-linked inverse time-domain simulations.

Chapter 4 develops the linear piezoelectric free-wave harvesting baseline. It introduces a classical piezoelectric periodic chain, derives the relevant electromechanical dispersion and time-domain response, and defines the settling-time-aware maximum steady-state power metric. This chapter establishes the analytical bridge between free-wave propagation and harvested-power prediction.

Chapter 5 extends the free-wave harvesting framework to an inertially coupled nonlinear piezomagnetoelastic chain. It studies the linearized intrawell regime, the general strongly nonlinear intrawell and interwell regimes. The chapter shows how magnetic bistability and suitably chosen inertial coupling can enhance harvesting, broaden the useful

operating band, and generate spatially localized power through transition-front propagation.

Chapter 6 introduces mass diatomicity into the nonlinear piezomagnetoelastic chain. It analyzes the resulting acoustic-like and optical-like branch structure, linearized and nonlinear harvested-power characteristics, nonsimilar acoustic–optical transition fronts, and numerical validation through finite-chain simulations.

Finally, Chapter 7 summarizes the main findings, explains how the Thesis fills the literature gap identified in this Introduction, and outlines future research directions including experimental validation, higher-dimensional nonlinear harvesting lattices, multimode beam models, adaptive circuits, and optimization under uncertainty.

Chapter 2

A review of vibration energy harvesting, periodic systems, and nonlinear wave dynamics

2.1 Scope of the review

The aim of this Chapter is to place the present research within the state of the art in vibration energy harvesting, periodic structures, and nonlinear wave dynamics. The central problem studied in this Thesis is to connect wave propagation, nonlinear dispersion, electromechanical transduction, and transient free-wave response into a single design framework. The relevant literature has been reviewed across the overlapping areas of: vibration energy harvesting from ambient structural motion, wave-based harvesting in periodic and metamaterial systems, nonlinear and multistable energy harvesters, analysis methods available for nonlinear periodic media, inerter-mechanisms and diatomicity, and transition front-based localization.

This Chapter is organized as follows. Section 2.2 discusses why vibration energy harvesting is needed from a practical engineering viewpoint and why piezoelectric transduction has become a major route for powering low-power devices. Section 2.3 explains why periodic structures are useful for energy harvesting, rather than only for filtering or vibration isolation. Section 2.4 reviews nonlinear and multistable harvesters and identifies their advantages and limitations. Section 2.5 reviews nonlinear analysis tools relevant to amplitude-dependent dispersion and strongly nonlinear Bloch-wave computation. Section 2.6 discusses inertial coupling effects, diatomicity, nonlinear lattices, and transition fronts. Finally, Section 2.7 synthesizes the existing literature and clarifies how the present work fits into the broader research landscape.

2.2 Vibration energy harvesting and engineering need

Vibration energy harvesting is motivated by the need to power distributed, embedded, and low-power electronic systems without relying entirely on wired power or repeated battery replacement. This is especially important in structural health monitoring, civil infrastructure, rotating machinery, aerospace structures, inaccessible industrial systems,

and wireless sensor networks, where the sensor power demand is small, but the cost of wiring, maintenance, or physical access is high. Early studies established ambient vibration as a practical power source for microsystems and wireless sensor nodes, and surveys of vibration energy harvesting have classified the main transduction routes as piezoelectric, electromagnetic, and electrostatic conversion [129, 65, 66]. Broader reviews and device-level studies further emphasized that vibration harvesters should be understood not merely as small generators, but as coupled mechanical–electrical systems whose performance depends simultaneously on environmental excitation, mechanical design, transduction efficiency, and electrical power management [130, 131, 132, 133].

Piezoelectric vibration energy harvesting is particularly relevant to our present work because piezoelectric patches can be bonded directly to slender beams, plates, and periodic structural members. The direct electromechanical coupling between strain and voltage allows the same structural motion that carries elastic-wave energy to generate electrical output. The suitability of piezoelectric materials for vibration to electric conversion has been reviewed extensively, with emphasis on their high energy density, compatibility with small-scale devices, and ability to be integrated into structural components [134, 72, 69]. Distributed-parameter models of cantilevered piezoelectric harvesters have also shown that the commonly used single degree of freedom approximation is not always sufficient, especially when modal participation, strain distribution, and electromechanical boundary conditions matter [135, 136]. This is relevant to the present Thesis, where the harvester, instead of being treated as a lumped oscillator, is embedded as a unit cell in a periodic electromechanical chain.

Another important aspect of vibration energy harvesting is the electrical interface. The harvested power depends simultaneously on the mechanical response, load resistance, capacitance, electrical time constants, and power-conditioning circuits. Analytical studies of piezoelectric power output have clarified the role of load resistance and electromechanical coupling in determining the power delivered to the circuit [137, 138]. Power-electronic studies have shown that adaptive circuits, switching interfaces, and nonlinear electrical processing can significantly alter harvesting performance [139, 140, 141]. In the present Thesis, the electrical interface is deliberately kept simple, usually a passive resistive or resistive-capacitive shunt, so that the role of wave propagation, dispersion, and nonlinear mechanics can be isolated. Nevertheless, a review of the existing literature is important because it shows that the electrical time scale is a true design parameter, and not a secondary post-processing element.

Most classical vibration harvesters are designed to operate near a resonance frequency. Resonance tuning can produce large output when the excitation frequency is known and sustained, but it becomes restrictive when disturbances are broadband, intermittent, slowly varying, or spatially distributed. This limitation is one of the main motivations for nonlinear harvesters, periodic harvesters, and the free-wave framework developed in this Thesis. In particular, Chapters 4–6 shift extensively from the conventional idea of an externally forced resonant oscillator and instead consider free-wave propagation generated solely by initial conditions. This is a natural abstraction for disturbances such as impacts, moving loads, snap-through events, and localized perturbations in extended structures.

2.3 Effectiveness of periodic structures in energy harvesting

Periodic structures are useful for energy harvesting because they allow the designer to control the spatial transport of mechanical energy before electromechanical conversion occurs. In a conventional isolated harvester, the primary design objective is to investigate or analyze how the local oscillator responds to the excitation. In a periodic harvester, an additional criterion is how the host structure guides, slows, attenuates, localizes, or redistributes the wave energy before it reaches the transducer. For this reason, periodic media, besides being used extensively for vibration isolation and wave filtering, are also relevant to energy harvesting.

The foundation of this idea comes from the theory of phononic crystals, acoustic metamaterials, and elastic periodic media. Periodic structures can create Bragg bandgaps, locally resonant bandgaps, evanescent decay, directional propagation, and slow-wave effects [1, 2, 3, 100]. Reviews of phononic crystals and phononic materials have shown how such structures can manipulate sound and elastic waves through bandstructure engineering, local resonances, and spatial dispersion [142, 5, 143]. The damped-wave mechanism is also important because energy harvesting is inherently dissipative. The piezoelectric circuit extracts energy from the mechanical field, and therefore complex wavenumbers and attenuating Bloch waves become physically meaningful [144]. This is systematically treated through an analytically tractable framework in Chapter 4, where the complex Bloch wavenumber is used to encode both propagation and attenuation in the free-wave harvesting model.

Periodic electromechanical structures have also been studied through shunted piezoelectric arrays. Early work on rods with periodically shunted piezoelectric patches demonstrated that electromechanical coupling and shunt circuits can create attenuation and localization of structural waves [145]. Subsequent studies showed that periodic arrays of resonant shunts can be designed as tunable acoustic or elastic metamaterials, with electrical parameters used to shift bandgaps and modify wave transmission [146, 147]. These works are important as a reference, because they establish the principle that piezoelectric patches are not merely passive sensors or local harvesters; when arranged periodically, they become part of the wave-bearing medium.

Wave-based energy harvesting extends this idea by using the periodic structure to concentrate energy near transducers. Acoustic mirrors, metamaterial-inspired harvesters, resonator arrays, defect states, and metasurfaces have shown that wave guiding and localization can improve electrical output by controlling where mechanical strain accumulates before transduction [81, 82, 85, 86]. Gradient-index and lens-based phononic structures provide another route, where wave focusing is used to enhance the response of a harvesting element [148]. Graded elastic metasurfaces and related elastic-wave devices further demonstrate that spatial variation in a periodic or locally periodic architecture can be used to steer and concentrate wave energy [84, 87]. These developments justify the use of periodic structures for energy harvesting in the first place: periodicity gives the designer a spatial mechanism for controlling the mechanical energy flow, not just a frequency-domain mechanism for blocking waves.

From an engineering viewpoint, the periodic-harvesting concept is attractive for modular structures, beams with repeated attachments, bridge or rail components with repeated

features, aircraft panels with embedded periodic stiffeners, and distributed sensing systems. The periodic unit cell can be designed so that wave attenuation, voltage generation, and energy localization occur together. However, most wave-based harvesting studies still focus on sustained harmonic forcing, defect modes, or frequency-domain response under prescribed excitation. Chapters 4–6 of the Thesis instead addresses whether free waves generated solely by initial conditions can be used as the fundamental object for harvesting design. This shift requires a metric that connects transient wave decay to post-transient power extraction, which motivates the settling-time framework in Chapter 4.

2.4 Nonlinear and multistable energy harvesting

Nonlinearity has been widely explored as a means to overcome the narrowband nature of resonance-tuned harvesters. In a linear harvester, high output is usually obtained only near a resonance frequency, whereas nonlinear restoring forces can bend resonance curves, create multiple stable responses, broaden the effective response bandwidth, or enable large-amplitude interwell motion. Early nonlinear energy-harvesting studies showed that stochastic resonance, Duffing-type potentials, and nonlinear oscillators can improve harvesting under broadband or random excitation conditions [90, 149, 150]. Magnetically coupled and magnetically levitated harvesters further showed that magnetic forces provide a practical way to realize nonlinear stiffness and multistable potentials [151, 152, 153]. These works form an important background for Chapter 5, where magnetic bi-stability is used to model a piezomagnetoelastic periodic chain.

Bi-stable and multistable harvesters are especially relevant because they can exhibit both intrawell oscillations and interwell transitions. Intrawell oscillations occur near one stable equilibrium and may behave approximately as nonlinear oscillations about a well. Interwell transitions cross the potential barrier and can produce larger deformation, stronger voltage generation, and more complex dynamics. Experimental and theoretical studies of magnetopiezoelastic and bi-stable harvesters have shown that high-energy orbits, reversible hysteresis, magnetic coupling, and broadband snap-through response can enhance power output under appropriate forcing conditions [154, 155, 156, 157]. Review studies on bi-stable harvesters also emphasize that these devices introduce new design challenges, because the response may depend sensitively on forcing amplitude, initial condition, potential well depth, and coexistence of attractors [91, 158, 114]. This is precisely why the present Thesis distinguishes between intrawell and interwell regimes and investigates phase-plane behavior before embedding the unit cell into a chain.

Other nonlinear strategies include Duffing-type broadening, nonlinear energy sinks, frequency up-conversion, plucking, and hybrid transduction. Duffing oscillators have been studied for broadband piezoelectric harvesting, while kinetic or bi-stable oscillators have been used to exploit random or low-frequency excitations [159, 160]. Frequency up-conversion and magnetic plucking are practically important because many environmental vibrations are too slow to efficiently excite a small harvester directly; recent studies have used rotational bi-stability and enhanced magnetic plucking to improve low-power sensing applications [92, 93]. Nonlinear energy sinks and preloaded piezoelectric beams provide additional routes for increasing the effective bandwidth or lowering the operating frequency [97, 98]. The common theme has been that nonlinearity can broaden or reshape the response, but much of the literature remains centered on forced oscillator dynamics.

A complementary strand of nonlinear-vibration research is the theory of nonlinear energy sinks and targeted energy transfer. An essentially nonlinear attachment can enter transient resonance with one or more modes of a host structure and draw energy into a localized dissipative degree of freedom without requiring tuning to a single linear natural frequency [161, 162, 163, 164]. Extensions from a single oscillator to finite and semi-infinite chains show that this transfer can also be interpreted as a wave-mediated interaction between a distributed linear subsystem and a local nonlinear attachment [165, 166]. The relevance to vibration energy harvesting is especially clear under impulsive excitation: strongly nonlinear electromechanical attachments have been shown to generate transient high-frequency responses and enhanced electrical extraction from a single mechanical impulse [167]. Such mechanisms are particularly relevant to self-powered monitoring applications in which useful mechanical energy may arrive through intermittent impacts or short-duration disturbances rather than through sustained harmonic forcing. These studies establish that passive nonlinear localization can concentrate transient structural energy at a conversion site; however, they largely concern a primary structure coupled to one localized attachment, rather than a periodically repeated electromechanical medium in which dispersion, attenuation, spatial energy transport, and cell-wise harvested power are designed together.

The present work differs from this dominant forced-response viewpoint in two ways. Firstly, the nonlinear harvester is embedded in a periodic chain, so the relevant response is not only a local oscillator trajectory but also a propagating or attenuating wave field. Secondly, the excitation is treated as a free-wave initial-condition problem, rather than as a sustained harmonic base excitation or forcing. Chapter 5 uses this approach to show that the strongly nonlinear intrawell regime does not merely increase one peak; instead, it can produce a broad quasi-saturated high-power region over a range of free wave frequencies. The interwell regime then creates transition fronts that localize harvesting spatially. Thus, the nonlinear-harvesting literature motivates the present work, but the Thesis extends it from isolated forced harvesters to nonlinear periodic electromechanical media.

2.5 Analysis of nonlinear periodic structures

The analysis of nonlinear periodic structures requires methods that combine nonlinear dynamics with wave mechanics. In a linear periodic structure, the Bloch ansatz reduces the infinite system to an eigenvalue problem on a representative unit cell. The resulting band structure is independent of amplitude. In nonlinear periodic structures, however, the effective stiffness, modal content, stability, and branch shape can depend on wave amplitude. Weakly nonlinear structures can often be treated using simple perturbation methods, multiple scales, or asymptotic corrections to linear dispersion branches [17, 18, 19]. These approaches provide analytical insight but are limited when the nonlinearities are strong, non-polynomial, or generated by inherent geometrical configurations.

Geometric nonlinearity can also be designed so that the strength and character of modal interactions vary with the input energy. Inclined spring–damper mechanisms have been shown to generate strongly nonlinear stiffness and damping, while studies of impulsively loaded beams with geometrically nonlinear boundary conditions reveal pronounced redistribution of broadband input energy between structural modes [168, 169, 170]. For periodic media, it has been demonstrated that harmonic balance and multiple-scales anal-

ysis can be combined to predict wave attenuation in nonlinear periodic structures [171]. Together, these studies reinforce the need for the introductory amplitude-locked, multi-harmonic and time-domain validated framework adopted in this Thesis, since a single small-amplitude dispersion profile cannot generally capture energy-dependent modal redistribution, high-harmonic content, or the branch selected by a transient initial condition.

Strongly nonlinear systems require a broader computational and analytical approach. Nonlinear normal modes, backbone curves, invariant manifolds, and spectral submanifolds provide ways to interpret nonlinear modal dynamics in finite-dimensional systems [172, 24, 28, 29]. Nonlinear system-identification and continuation methods also provide practical tools for analyzing experimentally or numerically generated nonlinear responses [173, 174]. Frequency-domain approaches such as harmonic balance, alternating frequency–time methods, and continuation-based algorithms are particularly useful when periodic or nearly periodic responses are sought [175, 176, 177]. These methods are central to Chapter 3, where the comprehensively proposed ALIGN framework uses multi-harmonic, Bloch-consistent harmonic balance and branch tracking to compute strongly nonlinear dispersion branches.

Periodic media also introduce additional difficulties beyond those encountered in isolated nonlinear oscillators. The computed nonlinear periodic orbit must be compatible with a prescribed Bloch phase, and neighboring branches may exchange modal content or merge as the wavenumber changes. In finite chains, boundary reflections, finite-size effects, and imperfect initialization can further obscure the connection between an infinite-chain Bloch branch and a time-domain simulation. Finite element and spectral element formulations have been used to treat wave propagation in more complex periodic structures, while numerical wavenumber-extraction methods have been developed for finite waveguides and structural systems [178, 179, 180]. Data-driven and finite element-based nonlinear dispersion methods have also added to the available tools for structured media with complex geometry [34, 33, 35].

The first work of the Thesis is motivated by precisely these methodological issues. The bi-stable inertially coupled chain considered in Chapter 3 contains non-polynomial geometric nonlinearities and a nontrivial mass matrix induced by inertial-coupling effects. A simple linear Bloch analysis is not sufficient, while a full finite-chain simulation for every amplitude and wavenumber is inefficient. The ALIGN framework therefore combines weakly nonlinear asymptotics, strongly nonlinear Bloch-consistent harmonic balance, robust branch matching, and amplitude-linked inverse time-domain validation. This places this introductory work within the broader state of the art in nonlinear modal analysis, nonlinear Bloch-wave computation, and numerical validation of strongly nonlinear periodic responses.

2.6 Inertial coupling, diatomicity, and nonlinear transition fronts

Inertial-coupling mechanisms and inerter-based concepts provide another important context for the present research work. The inerter was introduced as a mechanical network element that generates a force proportional to relative acceleration, thereby allowing effective inertial forces to be much larger than the physical mass of the device [181]. In civil and

mechanical vibration control, inerter-based devices have been used for vibration suppression, seismic mitigation, and tuned mass-damper-inerter configurations [182, 183, 184]. In acoustic and elastic metamaterials, inertial amplification provides a route to low-frequency attenuation without requiring very large local resonator masses [51, 52, 55]. The present Thesis uses inerters not as an isolated absorber, but as a unit-cell mechanism that reshapes dispersion, effective inertia, and localization in nonlinear periodic chains. Specifically, attention has been shifted to parameterized negative-inerter modules instead of conventional inertial amplifiers. A conventional inerter has a positive coefficient relating its terminal force to relative acceleration [55]. In the present reduced model, a negative signed inertance, $b_a < 0$, instead reduces the effective inertia associated with selected relative motions; it does not represent a negative physical mass. Architected systems with elastically supported masses and moment-free rigid links provide a precedent for stable negative inertial coupling [62]. Admissibility is assessed through positive definiteness of the complete mass matrix, not through the sign of an isolated coefficient. The coupling itself does not dissipate energy.

The reasons for the deliberate choice of a stable negative-inerter in context of the present work are significant and are outlined as follows:

1. Conventional inertial amplifiers add effective inertia and associated kinetic energy to the non-uniform wave modes and can render them unstable in transient free-wave regimes.

2. In contrast, negative-inertance reduces the effective inertia of selected non-uniform wave modes and at the same time retains stability of the complete lattice mass matrix by setting mathematically and dynamically well-defined positive-definiteness criterion resulting in admissibility thresholds which can be linked back directly to the inerter's design parameters.

3. The resulting inertial-reduction regime offers enhanced bandgap tunability which is predicted adequately via inexpensive harmonic balance algorithms, nonlinear broadening of the useful free-wave harvesting range, theoretically predictable front-mediated localization of voltage and power in a sufficiently interior portion of finite nonlinear periodic chains away from boundary effects, and enhanced nonlinear harvested power induced by mass-diatomic unit cells.

4. These desirable design outcomes are not realizable through our proposed harvesting/wave tuning nonlinear models using conventional inertial amplifiers which have been employed extensively in existing literature.

Diatomic and multiatomic unit cells have provided an additional route for band-structure enrichment. Even in a linear chain, mass contrast can create acoustic-like and optical-like branches, bandgaps, and modal separation. In nonlinear lattices, the interaction between mass contrast and amplitude-dependent stiffness can produce richer dispersion behavior, branch bending, and mode conversion. Granular crystals provide important examples of nonlinear wave propagation in discrete chains, including solitary waves, tunable bandgaps, and nonlinear coherent structures [185, 186, 187]. These studies are relevant to the work in Chapter 6 because the mass-diatomic piezomagnetoelastic

chain model developed there combines acoustic–optical branch structure with strong nonlinearity, but adds electromechanical conversion and harvesting metrics.

The granular-chain literature also establishes that strong nonlinearity can create transport and localization mechanisms with no direct linear analogue. In [188] an asymptotic solitary-wave description has been obtained for a Hertzian chain of elastic spheres, while experiments on strongly nonlinear phononic crystals have showed that solitary-wave speed and waveform can be tuned through material, geometric, and loading parameters [189]. Tensegrity lattices extend this idea to architected media whose solitary-wave response can be adjusted across multiple structural scales [190]. In diatomic granular crystals, discrete breathers provide a particularly relevant example of intrinsic energy localization associated with the richer spectral structure generated by the two-particle unit cell [191]. Nesterenko's monograph provides the broader foundation for strongly nonlinear impulse propagation, solitary waves, and energy localization in heterogeneous and particulate media [192]. These results motivate the present use of mass contrast, nonlinear branch structure and localized fronts, but they generally stop at mechanical transport or localization itself rather than coupling the localized wave field to a cell-wise electrical energy-harvesting metric.

Transition fronts and localized nonlinear waves provide another important connection between existing literature and the present work. In multistable mechanical systems, interwell transitions can propagate as fronts, domain walls, or solitary-like waves. These waves can carry concentrated mechanical energy and can switch the state of a lattice as they propagate [38, 125, 124]. Recent work has also connected topological ideas and mechanical lattice design to robust localization and wave transport [193, 194, 119]. In the present Thesis, interwell transition fronts are not used only as mechanical switching events. Instead, they are coupled to piezoelectric circuits so that their localized deformation fields generate localized voltage and harvested power. This is one of the key advancements and flexibilities of the present work from much of the transition-wave literature.

The diatomic extension in Chapter 6 brings these ideas together. The addition of a second principal mass creates acoustic-like and optical-like branches and introduces a mass-contrast design parameter. The nonlinear piezomagnetoelastic potential creates amplitude-dependent branch behavior and front propagation. The stable negative-inerter coupling reshapes effective inertia and admissible wavenumber ranges. Finally, the piezoelectric circuit converts the resulting deformation into electrical output. This combination shows why band structure alone is not enough for harvesting design: the useful branch must also have voltage-producing modal participation, appropriate decay, and favorable excitation by the initial condition.

2.7 Literature gap and position of the present work

The literature review shows that each element of the present research has had an independent foundation. Vibration energy harvesting provides the practical need and the electromechanical transduction mechanism. Periodic structures provide a way to control wave propagation and spatial energy distribution. Nonlinear dynamics provides amplitude dependence, multistability, and transition fronts. Inertial coupling and mass diatomicity provide passive routes to tune effective inertia, bandgaps, and branch structure. However, the intersection of these themes remains less developed than the individual areas.

Related pulse-interaction studies have further shown that a local strongly nonlinear element can alter reflection, transmission, and the direction of transient energy flow. In particular, the reflection of short pulses from a string coupled to a strongly nonlinear oscillator depends sensitively on the dynamics of the nonlinear attachment [195]. This provides an important mechanical precursor to the present Thesis: nonlinear attachments can redirect transient wave energy passively, but the remaining challenge is to repeat the attachment periodically, include electromechanical conversion, and quantify the resulting voltage and harvested power after the free-wave transient has settled on a smooth envelope.

Hence, moving forward from existing literature, the first identifiable gap is that vibration energy harvesting is still often formulated as a forced-resonance problem. This is appropriate when the excitation is sustained and close to a known frequency, but it is less natural for impacts, intermittent ambient disturbances, snap-through events, moving loads, or localized initial perturbations. Chapter 4 addresses this gap by developing a settling-time-aware free-wave harvesting framework for a piezoelectric periodic chain. This work uses the periodic structure to derive effective coefficients and a post-transient power metric for unforced (free) wave motion.

The second gap is that nonlinear energy harvesters are frequently studied as isolated oscillators, while periodic metamaterial harvesters are often studied through linear wave focusing, defect modes, or forced-response localization. Chapter 5 bridges these viewpoints by embedding a nonlinear piezomagnetoelastic harvester inside an inertially coupled periodic chain. In the intrawell regime, the strongly nonlinear dynamics broaden the useful high-power region. In the interwell regime, transition fronts create spatially localized harvesting. Thus, the harvester is not added to a waveguide as a separate element; it is part of the nonlinear wave-bearing medium.

The third gap is methodological. Strongly nonlinear periodic systems with geometric nonlinearities, inertial and electromechanical coupling are not easily handled by a single standard tool. Perturbation methods are useful near a stable equilibrium, but they do not capture strongly nonlinear branch merging and high-harmonic content. Direct simulations are reliable but expensive and may not directly resemble Bloch-compatible waveforms. Chapter 3 addresses this by developing ALIGN, a workflow that connects weakly nonlinear asymptotics, multi-harmonic harmonic balance, branch tracking, and amplitude-linked inverse time-domain validation.

The fourth gap concerns the role of richer unit-cell structure. Most harvesting studies focus on monoatomic chains or isolated harvesters. Chapter 6 shows that a mass-diatomic nonlinear piezomagnetoelastic chain can create acoustic-like and optical-like branches, nonsimilar acoustic–optical transition fronts, and substantially enhanced nonlinear harvested power. This places mass contrast alongside magnetic bi-stability, inertial coupling, and electrical loading as a genuine harvesting design parameter.

The overall approach of the Thesis is therefore as follows: It treats nonlinear periodic structures as wave-mediated electromechanical systems in which bandgap manipulation, transient free-wave propagation, nonlinear branch shaping, spatial localization, and harvested power must be designed together.

Chapter 3

Bandgap manipulation through a bi-stable inertially coupled strongly nonlinear periodic chain

3.1 A bi-stable-inertial unit cell underpinning nonlinear metamaterials

We start our investigation of bandgap engineering and hence tunable dispersion in nonlinear periodic structures through the analysis of a periodic chain constructed by repeating a bi-stable, inertially coupled, strongly nonlinear unit cell with coupled horizontal-vertical dynamics. This unit-cell structure is chosen because of the rich nonlinear dynamical behavior it can exhibit comprising bi-stability and inertial coupling. More specifically, we aim to include stable negative-inerter effects and geometric bi-stability within one coherent periodic structural model to establish a systematic and analytically tractable pathway for demonstrating tunable dispersion behavior for a fairly rich periodic structure. Bi-stability and negative-inertial coupling of relative motion play a key role both qualitatively and quantitatively in the free-wave energy harvesting behavior and trends of nonlinear periodic models studied in the present Thesis. So, this Chapter is intended as a starting point to propose and validate a general semi-analytical framework for discrete nonlinear periodic structures with a fairly complex underlying geometry and rich dynamical behavior before investigating the energy harvesting potential of such periodic models in general.

3.1.1 The mechanical model

We choose a 3 degree of freedom (DOF) model which consists of a bi-stable mass (m_2) constrained to move in the vertical direction coupled by inclined linear springs with two linear spring-mass oscillators having degrees of freedom in the horizontal direction (m_1 and m_3). The horizontally moving masses are fixed to rigid supports via linear horizontal springs. In addition, the masses m_1 and m_3 are coupled via rigid links to a stable negative inerter parameterized by the mass-dimensional design parameter m_a and the initial architectural tuning angle α of the rigid links with the horizontal axis, also constrained

to move in the vertical direction. The angle of inclination of the linear springs with the horizontal axis in the initial undeformed configuration is denoted by ϕ. We choose the design such that $\phi > \alpha$. The displacement of the two linear oscillators are denoted by u and w in the horizontal direction and the displacement of the bi-stable mass is denoted by v in the vertical direction. The natural length of the springs are denoted by L. The linear stiffness co-efficients of the inclined and horizontal springs are taken as k. A schematic diagram of the model is shown in Fig. 3.1.

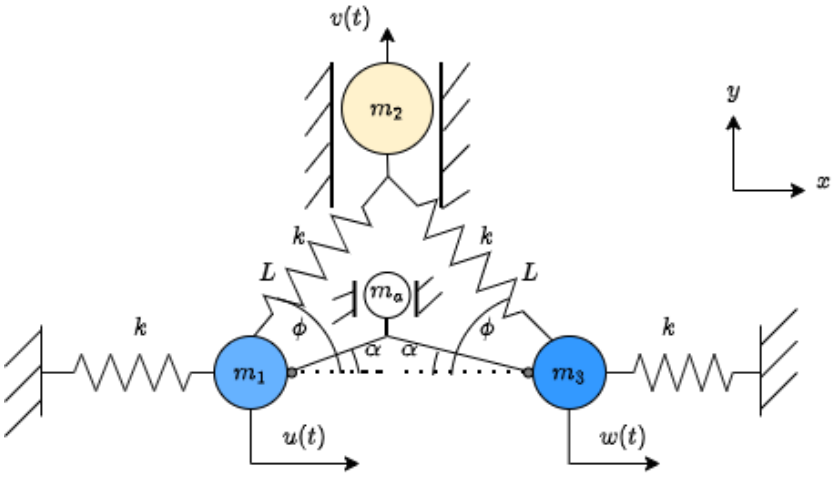


Fig. 3.1: The 3 degree of freedom bi-stable-inertial model fixed at both ends, where $u(t)$, $w(t)$ represent the horizontal degrees of freedom of masses m_1 and m_3 respectively, $v(t)$ represents the vertical degree of freedom of the bi-stable mass m_2, k denotes the linear stiffness co-efficients of all the springs, L denotes the natural length of the springs in the initial undeformed configuration, ϕ denotes the angle of inclination of the inclined linear springs with the horizontal axis in the initial undeformed configuration, α denotes the angle of inclination of the rigid links of the stable negative-inerter with the horizontal axis in the initial undeformed configuration, the closed gray-shaded circles at the rigid-link connections denote ideal, moment-free pin/hinge joints.

Here ϕ and α denote the fixed inclination of the springs and the rigid links respectively in the initial undeformed reference configuration shown in Fig. 3.1. These are geometric design parameters, not the instantaneous spring or link angles, consistently with standard snap-through spring or rigid-link inertial-mechanism reductions [38, 115]. Also, it is noted here that the schematic used to represent the stable negative-inerter module is a reduced-order conceptual schematic retaining the two physical design quantities m_a and α without claiming to be a detailed prototype design or fabrication drawing.

This specific model is chosen because of its rich dynamical configuration capable of showing both bi-stability and inerter effect with coupled horizontal-vertical dynamics and intrawell and interwell oscillations of the mass m_2. We hence perform a thorough dynamic analysis of the system behavior in the phase space before proposing this model as a constituent repeating unit cell for enhanced bandgap manipulation in nonlinear metamaterials.

3.1.2 Dynamic analysis in the phase plane

Equations of motion and non-dimensionalization

The displacements u and w are measured in the positive x direction from the reference points in the initial unstressed configuration as shown in Fig. 3.1, where all the springs are unstressed and are in their natural undeformed length L. The displacement v is measured in the positive y direction and the reference $v = 0$ is taken at the axis of the horizontal linear springs which is shown by dotted horizontal lines in Fig. 3.1. So, in the initial unstressed equilibrium configuration which is shown in Fig. 3.1, $v = L\sin\phi$. The elastic and bi-stable restoring-force contributions are obtained from the usual Lagrangian of the three principal masses and the linear springs. The inertial coupling between the horizontal coordinates u and w is introduced through the reduced two-terminal constitutive law of a stable negative inerter. The resulting equations are therefore obtained as:

$$m_1\ddot{u} + ku - k(L\cos\phi - u)\left(1 - \frac{L}{\sqrt{(L\cos\phi - u)^2 + v^2}}\right) + F\cos\alpha = 0 \tag{3.1}$$

$$m_2\ddot{v} + kv\left(2 - \frac{L}{\sqrt{(L\cos\phi - u)^2 + v^2}} - \frac{L}{\sqrt{(L\cos\phi + w)^2 + v^2}}\right) = 0 \tag{3.2}$$

$$m_3\ddot{w} + kw + k(L\cos\phi + w)\left(1 - \frac{L}{\sqrt{(L\cos\phi + w)^2 + v^2}}\right) - F\cos\alpha = 0 \tag{3.3}$$

Here, F denotes the signed equivalent internal terminal-force resultant transmitted by the stable negative-inerter coupling. The sign convention is chosen such that the generalized forces exerted by the coupling on the u and w co-ordinates are

$$Q_u^{\mathrm{NI}} = -F\cos\alpha, \qquad Q_w^{\mathrm{NI}} = +F\cos\alpha,$$

respectively. The relative displacement and acceleration across the two terminals of the negative inerter can be written in terms of the displacements of masses m_1 and m_3 as:

$$\begin{aligned} r(t) &= w(t) - u(t) \\ \ddot{r}(t) &= \ddot{w}(t) - \ddot{u}(t) \end{aligned} \tag{3.4}$$

The signed equivalent inertance is parameterized in terms of the mass-dimensional design parameter m_a and the architectural angle α as

$$b_a^{(3)} = -\beta_a^{(3)}, \qquad \beta_a^{(3)} = \frac{m_a}{4}\cot^2\alpha = \frac{m_a\cos^2\alpha}{4\sin^2\alpha} > 0. \tag{3.5}$$

Thus, $b_a^{(3)} < 0$ denotes the signed inertance, while $\beta_a^{(3)} = -b_a^{(3)} > 0$ denotes its magnitude. The two-terminal constitutive relation is

$$Q_u^{\mathrm{NI}} = b_a^{(3)}\ddot{r}, \qquad Q_w^{\mathrm{NI}} = -b_a^{(3)}\ddot{r}, \tag{3.6}$$

where Q_u^{NI} and Q_w^{NI} are the generalized forces exerted on the u and w coordinates, respectively.

In terms of the force notation used in Eqs. (3.1), (3.3) the terminal-force relation is equivalently obtained as:

$$F\cos\alpha = -b_a^{(3)}(\ddot{w} - \ddot{u}) = \frac{m_a\cos^2\alpha}{4\sin^2\alpha}(\ddot{w} - \ddot{u}). \tag{3.7}$$

With these relations (Eqs. (3.5), (3.7)), Eqs. (3.1), (3.2), (3.3) can be rewritten as

$$m_1\ddot{u} + ku - k(L\cos\phi - u)\left(1 - \frac{L}{\sqrt{(L\cos\phi - u)^2 + v^2}}\right) + \frac{m_a(\ddot{w} - \ddot{u})\cos^2\alpha}{4\sin^2\alpha} = 0 \quad (3.8)$$

$$m_2\ddot{v} + kv\left(2 - \frac{L}{\sqrt{(L\cos\phi - u)^2 + v^2}} - \frac{L}{\sqrt{(L\cos\phi + w)^2 + v^2}}\right) = 0 \quad (3.9)$$

$$m_3\ddot{w} + kw + k(L\cos\phi + w)\left(1 - \frac{L}{\sqrt{(L\cos\phi + w)^2 + v^2}}\right) - \frac{m_a(\ddot{w} - \ddot{u})\cos^2\alpha}{4\sin^2\alpha} = 0 \quad (3.10)$$

The characteristic length for non-dimensionalization is taken to be the natural length of the springs L. The non-dimensional time is taken as $\tau = \omega_n t$, where $\omega_n = \sqrt{\frac{k}{m_1}}$. The mass ratios are taken as $\frac{m_2}{m_1} = r_1$, $\frac{m_3}{m_1} = r_2$ and $\frac{m_a}{m_1} = r_a$. The non-dimensional displacements are obtained as $\eta = \frac{u}{L}$, $\xi = \frac{v}{L}$ and $\psi = \frac{w}{L}$. With this, the non-dimensional equations of motion are obtained as

$$\eta'' + \eta - (\cos\phi - \eta)\left(1 - \frac{1}{\sqrt{(\cos\phi - \eta)^2 + \xi^2}}\right) + \frac{r_a(\psi'' - \eta'')\cos^2\alpha}{4\sin^2\alpha} = 0 \quad (3.11)$$

$$r_1\xi'' + \xi\left(2 - \frac{1}{\sqrt{(\cos\phi - \eta)^2 + \xi^2}} - \frac{1}{\sqrt{(\cos\phi + \psi)^2 + \xi^2}}\right) = 0 \quad (3.12)$$

$$r_2\psi'' + \psi + (\cos\phi + \psi)\left(1 - \frac{1}{\sqrt{(\cos\phi + \psi)^2 + \xi^2}}\right) - \frac{r_a(\psi'' - \eta'')\cos^2\alpha}{4\sin^2\alpha} = 0 \quad (3.13)$$

Where prime denotes differentiation with respect to the non-dimensional time τ.

This specific model with a bi-stable mass coupled to two orthogonally moving linear oscillators is considered because of its unique coupled vertical-horizontal dynamics. Previous studies like [196] have considered either the bi-stable mass in isolation as a single DOF system or a periodic chain of single DOF bi-stable masses coupled to each other by horizontal linear springs acting as force transfer elements [38] capable of exhibiting only horizontal dynamics.

Throughout this Thesis, 'exact nonlinear equations' means the unlinearized equations of the adopted reduced-order physical model, with its stated kinematic, modal and constitutive assumptions retained. Exactness is therefore relative to that model, not a claim that it reproduces every feature of a real physical system.

Phase plane behavior

We investigate how the bi-stable mass (m_2) behaves when coupled to masses m_1 and m_3 in its phase plane (displacement ξ vs velocity ξ') by direct numerical simulations of the governing non-dimensional equations of motion (Eq. (3.11)-(3.13)) and plot the Poincare sections for different values of the system parameters.

The nonlinear elastic restoring force acting on the mass m_2 in non-dimensional form is given by

$$F_\xi = -\xi\left(2 - \frac{1}{\sqrt{(\cos\phi - \eta)^2 + \xi^2}} - \frac{1}{\sqrt{(\cos\phi + \psi)^2 + \xi^2}}\right) \quad (3.14)$$

This is a force which has been derived from a potential function. So, we can say that when this force becomes zero, those corresponding displacements η, ξ, ψ refer to a stationary (local minima/ local maxima) point for the mass m_2 in the coupled system. On considering the potential function of the system in the non-dimensional form as $U = U(\eta, \xi, \psi)$ and setting the partial derivative with respect to the degree of freedom ξ to zero like

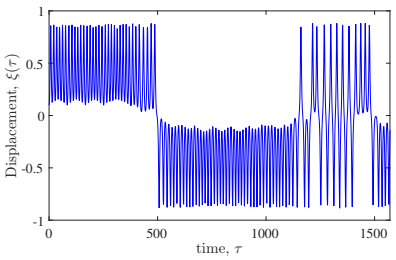
$$\frac{\partial U}{\partial \xi} = F_\xi = 0 \tag{3.15}$$

We obtain two energy minima for the mass m_2 in the coupled system at $(\eta, \xi, \psi) = (0, \pm \sin\phi, 0)$, which is quite evident from the stand-alone bi-stable nature of the oscillator m_2. Had the bi-stable oscillator been connected to rigid supports instead of masses m_1 and m_3, it would have two stable centers at $\xi = \pm \sin\phi$ and one unstable saddle at $\xi = 0$ taking into account that the same scheme of non-dimensionalization has been used.

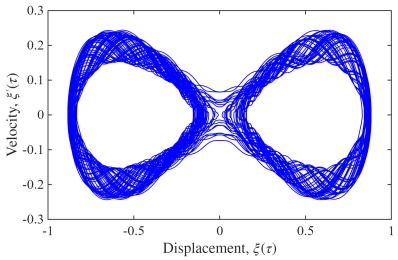
It is well-known from existing literature [197] that forced bi-stable oscillators or double-well oscillators exhibit chaotic strange attractor motion or transient chaos for large enough amplitude of the forcing when it undergoes interwell oscillations or snap-through motion. The corresponding Poincare map generates a scattered, non-repeating set of points which fall on a fractal set which can be interpreted as a cross-section for chaotic strange attractors for sustained chaos, and two sets of closed Poincare points for transient chaos where the motion ultimately settles into small periodic oscillations in one of the energy wells. In our chosen 3 DOF model, in contrast to a single DOF bi-stable mass connected to rigid supports, we have the bi-stable mass coupled to two orthogonal degrees of freedom. We examine the phase-plane behavior of this system and subsequent Poincare maps by taking projections of the six-dimensional phase space on two-dimensional planes, where for any particular mass, the projection is taken on the plane defined by its corresponding displacement and velocity. For examining the phase-plane behavior, we use direct numerical simulations with the fourth-order Runge-Kutta method (ode45 in MATLAB). For initial conditions of the system as for now, we keep the initial states of masses m_1 and m_3 at zero and apply an initial state of displacement and velocity on the bi-stable mass m_2 in order to study its rich dynamics specifically. Since we are interested in manipulating the dispersion characteristics of 'free' wave propagation using this model as a repeating block, we do not apply any kind of forcing in our system and study the phase behavior evolving solely due to the initial conditions imposed.

We use two sets of initial conditions for the double-well mass m_2 in the non-dimensional form, one keeping the mass m_2 close to its unstable equilibrium position or saddle at $\xi = 0$ and one keeping the mass m_2 close to one of its stable equilibrium positions at $\xi = \sin\phi$. Since we do not apply any driving force in our system and let it evolve freely, it is practically difficult to define a Poincare section even in a two-dimensional projection of the six-dimensional phase space. So, we obtain the Poincare map for m_2 by plotting the points $\xi(\tau)$ and $\xi'(\tau)$ whenever τ is an integer multiple of $\frac{2\pi}{\omega_\xi}$, where we define ω_ξ as the non-dimensional linearized natural frequency of m_2 which can be easily obtained by assuming small perturbations from the stable equilibrium point of m_2 at $\xi = \sin\phi$ and performing a Taylor series expansion. As will be shown later in Eq. (3.24), this non-dimensional linearized natural frequency is obtained as $\omega_\xi = \sqrt{\frac{2\sin^2\phi}{r_1}}$. Sampling at $T_\xi = 2\pi/\omega_\xi$ provides a reference stroboscopic map. It does not assume that the finite-amplitude period equals the linearized period. Frequency detuning can

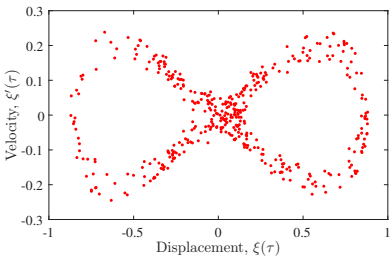
therefore spread the sampled points even for regular motion, so scattering alone is not evidence of chaos. Alternatives include a directed crossing of a fixed transverse phase-space section, or sampling at a period estimated from the nonlinear time history. For each set of initial conditions, we use three sets of values of the mass ratios r_1, r_2, r_a, keeping $r_2 = 1$ to maintain spatial symmetry and hence avoid the issues of non-similarity and energy-dependence of the modal curves as much as possible.



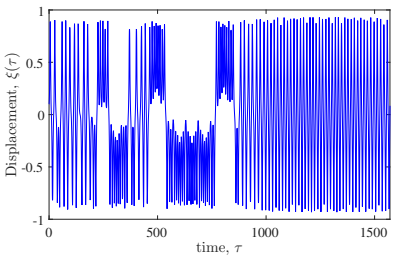
(a) Time-domain response for $r_1 = 1$, $r_2 = 1$, $r_a = 0.5$



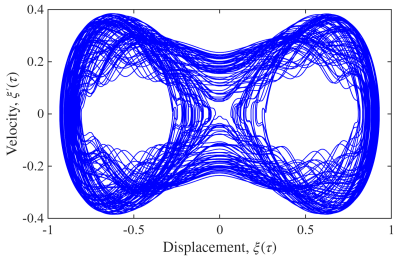
(b) Phase orbit for $r_1 = 1$, $r_2 = 1$, $r_a = 0.5$



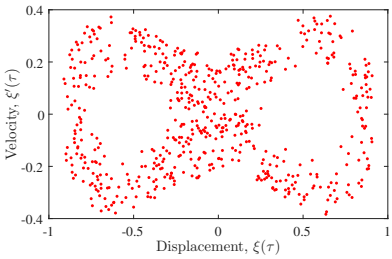
(c) Poincare map for $r_1 = 1$, $r_2 = 1$, $r_a = 0.5$



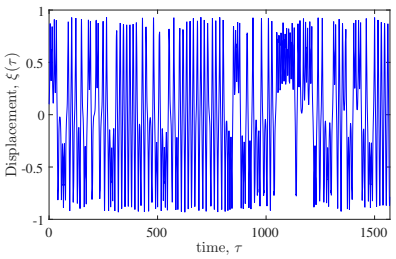
(d) Time-domain response for $r_1 = 0.5$, $r_2 = 1$, $r_a = 0.5$



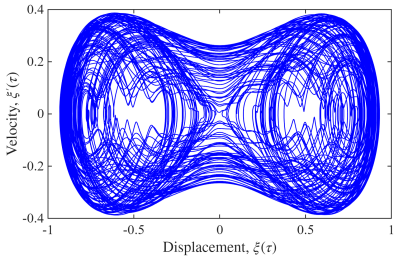
(e) Phase orbit for $r_1 = 0.5$, $r_2 = 1$, $r_a = 0.5$



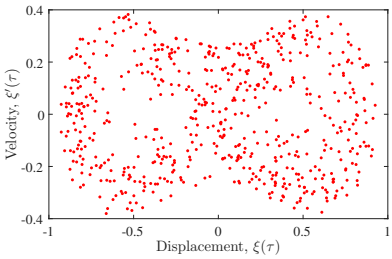
(f) Poincare map for $r_1 = 0.5$, $r_2 = 1$, $r_a = 0.5$



(g) Time-domain response for $r_1 = 0.5$, $r_2 = 1$, $r_a = 0.3$



(h) Phase orbit for $r_1 = 0.5$, $r_2 = 1$, $r_a = 0.3$

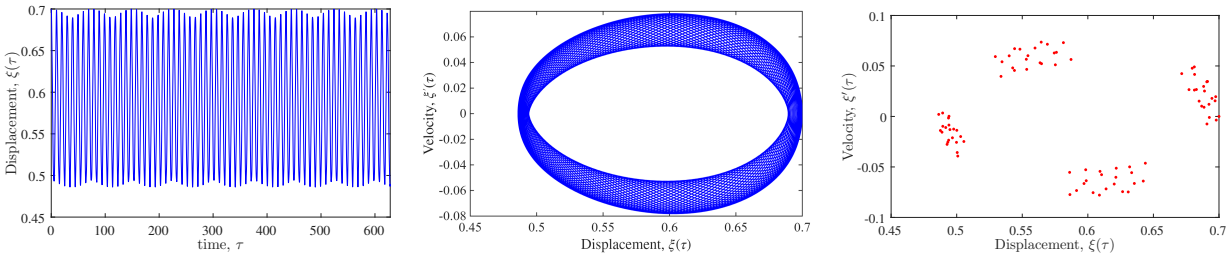


(i) Poincare map for $r_1 = 0.5$, $r_2 = 1$, $r_a = 0.3$

Fig. 3.2: Time-domain response, phase orbit and Poincare maps for the bi-stable mass m_2 in our chosen 3 DOF model for initial conditions, $\xi(0) = 0.1$, $\xi'(0) = 0$, keeping the initial states of masses m_1 and m_3 to be zero. Angles of inclination in the initial unstressed equilibrium configuration are taken as $\sin\phi = 0.6$ and $\sin\alpha = 0.5$

Fig. 3.2 and Fig. 3.3 show the time-domain response, phase orbit and Poincare maps for the bi-stable mass m_2 in our chosen 3 DOF model for two sets of initial conditions of m_2, keeping the initial states of masses m_1 and m_3 at zero.

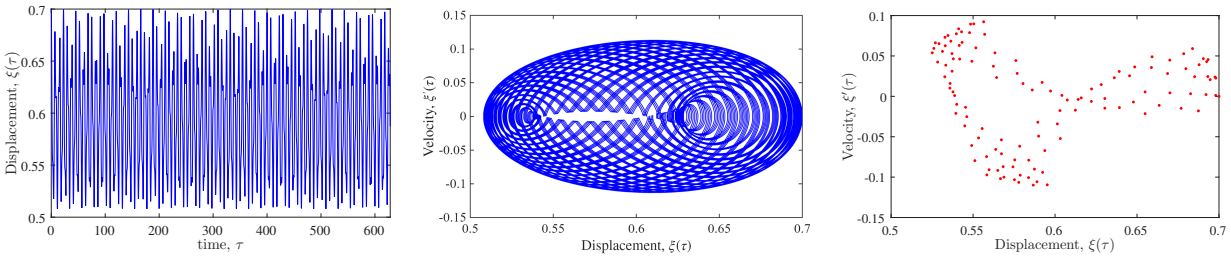
As we can see from Fig. 3.2, when we impose an initial displacement condition on



(a) Time-domain response for $r_1 = 1$, $r_2 = 1$, $r_a = 0.5$

(b) Phase orbit for $r_1 = 1$, $r_2 = 1$, $r_a = 0.5$

(c) Poincare map for $r_1 = 1$, $r_2 = 1$, $r_a = 0.5$



(d) Time-domain response for $r_1 = 0.5$, $r_2 = 1$, $r_a = 0.3$

(e) Phase orbit for $r_1 = 0.5$, $r_2 = 1$, $r_a = 0.3$

(f) Poincare map for $r_1 = 0.5$, $r_2 = 1$, $r_a = 0.3$

Fig. 3.3: Time-domain response, phase orbit and Poincare maps for the bi-stable mass m_2 in our chosen 3 DOF model for initial conditions, $\xi(0) = 0.7$, $\xi'(0) = 0$, keeping the initial states of masses m_1 and m_3 to be zero. Angles of inclination in the initial unstressed equilibrium configuration are taken as $\sin\phi = 0.6$ and $\sin\alpha = 0.5$

m_2 close to its unstable equilibrium point or saddle at $\xi = 0$, the time-domain response consists of several snap-through motions where the mass m_2 crosses the energy hump at $\xi = 0$ repeatedly and undergoes interwell oscillations between the two energy wells at $\xi = \pm\sin\phi = \pm 0.6$. The phase orbit shows a tangled set of pairs of homoclinic orbits due to multiple crossings of the energy hump for our chosen time window. The tangled appearance arises as an artifact of taking a two-dimensional projection of our six-dimensional phase space which is typical of systems with more than two variables in the phase space. The Poincare section instead of falling on a fractal set as was in the case of a single DOF forced double-well oscillator [197], shows multiple sets of pairs of homoclinic orbits. Although the time-domain motion is aperiodic and suggests the possibility of transient chaos, the Poincare section does not indicate the existence of a strange attractor, so we can draw a qualitative assumption that there can be transient chaos in our 3 DOF model before the mass m_2 settles down in one of its two potential wells or to periodic oscillations with large amplitudes around its saddle at $\xi = 0$. We also notice that the time-domain and phase-plane behavior is sensitively dependent on the combination of the mass ratios r_1, r_2, r_a while keeping the initial conditions and other parameters fixed. As we go from Fig. 3.2(a) and Fig. 3.2(b) to Fig. 3.2(d) and Fig. 3.2(e), keeping r_2 and r_a fixed, as $r_1 = \frac{m_2}{m_1}$ is decreased from 1 to 0.5, the mass m_2 undergoes more intrawell oscillations around the stable equilibrium points at $\xi = \pm\sin\phi$ and periodic oscillations with larger amplitudes around the saddle at $\xi = 0$ in addition to interwell oscillations. We notice this same trend as we go from Fig. 3.2(d) and Fig. 3.2(e)

to Fig. 3.2(g) and Fig. 3.2(h), keeping r_1 and r_2 fixed, and decreasing $r_a = \frac{m_a}{m_1}$ from 0.5 to 0.3, i.e. more intrawell oscillations around $\xi = \pm \sin\phi$ and periodic oscillations with large amplitudes around the saddle at $\xi = 0$ of the mass m_2. This dependence of intrawell oscillations and large-amplitude periodic motions on the mass ratios sets a useful motivation for using this model as a repeating unit for manipulating wave dispersion characteristics by varying the mass ratios in discrete nonlinear periodic structures or in general nonlinear metamaterials.

Fig. 3.3 shows the time-domain response, phase-plane behavior and Poincare section for the mass m_2 in our 3 DOF model, when we impose an initial displacement condition on m_2 sufficiently close to its stable equilibrium position at $\sin\phi = 0.6$ and keep the initial states of masses m_1 and m_3 at zero. Quite expectedly, the mass m_2 for this initial condition, remains close to its initial stable configuration and performs intrawell oscillations within the energy well at $\sin\phi = 0.6$ as can be seen from Fig. 3.3. For our chosen time window, we get repeated closed orbits each corresponding to one complete oscillation in the energy well. Although we see a dependence of the dynamic behavior on the mass ratios in this case as well. As we keep r_2 fixed and decrease both r_1 and r_a, we get more cycles of oscillations in the energy well. However, the mass m_2 for this initial condition close to its stable equilibrium position, even if coupled to orthogonally moving masses m_1 and m_3, never crosses the saddle or the energy hump at $\xi = 0$, and stays in its potential well at $\xi = \sin\phi$. This becomes useful if we want to study the behavior of a periodic structure composed of this 3 DOF model as a repeating unit, close to its global energy minima by using standard analytical techniques like perturbation methods or asymptotic analysis. The mass-ratio combinations in Fig. 3.2 and Fig. 3.3 were selected to represent the principal qualitative and quantitative variations observed in this phase-space study, including intrawell confinement and repeated interwell transitions. These representative cases are not intended as an exhaustive bifurcation diagram or to locate every transition threshold.

Overall, we can say that the double-well or bi-stable oscillator m_2 in spite of being coupled to two orthogonal degrees of freedom, preserves its rich and complex nonlinear dynamical behavior to a significant extent close to its stable/ unstable equilibrium points and this sets our motivation to use this 3 DOF model as a repeating unit for manipulating wave propagation properties in nonlinear periodic structures or fancily called nonlinear metamaterials.

3.2 A generalized, consolidated framework for discrete nonlinear periodic structures

The major challenge faced while performing the dynamic analysis of general strongly nonlinear discrete periodic systems is usually the lack of a generalized analytical framework which arises due to the coupled ordinary differential-difference equations with non-integrable, non-polynomial forcing terms. The next difficulty arises due to the sensitive dependence of the response of strongly nonlinear systems on the initial conditions which complexifies the direct time-domain validation of the analytical/ semi-analytical results across a wide range of input amplitudes. To capture the response of dynamic systems in their inherently strongly nonlinear regime, we often need to use more than a single harmonic

term for the displacement approximation in the steady state. This makes the direct time-domain validation complicated in the sense that what initial conditions we should impose on the system as a whole so that traveling waves can sustain in the system and the output amplitude envelope matches with the target amplitudes desired to achieve from those sets of initial conditions. To overcome these challenges, we develop an Amplitude-Locked, Inverse method-Guided, multi-harmonic Nonlinear framework (ALIGN), a framework that computes amplitude-dependent dispersion via multi-harmonic harmonic balance (HB) and validates it by inverse method (IM) simulations whose input envelopes are locked to the HB solution through a root mean square (RMS) amplitude target.

3.2.1 Notation and unit-cell modeling

We consider a one-dimensional (1D) periodic chain obtained by the repetition of an identical unit cell with d generalized coordinates (DOFs) $\mathbf{u}_n(t) \in \mathbb{R}^d$ denoting the vector of degrees of freedom (DOFs), where $n \in \mathbb{Z}$ indexes the cell and t is time. The equations of motion for an undamped, unforced system are written in standard form as

$$\mathbf{M}\,\ddot{\mathbf{u}}_n(t) + \mathbf{f}\big(\mathbf{u}_{n-1}(t),\, \mathbf{u}_n(t),\, \mathbf{u}_{n+1}(t)\big) \;=\; \mathbf{0} \tag{3.16}$$

where $\mathbf{M} \in \mathbb{R}^{d\times d}$ is the (constant, symmetric positive definite) mass matrix of the unit cell and $\mathbf{f}(\cdot)$ collects all internal forces, including linear couplings to the nearest neighbors and any nonlinear terms internal to the cell. We allow $\mathbf{f}$ to be non-integrable (e.g., algebraic and non-polynomial, possibly non-separable in the DOFs), as often arises in geometric or constraint-based nonlinearities.

Spatial periodicity is treated via the Bloch (Floquet) phase $\mu \in [0, \pi]$ (first Brillouin zone). For any field $\mathbf{u}_n$, Bloch quasi-periodicity implies $\mathbf{u}_{n\pm1}(t) = \mathbf{u}_n(t)\, e^{\pm i\mu}$ in the frequency-domain picture; in the time-domain implementation we enforce the same coupling at the level of unit-cell residuals.

3.2.2 Linear baseline and weakly nonlinear perturbations

Linearization of (3.16) around the trivial equilibrium yields the generalized eigenvalue problem

$$\big(\mathbf{K}(\mu) - \omega^2\,\mathbf{M}\big)\,\boldsymbol{\phi}(\mu) \;=\; \mathbf{0} \tag{3.17}$$

where $\mathbf{K}(\mu)$ is the Bloch-reduced stiffness matrix of size $d \times d$ and $\omega(\mu)$ are the linear dispersion branches. In the weakly nonlinear regime one may introduce a perturbation parameter ϵ multiplying the nonlinear part of $\mathbf{f}$ and apply an asymptotic expansion (e.g., multiple scales or averaging) to derive amplitude-dependent corrections to $\omega(\mu)$, modal interaction conditions (internal resonances), and slowly-varying envelope equations. This perturbative picture provides a baseline and a consistency check for the fully nonlinear computations that follow.

3.2.3 Generalized harmonic balance for strongly nonlinear responses

When nonlinearities are strong and/or non-polynomial, closed-form Fourier coefficients of $\mathbf{f}$ are typically unavailable. We therefore adopt a time-domain collocation (or quadrature)

variant of harmonic balance (HB). We seek time-periodic, Bloch-consistent solutions [14] with fundamental frequency $\omega > 0$ and N_h harmonics:

$$\mathbf{u}_n(t) \;\approx\; A\sum_{m=1}^{N_h}\Big[\mathbf{c}_m\cos\big(m(\mu n-\omega t)\big)+\mathbf{s}_m\sin\big(m(\mu n-\omega t)\big)\Big] \tag{3.18}$$

where $\mathbf{c}_m$, $\mathbf{s}_m \in \mathbb{R}^d$ are harmonic coefficient vectors, μ and ω are wavenumber and frequency respectively as used in their standard notations. A is an input amplitude parameter. To remove the trivial amplitude/phase indeterminacy we impose a gauge on the first harmonic (e.g., fix one component of $\mathbf{c}_1$ and leave the corresponding $\mathbf{s}_1$ free).

Let $\theta_k = 2\pi k/N_t$ $(k = 1, \ldots, N_t)$ be a uniform grid over one period, where N_t is the chosen number of points in the time-domain. Define the stacked vector of unknowns

$$\mathbf{X} \;=\; \big(\,\omega,\ \mathbf{c}_1, \mathbf{s}_1, \ldots, \mathbf{c}_{N_h}, \mathbf{s}_{N_h}\,\big)$$

with the chosen gauge enforced explicitly. For each θ_k we evaluate the kinematic fields implied by (3.18) and assemble the unit-cell residual

$$\mathbf{r}(\theta_k;\mathbf{X},\mu) \;=\; \mathbf{M}\,\ddot{\mathbf{u}}_0(\theta_k)+\mathbf{f}\Big(\mathbf{u}_{-1}(\theta_k),\,\mathbf{u}_0(\theta_k),\,\mathbf{u}_{+1}(\theta_k)\Big)$$

where $\mathbf{u}_{\pm1}(\theta_k) = \mathbf{u}_0(\theta_k)e^{\pm i\mu}$ (or, equivalently, the neighbor contributions are assembled using the Bloch phase). The HB residual is the time-projection of $\mathbf{r}$ onto the trigonometric basis, which we compute by numerical quadrature (e.g., trapezoidal rule over the N_t points). This yields a nonlinear system $\mathbf{R}(\mathbf{X};\mu;A) = \mathbf{0}$ of size $2N_hd$ (because of imposing the gauge and fixing the values of μ and A as inputs), which we solve by Newton's method with a backtracking line-search. The Jacobian $\partial\mathbf{R}/\partial\mathbf{X}$ is formed either analytically or robustly via complex-step differentiation, which is accurate and avoids step-size tuning issues.

Continuation in μ and branch stitching: For each μ we initialize Newton using the corresponding linear eigen pair of Eq. (3.17) (or the converged solution at the previous μ). To track branches consistently through crossings and near-degeneracies, we compare multi-harmonic feature vectors (all $\mathbf{c}_m, \mathbf{s}_m$ across the d DOFs) between successive μ-points using a modal assurance criterion (MAC), optionally regularized by a weak frequency-proximity weight. This provides a minimal, model-agnostic way to prevent branch swapping.

3.2.4 Inverse (time-domain) method for independent validation

To validate the semi-analytical HB dispersion, we simulate a long but finite chain in the time domain and extract the dominant frequency for each target (μ, branch). A localized, Bloch-consistent initial condition (IC) is synthesized by superposing the N_h harmonics from the HB coefficients,

$$u_j^{(q)}(0) \;\approx\; A\sum_{m=1}^{N_h}\big(c_m^{(q)}\cos(m\mu(j-j_0))+s_m^{(q)}\sin(m\mu(j-j_0))\big) \tag{3.19}$$

for each DOF $q = 1, \ldots, d$ over an excitation window centered at j_0. The index of the unit cells is represented by j and j_0 is the reference unit cell index. This excitation window can span the entire length of the finite version (say N) of the periodic structure or can extend from $j_0 - N_{exc}$ to $j_0 + N_{exc}$, where N_{exc} is the number of cells chosen for initial spatial

displacement excitation. We keep the initial velocities to be zero intentionally. Since we are considering more than one harmonic in the HB approximation, we need to set a target amplitude based on a rough approximation of the HB coefficients which we want the DOFs to achieve at steady state in the time-domain. We choose the root mean square (RMS) amplitude of the different HB coefficients multiplied by the input amplitude parameter A to be this target amplitude. We then propagate the full nonlinear dynamics over a time interval that excludes reflections/ boundary effects (absorbing or damping layers can be used at the boundaries) and spatially demodulate the response using $e^{-i\mu(j-j_0)}$ over a small measurement window to obtain a complex scalar trace $y^{(q)}(t)$ per DOF. A band-pass + Hilbert transform estimator around the HB ω (or a zero-crossing fallback) returns a measured frequency; if multiple DOFs are available, we retain the candidate closest to the HB target. This procedure (often called an "inverse method" in this context) provides branch-wise frequency curves from direct simulations, suitable for cross-checking the HB dispersion in both weakly and strongly nonlinear regimes.

3.2.5 Handling non-integrable, non-polynomial nonlinearities

A distinguishing feature of many metamaterial cells is the presence of non-integrable nonlinearities, for example algebraic, non-separable terms induced by geometric constraints or kinematic closures. Typical components of $\mathbf{f}$ may look like

$$g(\eta,\xi) \;=\; (\alpha \pm \eta)\left(1 - \frac{1}{\sqrt{(\alpha \pm \eta)^2 + \xi^2 + \delta^2}}\right)$$

where η, ξ are cell DOFs, α collects geometric parameters, and $\delta > 0$ is a small analytic regularizer that prevents singular denominators near kinematic limits. Such non-polynomial terms are generally not amenable to closed-form Fourier integrals. The HB strategy above circumvents this by:

- evaluating $\mathbf{f}$ pointwise in time on the collocation grid, so no harmonic integrals of $g(\cdot)$ are needed;
- using sufficiently fine N_t (e.g., $N_t \geq 512\, N_h$) to accurately resolve sharp features from the algebraic nonlinearity;
- employing complex-step differentiation to assemble a stable Jacobian for Newton, avoiding finite-difference cancellation when g is steep;
- applying a light harmonic taper in the branch-stitching features (e.g., weights $\propto 1/\sqrt{m}$) so high harmonics stabilize rather than destabilize continuation;
- enforcing a simple gauge (e.g., fix one component of $\mathbf{c}_1$) to remove global phase/scale ambiguity.

In practice this combination has two benefits: (a) it keeps the method generic, no model-specific Fourier algebra is required and (b) it remains applicable in the strongly nonlinear regime, where high harmonics are essential.

3.2.6 From weak to strong nonlinearity: one workflow

Bringing the elements together, a practical workflow that applies across discrete nonlinear periodic structures is:

- Linear baseline: compute $\omega(\mu)$ from Eq. (3.17) for intuition and seeding.
- HB sweep in μ: for each μ, solve $\mathbf{R}(\mathbf{X};\mu) = \mathbf{0}$ with $N_h \geq 1$, increase N_h as nonlinearity strengthens. Use MAC-based feature matching for branch assignment and a simple reseeding guard (fall back to linear seed if the converged ω collapses well below the linear ω).
- IM validation: build multi-harmonic, Bloch-consistent initial conditions (ICs) from the HB coefficients, set a target amplitude for the DOFs to achieve in the time-domain by using RMS approximation, demodulate, estimate frequency, and compare against HB.
- Nonstationarity and chaos checks: when needed, examine spectrograms, return maps, or Lyapunov exponents on the time traces to flag modulation/chaos. HB captures periodic responses and departures warn of quasiperiodicity or chaos.

The residual assembly in the HB step is parallel in μ and within a μ in the collocation points θ_k. For large sweeps, parallel execution across μ values and checkpointing the arrays $\{\omega(\mu), \mathbf{c}_m(\mu), \mathbf{s}_m(\mu)\}$ facilitates robust runs on HPC systems. The IM validation is likewise parallel across μ and across branches/initializations.

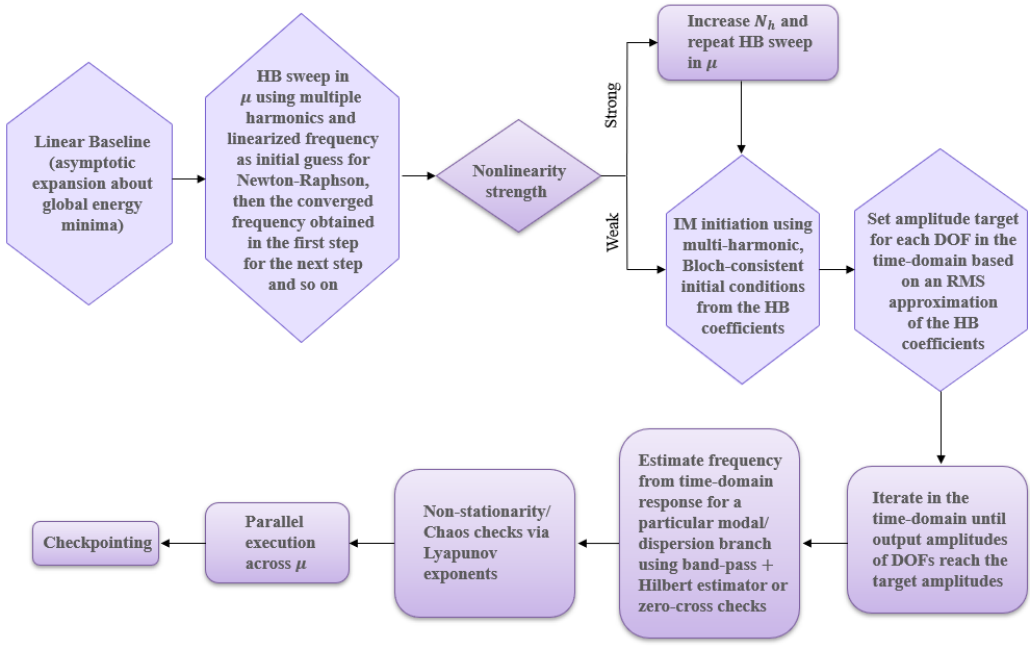


Fig. 3.4: ALIGN workflow: multi-harmonic Harmonic Balance (HB) with global branch stitching and amplitude-conditioned seeding, followed by Inverse Method (IM) validation using Root Mean Square (RMS) targeting and Hilbert-based frequency estimation. Stored coefficients $\{c_{mj}, s_{mj}\}$ enable multi-harmonic Initial Conditions (ICs) for the IM stage.

The formulation summarized in Fig. 3.4 is deliberately model-agnostic. It covers lattice cells with any number of DOFs, linear and nonlinear nearest-neighbor couplings, and both integrable (polynomial) and non-integrable (algebraic/geometry-induced) nonlinearities. It provides a single pipeline spanning weak to strong nonlinearity, from semi-analytical (HB) dispersion to independent time-domain validation (IM), and is intended to set up the problem-specific details that follow in Section 3.3.

3.3 Specific problem formulation: An inertially coupled strongly nonlinear periodic chain

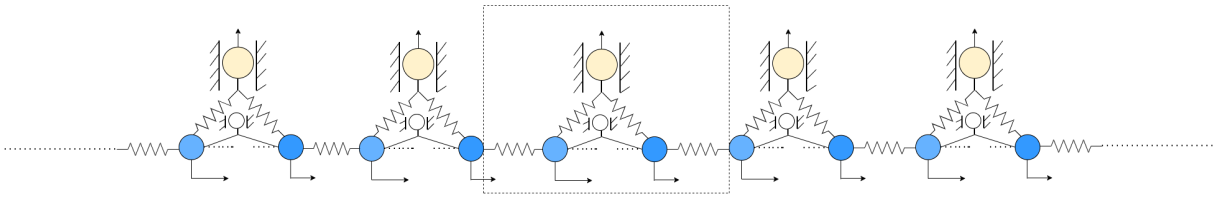
To arrive at a periodic one-dimensional chain, we consider an array of N unit cells where each repeating unit cell is our previously considered 3 degree of freedom model discussed in Section 3.1. The periodic chain is constructed by repeating the 3 DOF model and linking via horizontal linear coupling springs between m_1 and m_3 of adjacent unit cells in one dimension i.e. the horizontal direction. This appears to be a fairly intricate example of a discrete nonlinear periodic structure which can be tuned to design nonlinear metamaterials. A schematic diagram of the periodic chain constructed with the repeating unit cell is shown in Fig. 3.5. The non-dimensional equations of motion of the n-th unit cell, Eqs. (3.20)-(3.22) are obtained easily using the non-dimensional equations of motion of the 3 DOF model (Eqs. (3.11), (3.12), (3.13)) as reference.

$$\eta_n''+(\eta_n-\psi_{n-1})-(\cos\phi-\eta_n)\left(1-\frac{1}{\sqrt{(\cos\phi-\eta_n)^2+\xi_n^2}}\right)+\frac{r_a(\psi_n''-\eta_n'')\cos^2\alpha}{4\sin^2\alpha}=0 \quad (3.20)$$

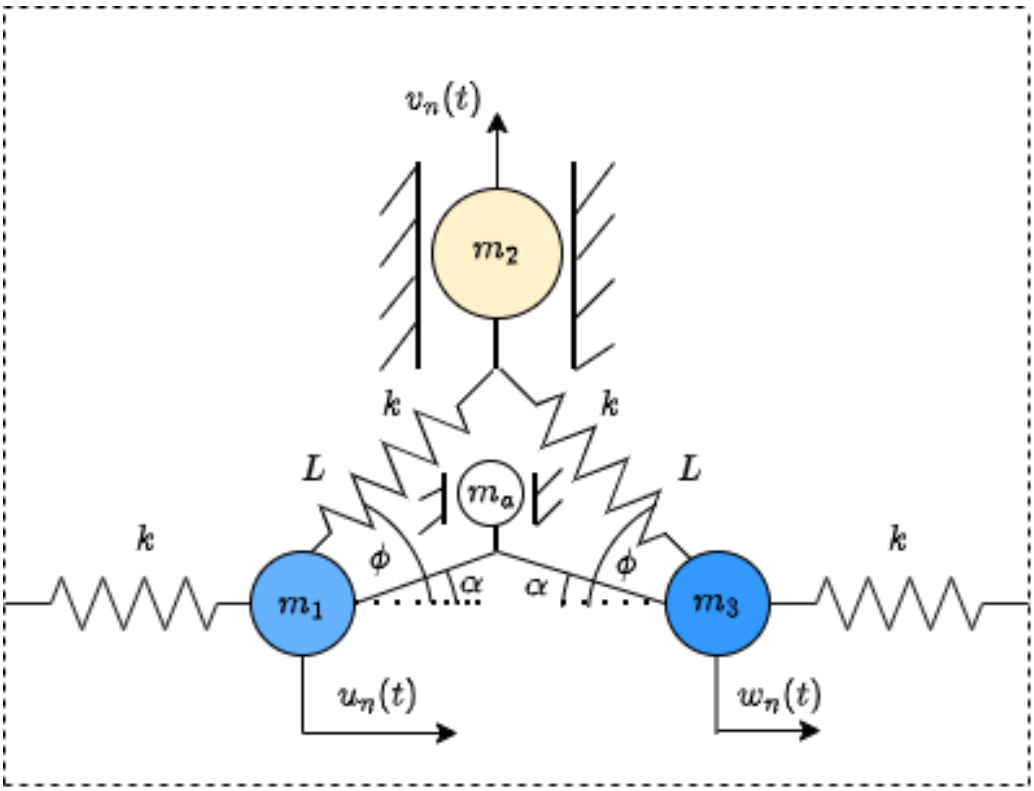
$$r_1\xi_n''+\xi_n\left(2-\frac{1}{\sqrt{(\cos\phi-\eta_n)^2+\xi_n^2}}-\frac{1}{\sqrt{(\cos\phi+\psi_n)^2+\xi_n^2}}\right)=0 \quad (3.21)$$

$$r_2\psi_n''+(\psi_n-\eta_{n+1})+(\cos\phi+\psi_n)\left(1-\frac{1}{\sqrt{(\cos\phi+\psi_n)^2+\xi_n^2}}\right)-\frac{r_a(\psi_n''-\eta_n'')\cos^2\alpha}{4\sin^2\alpha}=0 \quad (3.22)$$

Where prime denotes differentiation with respect to the non-dimensional time τ and the subscripts $n-1$, n, $n+1$ denote displacements in corresponding unit cells of the one-dimensional periodic chain.



(a) The periodic one-dimensional chain



(b) The repeating n-th unit cell

Fig. 3.5: The periodic chain showing the constitutive repeating unit cell where $u_n(t)$, $w_n(t)$ represent the horizontal degrees of freedom of masses m_1 and m_3 respectively, $v_n(t)$ represents the vertical degree of freedom of the bi-stable mass m_2 in the n-th unit cell, k denotes the stiffness co-efficients of all the springs, L denotes the natural length of the springs in the initial undeformed configuration, ϕ denotes the angle of inclination of the inclined linear springs with the horizontal axis in the initial undeformed configuration, α denotes the angle of inclination of the rigid links of the stable negative-inerter with the horizontal axis in the initial undeformed configuration.

3.4 Asymptotic analysis

3.4.1 Proximity to global energy minima and perturbation expansion

We assume that the two linear oscillators and the bi-stable mass remain close to their initial equilibrium configuration which are 0, 0 and $\sin\phi$ respectively. This configuration

is a global energy minima of the system under consideration. A Taylor series expansion is performed for the nonlinear functions in the equations of motion about those points by taking $\eta_n = 0 + \delta_n$, $\psi_n = 0 + \lambda_n$, $\xi_n = \sin\phi + \zeta_n$. Retaining upto quadratic terms in the expansion, we obtain the equations of motion for the system as:

$$\delta_n{}'' + (\delta_n - \lambda_{n-1}) - \Bigg(-\cos^2\phi\delta_n + \sin\phi\cos\phi\zeta_n + \frac{1}{2}\Big((3\cos\phi - 3\cos^3\phi)\delta_n^2 + 2\delta_n\zeta_n(-\sin\phi + 3\sin\phi\cos^2\phi) + (\cos\phi - 3\sin^2\phi\cos\phi)\zeta_n^2\Big)\Bigg) + \chi_a(\lambda_n'' - \delta_n'') = 0 \tag{3.23}$$

$$r_1\zeta_n{}'' + \Bigg(-\sin\phi\cos\phi\delta_n + 2\sin^2\phi\zeta_n + \sin\phi\cos\phi\lambda_n + \frac{1}{2}\Big(\delta_n^2(\sin\phi - \sin\phi\cos^2\phi) + \zeta_n^2(6\sin\phi - 6\sin^3\phi) + \lambda_n^2(\sin\phi - 3\sin\phi\cos^2\phi) + 2\delta_n\zeta_n(3\sin^2\phi\cos\phi - \cos\phi) + 2\delta_n\lambda_n(\cos\phi - 3\sin\phi\cos\phi)\Big)\Bigg) = 0 \tag{3.24}$$

$$r_2\lambda_n{}'' + (\lambda_n - \delta_{n+1}) + \Bigg(\sin\phi\cos\phi\zeta_n + \cos^2\phi\lambda_n + \frac{1}{2}\Big((\cos\phi - 3\sin^2\phi\cos\phi)\zeta_n^2 + 2\zeta_n\lambda_n(\sin\phi - 3\sin\phi\cos^2\phi) + (3\cos\phi - 3\cos^3\phi)\lambda_n^2\Big)\Bigg) - \chi_a(\lambda_n'' - \delta_n'') = 0 \tag{3.25}$$

where, $\chi_a = \frac{r_a\cos^2\alpha}{4\sin^2\alpha}$ is defined as the negative-inertance magnitude/factor.

According to our previous assumptions that the masses remain very close to their initial equilibrium configurations, an asymptotic expansion is done in Eqs. (3.23), (3.24), (3.25). We introduce a small parameter ϵ dependent upon the initial conditions such that $\delta_n = \epsilon\delta_n^{(0)} + \epsilon^2\delta_n^{(1)}$, $\zeta_n = \epsilon\zeta_n^{(0)} + \epsilon^2\zeta_n^{(1)}$ and $\lambda_n = \epsilon\lambda_n^{(0)} + \epsilon^2\lambda_n^{(1)}$. Inserting the chosen expansion into Eqs. (5.31), (3.24), (3.25), we get the linearized equations at different levels of approximation. We first consider the $O(\epsilon)$ equations to derive the linearized dispersion relations. The $O(\epsilon)$ equations are given as follows:

$$\delta_n^{(0)}{}'' + (\delta_n^{(0)} - \lambda_{n-1}^{(0)}) + \cos^2\phi\delta_n^{(0)} - \sin\phi\cos\phi\zeta_n^{(0)} + \chi_a(\lambda_n^{(0)}{}'' - \delta_n^{(0)}{}'') = 0 \tag{3.26}$$

$$r_1\zeta_n^{(0)}{}'' - \sin\phi\cos\phi\delta_n^{(0)} + 2\sin^2\phi\zeta_n^{(0)} + \sin\phi\cos\phi\lambda_n^{(0)} = 0 \tag{3.27}$$

$$r_2\lambda_n^{(0)}{}'' + (\lambda_n^{(0)} - \delta_{n+1}^{(0)}) + \sin\phi\cos\phi\zeta_n^{(0)} + \cos^2\phi\lambda_n^{(0)} - \chi_a(\lambda_n^{(0)}{}'' - \delta_n^{(0)}{}'') = 0 \tag{3.28}$$

These equations are then used in the next Section 3.4.2 to evaluate the linearized dispersion branches at the first level of approximation.

3.4.2 Linear dispersion analysis at first level of approximation

To derive the linear dispersion relationship, we apply Bloch's theorem to express the displacements in the successive unit cells in the form shown below.

$$\delta_n^{(0)} = \tilde{\delta}^{(0)}e^{i\mu n}e^{i\omega\tau} \tag{3.29}$$

$$\zeta_n^{(0)} = \tilde{\zeta}^{(0)}e^{i\mu n}e^{i\omega\tau} \tag{3.30}$$

$$\lambda_n^{(0)} = \tilde{\lambda}^{(0)}e^{i\mu n}e^{i\omega\tau} \tag{3.31}$$

Where μ is the dimensionless wavenumber and ω is the free wave frequency. Substituting the assumed forms of displacements in the $O(\epsilon)$ equations of motion Eqs. (3.26), (3.27) and (3.28), we obtain the following equations:

$$-\omega^2\tilde{\delta}^{(0)} + (\tilde{\delta}^{(0)} - \tilde{\lambda}^{(0)}e^{-i\mu}) + \cos^2\phi\tilde{\delta}^{(0)} - \sin\phi\cos\phi\tilde{\zeta}^{(0)} - \chi_a(\tilde{\lambda}^{(0)} - \tilde{\delta}^{(0)}) = 0 \tag{3.32}$$

$$-\omega^2 r_1\tilde{\zeta}^{(0)} - \sin\phi\cos\phi\tilde{\delta}^{(0)} + 2\sin^2\phi\tilde{\zeta}^{(0)} + \sin\phi\cos\phi\tilde{\lambda}^{(0)} = 0 \tag{3.33}$$

$$-\omega^2 r_2\tilde{\lambda}^{(0)} + (\tilde{\lambda}^{(0)} - \tilde{\delta}^{(0)}e^{i\mu}) + \sin\phi\cos\phi\tilde{\zeta}^{(0)} + \cos^2\phi\tilde{\lambda}^{(0)} + \chi_a(\tilde{\lambda}^{(0)} - \tilde{\delta}^{(0)}) = 0 \tag{3.34}$$

Separating the mass matrix and the wavenumber reduced stiffness matrix in the above three equations, we have

$$[\mathbf{M}] = \begin{bmatrix} 1-\chi_a & 0 & \chi_a \\ 0 & r_1 & 0 \\ \chi_a & 0 & r_2-\chi_a \end{bmatrix} \tag{3.35}$$

$$[\mathbf{K}(\mu)] = \begin{bmatrix} 1+\cos^2\phi & -\sin\phi\cos\phi & -e^{-i\mu} \\ -\sin\phi\cos\phi & 2\sin^2\phi & \sin\phi\cos\phi \\ -e^{i\mu} & \sin\phi\cos\phi & 1+\cos^2\phi \end{bmatrix} \tag{3.36}$$

Therefore the eigen value problem to derive the dispersion relation is formulated as:

$$([\mathbf{K}(\mu)] - \omega^2[\mathbf{M}])\tilde{X}^{(0)} = 0 \tag{3.37}$$

Where $\tilde{X}^{(0)} = \begin{Bmatrix} \tilde{\delta}^{(0)} \\ \tilde{\zeta}^{(0)} \\ \tilde{\lambda}^{(0)} \end{Bmatrix}$. To obtain the dispersion relation we set the determinant of $[\mathbf{K}(\mu)] - \omega^2[\mathbf{M}]$ to be equal to zero as is the standard method for obtaining non-trivial solutions.

From the eigenvalue problem described in Eq. (3.37), we can evaluate the frequencies numerically or analytically for a given specified range of wavenumbers. Since the eigenvalue problem results in a cubic polynomial equation in terms of ω^2, deriving analytical solutions will bring in very complicated and lengthy expressions. So, we solve the eigenvalue problem numerically over the first IBZ. This method of specifying the wavenumber μ and solving for the frequencies ω is known as the inverse method.

3.4.3 Positive definiteness of the unit cell mass matrix (Sylvester's criterion)

The unit-cell kinetic energy is

$$T = \frac{1}{2}\dot{\mathbf{q}}^T[\mathbf{M}]\dot{\mathbf{q}}, \tag{3.38}$$

where $\mathbf{q}$ is the generalized displacement vector of a representative repeating unit cell. Hence, physical admissibility requires the real, symmetric mass matrix $[\mathbf{M}]$ to be positive definite so that $T > 0$ for all $\dot{\mathbf{q}} \neq \mathbf{0}$. This also ensures that the generalized eigenvalue problem $[\mathbf{K}(\mu)]\tilde{X}^{(0)} = \omega^2[\mathbf{M}]\tilde{X}^{(0)}$ has real eigenvalues ω^2 (for Hermitian $[\mathbf{K}(\mu)]$), avoiding spurious non-physical instabilities stemming from an indefinite inertia operator.

For a real symmetric matrix $[\mathbf{M}] \in \mathbb{R}^{n\times n}$, Sylvester's criterion states that $\mathbf{M} \succ \mathbf{0}$ if and only if all leading principal minors are strictly positive:

$$\Delta_k = \det\big([\mathbf{M}]_{1:k,\,1:k}\big) > 0, \qquad k = 1, 2, \ldots, n. \tag{3.39}$$

From Eq. (3.35), the non-dimensional unit cell mass matrix is

$$[\mathbf{M}] = \begin{bmatrix} 1-\chi_a & 0 & \chi_a \\ 0 & r_1 & 0 \\ \chi_a & 0 & r_2-\chi_a \end{bmatrix}, \qquad \chi_a = \frac{r_a \cos^2\alpha}{4\sin^2\alpha}, \tag{3.40}$$

where χ_a is the negative-inertance magnitude. The leading principal minors are

$$\Delta_1 = 1-\chi_a, \tag{3.41}$$

$$\Delta_2 = \det\begin{bmatrix} 1-\chi_a & 0 \\ 0 & r_1 \end{bmatrix} = r_1(1-\chi_a), \tag{3.42}$$

$$\Delta_3 = \det(\mathbf{M}) = r_1 \det\begin{bmatrix} 1-\chi_a & \chi_a \\ \chi_a & r_2-\chi_a \end{bmatrix} = r_1\Big[(1-\chi_a)(r_2-\chi_a)-\chi_a^2\Big] = r_1\Big[r_2-\chi_a(r_2+1)\Big]. \tag{3.43}$$

Therefore, $\mathbf{M} \succ \mathbf{0}$ holds if and only if

$$r_1 > 0, \qquad \chi_a < 1, \qquad r_2 > \frac{\chi_a}{1-\chi_a} \quad \Big(\text{equivalently } \chi_a < \frac{r_2}{r_2+1}\Big). \tag{3.44}$$

The boundary case $\det(\mathbf{M}) = 0$ occurs at

$$r_{2,\text{crit}} = \frac{\chi_a}{1-\chi_a}, \tag{3.45}$$

beyond which the inertia operator becomes singular/indefinite, and the generalized eigenproblem may yield non-physical (imaginary) frequencies.

For the baseline choice $\sin\alpha = 0.5$ (thus $\cos^2\alpha/(4\sin^2\alpha) = 3/4$) and for $r_a = 0.5$, we obtain

$$\chi_a = \frac{3}{4}r_a = \frac{3}{8}, \qquad r_{2,crit} = \frac{\frac{3}{8}}{1-\frac{3}{8}} = \frac{3/8}{5/8} = \frac{3}{5} = 0.6. \tag{3.46}$$

Hence, for $r_1 = 1$ and $r_a = 0.5$ (with $\sin\alpha = 0.5$), the unit cell mass matrix is positive definite provided

$$r_2 > 0.6. \tag{3.47}$$

Similarly, using $\chi_a < \frac{r_2}{r_2+1}$, for the same baseline choice of $\sin\alpha = 0.5$ and taking the value of $r_2 = 1$, we get

$$\frac{3}{4}r_a < \frac{1}{2} \implies r_a < \frac{2}{3} \approx 0.7 \tag{3.48}$$

keeping upto one significant digit after the decimal place.

Thus, admissibility thresholds are directly linked back here to the negative-inerter's design parameters and will be compared later in both the linearized asymptotic and general strongly nonlinear regimes.

3.4.4 Second-order correction to the Dispersion Profiles

We now inspect the $O(\epsilon^2)$ equations to investigate the second order corrections in the dispersion profile. The $O(\epsilon^2)$ equations are obtained as follows:

$$\begin{aligned}\delta_n^{(1)''} + (\delta_n^{(1)} - \lambda_{n-1}^{(1)}) + \cos^2\phi\delta_n^{(1)} - \sin\phi\cos\phi\zeta_n^{(1)} + \chi_a(\lambda_n^{(1)''} - \delta_n^{(1)''}) \\ = \frac{1}{2}\Big((3\cos\phi - 3\cos^3\phi)\delta_n^{(0)^2} + 2\delta_n^{(0)}\zeta_n^{(0)}(-\sin\phi + 3\sin\phi\cos^2\phi) \\ +(\cos\phi - 3\sin^2\phi\cos\phi)\zeta_n^{(0)^2}\Big)\end{aligned} \tag{3.49}$$

$$\begin{aligned}&r_1\zeta_n^{(1)''} - \sin\phi\cos\phi\delta_n^{(1)} + 2\sin^2\phi\zeta_n^{(1)} + \sin\phi\cos\phi\lambda_n^{(1)} \\ &= -\frac{1}{2}\Big(\delta_n^{(0)^2}(\sin\phi - \sin\phi\cos^2\phi) + \zeta_n^{(0)^2}(6\sin\phi - 6\sin^3\phi) + \lambda_n^{(0)^2}(\sin\phi - 3\sin\phi\cos^2\phi) \\ &+ 2\delta_n^{(0)}\zeta_n^{(0)}(3\sin^2\phi\cos\phi - \cos\phi) + 2\delta_n^{(0)}\lambda_n^{(0)}(\cos\phi - 3\sin\phi\cos\phi)\Big)\end{aligned} \tag{3.50}$$

$$\begin{aligned}r_2\lambda_n^{(1)''} + (\lambda_n^{(1)} - \delta_{n+1}^{(1)}) + \sin\phi\cos\phi\zeta_n^{(1)} + \cos^2\phi\lambda_n^{(1)} - \chi_a(\lambda_n^{(1)''} - \delta_n^{(1)''}) \\ = -\frac{1}{2}\Big((\cos\phi - 3\sin^2\phi\cos\phi)\zeta_n^{(0)^2} + 2\zeta_n^{(0)}\lambda_n^{(0)}(\sin\phi - 3\sin\phi\cos^2\phi) \\ +(3\cos\phi - 3\cos^3\phi)\lambda_n^{(0)^2}\Big)\end{aligned} \tag{3.51}$$

The left hand sides of the $O(\epsilon^2)$ equations Eq. (3.49), (3.50) and (3.51) are same as the left hand side of the $O(\epsilon)$ equations Eq. (3.26), (3.27), (3.28) derived before. Hence, we will assume a secular Bloch solution for the equations above and investigate the second order correction to the frequency. We assume a series expansion of the free wave frequency ω in terms of the small parameter ϵ.

$$\omega = \omega_0 + \epsilon\omega_1 + O(\epsilon^2) \tag{3.52}$$

Now, ω_0 has already been found out in our linear dispersion analysis in Section 3.4.2 in terms of the wavenumber by solving the eigenvalue problem Eq. (3.37). We will then evaluate ω_1 in terms of the wavenumber and the amplitude by imposing the secularity condition as done in [14]. The second order correction to the j-th frequency $\omega_{1,j}$ is given by

$$\omega_{1,j}(A_0, \mu) = \frac{u_{0,j}^H(\mu)c_1(A_0)}{\omega_{0,j}A_0u_{0,j}^H(\mu)\mathbf{M}u_{0,j}(\mu)} \tag{3.53}$$

where $u_{0,j}$ represents the j-th normalized complex wave mode or the j-th eigenvector to the first order equations, $c_1(A_0)$ represents the co-efficient of the first harmonic in the Fourier series expansion of the nonlinear forcing function on the right hand side of the $O(\epsilon^2)$ equations (Eqs. (3.49)-(3.51)), $\mathbf{M}$ is the mass matrix, $u_{0,j}^H(\mu)$ is the Hermitian or the complex conjugate transpose of the j-th complex wave mode or the normalized eigenvector and A_0 is the free wave amplitude of the $O(\epsilon)$ equations which is considered as a parameter dependent upon the initial conditions. It is worthwhile to note here that this second-order correction to the frequency by imposing the secularity condition will hold true even in the case of a complex μ dependent stiffness matrix [14] and fully populated mass matrix [**M**] with non-zero off-diagonal terms [198].

3.4.5 Dispersion diagrams from asymptotic analysis

If we vary the three different mass ratios, the dispersion profiles will show varying characteristics. This is a subject of study in the current work, where we will vary the system parameters and study how the dispersion characteristics depend on them.

We first vary the mass ratio r_1 and keep the other parameters same. We vary r_1 from 0.1 to 1 and plot the frequency as a function of wavenumber in Fig. 3.6 for the following set of values of the other system parameters. $r_a = 0.5, r_2 = 1, \sin\phi = 0.6, \sin\alpha = 0.5$, $\epsilon = 0.1$ The initial conditions at the $O(\epsilon)$ level are taken as

$$\begin{Bmatrix} {\delta_n}^{(0)} \\ {\zeta_n}^{(0)} \\ {\lambda_n}^{(0)} \end{Bmatrix} (\tau = 0) = \begin{Bmatrix} 1 \\ 1 \\ 1 \end{Bmatrix} \tag{3.54}$$

The initial conditions at $O(\epsilon^2)$ level are all taken to be zero. So the net initial conditions are obtained as

$$\begin{Bmatrix} \delta_n \\ \zeta_n \\ \lambda_n \end{Bmatrix} (\tau = 0) = \epsilon \begin{Bmatrix} 1 \\ 1 \\ 1 \end{Bmatrix} + \epsilon^2 \begin{Bmatrix} 0 \\ 0 \\ 0 \end{Bmatrix} = \begin{Bmatrix} 0.1 \\ 0.1 \\ 0.1 \end{Bmatrix} \tag{3.55}$$

These set of initial conditions are in agreement with our initial assumption for asymptotic analysis that the masses remain close to their initial equilibrium positions.

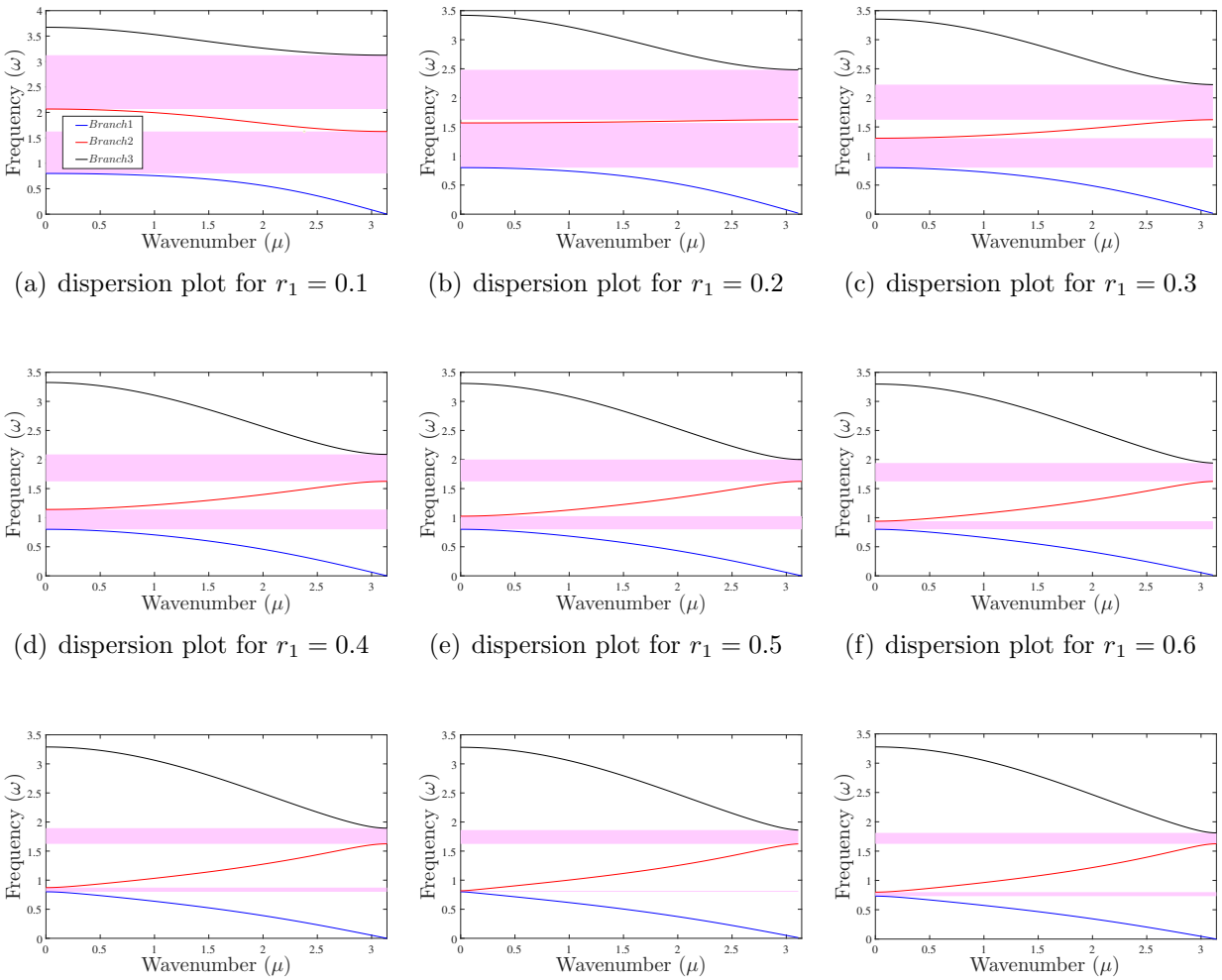
Next, we vary the mass ratio r_2 from 0.7 to 1 and plot the dispersion profiles in Fig. 3.7 with the values of the other parameters kept fixed at $r_a = 0.5, r_1 = 1, \sin\phi = 0.6, \sin\alpha = 0.5$, $\epsilon = 0.1$. The initial conditions are kept the same as before. Below the values of $r_2 = 0.7$, and reducing by one significant digit after the decimal place, i.e. for $r_2 = 0.6, 0.5, ...0.1$ as obtained previously in Section 3.4.3, Eq. (3.47), the frequencies become imaginary for the wavenumber varying over the first IBZ, which is not realizable for an undamped physical system like ours. So, we refrain from plotting them.

Next, we vary the inerter mass-parameter ratio r_a from 0.1 to 0.6 and plot the dispersion profiles in Fig. 3.8. The values of the other system parameters are taken as $r_1 = 1, r_2 = 1, \sin\phi = 0.6, \sin\alpha = 0.5$, $\epsilon = 0.1$. The initial conditions are kept the same as before. Beyond the values of $r_a = 0.6$, and increasing by one significant digit after the decimal place, i.e. for $r_a = 0.7, 0.8.....1$ as obtained in Section 3.4.3, Eq. (3.48), the frequencies become imaginary which is not realizable for an undamped physical system. So, we refrain from plotting them.

Physical interpretation of critical thresholds: The critical mass ratio values ($r_2 > 0.6$, $r_a < 0.7$ with baseline angles ϕ and α kept fixed) correspond to dynamic instability boundaries rather than geometric buckling.

For $r_2 \leq 0.6$ (mass m_3 too light): The horizontally oscillating mass m_3 becomes insufficiently inertial to maintain effective coupling with the bistable element m_2. This creates dynamic decoupling where the vertical bistable motion cannot effectively transfer energy to the adjacent unit cell, resulting in evanescent (exponentially decaying) waves rather than propagating waves. Mathematically, this manifests as imaginary frequencies for all $\mu \in [0, \pi]$.

For $r_a > 0.6$ (inerter design-mass too large): Excessive inertial coupling-level creates a negative effective mass effect in the coupled horizontal DOFs. From Eqs. (3.20) and (3.22), the negative inerter contributes terms $\pm\frac{r_a \cos^2\alpha}{4\sin^2\alpha}$ to the effective mass matrix. When



(a) dispersion plot for $r_1 = 0.1$ (b) dispersion plot for $r_1 = 0.2$ (c) dispersion plot for $r_1 = 0.3$

(d) dispersion plot for $r_1 = 0.4$ (e) dispersion plot for $r_1 = 0.5$ (f) dispersion plot for $r_1 = 0.6$

(g) dispersion plot for $r_1 = 0.7$ (h) dispersion plot for $r_1 = 0.8$ (i) dispersion plot for $r_1 = 1$

Fig. 3.6: Dispersion diagrams from asymptotic analysis showing the three branches of frequency varying with the wavenumber and the relevant bandgaps for mass ratio r_1 varying from 0.1 to 1 and the values of the other parameters kept fixed.

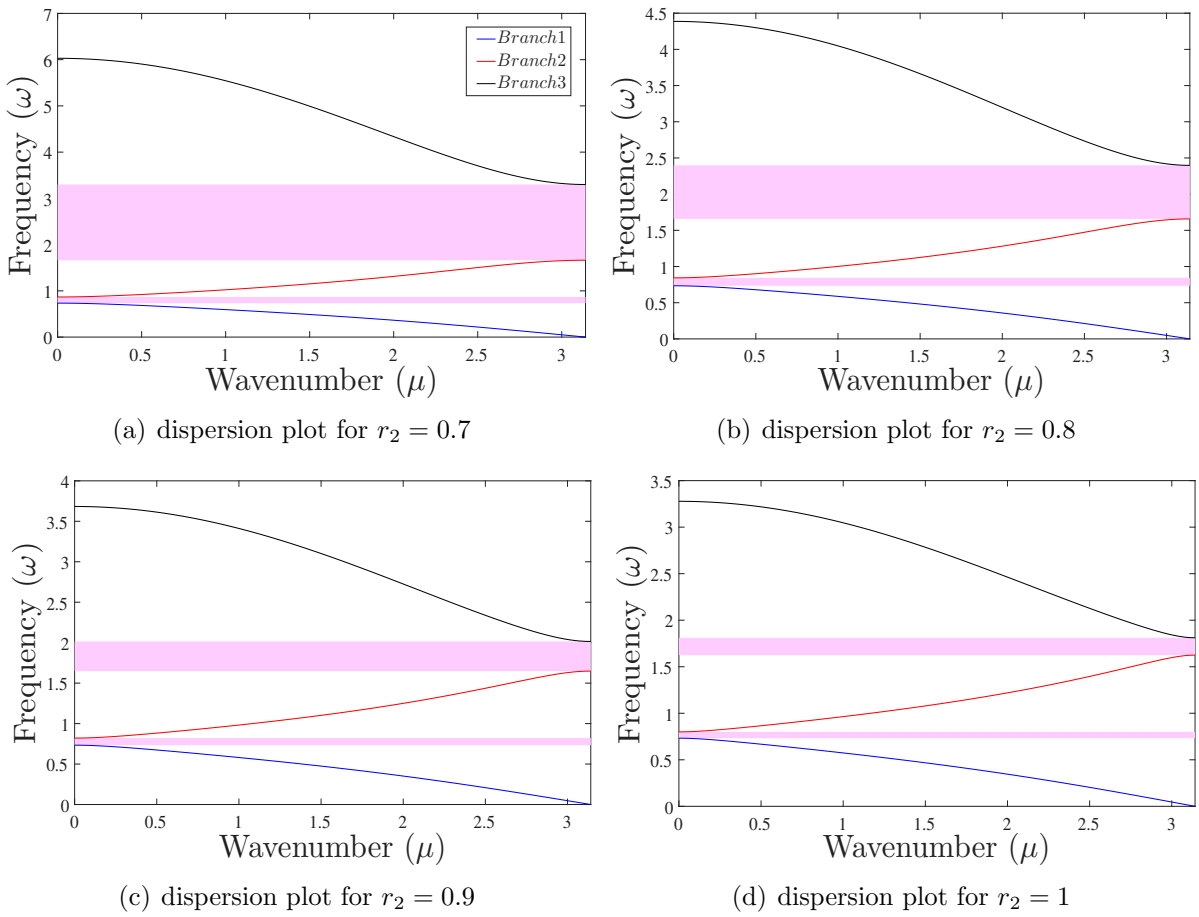
r_a exceeds the critical threshold, these terms dominate and produce negative eigenvalues of the mass matrix, indicating system instability.

These two critical values of r_2 and r_a below which and beyond which traveling waves cannot propagate, with other system parameters kept fixed, are noted down to check as a reference for the strongly nonlinear system.

3.4.6 Bandgap variation with the mass ratios

We now vary the three different mass ratios one at a time and check how the lower and upper bandgaps vary with them. We also evaluate another quantity which is the difference between the midpoints of the successive frequency curves and plot them alongwith the bandgaps for the three different mass ratios.

First, we vary the mass ratio r_1 from 0.1 to 1 and plot the bandgaps and the midpoint frequency difference (Fig. 3.9), keeping the other parameters at $r_2 = 1, r_a = 0.5, \sin\phi =$



(a) dispersion plot for $r_2 = 0.7$

(b) dispersion plot for $r_2 = 0.8$

(c) dispersion plot for $r_2 = 0.9$

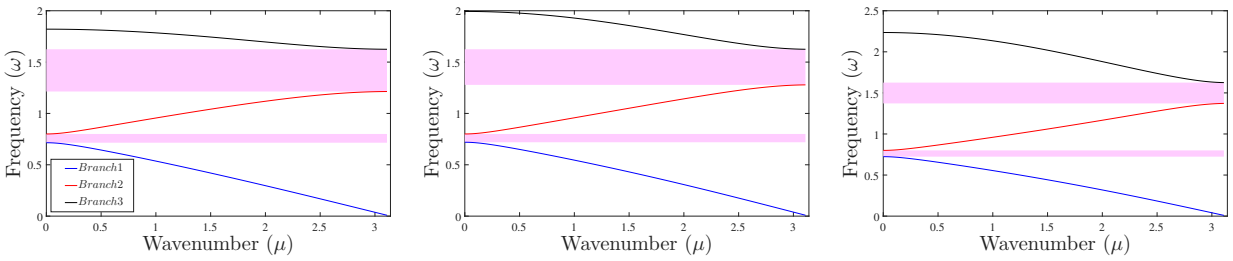
(d) dispersion plot for $r_2 = 1$

Fig. 3.7: Dispersion diagrams from asymptotic analysis showing the three branches of frequency varying with the wavenumber and the relevant bandgaps for mass ratio r_2 varying from 0.7 to 1 and the values of the other parameters kept fixed.

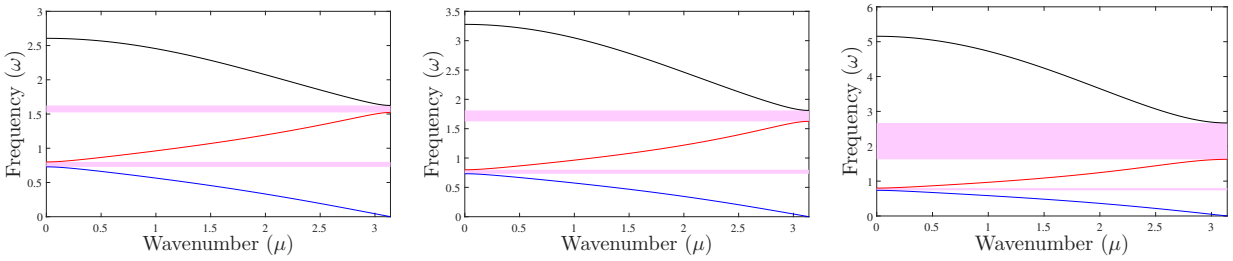
$0.6, \sin\alpha = 0.5$. As we can see in Fig. 3.9, the upper and lower bandgaps more or less show a decreasing pattern with increasing mass ratio r_1. The lower midpoint frequency difference uniformly decreases with increasing r_1. The upper midpoint frequency difference initially decreases upto approximately $r_1 = 0.15$ and the increases with increasing r_1.

Next, we vary the mass ratio r_2 from 0.7 to 1 that is the physically realizable region for travelling waves and plot the same quantities i.e. bandgaps and midpoint frequency differences (Fig. 3.10), keeping the other parameters as $r_1 = 1, r_a = 0.5, \sin\phi = 0.6, \sin\alpha = 0.5$. As we can see from Fig. 3.10, and as it is evident from the dispersion plots Fig. 3.7, the lower bandgap and hence the lower midpoint frequency difference remain more or less constant with a slight decreasing pattern with the mass ratio r_2. The upper bandgap and upper midpoint frequency difference decrease uniformly with r_2.

Finally, we vary the mass ratio r_a from 0.1 to 0.6 that is the physically realizable region for travelling waves and plot the same quantities i.e. bandgaps and midpoint frequency differences (Fig. 3.11), keeping the other parameters as $r_1 = 1, r_2 = 1, \sin\phi = 0.6, \sin\alpha = 0.5$. As we can see from Fig. 3.11, and as it is evident from the dispersion plots Fig. 3.8, the lower bandgap and hence the lower midpoint frequency difference remain more or less constant with a very slight decreasing pattern with the mass ratio r_a. The upper



(a) dispersion plot for $r_a = 0.1$ (b) dispersion plot for $r_a = 0.2$ (c) dispersion plot for $r_a = 0.3$



(d) dispersion plot for $r_a = 0.4$ (e) dispersion plot for $r_a = 0.5$ (f) dispersion plot for $r_a = 0.6$

Fig. 3.8: Dispersion diagrams from asymptotic analysis showing the three branches of frequency varying with the wavenumber and the relevant bandgaps for mass ratio r_a varying from 0.1 to 0.6 and the values of the other parameters kept fixed.

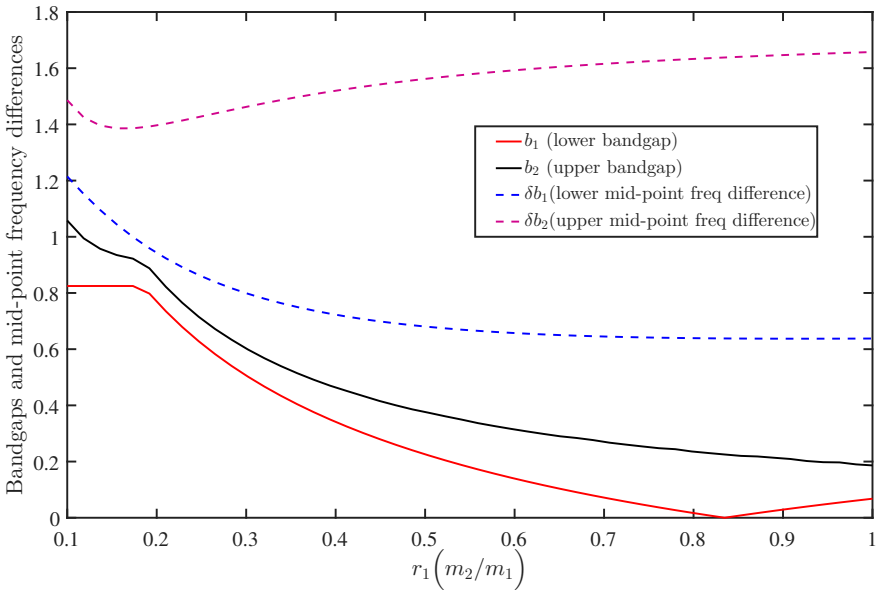


Fig. 3.9: Bandgap and midpoint frequency difference variation with the mass ratio r_1 keeping all the other parameters fixed.

bandgap first decreases upto a value of approximately $r_a = 0.45$ and then increases with r_a. The upper midpoint frequency difference increases uniformly with r_a. Table 3.1 summarizes the bandgap behavior in the weakly nonlinear regime with critical parameter values specified.

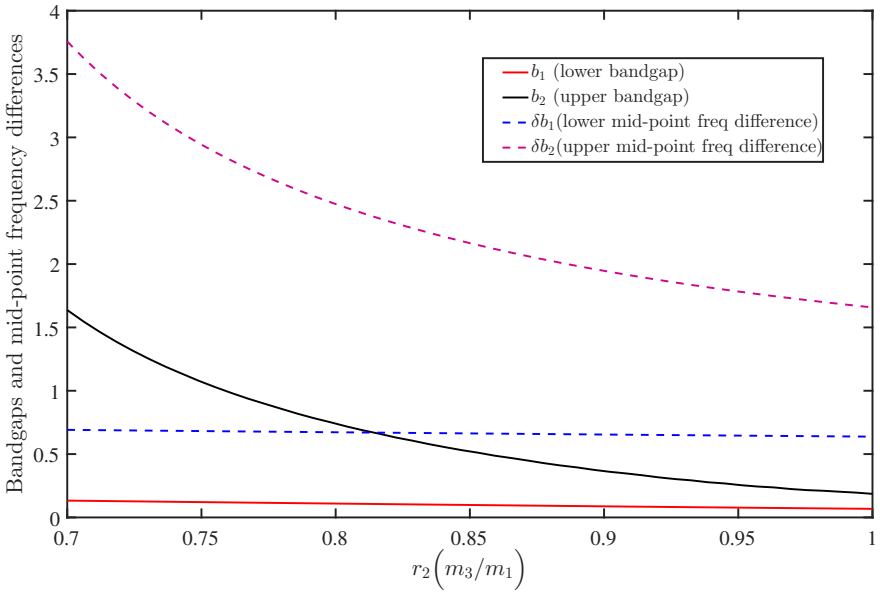


Fig. 3.10: Bandgap and midpoint frequency difference variation with the mass ratio r_2 keeping all the other parameters fixed.

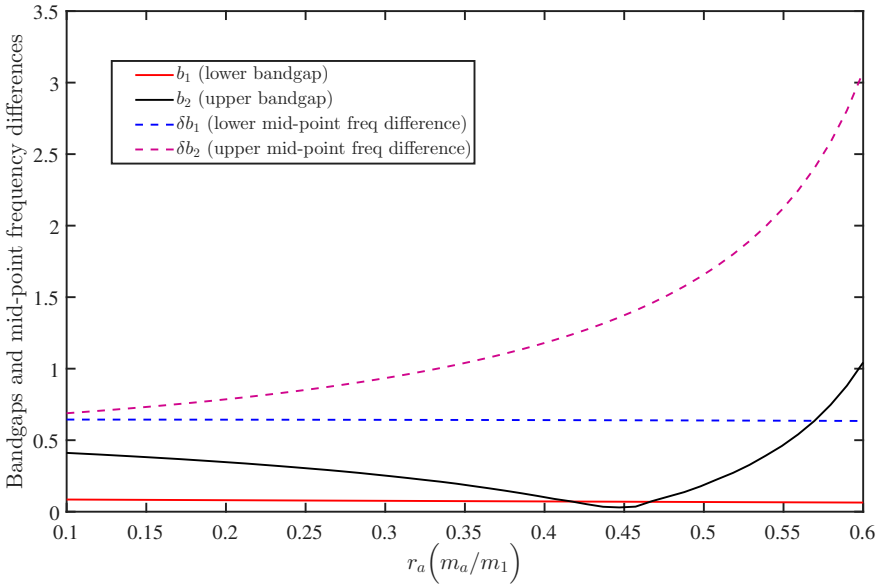


Fig. 3.11: Bandgap and midpoint frequency difference variation with the mass ratio r_a keeping all the other parameters fixed.

So, in this section we have indeed manipulated the bandgap by tuning three crucial system parameters that is the three mass ratios. This can come in very useful in analyzing the dynamic behavior of the periodic lattice in its weakly nonlinear regime and also in tuning the wave propagation characteristics of the system such as filtering, vibration attenuation, vibration suppression, etc..

Parameter	Range studied	Lower bandgap trend	Upper bandgap trend	Critical value	Notes
r_1	0.1-1.0	Decreases	Decreases	None	Both branches shift downward
r_2	0.7-1.0	Slight decrease	Decreases	< 0.7 (instability)	Strong upper gap sensitivity
r_a	0.1-0.6	Nearly constant	Non-monotonic	> 0.6 (instability)	Upper gap: decreases then increases

Table 3.1: Summary of bandgap behavior in weakly nonlinear regime ($\epsilon = 0.1$) for baseline angles $\sin\phi = 0.6$, $\sin\alpha = 0.5$. Trends indicate behavior as parameter increases.

3.4.7 Dispersion profile by the direct method in the linearized domain

Next, we adopt the direct procedure of plotting the dispersion profiles. From the eigenvalue problem described in Section 3.4.2, we derive an expression for μ in terms of ω. Expanding the characteristic polynomial in the eigenvalue problem (3.37), we get the following expression for μ.

$$\cos\mu = \frac{a_1\omega^6 + b_1\omega^4 + c_1\omega^2 + d_1}{a_2\omega^4 + b_2\omega^2 + c_2} \tag{3.56}$$

Where the co-efficients of the different powers of ω are explicitly dependent on the five system parameters r_1, r_2, r_a, ϕ and α. The expressions are not shown here due to very lengthy forms. The frequency ω is varied over a range of values and the real and imaginary parts of the wavenumber are plotted in Fig. 3.12 for values of the the system parameters kept at $r_1 = 1$, $r_2 = 1$, $r_a = 0.5$, $\sin\phi = 0.6$, $\sin\alpha = 0.5$. We can also choose different sets of values of the five system parameters and inspect how the dispersion profile characteristics vary with those values. The real values of the wavenumber μ correspond to propagating waves whereas the imaginary values correspond to attenuating waves.

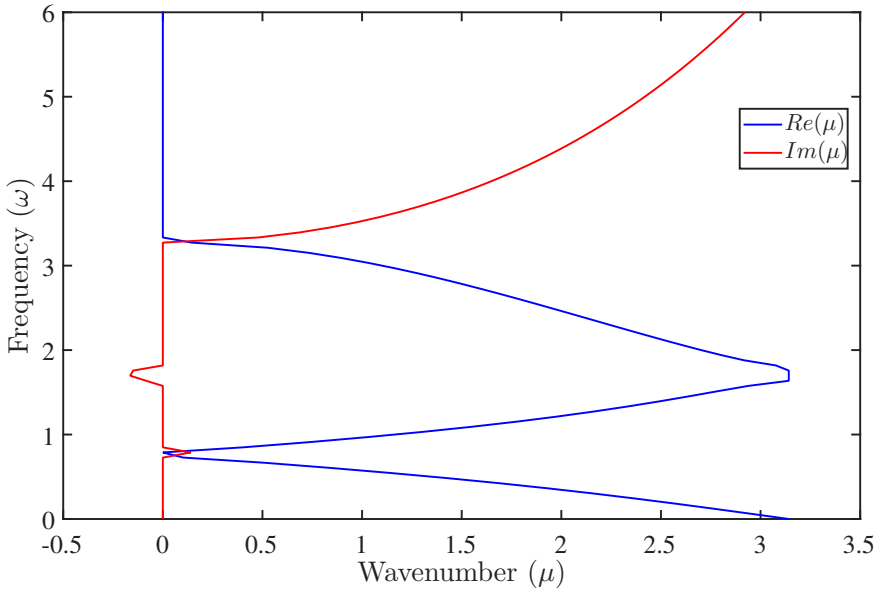


Fig. 3.12: Dispersion profile showing the real and imaginary parts of the wavenumber for a range of varying frequency

3.5 Generalized harmonic balance (HB) method for strongly nonlinear regime

3.5.1 Generalized harmonic approximation

When the masses in the periodic lattice do not remain very close to their initial equilibrium configuration, the equations of motion governing the dynamics are strongly nonlinear as is evident from equations Eqs. (3.20), (3.21), (3.22). So, asymptotic analysis can no longer be used to obtain the time-domain response or the dispersion profiles. Hence, we use a generalized harmonic balance method from [14] to obtain the dispersion profiles. The essence of this method is to assume a Bloch-consistent harmonic expansion for the displacement of the n-th unit cell in a general 2-D nonlinear periodic lattice as

$$\mathbf{u_{n_1,n_2}} = A\left(\sum_{m=1}^{M} \mathbf{c}_m \cos\left[m(\mu.\mathbf{n} - \omega\tau)\right] + \mathbf{s}_m \sin\left[m(\mu.\mathbf{n} - \omega\tau)\right]\right) \tag{3.57}$$

where $\mu.\mathbf{n} = \mu_1 n_1 + \mu_2 n_2$ is the inner product of the wavenumber vector with the directional vector of the general 2-D periodic lattice. A is the free wave amplitude which can be considered as an input parameter dependent on the initial conditions, $\mathbf{c}_m$ and $\mathbf{s}_m$ are the unknown harmonic coefficient column vectors to be determined. The key reasoning behind this 'Bloch-consistent' harmonic approximation in the generalized nonlinear regime is the fact that in our chosen periodic model, the nonlinearities are confined within the repeating unit cell and there is no nonlinear coupling between adjacent unit cells as the intercellular horizontal coupling springs have been chosen to have only a linear stiffness coefficient.

Since our system is a 1-D periodic lattice, $n_2 = 0$ and if we choose a unit vector along the axis of our lattice that is the x-axis, then $\mu.\mathbf{n}$ will be just the non-dimensional

wavenumber μ. After substitution of Eq. (3.57) in the governing equations of motion of a general 2-D periodic lattice, and some algebraic manipulations, a set of coupled nonlinear ordinary differential equations is obtained. Then by using Galerkin projection those equations are reduced from differential to algebraic form. Thus, a set of coupled time-independent algebraic equations are obtained with the harmonic co-efficients, the free wave frequency ω, wavenumber μ and the amplitude A as the unknowns. Since our objective is to obtain dispersion relations, we fix μ and A and thus the number of unknowns becomes exactly equal to the number of equations. These equations are then solved by an iterative Newton-Raphson method. We implement this algorithm in Matlab and obtain the dispersion profiles.

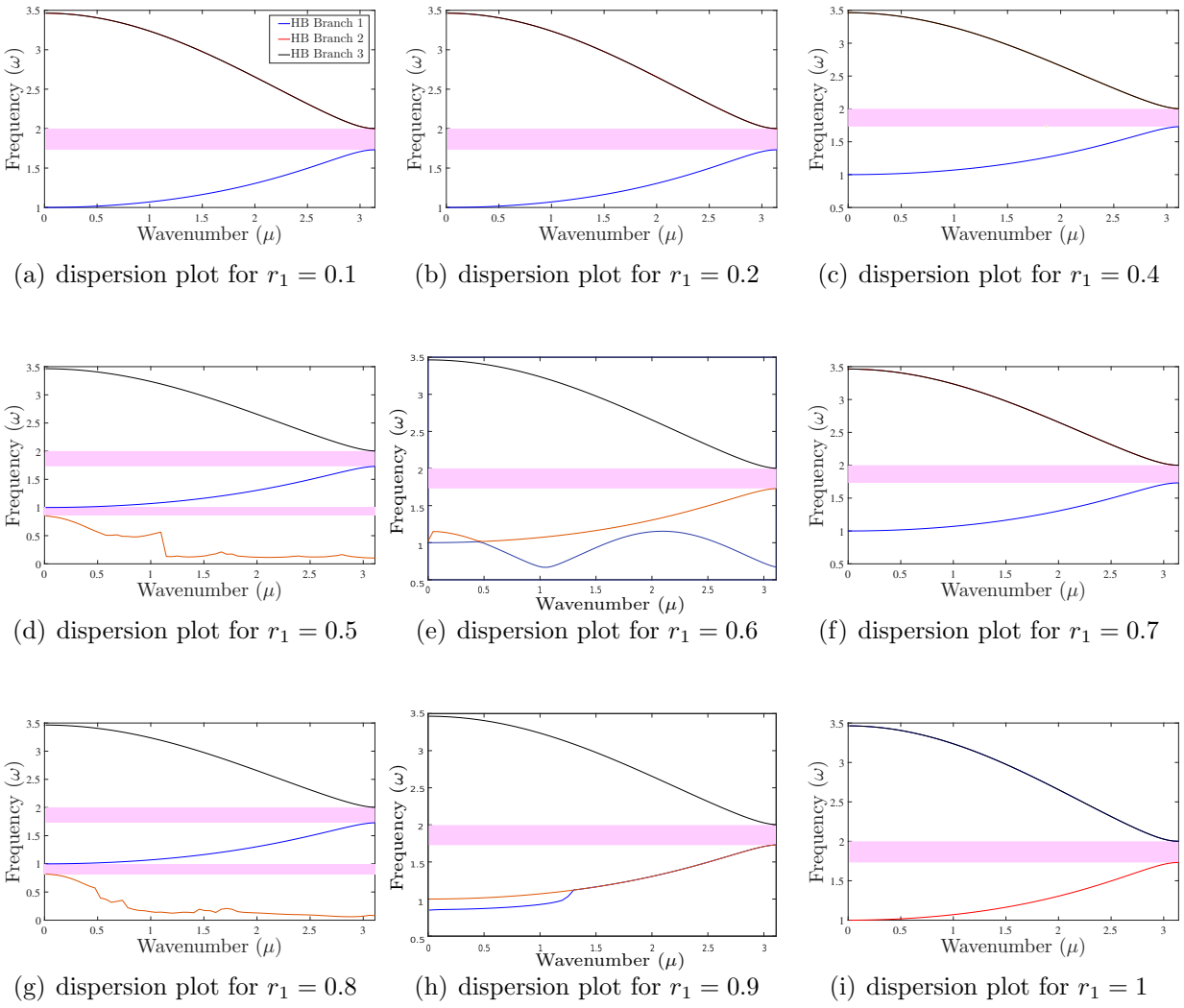
3.5.2 Dispersion profiles obtained using the generalized harmonic balance method

Just like we did for the weakly nonlinear system, here also we will vary the three mass ratios one at a time to get a better understanding of the dispersion characteristics of the system.

First we vary the mass ratio r_1 from 0.1 to 1 and plot the dispersion profiles keeping the other parameters as $r_2 = 1$, $r_a = 0.5$, $\sin\phi = 0.6$, $\sin\alpha = 0.5$. The value of the amplitude parameter A is taken to be 0.1 for a consistent comparison with the results from asymptotic analysis as was done in Section 3.4.5, Eq. (3.55). We always choose a number of harmonics M such that $M \geq 5$ for smooth dispersion branches in the strongly nonlinear regime.

So, the dispersion profiles are shown with varying mass ratio r_1 in Fig. 3.13. As we can see for axial wave propagation in our periodic chain, two visible dominant dispersion branches emerge in most of the cases with the third branch partially or fully merging with either one of the other two branches. This can be inferred to the existence of two dominant DOFs in each unit cell with inter-cell coupling with the middle vertical DOF transferring the energy of wave propagation within a particular unit cell between the horizontal DOFs in the strongly nonlinear regime. From $r_1 = 0.1$ to $r_1 = 0.4$, there is not much visible change in bandgap behavior or position of the dispersion branches with branch 2 and branch 3 merging together. The width of the frequently occurring visible bandgap and the average positions of the dispersion branches remain fairly constant with increasing r_1 and the other system parameters kept fixed. Though for some values of r_1 such as $r_1 = 0.5, 0.8$ we notice the emergence of the third dominant branch and a second visible bandgap. Next, our objective will be to examine this behavior of the bandgap and the dispersion branches for the other two mass ratios, r_2 and r_a. This variation of bandgap behavior with non-dimensional system parameters can become very useful in vibration monitoring and vibration isolation.

Next, as discussed, we will vary the mass ratio r_2 from 0.7 to 1 i.e. the stability region observed in the weakly nonlinear regime and plot the dispersion profiles with varying μ in Fig. 3.14. The other parameters are taken as $r_1 = 1$, $r_a = 0.5$, $\sin\phi = 0.6$, $\sin\alpha = 0.5$. As we can see in Fig. 3.14, the width of the bandgap decreases steadily from $r_2 = 0.7$ to $r_2 = 1$. We also observe the existence of two visible dominant dispersion branches, with the third branch merging with either of the other two for wave propagation along the axial (horizontal) direction. Also, it can be seen that the two visible dispersion branches



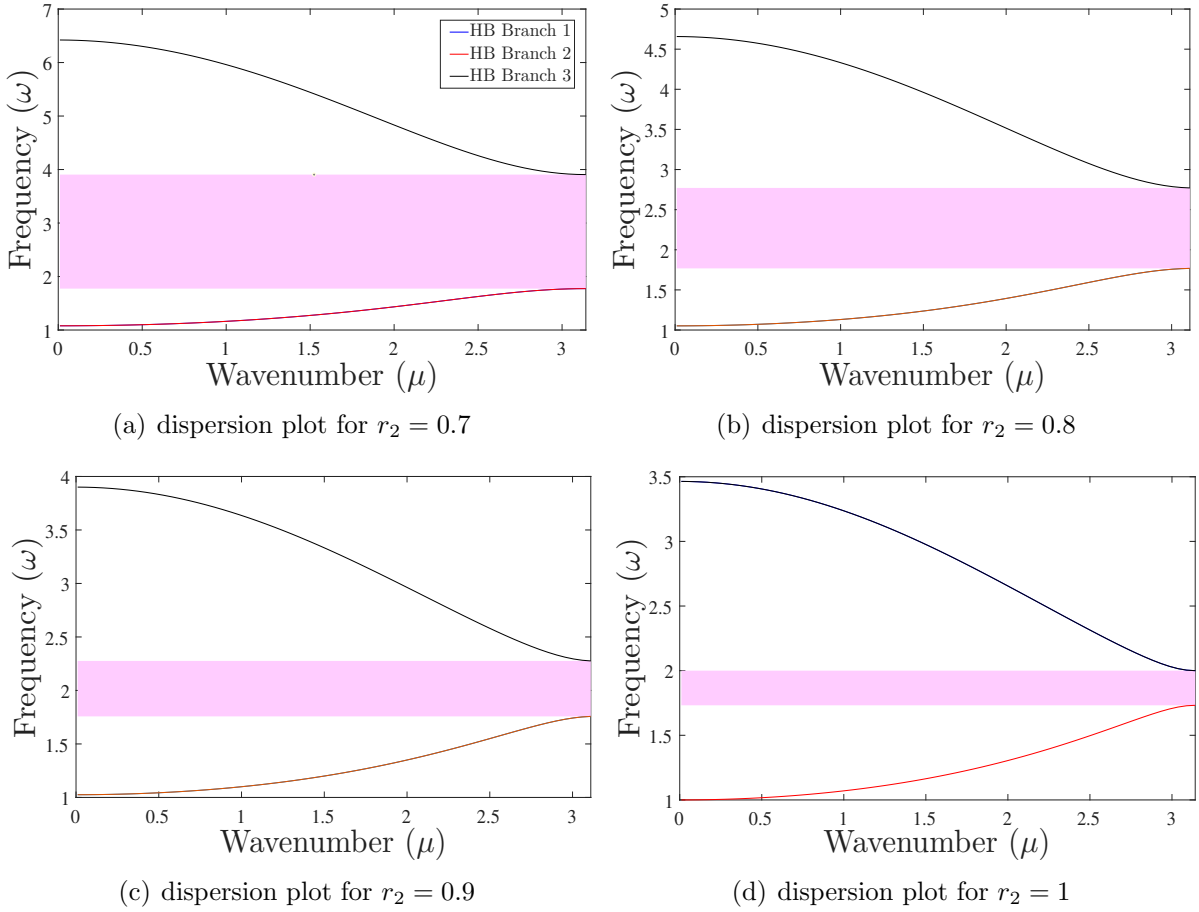
(a) dispersion plot for $r_1 = 0.1$ (b) dispersion plot for $r_1 = 0.2$ (c) dispersion plot for $r_1 = 0.4$

(d) dispersion plot for $r_1 = 0.5$ (e) dispersion plot for $r_1 = 0.6$ (f) dispersion plot for $r_1 = 0.7$

(g) dispersion plot for $r_1 = 0.8$ (h) dispersion plot for $r_1 = 0.9$ (i) dispersion plot for $r_1 = 1$

Fig. 3.13: Dispersion diagrams obtained from the generalized harmonic balance method showing the branches of frequency (ω) varying with the wavenumber (μ) and the relevant bandgaps for mass ratio r_1 varying from 0.1 to 1 and the values of the other parameters kept fixed, the weak ripples on the red HB branch near branch-merging and band-edge regions are interpreted in the context of the changes in modal participation and harmonic content discussed later in this Section 3.5.2, they are not identified here as separate bifurcations.

shift downwards with increasing r_2. This is in contrast to increasing r_1 before in Fig. 3.13, where the width of the bandgap and the positions of the dispersion branches remained fairly constant. Below the values of $r_2 = 0.7$ and reducing by one significant digit after the decimal place, i.e. for $r_2 = 0.6, 0.5.....0.1$, we observed that one or more the three frequencies go to zero or become imaginary for all values of the wavenumber from 0 to π. Since we are interested in traveling wave solutions in an undamped physical system, we will treat this value of $r_2 = 0.7$ as a lower critical bound (considering one significant digit after the decimal place) with values of r_1 and r_a set to 1 and 0.5 respectively. This outcome is consistent with the behavior in the weakly nonlinear regime where below the same value of $r_2 = 0.7$ (again considering one significant digit after the decimal place)



(a) dispersion plot for $r_2 = 0.7$

(b) dispersion plot for $r_2 = 0.8$

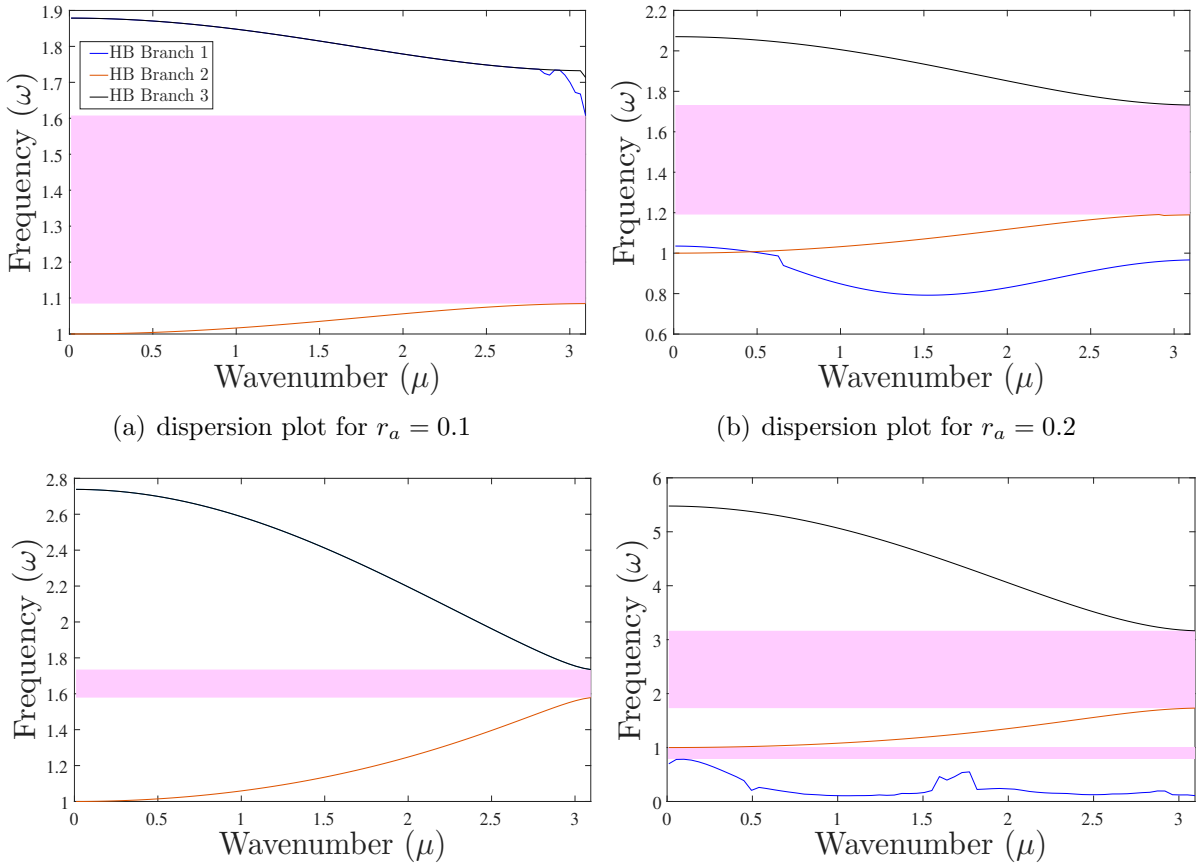
(c) dispersion plot for $r_2 = 0.9$

(d) dispersion plot for $r_2 = 1$

Fig. 3.14: Dispersion diagrams obtained from the generalized harmonic balance method showing the branches of frequency (ω) varying with the wavenumber (μ) and the relevant bandgaps for mass ratio r_2 varying from 0.7 to 1 and the values of the other parameters kept fixed.

and same other fixed values of the system parameters, we found the frequencies to be imaginary for the same range of varying μ which was again physically not realizable for a traveling wave in the same undamped system.

Finally, we vary the inertance mass-parameter ratio r_a from 0.1 to 0.6, i.e. the stability region observed in the weakly nonlinear regime and plot the dispersion profiles for the same range of μ in Fig. 3.15. The other parameters are taken as $r_1 = 1$, $r_2 = 1$, $\sin\phi = 0.6$, $\sin\alpha = 0.5$. Just like the cases of varying r_1 and r_2, here also we observe mostly the existence of two dominant visible dispersion branches in Fig. 3.15 participating in wave propagation along the axial direction. There is a third branch because of our chosen 3 DOF unit cell, but in most of the cases, it merges with either one of the other two branches producing two visible branches as the net output. The width of the prominent visible bandgap decreases steadily from $r_a = 0.1$ upto $r_a = 0.4$ and then remains fairly constant upto $r_a = 0.5$. At $r_a = 0.6$, the upper bandgap increases more in width and we see the emergence of a third trivial branch near zero which remains fairly constant over the wavenumber μ. One more visible feature to note is that both the visible, non-trivial, dominant branches of the frequency shift upward with increasing r_a, with the shift being



(a) dispersion plot for $r_a = 0.1$

(b) dispersion plot for $r_a = 0.2$

(c) dispersion plot for $r_a = 0.4$

(d) dispersion plot for $r_a = 0.6$

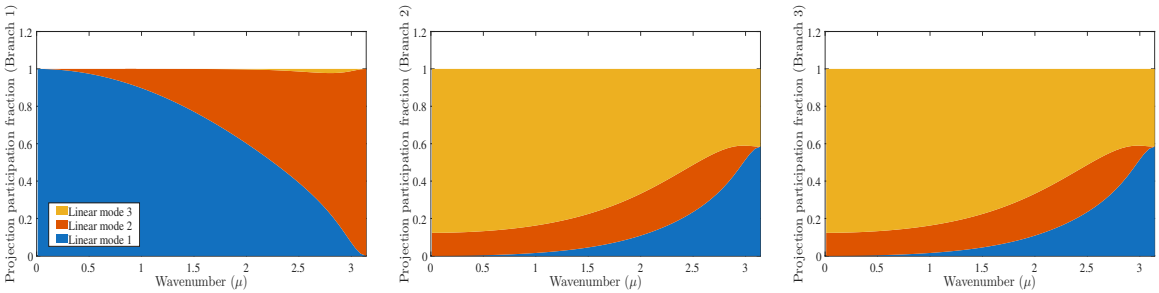
Fig. 3.15: Dispersion diagrams obtained from the generalized harmonic balance method showing the branches of frequency (ω) varying with the wavenumber (μ) and the relevant bandgaps for mass ratio r_a varying from 0.1 to 0.6 and the values of the other parameters kept fixed, the weak ripples on the red HB branch near branch-merging and band-edge regions are interpreted in the context of the changes in modal participation and harmonic content discussed later in this Section 3.5.2, they are not identified here as separate bifurcations.

more prominent for the higher branch. This is in contrast to increasing r_2 where both the branches shifted downwards in Fig. 3.14. Beyond the values of $r_a = 0.6$ and increasing by one significant digit after the decimal place,i.e. for $r_a = 0.7, 0.8.....1$, we observe as in the previous case that one or more of the frequencies become imaginary for all μ which is not realizable for an undamped physical system. The emergence of the third trivial branch near zero at $r_a = 0.6$ might be due to close proximity to the critical zone for the system parameters. As was observed in the previous case of varying r_2, beyond this same value of $r_a = 0.6$ (considering one significant digit after the decimal place), for the weakly nonlinear regime, we had imaginary values of the frequency for the same range of μ and same values of the other system parameters.

Understanding branch merging in the strongly nonlinear regime: Despite three DOFs per unit cell (η, ξ, ψ), predominantly two dominant dispersion branches emerge for axial wave propagation (Fig. 3.13-3.15). This phenomenon reflects modal energy redistribution

among coupled DOFs. For axial propagation, the horizontal DOFs (η, ψ) dominate inter-cell wave transmission through the horizontal springs (k-stiffness connections between unit cells). The vertical bi-stable DOF (ξ) participates primarily in intra-cell energy transfer, coupling the two horizontal masses within each unit cell but not directly transmitting waves between cells.

Fig. 3.16(a)-Fig. 3.16(c) report the projection-based modal participation fractions obtained by projecting the HB solution for all the three dispersion branches at each wavenumber μ onto the corresponding linear Bloch eigenvectors and normalizing the squared projection amplitudes such that $\sum_{i=1}^{3} p_i(\mu) = 1$. A representative combination of mass ratios $r_1 = 0.2, r_2 = 1, r_a = 0.5$, i.e. the same as chosen for Fig. 3.13(b) is considered to perform this modal participation analysis. While Branch 1 exhibits a progressive transfer of participation from linear mode 1 to linear mode 2 as μ increases (Fig. 3.16(a)), Branches 2 and 3 display identical participation trends (Fig. 3.16(b), Fig. 3.16(c)). Both are dominated by linear mode 3 over most of the Brillouin zone, with a growing contribution from mode 1 toward the zone boundary. This near-coincidence of the modal participation signatures indicates that, in the parameter set considered, the HB solutions on Branches 2 and 3 occupy essentially the same linear modal subspace, i.e., they correspond to the same hybridized periodic motion. Consequently, their dispersion curves HB Branch 2 and HB Branch 3 coalesce, which is observed as the merging of Branches 2 and 3 in the HB dispersion plot in Fig. 3.13(b).



(a) Modal participation fraction for HB Branch 1

(b) Modal participation fraction for HB Branch 2

(c) Modal participation fraction for HB Branch 3

Fig. 3.16: Modal participation fractions along the HB dispersion branches for $r_1 = 0.2, r_2 = 1, r_a = 0.5$, which is the same combination of mass ratios as chosen in Fig. 3.13(b), stacked areas show the normalized projection of the HB solution onto the three linear eigenmodes versus wavenumber (μ), the identical modal content of HB Branches 2 and 3 at all μ is consistent with their observed merging in Fig. 3.13(b).

The weak 'jagged' variations seen on some HB branches in Fig. 3.13, Fig. 3.15 are most pronounced near branch-merging/band-edge regions, where the vertical bi-stable DOF ξ behaves as a nonlinear internal resonator and intermittently exchanges energy with the horizontal DOFs (η, ψ) and higher harmonics. In these intervals, small changes in wavenumber μ can produce noticeable changes in harmonic content and even nearby coexisting periodic states, so the reported fundamental frequency $\omega(\mu)$ may exhibit mild ripples rather than a perfectly smooth trend.

Table 3.2 summarizes the bandgap behavior in the strongly nonlinear regime. Table 3.2 and 3.1 synthesize parametric trends observed across Fig. 3.6-3.8 and Fig. 3.13-3.15 re-

Parameter	**Range studied**	**Lower bandgap trend**	**Upper bandgap trend**	Dominant branches	**Critical value**	**Notes**
r_1	0.1-1.0	Approximately constant	Approximately constant	2 (merged)	None	Branch merging patterns vary
r_2	0.7-1.0	Nearly constant	Decreases strongly	2 (merged)	< 0.7 (instability)	Branches shift downward
r_a	0.1-0.6	Slight decrease	Non-monotonic	2 (merged)	> 0.6 (instability)	Third trivial branch emerges at $r_a = 0.6$

Table 3.2: Summary of bandgap behavior in strongly nonlinear regime for baseline angles $\sin\phi = 0.6$, $\sin\alpha = 0.5$. Trends indicate behavior as parameter increases.

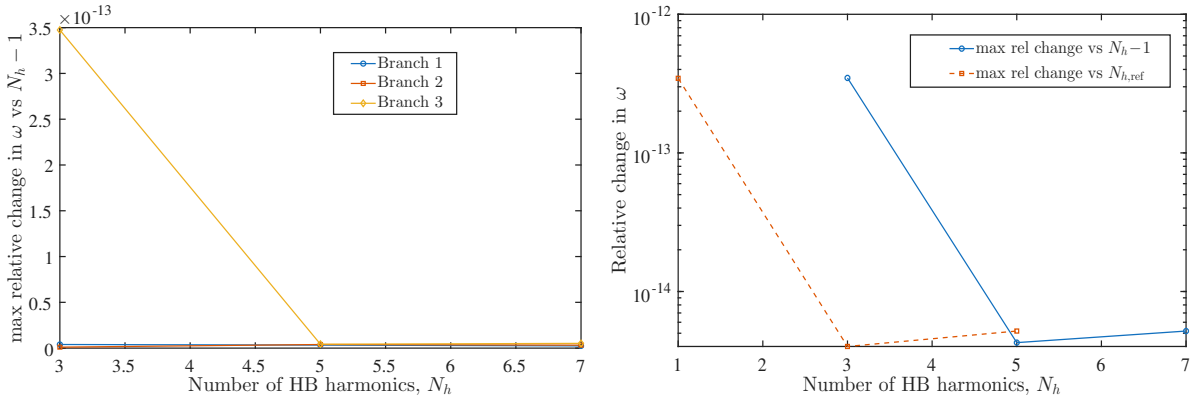
N_h	$\max_\mu \lvert\Delta\omega/\omega\rvert$ (vs. previous)	$\mathrm{RMS}_\mu \lvert\Delta\omega/\omega\rvert$ (vs. previous)	$\max_\mu \lvert\Delta\omega/\omega\rvert$ (vs. $N_{h,\mathrm{ref}} = 7$)	$\mathrm{RMS}_\mu \lvert\Delta\omega/\omega\rvert$ (vs. $N_{h,\mathrm{ref}} = 7$)
1	–	–	3.45×10^{-13}	8.91×10^{-14}
3	3.47×10^{-13}	8.97×10^{-14}	4.01×10^{-15}	1.61×10^{-15}
5	4.28×10^{-15}	2.30×10^{-15}	5.18×10^{-15}	2.26×10^{-15}
7	5.18×10^{-15}	2.26×10^{-15}	0	0

Table 3.3: (HB convergence study) Maximum and RMS relative changes in the HB-predicted dispersion frequency $\omega(\mu)$ when increasing the number of retained harmonics $N_h \in \{1, 3, 5, 7\}$ with $N_{h,\mathrm{ref}} = 7$ as reference, evaluated over $\mu \in [0.01, 0.5\pi]$ sampled at five points, 'previous' denotes the preceding N_h in the list, mass ratio combination is taken the same as for Fig. 3.13(a)

spectively. Key observations: (i) Critical threshold values are consistent across weakly and strongly nonlinear regimes, validating them as fundamental stability boundaries. (ii) The lower bandgap shows relatively consistent behavior across mass ratio variations in both regimes. (iii) The upper bandgap exhibits strong sensitivity to r_2 and r_a, offering design handles for bandgap tuning. (iv) In the strongly nonlinear regime, branch merging reduces three nominal branches to two dominant branches, reflecting modal redistribution.

This modal behavior is characteristic of systems with strong geometric coupling between orthogonal DOFs and represents genuine physical modal interaction, not numerical artifact. Direct time-domain simulations (Section 3.6) confirm that predominantly two frequencies dominate the steady-state response at most wavenumbers, validating the branch merging observed in harmonic balance analysis.

Convergence with respect to the HB harmonic truncation: We repeated the HB dispersion computation for $N_h = \{1, 3, 5, 7\}$ (with time grid $N_t = 512\, N_h$) using the mass ratio combination of Fig. 3.13(a), i.e., $r_1 = 0.1, r_2 = 1, r_a = 0.5$, and $\sin\phi = 0.6$, $\sin\alpha = 0.5$, and $A = 0.1$, but on a reduced wavenumber grid $\mu \in [0.01, 0.5\pi]$ sampled at five points. Taking $N_{h,\mathrm{ref}} = 7$ as the reference, we evaluated the maximum and RMS relative changes in the predicted dispersion frequency, both (i) between successive truncations N_h and the preceding case in the list and (ii) relative to $N_{h,\mathrm{ref}}$. The branch-wise and global convergence trends (Fig. 3.17(a) and Fig. 3.17(b)) show rapid saturation. The maximum relative deviation drops to $O(10^{-15})$ for $N_h = 3$ to 5, and the change between $N_h = 5$ and 7 remains below 6×10^{-15} as reported in Table 3.3. Accordingly, we have used $N_h \geq 5$ for the HB results reported in this work.



(a) Branch-wise maximum relative change in the HB frequency ω when increasing the harmonic truncation N_h (relative to the preceding N_h in the list).

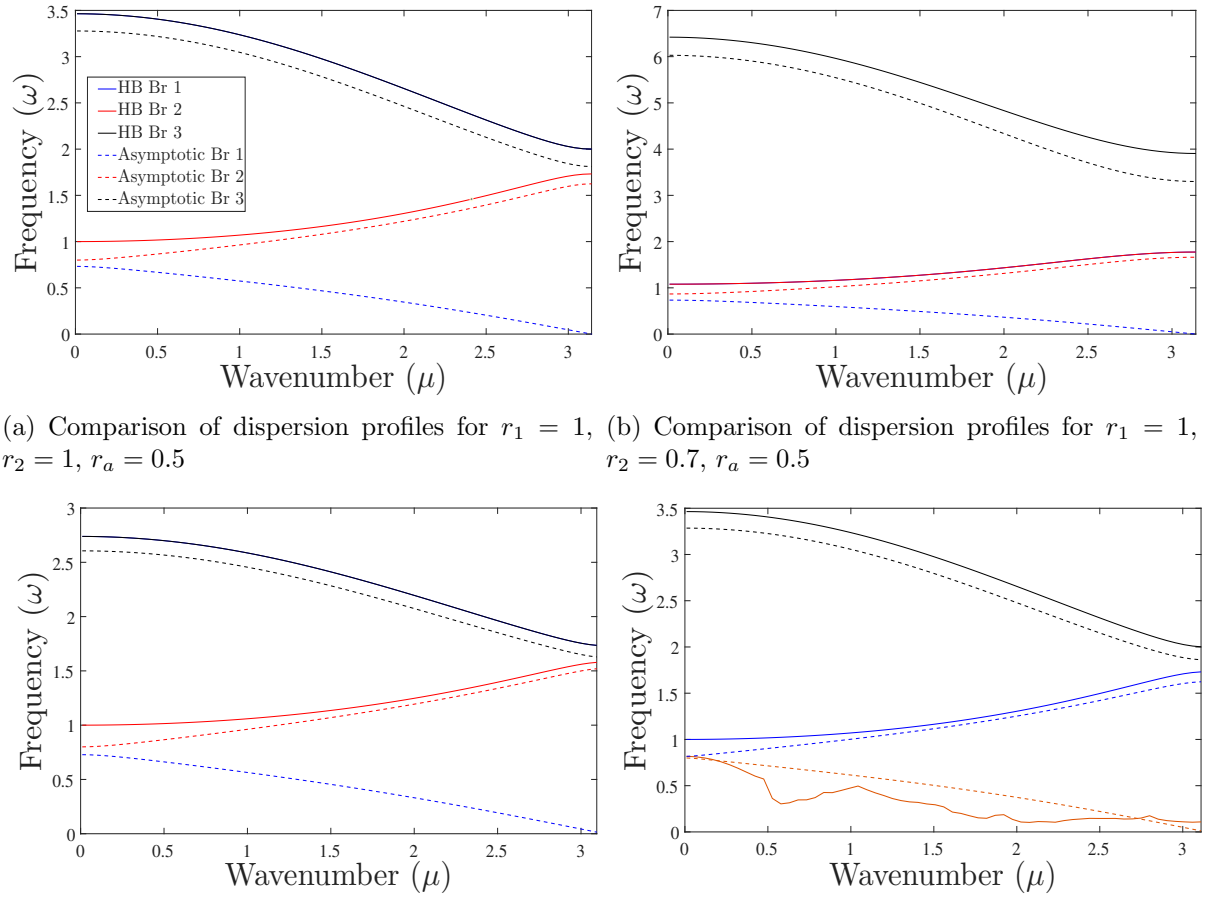
(b) Global convergence metrics for the HB dispersion: maximum relative change in ω versus N_h, computed (i) against the preceding N_h and (ii) against the reference $N_{h,\text{ref}} = 7$.

Fig. 3.17: Branch-wise and global convergence metrics for HB dispersion with increasing HB truncation N_h using the same parameter set as in Fig. 3.13(a).

3.5.3 Comparison of HB results with results from asymptotic analysis

Now, we compare the dispersion results obtained from HB method with the dispersion results obtained from asymptotic/ perturbation analysis in Section 3.4.5. We choose four sets of values of the system parameters r_1, r_2, r_a, keeping the initial angles of inclination fixed at $\sin\phi = 0.6$ and $\sin\alpha = 0.5$ and plot the dispersion profiles in Fig. 3.18.

As we can see from the comparison between the two methods in Fig. 3.18, the HB branches lie a bit higher than the asymptotic branches which is quite expected for hardening springs as in our case. The more we consider the number of terms in the Taylor series expansion around the global energy minima for asymptotic analysis, the more the dispersion branches obtained using the perturbation method will approach the branches obtained using HB method. One more observation is that for the HB method used for the strongly nonlinear regime in most of the cases keeping r_1 constant at $r_1 = 1$ (Fig. 3.18(a), Fig. 3.18(b), Fig. 3.18(c)), branch 1 (blue solid) merges with either branch 3 (black solid) or branch 2 (red solid), while for the asymptotic analysis, branch 1 (blue dashed) remains separate which again proves the partial failure of perturbation method for the strongly nonlinear regime. But, still it can be said that the perturbation method can provide a basis linear framework for predicting dispersion branches even for a fairly intricate, geometrically nonlinear system such as our model and reduce the computational cost effectively for atleast a considerable number of branches.



(a) Comparison of dispersion profiles for $r_1 = 1$, $r_2 = 1$, $r_a = 0.5$

(b) Comparison of dispersion profiles for $r_1 = 1$, $r_2 = 0.7$, $r_a = 0.5$

(c) Comparison of dispersion profiles for $r_1 = 1$, $r_2 = 1$, $r_a = 0.4$

(d) Comparison of dispersion profiles for $r_1 = 0.8$, $r_2 = 1$, $r_a = 0.5$

Fig. 3.18: Comparison of dispersion profiles obtained using HB method and asymptotic analysis for four different sets of values of the mass ratios keeping the initial angles of inclination of the springs and rigid links at $\sin\phi = 0.6$ and $\sin\alpha = 0.5$ respectively.

3.6 Time-domain simulation of the finite chain and comparison with HB results

3.6.1 Inverse Method (IM)

We now use direct numerical time-domain simulation of a finite chain composed of our chosen repeating unit cell to verify our semi-analytical (HB) results. The term 'inverse method' follows from Campana et al. [199], who use a similar finite-chain numerical approach to benchmark nonlinear dispersion results, including comparison with harmonic balance. The wavenumber is prescribed through the initial displacement field, and the corresponding frequency is identified from the ensuing free response. The present implementation applies this strategy to validate the HB dispersion branches.

We use this approach to obtain dispersion relations of a large enough finite chain consisting of 300 unit cells and free at both ends. We use this inverse method to obtain the dispersion relations to compare with our semi-analytical results obtained using

the generalized Harmonic Balance Method for the infinite periodic chain in the strongly nonlinear regime. This indeed means that we simulate our exact nonlinear equations of motion in the time-domain. We impose the wavenumber for our structure as an initial condition and release the system in time and then obtain the frequency corresponding to that imposed wavenumber from the time-domain results of a chosen measurement region far away from both boundaries or the reference unit cell located in the middle of the structure. We consider our exact nonlinear and non-dimensionalized equations of motion Eqs. (3.20)-(3.22) and choose our initial conditions as follows.

$$\begin{aligned}
\eta_j(0) &= \sum_{m=1}^{N_h} \Big[A_{\eta m} \cos\big(m\mu(j-j_0)\big) + B_{\eta m} \sin\big(m\mu(j-j_0)\big) \Big] \\
\dot{\eta}_j(0) &= 0 \\
\xi_j(0) &= \sum_{m=1}^{N_h} \Big[A_{\xi m} \cos\big(m\mu(j-j_0)\big) + B_{\xi m} \sin\big(m\mu(j-j_0)\big) \Big] \\
\dot{\xi}_j(0) &= 0 \\
\psi_j(0) &= \sum_{m=1}^{N_h} \Big[A_{\psi m} \cos\big(m\mu(j-j_0)\big) + B_{\psi m} \sin\big(m\mu(j-j_0)\big) \Big] \\
\dot{\psi}_j(0) &= 0 \\
j &\in \{1, \ldots, 300\}
\end{aligned} \tag{3.58}$$

So, the initial velocities of the masses are considered to be 0 and we impose an initial spatial wave displacement dependent on the wavenumber μ. The reference unit cell j_0 is chosen in the middle of the chain to minimize boundary effects. N_h is the number of harmonic terms considered for theoretical (HB) results. The amplitudes of the different harmonics $A_{\eta m}$, $B_{\eta m}$, $A_{\xi m}$, $B_{\xi m}$, $A_{\psi m}$, $B_{\psi m}$ are chosen based on the corresponding amplitudes obtained from the Harmonic Balance (HB) method after convergence of the Newton-Raphson algorithm. We choose to iterate every new input amplitude based on a linear scaling factor determined by the previous output amplitude and use this linear scaling factor as an individual gain to update each of the three initial/ input amplitudes individually in every iteration until they reach the targets set by the HB method within a certain tolerance (5×10^{-4}). We also use a damping profile which is maximum at the boundaries of our finite chain and decreases almost exponentially to zero in the middle of the chain to minimize the boundary effects as done in [199]. We apply the damping on the horizontally moving masses represented by η and ψ in every unit cell since they are the masses with inter-cell connections.

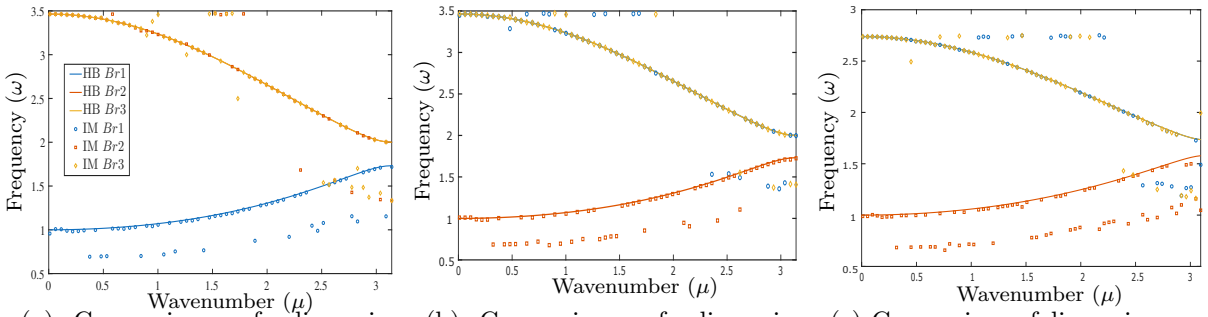
After convergence, we neglect the initial transients that might be arising from numerical issues, by allowing a settling time of $25T_0$, where $T_0 = \frac{2\pi}{\omega}$ and ω is the frequency already obtained from the HB method. Then, we extract the frequency from the time-domain results by using two methods. We consider the time-domain response of the reference unit cell located at j_0 and measure the global frequency by calculating the average time-period. Next, we choose a measurement region consisting of 30 unit cells in the center of the chain and use a complex spatial demodulation factor to eliminate noise from displacements in the time-domain. Then, we estimate the branch frequency directly from the time-domain response using a phase-slope method anchored to the Harmonic Balance

target. The time-domain signal is first resampled onto a uniform grid and, when sufficient cycles are present, passed through a zero-phase third-order Butterworth band-pass centered at the target angular frequency with a relative half-bandwidth. For real inputs we form the analytic signal with the Hilbert transform (complex inputs skip this step), unwrap its phase, and fit a straight line to the central 10–90% of the record, the slope yields the frequency estimate, while the median envelope over the same window gives a robust output amplitude. The procedure is tolerant to uneven sampling and slow drifts, and includes guards for short/noisy records; if the phase fit is ill-conditioned, it falls back to a simple zero-crossing estimate. After we evaluate the frequency from these two procedures, we report the one closest to that obtained using the Harmonic Balance method for that specific wavenumber.

We use a sufficiently large number of harmonics ($N_h \geq 5$) for the HB method to obtain smoother results. So, the net target amplitude set for a DOF to achieve in direct time-domain simulation is obtained through a rough approximation by taking the root mean square (RMS) of the amplitudes ($A_{\eta m}$, $B_{\eta m}$, $A_{\xi m}$, $B_{\xi m}$, $A_{\psi m}$, $B_{\psi m}$) of the different harmonics.

3.6.2 Dispersion plots showing comparison between harmonic balance and IM results, an error quantification and computational speedup

We now show three dispersion plots (Fig. 3.19) showing the comparison between harmonic balance (HB) results and the results obtained by direct time-domain simulation using the inverse method discussed in the previous section. We choose three representative sets of values of system parameters as in the mass ratios r_1, r_2, r_a and keep our initial angles in the unstressed equilibrium configuration fixed at $\sin\phi = 0.6$ and $\sin\alpha = 0.5$. We use the explicit ode45 solver in Matlab to run our time-domain simulations. We also keep the value of $r_2 = \frac{m_3}{m_1}$ at 1 to maintain the spatial symmetry of the unit cell to avoid the issues of non-similarity and energy-dependence of the modal curves as much as possible.



(a) Comparison of dispersion profiles for $r_1 = 0.1$, $r_2 = 1$, $r_a = 0.5$

(b) Comparison of dispersion profiles for $r_1 = 1$, $r_2 = 1$, $r_a = 0.5$

(c) Comparison of dispersion profiles for $r_1 = 1$, $r_2 = 1$, $r_a = 0.4$

Fig. 3.19: Comparison of harmonic balance (HB) results with direct time-domain (IM) simulations (wavenumber μ vs frequency ω) for three different sets of values of mass ratios keeping the initial angles of inclination of the springs and rigid links at $\sin\phi = 0.6$ and $\sin\alpha = 0.5$ respectively.

Branch	**Mean rel. error** $\bar{e}$	**RMS rel. error** e_{rms}	**Max rel. error** $e_{\max}$
1	0.0863	0.158	0.333
2	0.0408	0.105	0.333
3	0.0619	0.128	0.333

Table 3.4: Relative error metrics between the Harmonic Balance (HB) dispersion predictions and the Inverse Method (IM) time-domain validation. The pointwise relative error is defined as $e(\mu) = \left|\frac{\omega_{\text{IM}}(\mu)-\omega_{\text{HB}}(\mu)}{\omega_{\text{HB}}(\mu)}\right|$. Reported values are computed over all sampled wavenumbers for each dispersion branch for a combination of mass ratios taken the same as for Fig. 3.19(a).

Fig. 3.19(a), Fig. 3.19(b) and Fig. 3.19(c) might look the same quantitatively, but there is a qualitative difference. In Fig. 3.19(a), branch 2 merges with branch 3 for both semi-analytical HB model and numerical IM model, and effectively we see two dominant branches which is according to our expectations for the strongly nonlinear regime as discussed in Section 3.5. In Fig. 3.19(b) and Fig. 3.19(c), we notice the same branch merging and effective existence of two dominant branches but in this case, branch 1 merges with branch 3 for both analytical and time-domain simulation results.

We show an explicit error quantification between dispersion results obtained from the HB method and direct time-domain IM method in Table 3.4. We choose the values of the mass ratios as $r_1 = 0.1, r_2 = 1, r_a = 0.5$ which is the same combination of mass ratios as chosen in Fig. 3.19(a), keeping the initial angles of inclination of the springs and rigid links at $\sin\phi = 0.6$ and $\sin\alpha = 0.5$ respectively. For each of the three dispersion branches, we evaluate the relative error $\left|\frac{\omega_{\text{IM}}(\mu)-\omega_{\text{HB}}(\mu)}{\omega_{\text{HB}}(\mu)}\right|$ and report the mean, maximum and rms relative errors in Table 3.4.

The raw relative error is also plotted against the wavenumber μ in Fig. 3.20. The HB method took a time of 865.91 seconds or approximately 14.4 minutes to implement in a Matlab platform on a single-processor machine. The direct time-domain integration or IM method for our chosen finite chain comprising of 300 unit cells took 3997.40 seconds or approximately 1.1 hours to implement in a Matlab platform on the same machine. So, it can bee seen that the HB method provides a computational speedup of atleast 4.5 times than direct time-domain simulations while still predicting the dispersion behavior in the generalized strongly nonlinear regime with a significant level of accuracy.

3.6.3 Discussion of the comparison between time-domain simulation and HB results, possible chaos and nonlinear modal interactions

As we can see from the results in our previous Section 3.6.2, the frequency values obtained by time-domain simulation of our exact nonlinear, long enough, finite periodic chain match quite well with the patterns obtained from the HB method for most of the values of the wavenumber (μ). But, we also notice some outliers for some values of the wavenumber. To further investigate this disparity at some places, we shift our focus onto checking whether our system in the strongly nonlinear regime shows transient chaos as discussed

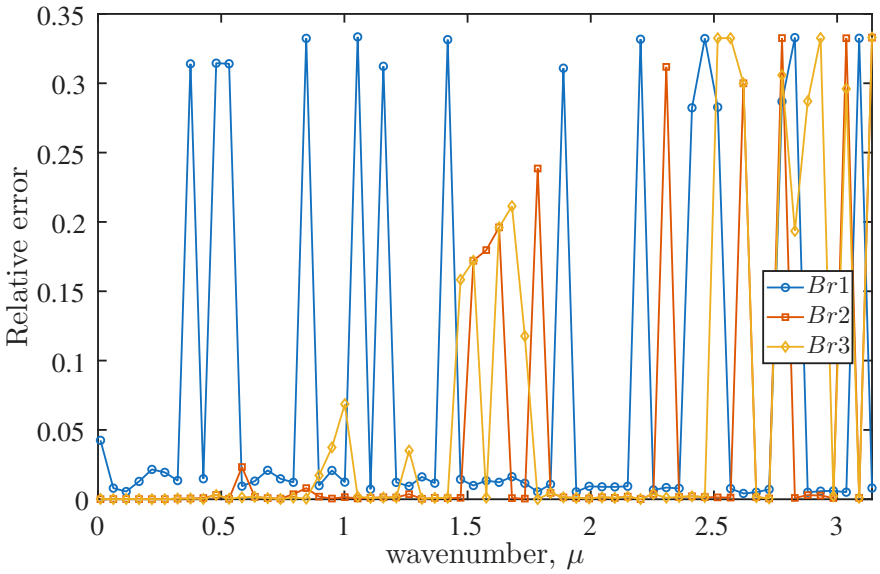


Fig. 3.20: Relative error $\left|\frac{\omega_{\mathrm{IM}}(\mu)-\omega_{\mathrm{HB}}(\mu)}{\omega_{\mathrm{HB}}(\mu)}\right|$ plotted against the wavenumber μ for all the three dispersion branches for a combination of mass ratios taken the same as for Fig. 3.19(a)

when proposing the unit cell model in Section 3.1. We check the time-domain behavior of our periodic chain for some specific values of wavenumber μ to check if the long-term behavior is aperiodic since that is one of the minimal necessary criteria for chaos [197]. We do not notice aperiodicity in the time-domain over a significantly large time window. Since our system is deterministic in the sense that there is no random input, we go on to check the last necessary criterion for chaos i.e. positive Lyapunov exponent or in other words, a sensitive dependence on initial conditions. Two of the Lyapunov coefficients turned out to be greater than zero for the same system parameters. If the system is indeed chaotic, then the Nonlinear Normal Mode (NNM) solutions obtained through the convergence of the HB method would not be able to capture the actual physical behavior of a finite version of our model, because HB method inherently assumes periodic behavior in the steady state which contradicts the existence of chaos in any form. But, still the HB method can be a good framework to predict the system behavior in the non-chaotic or periodic regime and can efficiently reduce the computational cost of long time-domain simulations.

Nonlinear Floquet stability of the HB periodic Bloch orbits: To quantitatively assess whether the Harmonic Balance (HB) dispersion branches correspond to stable time-periodic Bloch waves, we compute the nonlinear Floquet multipliers ρ by linearizing the dynamics about each converged HB periodic orbit over one period (Hill/Floquet expansion with $N_{floq} = 5$ sideband harmonics and 9 samples of the perturbation Bloch phase ν) and plot $\max|\rho|$ with the wavenumber μ in Fig. 3.21. For the parameter set used in Fig. 3.19(a) ($r_1 = 0.1$, $r_2 = 1$, $r_a = 0.5$), the HB periodic solutions are found to be linearly unstable over the Brillouin zone. The maximum magnitude of the nontrivial multipliers, excluding the neutral multiplier $\rho \approx 1$ associated with time-shift invariance, reaches $\max_\mu |\rho| \approx 15.7$ for Branch 1 and $\max_\mu |\rho| \approx 4.08$ for Branches 2, 3. This provides a direct stability-based explanation consistent with the previously observed positive Lyapunov exponents. While HB can still compute the underlying periodic Bloch orbits, their loss of stability implies

that time-domain trajectories may drift toward modulated or quasiperiodic responses in certain regimes, so the HB dispersion curves should be interpreted as continuations of periodic solutions rather than guaranteed stable propagating waves.

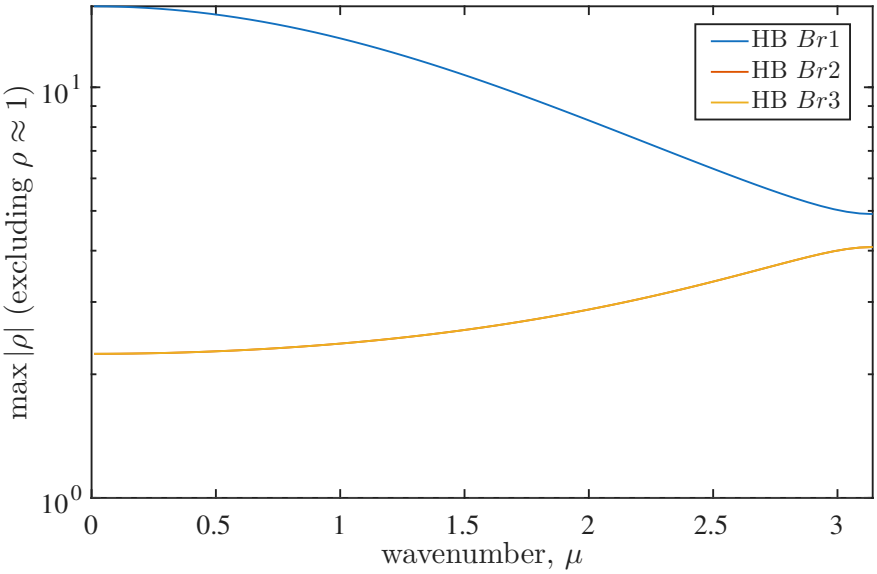


Fig. 3.21: Nonlinear Floquet stability of the harmonic balance (HB) periodic Bloch orbits for $r_1 = 0.1, r_2 = 1, r_a = 0.5$ (same parameter set as Fig. 3.19(a)), the quantity shown is the maximum modulus of the non-trivial Floquet multipliers, $\max_{\ell \neq triv} |\rho_\ell(\mu)|$, as a function of the Bloch wavenumber μ, Floquet multipliers are computed using a Hill/Floquet harmonic expansion retaining $N_{floq} = 5$ sideband harmonics, i.e. $2N_{floq} + 1 = 11$ Fourier sidebands in the perturbation ansatz, values above unity indicate linear instability of the corresponding periodic orbit.

The other reason for this disparity between HB and IM results might be the root mean square (RMS) approximation to set the target amplitude for IM time-domain simulations. Our next approach in the future will be to find better methods of approximating the target amplitudes from the multi-harmonic HB steady state results. One more plausible reason for the discrepancy at few places could be due to the boundary effects which arises as an artifact of considering a finite chain for the purpose of numerical simulations. Though a damping layer has been used to minimize these boundary effects and the reference unit cell has been considered in the centre far away from the boundaries, in the strongly nonlinear regime, the wave profile might get distorted at some places due to reflections from the boundaries.

3.7 Concluding remarks

An Amplitude-Locked, Inverse-method-Guided, multi-harmonic Nonlinear (ALIGN) framework, a comprehensive semi-analytical methodology for analyzing strongly nonlinear discrete periodic structures with non-integrable geometric nonlinearities has been presented. This method addresses three key challenges that limit existing approaches: (i) handling non-polynomial, algebraic forcing terms through time-domain collocation with complex-

step differentiation, (ii) systematic validation via amplitude-locked time-domain simulations with RMS-targeted multi-harmonic initial conditions, and (iii) robust branch tracking through degeneracies using MAC-based feature matching on high-dimensional harmonic coefficient vectors. A summary of the methodology developed is shown in Fig. 3.22. The methodology was demonstrated on a bi-stable-inertial periodic chain ex-

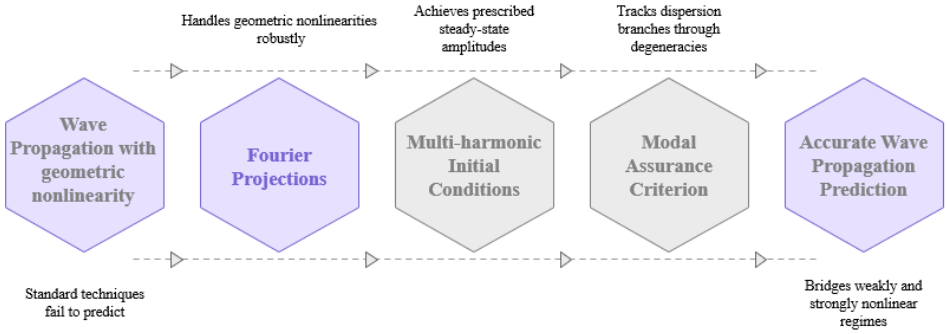


Fig. 3.22: A Generalized Framework for Discrete Nonlinear Periodic Structures.

hibiting the full spectrum of computational difficulties: coupled horizontal-vertical dynamics, non-integrable square-root terms from geometric constraints (Eq. (3.20)-(3.22)), and amplitude-dependent behavior requiring multiple harmonics ($N_h \geq 5$) for accurate representation. This successfully bridged weakly nonlinear (perturbation-based, Section 3.4) and strongly nonlinear (multi-harmonic balance, Section 3.5) regimes, with time-domain validation (Section 3.6) confirming amplitude-dependent dispersion predictions for a significant portion of the parameter space. The results obtained will have a significant impact on understanding the dynamical behavior and wave propagation characteristics of a fairly complex dynamical system both in its strongly and weakly nonlinear regime. Such a periodic lattice can be used for vibration suppression, vibration monitoring, vibration isolation and noise filtering among other applications. Key findings from the demonstration system include:

- Identification of critical parameter thresholds ($r_2 > 0.6$ keeping other mass ratios fixed, $r_a < 0.7$ keeping other mass ratios fixed) defining stability boundaries, consistent across weakly and strongly nonlinear regimes.

- Systematic bandgap manipulation through mass ratio variations and its predictability through inexpensive HB algorithms or familiar perturbation methods (Table 3.1, 3.2).

- Modal redistribution in strongly nonlinear regime producing two dominant branches despite three DOFs per unit cell (explained in Section 3.5.2).

- Computational efficiency: The framework developed enables design space exploration significantly faster than direct time-domain simulation while maintaining accuracy for periodic solutions.

Key novel features of this framework include:

- The main novelty of this framework is highlighted in the analytically tractable treatment of the dynamical system considered in this Chapter by itself, i.e., a periodic lattice with geometric nonlinearity and inertial coupling which has not been analyzed in the existing literature in terms of bandgap engineering.

- In spite of being employed on this specific dynamic model, this framework is not restricted to the bi-stable-inertial system but applies to any discrete periodic structure with geometric, kinematic, or constraint-based nonlinearities expressible as algebraic functions. Examples include tensegrity metamaterials, origami-inspired structures, compliant mechanisms, granular chains with geometric contacts, and bio-inspired lattices with coupled rotational-translational DOFs.

- Systematic treatment of non-integrable nonlinearities via time-domain collocation with complex-step differentiation, generalizable to any algebraic geometric nonlinearity

- Amplitude-locked validation strategy with RMS-targeted multi-harmonic initial conditions enabling systematic time-domain verification across amplitude-wavenumber space. The amplitude-dependent dispersion curves and parametric maps (Fig. 3.6-3.19, Table 3.1, 3.2) provide systematic design guidance for achieving desired bandgap characteristics. Designers can rapidly explore mass ratio, geometric angle, and amplitude parameter spaces without expensive time-domain simulations.

- Robust branch tracking through MAC-based feature matching preventing branch swapping through degeneracies and crossings.

- Unified framework spanning weakly to strongly nonlinear regimes with validated consistency between perturbation and harmonic balance approaches providing significant computational efficiency over direct time-domain simulation while maintaining accuracy for periodic solutions.

This Chapter was intended as an introductory starting work to demonstrate bandgap engineering and tunable dispersion behavior in fairly complex nonlinear periodic structures combining the elements of bi-stability and stable negative inerters through an analytically tractable, comprehensively formulated general framework. Henceforth, we shall use key ideas from this proposed generalized framework to investigate tunable energy harvesting characteristics in suitably engineered nonlinear periodic structures where bistability and negative inertial coupling will be shown to both qualitatively and quantitatively improve the free-wave (unforced) harvesting landscape for beneficial engineering designs.

Chapter 4

Energy harvesting from transient free waves in a piezoelectric periodic chain: a settling-time approach

4.1 Introducing the baseline model for free-wave energy harvesting

As a step forward from introducing the consolidated, generalized framework in Chapter 3 for analyzing tunable dispersion characteristics in nonlinear periodic structures to characterizing free-wave energy harvesting in periodic structures, we start with a simple linear periodic model of a piezoelectric harvester and propose an analytically tractable approach to evaluate the harvesting behavior in the absence of sustained external forcing. Conventional vibration energy harvesting is typically based on sustained external forcing and operation in the vicinity of a resonant frequency. This generally necessitates careful resonance tuning and can limit practical performance when the excitation is intermittent, transient, or not externally controlled. Hence, this Chapter yields an independent framework for identifying the operating regime of the system parameters for optimal energy harvesting with out the need for external forcing or resonance tuning. The proposed method thus represents a significant step beyond energy harvesting in forced single degree of freedom oscillators near resonance, by exploiting the free-wave propagation characteristics of unforced periodic systems around an optimum frequency determined independently and solely by the system's inherent structural, geometrical, and electrical parameters.

4.1.1 Linear piezoelectric harvester

We consider a linear piezoelectric energy harvester represented by a periodic chain composed of a vertical cantilever Euler-Bernoulli beam with uniform cross-section of length L, width w and thickness h with a tip mass M_t and a piezoelectric patch at the base near the fixed end. The tip mass is considered to be significantly larger than the mass of the beam. The periodic chain is constructed by coupling the tip mass to adjacent unit cells via horizontal linear springs as shown in Fig. 4.1. Piezoelectric patches are pasted in a bimorph 31 configuration near the fixed end of each beam in the chain for electrical energy

harvesting from free wave motion through the chain. The beam material is considered to be isotropic with density ρ.

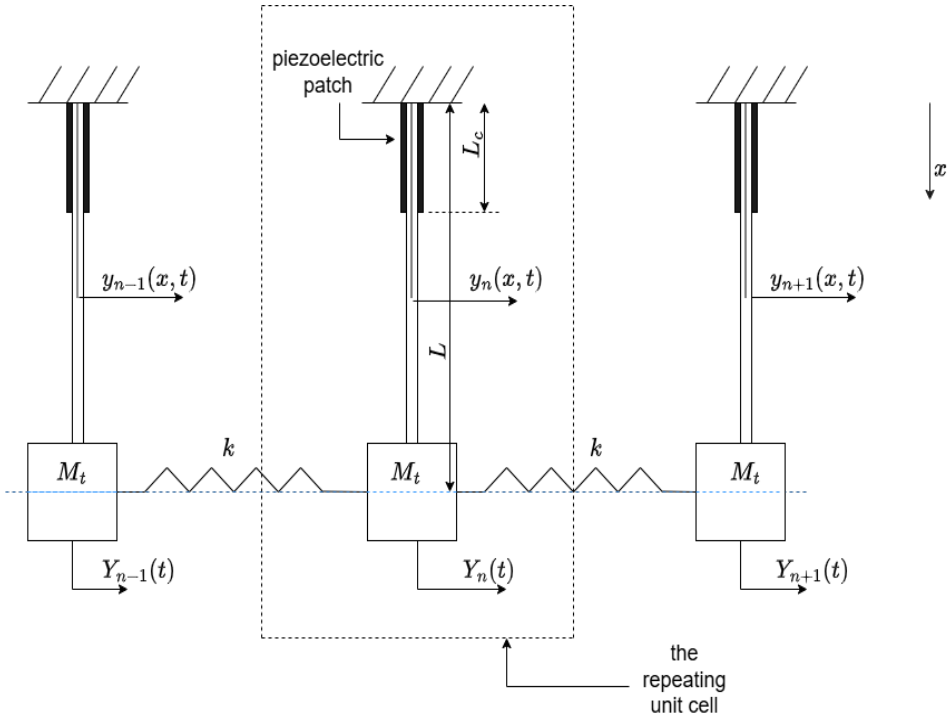


Fig. 4.1: The repeating n-th unit cell with tip masses and beams of adjacent cells shown.

4.1.2 Equations of motion

The equations of motion are derived from the Lagrangian of the system. The axial displacement of the beam and hence the tip mass are considered to be negligible in comparison to the transverse displacement. Since the mass of the beam is considered to be negligible when compared to the tip mass, the beam is considered as a purely flexural element and the kinetic energy of the system arises only due to the tip mass. For the same reason, the general transverse displacement at any point in the beam can be expressed in terms of the tip mass displacement using a relationship based on the first mode of the linear mode shape of the beam. Essentially, we use a single mode approximation for the beam displacement neglecting the contribution from higher modes of vibration.

The single-mode reduction is intended as a leading-order description of the periodic system in the low-frequency, tip-mass-dominated regime considered here without loss of generality for the present objective. It is expected to remain appropriate so long as the response is governed predominantly by the fundamental flexural mode, i.e., when the dynamics are controlled by the global tip motion rather than by short-wavelength bending of the beam. The free waves studied here are generated by initial conditions imposed on the proof masses and correspond to the lowest collective branch of the periodic chain, rather than to local high-frequency bending dynamics of the individual beams. The approximation may lose quantitative accuracy when in nonlinear models, snap-through becomes sufficiently abrupt to generate appreciable higher-mode content, strong curvature

localization develops near the clamp, or the relevant time scales approach those of the higher flexural modes. In this sense, the present formulation should be viewed as a reduced model for the collective horizontal (axial) wave dynamics and harvesting trends, rather than as a full structural representation of all beam modes. Using the dimensional parameters of the system as given in Table 4.1, the bare beam mass is approximately 0.616 g, while the tip mass is 10 g. Thus, the tip mass is about 16.2 times larger than the beam mass, so the dominant inertia is concentrated at the tip and a low-frequency disturbance couples primarily to the fundamental flexural coordinate. It is also noteworthy here that for the admissible functions used in the model, the second flexural mode is approximately 81 times stiffer than the first mode and its natural frequency is therefore much higher in the tip-mass-dominated limit. Later, it will be shown that the operating frequency range of interest for free wave propagation in the horizontal axial direction of the periodic chain generated solely due to initial conditions on the tip mass will be lower than the fundamental natural frequency of the isolated beam-tip-mass unit cell and much lower than the second natural frequency of the same which again justifies the single-mode reduction for studying the global collective axial wave dynamics and energy harvesting trends.

The kinetic energy arising due to the tip mass M_t is given by

$$T = \frac{1}{2} M_t \dot{Y_n}^2 \tag{4.1}$$

where $Y_n(t)$ is the displacement of the tip mass in the transverse/ horizontal direction in the n-th unit cell.

The potential energy of the system or the unit cell under consideration comprises of the beam's elastic strain energy, the elastic potential energy stored in the linear horizontal intercellular springs and the negative of the electrical work done by the piezoelectric patch and is given by:

$$\begin{aligned} U = \frac{1}{2} EI \int_0^L \left(\frac{\partial^2 y_n}{\partial x^2} \right)^2 dx + \frac{1}{2} k (Y_n - Y_{n-1})^2 \\ + \frac{1}{2} k (Y_n - Y_{n+1})^2 - W_E \end{aligned} \tag{4.2}$$

EI is the flexural rigidity of the beam, $y_n = y_n(x,t)$ is the general lateral beam displacement in the n-th unit cell, $Y_n = y_n(L,t)$ is the displacement of the tip mass in the n-th unit cell, k is the stiffness co-efficients of the linear springs, W_E is the electrical work done by the piezoelectric patches. It has been considered that the displacement-curvature relationship of the beam is linear.

Since we are interested in the first mode-motion of beam displacement, the general lateral displacement at any point in the beam will have identical harmonic time history corresponding to the first natural frequency of vibration of the cantilever beam with tip mass. So, the general lateral displacement $y(x,t)$ can be related to the displacement of the tip mass Y by any admissible function satisfying the geometric boundary conditions at the fixed end of the beam [110].

$$y_n(x,t) = y_n(L,t)\phi(x) = Y_n(t)\phi(x) \tag{4.3}$$

where the admissible function is chosen to be $\phi(x) = 1 - \cos\left((2j-1)\frac{\pi x}{2L} \right)$, j being an integer. It is important to note that it cannot be assumed that $Y_n(t)$ will be a harmonic

motion with the lowest natural frequency of an isolated cantilever beam with tip mass because we are imposing additional constraints to the isolated beam-mass system by constructing a periodic chain with intercellular linear spring elements. So, the frequency (ω) of the tip mass $Y_n(t)$ in our periodic system has to be derived following the standard theories of free harmonic wave propagation in periodic structures and in the most generalized case, it will be a function of the wavenumber (μ).

With the chosen $\phi(x)$, the strain energy of the beam can be obtained as

$$\begin{aligned}\frac{1}{2}EI\int_0^L\left(\frac{\partial^2 y_n}{\partial x^2}\right)^2 dx &= \frac{1}{2}EIY_n^2\int_0^L\left(\frac{d^2\phi}{dx^2}\right)^2 dx \\ &= \frac{1}{2}EIY_n^2\left(\frac{(2j-1)^4\pi^4}{32L^3}\right)\end{aligned} \tag{4.4}$$

The electrical work W_E in the n-th unit cell is derived from the moment produced by a voltage V_n across the piezoelectric layer. The moment is given by $M_\Lambda = \gamma_c V_n(t)$, where γ_c is a constant dependent on the geometry and configuration of the piezoelectric transducer. So, the electrical work can be obtained by multiplying the moment with the curvature of the beam and is given by

$$\begin{aligned}W_E &= \int_0^{L_c}\gamma_c V_n\frac{\partial^2 y_n}{\partial x^2}\,dx \\ &= \gamma_c V_n Y_n\int_0^{L_c}\frac{d^2\phi(x)}{dx^2}\,dx \\ &= \gamma_c V_n Y_n\int_0^{L_c}(2j-1)^2\frac{\pi^2}{4L^2}\cos\left((2j-1)\frac{\pi x}{2L}\right)dx \\ &= \gamma_c(2j-1)\frac{\pi}{2L}\sin\left((2j-1)\frac{\pi L_c}{2L}\right)V_n Y_n \\ &= \Theta\, Y_n V_n.\end{aligned} \tag{4.5}$$

where L_c is the length of the piezoelectric patch and the constant Θ is given by

$$\Theta = \gamma_c(2j-1)\frac{\pi}{2L}\sin\left((2j-1)\frac{\pi L_c}{2L}\right). \tag{4.6}$$

For a bimorph piezoelectric patch, γ_c can be evaluated [107] as

$$\gamma_c = Ed_{31}w_c(h+h_c) \tag{4.7}$$

where E is the modulus of elasticity of the beam, h is the thickness of the beam, h_c is the thickness of the piezoelectric patch, w_c is the width of the piezoelectric patch and d_{31} is the piezoelectric constant.

Using Lagrange's equation $\frac{d}{dt}\left(\frac{\partial L_a}{\partial \dot{Y}_n}\right) - \frac{\partial L_a}{\partial Y_n} = 0$, the equations of motion of the representative n-th unit cell can be derived in terms of the beam tip displacement for single-mode approximation. The equations of motion of the tip mass in the n-th unit cell in terms of beam tip mass displacement for single- mode approximation are hence obtained as (taking the integer $j = 1$ without loss of generality):

$$M_t\ddot{Y}_n + \frac{EI\pi^4}{32L^3}Y_n + k\Big(2Y_n - Y_{n-1} - Y_{n+1}\Big) - \Theta V_n = 0 \tag{4.8}$$

On the electrical side, considering the piezoelectric patches as a capacitor, the electrical governing differential equation can be obtained as:

$$C_p\dot{V}_n + \frac{V_n}{R_l} + \Theta\dot{Y}_n = 0 \tag{4.9}$$

where R_l is the load resistor and C_p is the capacitance of the piezoelectric patches.

4.2 Dispersion characteristics in the regime of free wave propagation

Assuming a Bloch solution for plane wave propagation, we obtain

$$\begin{aligned} Y_{n+1}(t) &= Y_n(t)e^{i\mu} \\ Y_{n-1}(t) &= Y_n(t)e^{-i\mu} \end{aligned} \tag{4.10}$$

where μ is the non-dimensional wavenumber. Introducing $\tau = \omega_n t$, $\tilde{Y}_n = Y_n/L$, $\hat{\tau}_e = \omega_n R_l C_p$, $\tilde{V}_n = V_n/V_0$ with $\omega_n = \sqrt{\frac{k}{M_t}}$, $V_0 = \frac{\Theta L}{C_p}$ defined as a natural voltage scale in the open-circuit limit $R_l \to \infty$, $\tilde{k} = k_{eff}/k$, $k_{eff} = EI\pi^4/(32L^3)$ and $\theta = \Theta^2/(C_p k)$, the Bloch-reduced electromechanical equations become (prime denoting differentiation with respect to τ):

$$\tilde{Y}_n'' + \Big(2(1-\cos\mu) + \tilde{k}\Big)\tilde{Y}_n - \theta\tilde{V}_n = 0 \tag{4.11}$$

$$\tilde{V}_n' + \frac{\tilde{V}_n}{\hat{\tau}_e} + \tilde{Y}_n' = 0 \tag{4.12}$$

while the equivalent electrical equation in the form of stored charge $\tilde{q}_n$ is

$$\hat{\tau}_e\tilde{q}_n'' + \frac{1}{\hat{\tau}_e}\tilde{q}_n + \tilde{Y}_n' = 0 \tag{4.13}$$

where, $\tilde{q}_n = \frac{q_n}{q_0}$ and $q_0 = \Theta L$ is a natural charge scale in the open-circuit limit. This scheme of non-dimensionalization of the electrical parameters is useful because it results in $\tilde{V}_n \equiv \tilde{q}_n$, so it is relatively easier to switch according to our needs. Seeking the temporal part of the solutions to (4.11) and (4.13) in steady state in the form [111]

$$\tilde{q}_n(\tau) = Qe^{i\omega\tau} \tag{4.14}$$

where we call ω the non-dimensional free wave frequency in a colloquial terminology and consider it as a book-keeping parameter as of now. Applying the method of harmonic balance to Eq. 4.11 and Eq. 4.13 gives the dispersion relation

$$\cos\mu = 1 - \frac{\Big(\omega^2 - \tilde{k}\Big)\Big(1 - \omega^2\hat{\tau}_e^2\Big) + \theta i\omega\hat{\tau}_e}{2\Big(1 - \omega^2\hat{\tau}_e^2\Big)} \tag{4.15}$$

Without the piezoelectric harvester, this reduces to

$$\cos\mu = 1 - \frac{\Big(\omega^2 - \tilde{k}\Big)}{2} \tag{4.16}$$

Elastic beam, Tip mass		**Piezoelectric Patches**	
Parameters	**Values**	**Parameters**	**Values**
ρ	$2700\,\mathrm{kg\,m^{-3}}$	L_c	$30\,\mathrm{mm}$
E	$70\,\mathrm{GPa}$	w_c	$9.3\,\mathrm{mm}$
w	$9.5\,\mathrm{mm}$	h_c	$0.5\,\mathrm{mm}$
h	$0.25\,\mathrm{mm}$	d_{31}	$-210\,\mathrm{pC\,N^{-1}}$
L	$96.1\,\mathrm{mm}$	C_p	$51.4\,\mathrm{nF}$
M_t	$10\,\mathrm{g}$	R_l	$20\,\mathrm{M\Omega}$

Table 4.1: Dimensional parameters chosen for the electromechanical model.

It is noteworthy to mention here that harmonic balance method (HBM) can be typically applied to steady-state periodic motion in forced systems. Though we do not have any explicit external forcing/ excitation in our system, still the electromechanical coupling Θ or equivalently θ can and will essentially induce a qualitative dynamic behavior in our system similar to that of an oscillator driven by an external periodic force/ excitation. So, using the traditional HBM for our coupled electromechanical system seems to be justified and reasonable [200].

Also, we wish to report here that we rewrote the voltage equation (4.12) in terms of charge $\tilde{q}_n$, i.e., Eq. (4.13), which resembles a second-order undamped equation, in order to explicitly apply the well-known harmonic balance method (HBM) to evaluate a closed-form expression of the dispersion relation (4.15) which can capture, in the most generalized regime, both the propagating and attenuating components. Had we retained the voltage equation in its original form as in (4.9) or equivalently (4.12), applying the harmonic balance method would have generated a dispersion relation that only corresponds to standing waves with $\cos\mu = 1 \implies \mu = 0$ in the irreducible Brillouin zone (IBZ).

The values of the dimensional parameters are taken as in [108] and summarized in Table 4.1. For obtaining the dispersion profiles, we adopt the direct procedure, that is, fix the value of the frequency and evaluate the wavenumber by using the dispersion relations (4.15) and (4.16).

4.2.1 Band structure behavior with the electrical and structural parameters

The non-dimensional stiffness parameter $\tilde{k} = \frac{k_{eff}}{k}$ has been chosen to be $\tilde{k} = 2$.

Fig. 4.2 shows how the Bloch wavenumber changes as the load resistance R_l or in other words, the non-dimensional electrical time constant $\hat{\tau}_e = \omega_n R_l C_p$ is increased while all mechanical parameters and the piezoelectric capacitance C_p are kept fixed. It is important to note that increasing the value of the capacitance C_p while keeping the resistance R_l and other parameters fixed will have the same effect on the band structures, and so will be the effect of increasing R_l and C_p simultaneously because all these scenarios will increase the effective electrical time constant $\tau = R_l C_p$ or equivalently $\hat{\tau}_e = \omega_n R_l C_p$ in non-dimensional form. Hence, these results are not shown here for redundancy.

Next, we will study the effect of varying the stiffness coefficient of the springs (k) or equivalently the non-dimensional stiffness parameter $\tilde{k}$ on the band structures in the

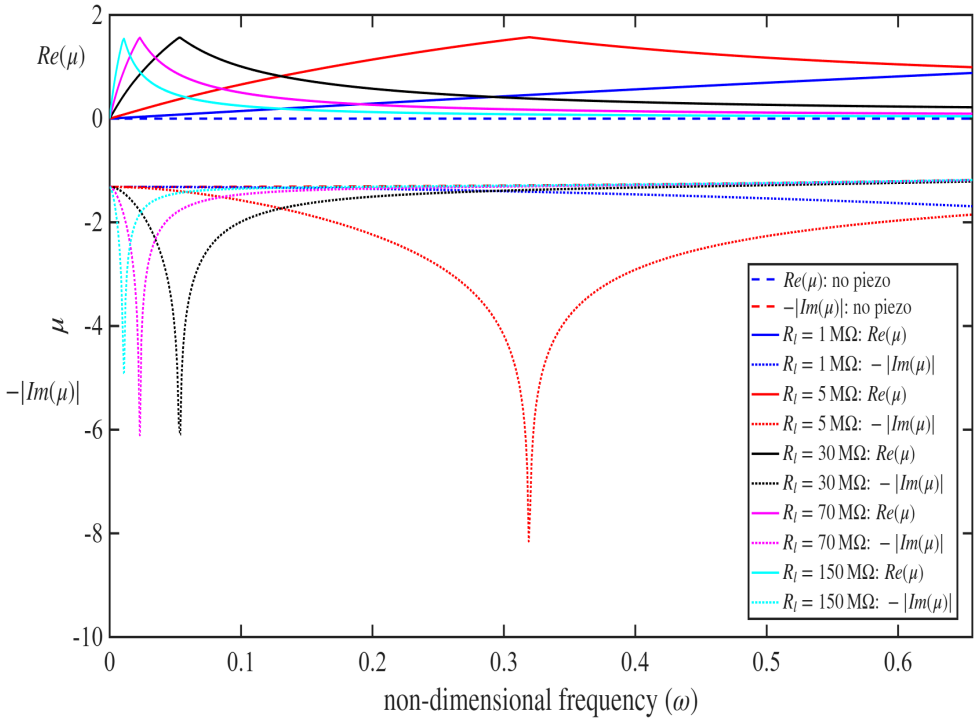


Fig. 4.2: Dispersion profiles obtained with and without the piezoelectric energy harvester, solid, dashed-dotted lines show the dispersion profiles with the piezoelectric patches and dashed lines show the dispersion profiles without the piezoelectric patches, the dispersion profiles are shown with increasing values of the load resistor R_l keeping the value of the capacitance C_p and all the other parameters fixed as in Table 4.1, real parts of wavenumber (μ) shown with solid curves indicate propagating waves and imaginary parts of wavenumber (μ) shown with dashed-dotted curves indicate attenuating waves (with the piezoelectric harvester), the imaginary components have been reversed in sign only for the purpose of clarity between propagation and attenuation regions which does not alter the physical interpretation.

regime of free wave propagation. We keep all the other parameters fixed as chosen in Table 4.1. We increase the stiffness coefficient of the horizontal linear springs from $k = 0.5k_{eff}$ to $k = 5k_{eff}$ or equivalently decrease the stiffness parameter from $\tilde{k} = 2$ to $\tilde{k} = 0.2$. Fig. 4.3 summarizes the band structure behavior with increasing values of the spring stiffness coefficient k. We have used continuous and dotted lines for showing the real and imaginary parts of the wavenumber μ respectively with the piezoelectric harvester and dashed and dashed-dotted lines respectively for showing the same without the piezoelectric harvester in Fig. 4.3.

From an energy-harvesting perspective, the key implication of the band structure results is that the regions where the piezoelectric patches induce larger attenuation (larger $|Im(\mu)|$ relative to the no piezo case) correspond to frequency ranges in which mechanical wave energy is more effectively transferred into the electrical domain and dissipated through the resistive load. In particular, tuning the electrical time constant $\tau = R_l C_p$ shifts and reshapes the attenuation features because τ controls the phase and magnitude of the shunt response; this suggests that the harvested power can be enhanced by choosing

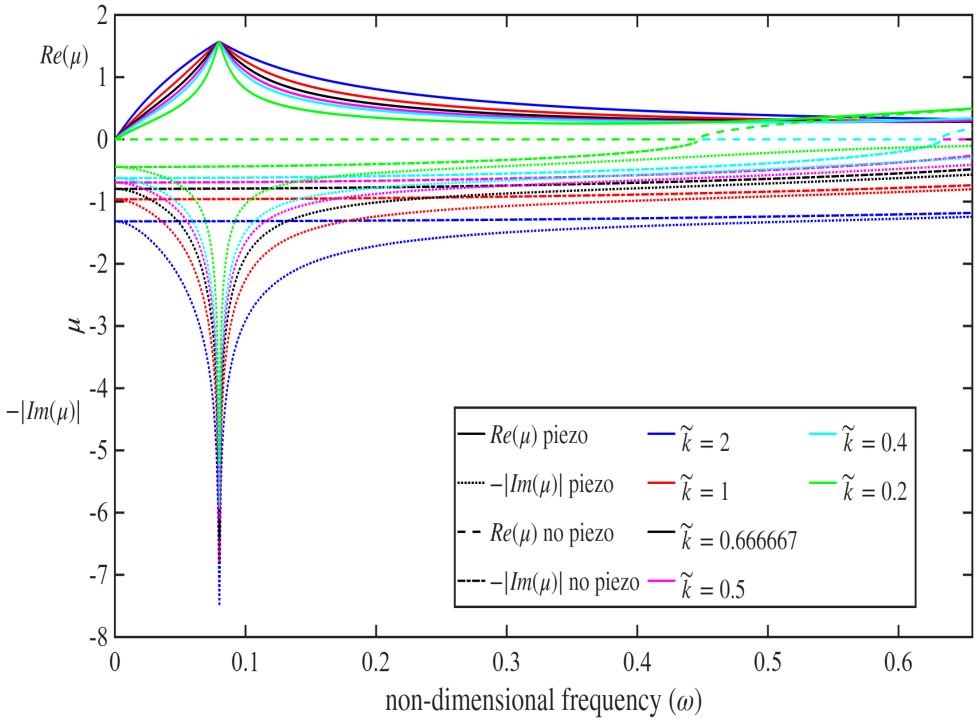


Fig. 4.3: Dispersion profiles obtained with and without the piezoelectric energy harvester, solid, dotted lines show the dispersion profiles with the piezoelectric patches and dashed, dashed-dotted lines show the dispersion profiles without the piezoelectric patches, the dispersion profiles are shown with increasing values of the spring stiffness coefficient k keeping all the other parameters fixed as in Table 4.1, real parts of wavenumber (μ) indicate propagating waves and imaginary parts of wavenumber (μ) indicate attenuating waves, the imaginary components have been reversed in sign only for the purpose of clarity between propagation and attenuation regions which does not alter the physical interpretation.

R_l (or C_p) such that the dominant wave propagation frequencies fall in the range where the piezo-induced attenuation is strongest (typically when $\omega\tau = O(1)$). At very small or very large τ, the shunt tends toward the limiting short-/open-circuit like behaviors and the dispersion approaches the no piezo response, indicating weaker electrical extraction.

The mechanical tuning results further indicate how the unit-cell design governs not only wave propagation but also the availability of strain energy for conversion by the piezoelectric patches. Increasing the spring stiffness k constrains the internal relative motion in the unit cell and makes the piezo curves approach the no piezo baseline, which is consistent with reduced electromechanical interaction and hence reduced harvesting influence on the band structure. These trends imply an inherent trade-off for distributed harvesting in a finite chain. Strong attenuation can increase local electrical extraction near the dominant wave frequency but also reduces how far wave energy penetrates downstream, potentially lowering the contribution of patches located deeper in the chain in a finite real-world model. Therefore, the non-dimensionalized dispersion analysis provides practical design guidance for selecting (R_l, C_p) and the mechanical parameters (k) to place attenuation peaks and band-edge slow-propagation regions near targeted operating frequencies,

thereby maximizing electrical energy extraction while controlling the spatial distribution of harvested energy along the chain.

4.3 Energy harvested through free wave propagation

The average power harvested by the piezoelectric patch over one time period of dimensional free wave frequency Ω can be calculated as

$$P_{ave} = \frac{\Omega}{2\pi} \int_0^{\frac{2\pi}{\Omega}} \frac{V_n^2(t)}{R_l}\, dt \tag{4.17}$$

or, equivalently, in non-dimensional form as

$$\tilde{P}_{ave} = \frac{\omega}{2\pi} \int_0^{\frac{2\pi}{\omega}} \tilde{V}_n^2(\tau)\, d\tau \tag{4.18}$$

where $\tilde{P}_{ave} = P_{ave}/P_0$, $\omega = \frac{\Omega}{\omega_n}$ and $P_0 = V_0^2/R_l$. Time-domain simulations are carried out by numerically integrating Eqs. (4.11) and (4.12); for a complex wavenumber $\mu = \alpha + i\beta$, we retain the attenuating component through $\cos\mu = \cos(i\beta) = \cosh\beta$. Throughout this section and in general, the feasible regime is defined by $K(\mu) = 2(1 - \cos\mu) + \tilde{k} > 0$ and $Re(\mu) \in [0, \pi]$.

The power defined in Eqs. (4.17) and (4.18) should be interpreted as the harvested power associated with a representative unit cell of the periodic chain. For a finite chain of N piezoelectric harvesters, each connected to an identical load resistance, the instantaneous total electrical power is obtained by summing the contribution from all cells,

$$P_{tot}(t) = \sum_{n=1}^{N} \frac{V_n^2(t)}{R_l},$$

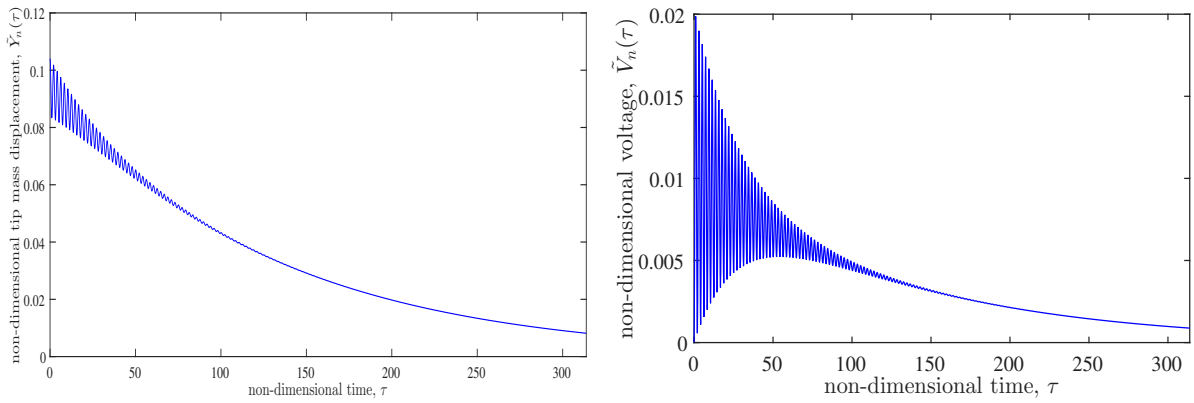
and the corresponding averaged power is the sum of the averaged cell-wise powers. In a perfectly periodic chain operating on a weakly attenuating Bloch branch, the interior cells have comparable amplitudes and one may expect the total output to scale approximately as $P_{tot} \simeq NP_{cell}$. By contrast, for an attenuating free wave with $Y_n \propto e^{i\alpha n - \beta n}$, the displacement amplitude decreases along the chain and the harvested power contribution from successive cells decreases approximately with the factor $e^{-2\beta n}$. Therefore, a multiple-harvester array differs from an isolated single harvester not only by increasing the number of transduction units, but also by introducing wave transport, attenuation, and spatial energy redistribution through the periodic structure. A detailed finite-chain comparison including boundary reflections and non-uniform initial conditions is beyond the scope of the present Bloch-based analytical study, but constitutes a natural extension of the framework.

For the representative non-dimensional initial condition (taken from the parameter set of Table 4.1), $\tilde{Y}_n(0) = 0.104$, $\tilde{Y}_n'(0) = 0$, and non-dimensional free wave frequency $\omega = 1$, the transient responses of the tip mass and generated voltage are shown in Fig. 4.4. To obtain $\tilde{V}_n(\tau)$ in the regime of Bloch-wave propagation, we numerically integrate equations (4.11) and (4.12) in the time-domain using the fourth-order Runge-Kutta (ode45) algorithm in Matlab after rewriting $\tilde{V}_n \equiv \tilde{q}_n$. We resort to convert the charge equation back to voltage while performing the time-domain integration because equation (4.13) represents

a lossless second-order oscillator in $\tilde{q}_n$ which when coupled to the second-order mechanical DOF (4.11) through θ, the combined electromechanical system can develop an unstable pair of eigenvalues, i.e. behaving like a negative damping or active feedback and hence causing the system response to blow up numerically in time. This will not be suitable to capture the attenuation/ decay of spatial waves resulting in the harvested power through the piezoelectric patch via numerical simulations.

To calculate the wavenumber μ for a given non-dimensional free wave frequency ω, we use the dispersion relation derived in (4.15). Since the imaginary part of the wavenumber μ is accountable for mechanical energy dissipation manifesting in the harvested electrical power, we ignore the real part of μ. For complex $\mu = \alpha + i\beta$, we take $\cos\mu = \cos i\beta = \cosh\beta$. We set the value of the non-dimensional free wave frequency ω and evaluate α and β using (4.15) and run our time-domain simulation for 50 cycles of the non-dimensional free wave frequency and compute the power using (4.18) over a cycle when the initial oscillatory mechanical transients induced due to the initial displacement/ velocity conditions imposed on the tip mass and hence the initial oscillatory electrical transients generated in the piezoelectric patch/ harvester die out completely resulting in $\tilde{Y}_n$ or $\tilde{V}_n$ to decay along a smooth envelope and the magnitude of the voltage, $|\tilde{V}_n(t)|$ becomes the largest irrespective of sign (because the power harvested depends on $\tilde{V}_n^2$) to obtain the maximum steady-state power. In the example plot shown in Fig. 4.4, with an input non-dimensional frequency value of $\omega = 1$, this happens approximately at non-dimensional time $\tau = \tau_s \approx 150$ from an apparent visual glance. An initial displacement in dimensional form $Y_n(0) = 10$ mm is imposed on the tip mass, while the initial velocity is kept at $\dot{Y}_n = 0$. Using the value of L as in Table 4.1, this results in the representative non-dimensional initial condition of $\tilde{Y}_n(0) = \tilde{Y}_0 = 0.104, \tilde{Y}_n'(0) = 0$, which has been and will be henceforth imposed on the tip mass to generate free wave motion in the periodic system. In a general scenario, we will use a stiffness parameter value of $\tilde{k} = 2$, and other parameter values from Table 4.1.

As soon as the tip mass begins to move, the electromechanical coupling converts the mechanical velocity into an electrical response through the RC shunt relation (4.12), so $\tilde{V}_n$ departs from zero once $\tilde{Y}_n' \neq 0$. The initial sign of the non-dimensional voltage is set by our sign conventions and the negative d_{31} embedded in Θ and hence in the natural voltage scale V_0, but it does not affect the harvested energy because the electrical power scales with $\tilde{V}_n^2$. The oscillatory nature of $\tilde{V}_n(\tau)$ reflects the underlying coupled electromechanical vibration, while its decaying envelope indicates that the stored mechanical energy is progressively transferred to the electrical domain and dissipated in the resistor. After a sufficient amount of time, the decay is dominated by the non-dimensional electrical time constant $\hat{\tau}_e = \omega_n R_l C_p$. Using $\cos\mu = \cosh\beta$ with $\mu = \alpha + i\beta$, $\alpha \in [0, \pi]$ from (4.15) effectively imposes a purely evanescent (stopband) Bloch condition, modifying the effective inertia/stiffness in the mechanical equation via $1 - \cos\mu < 0$ and thereby capturing, in a single representative cell's time-domain simulation, the enhanced attenuation or energy-extraction behavior associated with the bandgap.



(a) Non-dimensional tip mass displacement $\tilde{Y}_n(\tau)$ (b) Non-dimensional voltage generated $\tilde{V}_n(\tau)$

Fig. 4.4: Representative free-response histories of $\tilde{Y}_n(\tau)$ and $\tilde{V}_n(\tau)$ for $\tilde{Y}_n(0) = 0.104$, $\tilde{Y}_n'(0) = 0$, $\omega = 1$ and the parameters in Table 4.1.

4.3.1 Dependence of maximum steady-state power on non-dimensional free wave frequency ω

By free wave frequency, we refer to the frequency of steady-state free wave propagation in the system generated 'solely' due to an initial condition imposed on the tip mass in the absence of any external forcing/ base excitation. Hence, when we say that we consider the free wave frequency as an 'input', it is not an arbitrary input decided automatically. In essence what we would want to input or prescribe or 'design' for the system is the combination of values of the system parameters which will manifest in steady-state free wave propagation with maximum harvested power at a particular value of this frequency ω as a result of an initial condition (initial displacement/ velocity or both) imposed on the tip mass. Later we will show in Section 4.4.1 how by imposing a constraint for maximum power in the steady state, we can get back this particular value of frequency as a function of solely the system parameters. Till then, we shall treat ω as a book-keeping parameter.

The free wave frequency ω (which we consider as a book-keeping parameter, again re-emphasizing the fact that it has to be and will be prescribed essentially by accordingly choosing the values of the system design parameters) is swept over a range of values and the power harvested over a cycle when initial oscillatory transients generated due to the initial conditions imposed on the tip mass die out completely and voltage generated is maximum in magnitude, is evaluated and plotted with ω. We use a value of the non-dimensional stiffness parameter $\tilde{k} = 2$, and keep the values of the other parameters fixed as defined in Table 4.1. We also impose the same two conditions as done before for practical feasibility:

1. $K(\mu) = 2(1 - \cos\mu) + \tilde{k} > 0$ from equation (4.11).

2. Real part of the wavenumber, i.e. the propagation component remains in the Irreducible Brillouin Zone (IBZ), i.e. $Re(\mu) \in [0, \pi]$.

Fig. 4.5 shows the power harvested in the regime of free wave propagation over the cycle of maximum steady-state voltage amplitude from free wave motion through our chosen

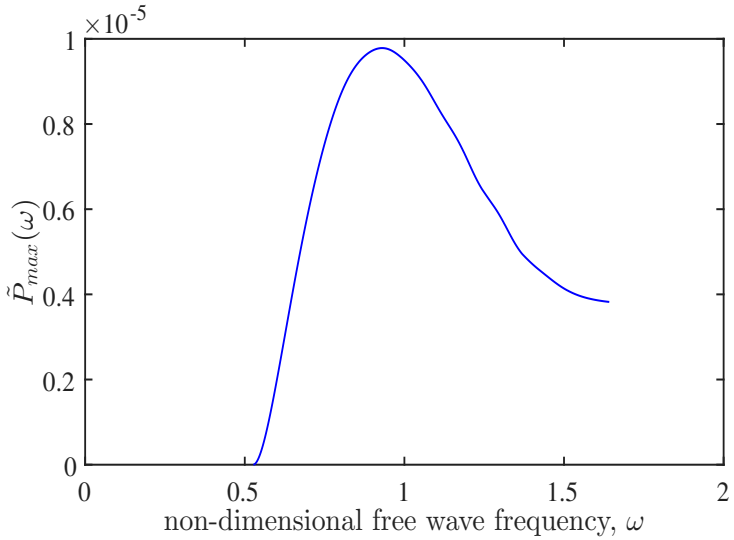


Fig. 4.5: Variation of maximum steady-state harvested power with free-wave frequency ω for $\tilde{Y}_n(0) = 0.104$ and $\tilde{Y}_n'(0) = 0$.

piezoelectric periodic chain for a range of free wave frequencies ω with initial conditions for the tip mass chosen the same as in Fig. 4.4. It is observed that the maximum steady-state power or in other words, the maximum steady-state energy is harvested through the piezoelectric patch from free wave motion through our system at a particular value of non-dimensional frequency ω (which happens to be approximately around $\omega = 1$ in Fig. 4.5), while keeping the structural and electrical parameters of the system fixed. We denote this non-dimensional frequency corresponding to maximum harvested energy/ power in the steady state as $\omega = \omega_e \approx 1$ for our chosen system parameters. To generate the curve depicting the dependence of maximum steady-state power on non-dimensional frequency ω, we have extracted the voltage after a certain settling time when the initial oscillatory transients die out and the voltage $\tilde{V}_n(\tau)$ evolves along a smooth envelope.

As of now, we have used a value of the settling time as $\tau_s = 150$ from our visual approximation from Fig. 4.4(b) which was obtained by setting $\omega = 1$. We have used this same value of visually approximated settling time to obtain the power vs frequency curve shown in Fig. 4.5, for every input frequency ω over the sweeping interval chosen. Later, we will propose a systematic analytical approach in Section 4.4.3 to derive a compact closed-form expression for this settling time which we will denote by $\tau_s(\omega)$ in terms of the input free wave frequency ω or in other words the system parameters. We will also show that the optimum frequency value $\omega = \omega_e$ corresponding to the peak power level in Fig. 4.5 is independent of the value of τ_s chosen, but the magnitude of the peak power harvested in the steady-state regime denoted by the isolated peak in Fig. 4.5 is dependent on this settling time $\tau_s(\omega)$.

4.3.2 Dependence of maximum steady-state power on structural and electrical parameters

Structural parameters

With the parameters fixed as in Table 4.1, the non-dimensional stiffness ratio $\tilde{k} = k_{eff}/k$ is varied from 0.1 to 5 while the free-wave frequency is fixed at $\omega = \omega_e \approx 1$. We choose four different representative values of load resistance R_l or equivalently the non-dimensional electrical time constant $\hat{\tau}_e = \omega_n R_l C_p$ to show the variation of maximum steady-state power with $\tilde{k}$.

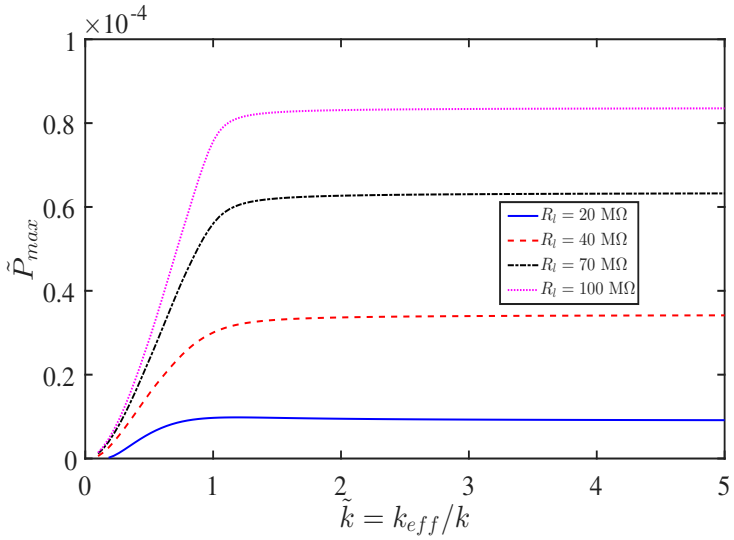


Fig. 4.6: Variation of maximum steady-state power with the non-dimensional stiffness parameter $\tilde{k}$ for $\omega = \omega_e \approx 1$ for four different chosen representative values of load resistance R_l or equivalently the non-dimensional electrical time constant $\hat{\tau}_e$ and values of other parameters kept as in Table 4.1.

Fig. 4.6 shows that the maximum steady-state harvested power increases with $\tilde{k}$ and then saturates. We denote this value of $\tilde{k}$ when saturation occurs by $\tilde{k}_s = \left(k_{eff}/k\right)^s$. As the load resistance R_l and hence the non-dimensional electrical time constant $\hat{\tau}_e = \omega_n R_l C_p$ increases, the value of $\tilde{k}_s$ decreases. Initial conditions have been taken the same as before $\tilde{Y}_n(0) = 0.104, \tilde{Y}_n'(0) = 0$. We have imposed the same condition for $Re(\mu) \in [0, \pi]$ like before, but this time we have allowed our net wavenumber-dependent stiffness $K(\mu) = 2(1 - \cos\mu) + \tilde{k}$ from Eq. (4.11) to be negative as well:

- $K(\mu) = 2(1 - \cos\mu) + \tilde{k} \neq 0$ from equation (4.11).

Fig. 4.6 can be interpreted as the effect of mechanical compliance on the local electromechanical conversion while the electrical side is held at a few representative values of R_l (equivalently $\hat{\tau}_e$). Since $\tilde{k} = k_{eff}/k$, increasing $\tilde{k}$ means decreasing the physical intercell spring stiffness k, so the periodic chain becomes progressively more compliant. For small $\tilde{k}$ (large k), neighboring cells are strongly coupled and the free wave is transmitted with relatively limited local relative motion, which restricts beam bending near the piezoelectric patch and therefore the generated voltage. As $\tilde{k}$ increases, the unit cells are allowed

to deform more independently, the local strain energy available to the piezoelectric patch increases, and the harvested maximum steady-state power rises. The subsequent saturation near $\tilde{k} = \tilde{k}_s$ indicates that once the intercell springs become sufficiently soft, the response is governed mainly by the local beam–tip-mass dynamics and further reduction of k produces only a marginal increase in the windowed steady-state power. The separation of the four curves with increasing R_l is physically consistent with the shunt becoming less short-circuit-like, i.e., a larger R_l allows charge to leak more slowly, so a larger voltage can build up across the piezoelectric patch for the same mechanical motion, and the electrical back-action persists for longer. The fact that $\tilde{k}_s$ decreases as R_l increases means that when the electrical time constant is larger, only a moderate amount of mechanical compliance is needed before the electrical subsystem itself becomes the limiting factor, beyond which additional softening of the chain yields little further gain.

Electrical parameters

Next, with the parameters fixed as in Table 4.1, the load resistance R_l is varied through the non-dimensional electrical time constant $\hat{\tau}_e = \omega_n R_l C_p$. We distinguish the passive constraint $K(\mu) > 0$ (condition I) from the relaxed constraint $K(\mu) \neq 0$ (condition II), while keeping $Re(\mu) \in [0, \pi]$.

The physically relevant trend under condition I is shown in Fig. 4.7 with four different representative values of the non-dimensional stiffness parameter $\tilde{k}$. The harvested power first rises with $\hat{\tau}_e$, reaches a maximum, and then decreases as the shunt transitions from a short-circuit-like to an open-circuit-like regime. As $\tilde{k}$ decreases, both the location of the peak power and the feasible operating range satisfying condition I shift towards increasing $\hat{\tau}_e$.

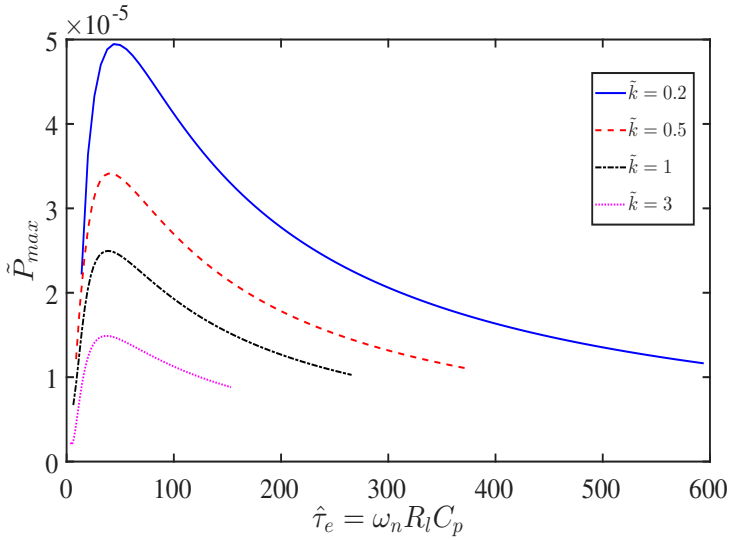


Fig. 4.7: Variation of maximum steady-state power with the non-dimensional electrical time constant $\hat{\tau}_e$ at $\omega = \omega_e \approx 1$ for four different representative values of the stiffness parameter $\tilde{k}$, imposing condition I.

Allowing condition II shows the same trend globally, but within a very small range of values of R_l or equivalently $\hat{\tau}_e$, where $K(\mu)$ becomes negative and we allow this to happen

according to condition II, the harvested power spikes to an abruptly high value for the same values of other system parameters and non-dimensional free wave frequency ω. But, this narrow R_l window is not to be misconceptualized as a super-harvesting sweet spot in a passive sense. If we allow $K(\mu) < 0$, the mechanical part of the reduced equation (4.11) is effectively an inverted stiffness (a linear divergence/instability in the time-domain). In that regime, the homogeneous mechanical response is no longer purely oscillatory and it can develop exponential growth, which in turn can cause the voltage $\tilde{V}_n(\tau)$ to explode in time and appear the power generated to blow up. So, the abrupt spike for condition II is best interpreted by stating that the reduced Bloch-based single-cell time simulation has entered a parameter window where the effective dynamic stiffness becomes negative, and the resulting time-domain model becomes unstable, causing a numerical/analytical amplification that is not representative of passive energy harvesting from bounded free waves. On the other hand, if according to condition I, we impose $K(\mu) > 0$, the mechanical DOF $\tilde{Y}_n(\tau)$ behaves like a stable harmonic oscillator and in the absence of forcing, energy decays due to the resistive electrical dissipation which is our primary objective.

We note here that increasing the value of the capacitance C_p while keeping the load resistance R_l fixed or increasing both the values of C_p and R_l simultaneously produces the same qualitative behavior of harvested power, which can be traced to the fact all of these scenarios effectively increases the non-dimensional electrical time constant $\hat{\tau}_e = \omega_n R_l C_p$.

So, if the goal is passive vibration/ wave energy harvesting by tuning the external circuit i.e. by sweeping R_l or C_p over a wide range of values, then condition I is much more physically realizable and should be imposed as a constraint. However, we observed that while varying the structural parameters, imposing condition sets I and II one at a time doesn't alter the energy harvesting characteristics significantly or doesn't cause an abrupt spike in harvested power. So, while varying the structural parameters or in other words for the purpose of structural design optimization, even if we allow our net wavenumber-dependent dynamic stiffness to be negative, our designed periodic piezoelectric energy harvester won't have any divergence/ instability issues.

4.4 An analytical approach to characterize harvested power through free wave propagation

4.4.1 Analytical framework in the time-domain to find optimum frequency for maximum steady-state power

Modal expansion of state space vector

In the regime of free wave propagation, Eqs. (4.11) and (4.12) can be written in state-space form $\mathbf{A}\mathbf{y}' + \mathbf{B}\mathbf{y} = \mathbf{0}$, where the state vector $\mathbf{y}$ and matrices $\mathbf{A}, \mathbf{B}$ are given by:

$$\mathbf{y} = \begin{Bmatrix} \tilde{Y}_n(\tau) \\ \tilde{Y}_n'(\tau) \\ \tilde{V}_n(\tau) \end{Bmatrix}, \quad \mathbf{A} = \begin{bmatrix} 1 & 0 & 0 \\ 0 & 1 & 0 \\ 0 & 0 & 1 \end{bmatrix}, \mathbf{B} = \begin{bmatrix} 0 & -1 & 0 \\ K(\mu) & 0 & -\theta \\ 0 & 1 & \frac{1}{\hat{\tau}_e} \end{bmatrix} \tag{4.19}$$

where $K(\mu) = 2(1-\cos\mu)+\tilde{k}$. Using the purely evanescent approximation $\cos\mu \approx \cosh\beta$, $K(\mu)$ remains real, and the characteristic polynomial of the state matrix becomes

$$\lambda^3 + a\lambda^2 + b\lambda + c = 0 \tag{4.20}$$

where $a = \frac{1}{\hat{\tau}_e}$, $b = K(\mu) + \theta$, and $c = \frac{K(\mu)}{\hat{\tau}_e}$. The state vector can therefore be expressed through modal superposition as

$$\mathbf{y}(\tau) = \begin{Bmatrix} \tilde{Y}_n(\tau) \\ \tilde{Y}_n'(\tau) \\ \tilde{V}_n(\tau) \end{Bmatrix} = c_1 v_1 e^{\lambda_1 \tau} + c_2 v_2 e^{\lambda_2 \tau} + c_3 v_3 e^{\lambda_3 \tau} \tag{4.21}$$

λ_i, v_i are eigenpairs and the coefficients c_1, c_2, c_3 are determined from the initial conditions. Here, we have posed a general eigenvalue problem for free response of linear systems whereas in the next section Section 4.4.1, we will show how the book-keeping parameter ω comes into the picture through the stiffness term $K\Big(\mu(\omega)\Big)$ or equivalently $\mathbf{B}(\omega)$ in the regime of free wave propagation through linear periodic systems.

Step by step analytical formulation for obtaining maximum steady-state power

For each prescribed free wave frequency ω, the dispersion relation provides $\mu(\omega)$ through

$$\cos\mu(\omega) = 1 - \frac{\Big(\omega^2 - \tilde{k}\Big)\Big(1 - \omega^2\hat{\tau}_e^2\Big) + \theta i\omega\hat{\tau}_e}{2\Big(1 - \omega^2\hat{\tau}_e^2\Big)} \tag{4.22}$$

which closes the frequency-dependent Bloch-reduced model. The voltage can then be written as

$$\begin{aligned} \tilde{V}_n(\tau) &= \mathbf{e}_3^T \mathbf{y}(\tau) = \sum_{i=1}^{3} c_i(\omega)\, e^{\lambda_i(\omega)\tau}, \\ c_i(\omega) &= \Big(\mathbf{e}_3^T \mathbf{v}_i(\omega)\Big)\Big(\mathbf{w}_i(\omega)^T \mathbf{y}_0\Big) \end{aligned} \tag{4.23}$$

where $\mathbf{e}_3 = [0\ 0\ 1]^T$, $(\mathbf{v}_i, \mathbf{w}_i)$ are right/left eigenvectors of $\mathbf{S}(\omega) = -\mathbf{A}^{-1}\mathbf{B}(\omega)$. Over one wave period $T(\omega) = 2\pi/\omega$, starting at settling time τ_s, the non-dimensional average harvested power is

$$\tilde{P}_{ave}(\tau_s, \omega) = \frac{1}{T(\omega)} \int_{\tau_s}^{\tau_s + T(\omega)} \tilde{V}_n(\tau)^2\, d\tau \tag{4.24}$$

which becomes

$$\begin{aligned} \tilde{P}_{ave}(\tau_s, \omega) =& \frac{1}{R_l\, T} \sum_{i=1}^{3}\sum_{j=1}^{3} \frac{c_i c_j\, e^{(\lambda_i+\lambda_j)\tau_s}\Big(e^{(\lambda_i+\lambda_j)T} - 1\Big)}{\lambda_i + \lambda_j} \\ \text{where} \qquad & T = \frac{2\pi}{\omega}. \end{aligned} \tag{4.25}$$

The post-transient optimum satisfies the stationarity conditions

$$E(\tau_0, \omega) := \frac{\partial \tilde{P}_{ave}}{\partial \tau}(\tau, \omega) = 0 \tag{4.26}$$

and

$$F(\tau_0(\omega),\omega) := \frac{\partial \tilde{P}_{ave}}{\partial \omega}\Big(\tau_0(\omega),\omega\Big) = 0 \tag{4.27}$$

The fully expanded forms follow directly from Eq. (4.25) and are omitted here for brevity and are evaluated numerically in the present study. Solving this transcendental equation gives the value for ω and hence $\tau_0(\omega)$ in terms of known or designed system parameters, so that they do not remain arbitrary external inputs or book-keeping parameters henceforth and provide a design/ operating range of our system parameters to obtain maximum harvested power through free wave motion in a steady state. The only thing remaining is to establish the same for the settling time $\tau_s(\omega)$ in terms of system parameters which we will derive in Section 4.4.3.

4.4.2 An alternative analytical approach in the Laplace domain to find maximum steady-state power and the corresponding optimum frequency and the extent of its validity

The Laplace-domain formulation is introduced to obtain a compact algebraic representation of the free response with its initial conditions retained. Its common denominator exposes the poles governing oscillation and decay, which supports the parameter-level settling-time approximation without repeated time integration. This complements, rather than replaces, the time-domain calculation. Maximizing the response on the imaginary axis does not enforce the same post-transient power-averaging window.

Transfer function evaluation

Applying the Laplace transform to Eqs. (4.11) and (4.12) gives

$$\underbrace{\begin{bmatrix} s^2+K(\mu) & -\theta \\ s & s+\dfrac{1}{\hat{\tau}_e} \end{bmatrix}}_{\mathbf{D}(s;\mu)} \begin{bmatrix} \tilde{Y}_n(s) \\ \tilde{V}_n(s) \end{bmatrix} = \begin{bmatrix} s\,\tilde{Y}_n(0)+\tilde{Y}_n'(0) \\ \tilde{V}_n(0)+\tilde{Y}_n(0) \end{bmatrix} \tag{4.28}$$

with common denominator $\tilde{\Delta}(s;\mu) = \det \mathbf{D}(s;\mu) = (s^2+K(\mu))\left(s+\frac{1}{\hat{\tau}_e}\right)+\theta s$. For the free-response initial conditions $\tilde{Y}_n(0)=\tilde{Y}_0$, $\tilde{Y}_n'(0)=0$, $\tilde{V}_n(0)=0$, the voltage simplifies to

$$\tilde{V}_n(s) = \frac{K(\mu)\,\tilde{Y}_0}{\tilde{\Delta}(s;\mu)} \tag{4.29}$$

Restricting to the imaginary axis, $s=i\omega$, gives

$$\widehat{\tilde{V}}_n(\omega) = \frac{K(\omega)\,\tilde{Y}_0}{\left(i\omega+\dfrac{1}{\hat{\tau}_e}\right)(K(\omega)-\omega^2)+i\omega\,\theta} \tag{4.30}$$

and the frequency-axis power estimate

$$\tilde{P}(\omega) = \frac{1}{2}\left|\widehat{\tilde{V}}_n(\omega)\right|^2 \tag{4.31}$$

With $\tilde{N}(\omega) = K(\omega)\tilde{Y}_0$ and $\tilde{D}(\omega) = \left(i\omega + \frac{1}{\hat{\tau}_e}\right)(K(\omega) - \omega^2) + i\omega\theta$, the stationarity condition is

$$\frac{d\tilde{P}(\omega)}{d\omega} = 0 \quad \Longleftrightarrow \quad Re\left\{\frac{\tilde{N}'(\omega)}{\tilde{N}(\omega)} - \frac{\tilde{D}'(\omega)}{\tilde{D}(\omega)}\right\} = 0 \tag{4.32}$$

The detailed derivation from Eq. (4.32) to the exact closed-form optimum-frequency equation is provided later in Chapter 5 in a qualitatively similar context.

Extent of validity of the Laplacian framework and possible advantages

The Laplace-domain framework provides a compact analytical estimate of attainable power levels and reveals how the electrical and mechanical parameters enter the response. However, maximizing $|\tilde{V}_n(i\omega)|$ is not equivalent to maximizing the post-transient one-period average used in Eq. (4.24). The time-domain metric depends on decay rates, modal interference, and the steady-time threshold $\tau \geq \tau_s$, so the Laplace-axis optimum can be shifted relative to the true deterministic optimum. Its main advantage here is therefore not the exact prediction of ω_e, but the efficient derivation of a useful settling time approximation without actually having to solve for the roots of the cubic characteristic polynomial Eq. (4.20), as shown later in Section 4.4.3.

4.4.3 An approximate analytical approach to characterize the settling time $\tau_s(\omega)$ introduced in Section 4.3

As discussed in Section 4.3 and Section 4.4.1, we require the time τ_s after which the initial oscillatory transients die out and also the magnitude of the generated voltage becomes maximal over a smooth envelope. A practical approximation is to model the displacement and hence voltage as a superposition of a smooth decaying contribution and a decaying oscillatory transient,

$$\tilde{V}_n(\tau) \approx Ae^{-s\tau} + Be^{\left(-\sigma \pm i\omega_d\right)\tau} \tag{4.33}$$

Using Eq. (4.22), we write the complex argument of the inverse cosine as $a + ib$, where

$$a = 1 - \frac{\omega^2 - \tilde{k}}{2}, \qquad b = -\frac{\theta\omega\hat{\tau}_e}{2(1 - \omega^2\hat{\tau}_e^2)} \tag{4.34}$$

For $|a| < 1$ and sufficiently small $|b|$, the Taylor series expansion of $\cos^{-1}(a + ib)$ about a gives

$$\cos^{-1}(z) \approx \cos^{-1}(a + ib) = \cos^{-1}(a) - i\frac{b}{\sqrt{1 - a^2}} + \frac{ab^2}{2(1 - a^2)^{\frac{3}{2}}} + i\frac{(1 + 2a^2)b^3}{6(1 - a^2)^{\frac{5}{2}}} \tag{4.35}$$

so that

$$Im\Big(\cos^{-1}(a + ib)\Big) \approx -\frac{b}{\sqrt{1 - a^2}} + \frac{(1 + 2a^2)b^3}{6(1 - a^2)^{\frac{5}{2}}} \tag{4.36}$$

Hence,

$$\cos\mu(\omega) = \cosh\beta(\omega) \approx \cosh\left(\operatorname{sgn}\left(1-\frac{\omega^2-\tilde{k}}{2}\right)\left|-\frac{b(\omega)}{\sqrt{1-a(\omega)^2}}+\frac{(1+2a(\omega)^2)b(\omega)^3}{6(1-a(\omega)^2)^{\frac{5}{2}}}\right|\right) \tag{4.37}$$

This provides a compact approximation for the real-valued attenuation parameter needed in the settling-time estimate.

Concept of 'settling time' adapted to the free-decay voltage

For each fixed free-wave frequency ω, the electromechanical model defines a linear time-invariant (LTI) system whose free response can be written as

$$\tilde{V}_n(\tau;\omega) = \sum_j A_j(\omega)\, e^{s_j(\omega)\,\tau} \tag{4.38}$$

where $\{s_j(\omega)\}$ are the poles of the reduced model. If the dominant transient is governed by an underdamped complex-conjugate pair

$$s_{2,3}(\omega) = -\sigma(\omega) \pm i\,\omega_d(\omega) \tag{4.39}$$

then the oscillatory envelope decays as $e^{-\sigma(\omega)t}$ and the usual settling-time estimate is

$$t_s(\omega) \approx \frac{\ln(1/\epsilon)}{\sigma(\omega)} \tag{4.40}$$

In the present free-decay setting, the final value of $\tilde{V}_n(\tau)$ is zero, so we define the ω-dependent transient decay time or the settling time to a prescribed tolerance ϵ to be estimated by

$$\tau_s(\omega) \approx \frac{\ln(1/\epsilon)}{\sigma_{\text{osc}}(\omega)} \tag{4.41}$$

with $\sigma_{\text{osc}}(\omega)$ taken from the oscillatory pole pair, because this quantity governs when the voltage envelope becomes smooth over one period.

Explicit parameter-level approximation for $\sigma_{\text{osc}}(\omega)$ and $\tau_s(\omega)$ and comparison with numerical results

From the Laplace-domain formulation, the transient decay is governed by the denominator

$$\tilde{\Delta}(s;\mu) = \det\mathbf{D}(s;\mu) = \big(s^2 + K(\mu)\big)\left(s+\frac{1}{\hat{\tau}_e}\right) + \theta s \tag{4.42}$$

which expands to

$$s^3 + \frac{1}{\hat{\tau}_e}\,s^2 + \big(K(\omega)+\theta\big)s + \frac{K(\omega)}{\hat{\tau}_e} = 0 \tag{4.43}$$

In the common regime where the roots separate into one predominantly real slow pole and one underdamped complex-conjugate pair, a useful approximation for the slow real pole is

$$s_r(\omega) \approx -\frac{K(\omega)}{K(\omega)+\theta}\,\frac{1}{\hat{\tau}_e}$$

Using the sum of roots relation for a cubic equation and requiring stable decay gives

$$-2\,\sigma_{\mathrm{osc}}(\omega) + s_r(\omega) \approx -\frac{1}{\hat{\tau}_e} \implies \sigma_{\mathrm{osc}}(\omega) \approx \frac{1}{2\hat{\tau}_e}\,\frac{\theta}{K(\omega)+\theta} \tag{4.44}$$

Therefore,

$$\tau_s(\omega) \approx \frac{\ln(1/\epsilon)}{\sigma_{\mathrm{osc}}(\omega)} \approx 2\hat{\tau}_e\,\frac{K(\omega)+\theta}{\theta}\,\ln\!\left(\frac{1}{\epsilon}\right) \tag{4.45}$$

and, for the standard 1% settling tolerance $\epsilon = 0.01$,

$$\tau_s(\omega) \approx 9.2\,\hat{\tau}_e\,\frac{K(\omega)+\theta}{\theta} \tag{4.46}$$

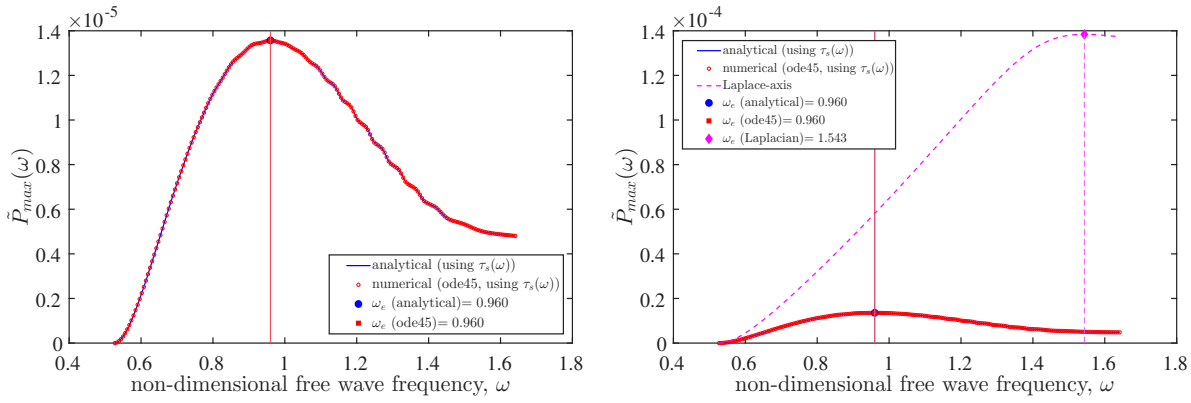
For $\omega = 1$, the same representative case used in Fig. 4.4, this expression yields

$$\tau_s \approx 127.862 \tag{4.47}$$

which agrees well with the numerically observed decay to a smooth envelope in Fig. 4.4. In dimensional units this corresponds to $t_s = \tau_s/\omega_n \approx 10.4927\,\mathrm{s}$ for the chosen parameter set. The analytical estimate is approximately 15% below the visually identified value of $\tau_s \approx 150$ used in Section 4.3, which is expected given the conservative nature of the visual approximation. Both values lie well within the 300 units simulation window in Fig. 4.4, and the optimum frequency ω_e is insensitive to this difference, as demonstrated in Fig. 4.8(a).

4.4.4 Comparison of theoretical power with numerical time-domain integration

Using the same initial conditions for both approaches, $\tilde{Y}_n(0) = 0.104$, $\tilde{Y}_n'(0) = 0$, and $\tilde{V}_n(0) = 0$, Fig. 5.9 compares the analytical time-domain prediction, direct numerical integration using `ode45`, and the Laplace-axis estimate. The non-dimensional stiffness parameter is fixed at $\tilde{k} = 2$, with the remaining parameters as in Table 4.1.



(a) Analytical time-domain prediction versus direct numerical integration

(b) Analytical, numerical, and Laplace-axis predictions

Fig. 4.8: Comparison of analytical, numerical, and Laplace-axis power predictions using $\tau_s(\omega)$ from Eq. (4.46), for the chosen parameter set, $\tau_s(\omega)$ varies from 115.39 to 142.73 over the plotted frequency range.

Both the analytical time-domain framework and direct numerical integration predict the same optimum frequency, $\omega_e = 0.960008$, and the same corresponding peak power, $\tilde{P}_{max}(\omega_e) = 1.357082 \times 10^{-5}$, when the one-period average is evaluated after the settling time $\tau_s(\omega)$ as calculated from Eq. 4.46. The Laplace-axis estimate, by contrast, gives $\omega_e = 1.54311$ and $\tilde{P}_{max}(\omega_e) = 1.384109 \times 10^{-4}$ because it does not enforce the same post-transient windowing criterion. The excellent agreement between the analytical time-domain prediction and the `ode45` results confirms that the proposed framework reproduces both the peak location and the peak magnitude once the same extraction rule is enforced. It also confirms that the optimum frequency is insensitive to the precise settling time used, whereas the peak power level depends on the chosen or calculated value of $\tau_s(\omega)$. This observation can be traced back to the fact that in Fig. 4.5, we used a visually approximated settling time of $\tau_s = 150$ for every frequency value ω to generate the power vs frequency curve, but still our peak occurred at the same location of $\omega_e = 0.960008 \approx 1$, but the magnitude of the peak power was $\approx 1 \times 10^{-5}$, while in Fig. 4.8(a) with the actual calculated values of $\tau_s(\omega)$ from (4.46), we got a peak power magnitude of 1.357082×10^{-5}.

The Laplace-axis curve remains useful for fast magnitude estimates and for deriving the settling-time approximation, but recovering an optimum frequency consistent with the deterministic free-decay metric requires reconstructing the time-domain response and applying the same $\tau_s(\omega)$-based power criterion. The non-dimensional quantities can always be converted to dimensional values through $t_s = \tau_s/\omega_n$, $\Omega_e = \omega_e\omega_n$, and $P_{max}(\Omega_e) = P_0\tilde{P}_{max}(\omega_e)$.

In dimensional values the optimum value of the free wave frequency is obtained as $\Omega_e = 11.6985$ rad/s and the first/fundamental and second natural frequencies of the isolated beam-tip-mass unit cell model are obtained as 16.99 and 615.8 rad/s respectively. The considerably lower magnitude of the optimum frequency Ω_e compared to the first and second natural frequencies of the beam-tip-mass unit cell again justifies the single-mode reduction introduced in Section 4.1.2. Retaining only the first beam mode restricts the dispersion and power predictions to fundamental-flexural, low-frequency dynamics; higher-mode branches and their associated strain and voltage contributions are not represented. The frequency separation reported above supports this approximation for the operating regime examined here, whereas excitation with appreciable higher-mode content would require a multimode reduction.

4.5 Concluding remarks

This chapter develops a systematic analytical framework for characterizing the energy-harvesting potential of a linear periodic piezoelectric harvester in the regime of free wave propagation in the absence of external forcing or excitation. The primary contribution is the modeling and design of physically realizable energy harvesters based on piezoelectric periodic elements in situations where sustained, time-dependent forcing functions are impractical to prescribe or implement. Instead, the proposed approach is based on the free response of the system generated by arbitrary and intermittent disturbances represented as initial conditions, rather than by persistent external forcing, and is therefore more naturally suited to realistic operating environments.

The central methodological contribution is a compact non-dimensional analytical pipeline that links Bloch dispersion and attenuation content to a closed-form time-domain response

and, in turn, to the extraction of maximum steady-state power under physically motivated transient-decay criteria. This pipeline yields an inverse map: for given structural, geometric, and electrical parameters of the system, it identifies the optimum free-wave frequency at which harvesting is most effective, without the need for external forcing or resonance tuning.

A key novel element of the framework is the introduction of settling time in the context of free-wave energy harvesting. Rather than relying on ad hoc cycle counting or assumptions borrowed from persistently excited systems, the analysis defines a principled threshold $\tau_s(\omega)$ beyond which the voltage envelope becomes smooth and the one-period average power can be evaluated consistently. A closed-form approximation for $\tau_s(\omega)$, expressed in terms of the electrical time constant and the frequency-dependent effective stiffness, is derived and shown to be in good agreement with direct numerical simulations.

The analysis further shows that the optimum frequency ω_e is robust with respect to the precise value of τ_s employed, whereas the magnitude of the peak harvested power remains dependent on it. Taken together, these results provide a systematic basis for the design of piezoelectric periodic harvesters intended for intermittent or impulsive excitation environments.

In summary, the proposed method provides a novel and previously unexplored route for identifying a definite, independent, and internally consistent operating regime around an optimum frequency determined solely by the inherent parameter space of the system, without requiring fine tuning relative to the resonant frequency of an externally applied forcing or excitation.

The next work in Chapter 5 will extend the present framework to nonlinear piezoelectric chains, where amplitude-dependent dispersion together with bi-stable magnetic potential landscape will be shown to give rise to qualitatively new harvesting regimes.

Chapter 5

Energy harvesting potential of inertially coupled nonlinear piezomagnetoelastic chains

5.1 Extending free-wave harvesting framework to nonlinear periodic systems

In this Chapter, we extend the settling-time based free-wave energy harvesting framework developed just before in Chapter 4 to nonlinear periodic piezoelectric harvesters to investigate qualitatively new harvesting regimes. Inertial coupling and bi-stability induced due to magnets are both incorporated into the chosen nonlinear periodic model. In Chapter 3, it was already noticed that bi-stability arising inherently due to a fairly rich underlying geometric configuration and suitably chosen inertial coupling of relative DOFs could both effectively tune bandgaps and in general dispersion behavior in nonlinear periodic lattices. The geometric nonlinearity is replaced here by a magnetic nonlinearity arising due to a bi-stable magnetic potential landscape. The advantage of using magnetic bi-stability and piezomagnetoelastic unit-cell configurations is that pronounced effects of nonlinearity can be obtained on the general dynamic behavior even for simple geometric configurations of the underlying structure. Hence, to extend the harvesting framework developed previously in the absence of sustained external forcing to nonlinear periodic systems, we resort to nonlinearities induced by the effects of magnets, so that even for a simple geometric configuration, the effect of nonlinearity can generate observably rich harvesting behavior and the analytical formulation developed for unforced linear periodic models can be naturally extended to nonlinear versions without facing the challenges of tedious algebraic calculations or manipulations.

The state-space based dispersion and settling-time formulation from Chapter 4 are retained in this Chapter for the linearized regime for maintaining self-continuity and to signify quantitative differences arising due to the magnets and inerters in the analytical calculations and results.

5.2 A piezomagnetoelastic unit-cell model

As a repeating unit-cell model for our periodic structure, we consider a vertical cantilever Euler-Bernoulli beam with uniform cross-section of length L, width w and thickness h with a tip mass M_t and a piezoelectric patch at the base near the fixed end. The tip mass is subject to a magnetic field created by two repelling permanent magnets located symmetrically with the north pole facing upwards, on either side of the clamped position of the beam. The tip mass is considered to be significantly larger than the mass of the beam. A schematic diagram of the beam-mass-magnet unit cell is shown in Fig. 5.1 with the dimensions labeled. Each of the two permanent magnets is considered to have a radius a in the horizontal direction and length $2b$ in the vertical direction. The vertical distance between the center of the tip mass and the center of base magnets is denoted as d_v and the horizontal distance between the center of the tip mass and the center of either magnet is denoted as d_h. Piezoelectric patches are pasted in a bimorph 31 configuration near the fixed end of each beam in the chain for electrical energy harvesting from free wave motion through the chain. The beam material is considered to be isotropic with density ρ.

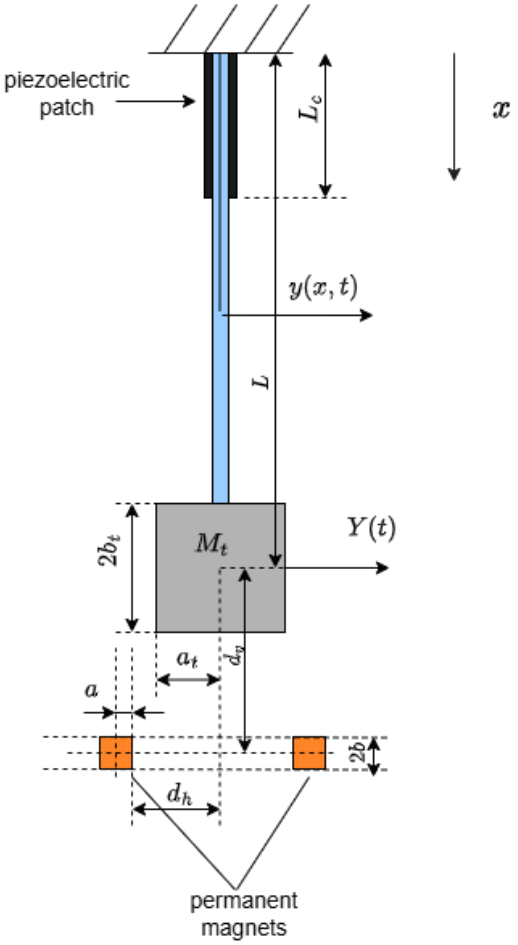


Fig. 5.1: The repeating piezomagnetoelastic unit-cell model.

The magnetic forces acting on the tip mass are considered to be derived from a potential function represented by a fourth order polynomial. The axial displacement of the beam and hence the tip mass are considered to be negligible in comparison to the

transverse displacement. Since the mass of the beam is considered to be negligible when compared to the tip mass, the beam is considered as a purely flexural element with flexural rigidity EI and the kinetic energy of the system arises only due to the tip mass. For the same reason, the general transverse displacement at any point in the beam can be expressed in terms of the tip mass displacement using a relationship based on the first mode of the linear mode shape of the beam. Essentially, we use a single mode approximation for the beam displacement neglecting the contribution from higher modes of vibration.

The magnetic potential energy is considered in accordance to the Moon and Holmes model [106] where it has been considered to be a sixth order polynomial in terms of the beam tip displacement as:

$$\pi_M = c_0 + c_1 Y^2 + c_2 Y^4 + c_3 Y^6 \tag{5.1}$$

where c_0, c_1, c_2, c_3 are constant coefficients dependent on the magnetic parameters of the system. This magnetic potential energy function can be studied to find its stationary points or in other words the fixed points of the system where the nonlinearities arise solely due to the external magnets and the dependence of those fixed points on the system parameters to characterize the different types of system bifurcations [108]. Since the present objective is to capture the leading order physics of free intrawell and interwell wave propagation and energy harvesting in a symmetric bi-stable regime, we adopt a fourth-order truncation of the Moon–Holmes magnetic potential. This is the lowest order polynomial that preserves the qualitative phase-space topology relevant to the analysis, namely two stable equilibria separated by an unstable saddle, and therefore retains the essential ingredients for barrier crossing, intrawell dynamics, and localized electromechanical energy conversion. In this sense, the quartic potential is used here as a normal-form representation of the magnetic nonlinearity over the dynamically relevant displacement range explored by the transient wave and transition fronts. The neglected sixth-order contribution is expected mainly to modify the far-from-equilibrium stiffness and the quantitative well depth at larger amplitudes, rather than the existence of the bi-stable landscape itself. Accordingly, the fourth-order truncation is most appropriate for trajectories that explore the two wells and the intervening barrier without relying on extreme far-field excursions. We therefore emphasize that the quartic model is not intended as an exact global reconstruction of the full magnetostatic interaction, but as a controlled reduced model for the qualitative intrawell and interwell-wave and associated harvesting mechanisms studied here.

The constants c_0, c_1, c_2 can be obtained as [108]:

$$\begin{aligned} c_0 &= -\frac{m_t}{16L^2} 8a_0 L^2 \\ c_1 &= -\frac{m_t}{16L^2}(8a_1 L^2 + 8b_1 L) \\ c_2 &= -\frac{m_t}{16L^2}(8a_2 L^2 + 8b_2 L) \end{aligned} \tag{5.2}$$

where m_t is the magnetic moment of the tip mass M_t if we consider it to be made up of a magnetic material. m_t is a constant and depends on the geometric and magnetic properties of the tip mass. The geometric properties of the tip mass considered as a magnet are denoted by a_t which is its radius in the horizontal direction and $2b_t$ which is its length in the vertical direction. a_0, a_1, b_1, a_2, b_2 are coefficients of the different powers of

the tip mass displacement Y_n in the Taylor series expansion of the radial (horizontal) and axial (vertical) components of the resultant magnetic field at the point where the beam is attached to the tip mass in terms of the tip mass displacement. These coefficients are computed symbolically using Mathematica and then numerically evaluated by substituting suitable values of system parameters as per our objective. Considering the tip mass to be a permanent magnet, its magnetic moment can be evaluated as [108]:

$$m_t = \frac{2B_t}{\mu_0}\pi(a_t)^2\sqrt{(2b_t)^2 + (a_t)^2} \tag{5.3}$$

where B_t denotes the field strength at tip magnet's surface on its axis and μ_0 is the magnetic permeability.

The single-mode reduction as discussed before in Chapter 4 is intended as a leading-order description of the unit cell in the tip mass dominated regime considered here. It is expected to remain appropriate so long as the response is governed predominantly by the fundamental flexural mode, i.e., when the dynamics are controlled by the global tip motion rather than by short-wavelength bending of the beam. The approximation may lose quantitative accuracy when snap-through becomes sufficiently abrupt to generate appreciable higher-mode content, strong curvature localization develops near the clamp, or the relevant time scales approach those of the higher flexural modes. In this sense, the present formulation should be viewed as a reduced model for the collective wave dynamics and harvesting trends, rather than as a full structural representation of all beam modes. Also, on specifying the values of the system parameters in Table 5.1, it will be apparent that for our chosen symmetric bi-stable magnetic potential design, the distance from the unstable equilibrium point in the middle to the stable equilibrium points on either side will be sufficiently small compared to the length of the beam for neglecting large axial beam motion and nonlinear strain-curvature relations.

The equations of motion for single-mode approximation for the isolated unit cell are obtained from the Lagrangian and the electromechanical coupling term is obtained by evaluating the electrical work in terms of the tip mass displacement as done previously in Chapter 4 and so is the electrical equation.

$$M_t\ddot{Y} + EI(2j-1)^4\frac{\pi^4}{32L^3}Y + 2c_1Y + 4c_2Y^3 - \Theta V = 0 \tag{5.4}$$

$$C_p\dot{V} + \frac{V}{R_l} + \Theta\dot{Y} = 0 \tag{5.5}$$

where, C_p and R_l are the capacitance and load resistance of the piezoelectric circuit, V is the voltage generated and j is an integer. The piezoelectric coupling parameter Θ is given by

$$\Theta = \gamma_c(2j-1)\frac{\pi}{2L}\sin\left((2j-1)\frac{\pi L_c}{2L}\right). \tag{5.6}$$

where γ_c is the piezoelectric constant and L_c is the length of the piezoelectric patch. For a bimorph piezoelectric patch, γ_c can be evaluated [107] as

$$\gamma_c = Ed_{31}w_c(h + h_c) \tag{5.7}$$

Eq. (5.4) represents a duffing type oscillator equation with an electromechanical parameter coupling it to the voltage variable V in (5.5). We study the phase plane behavior of the tip mass $Y(t)$ where the phase space for Y is obtained by taking a two-dimensional

projection on the plane $(Y, \dot{Y})$ of the actual three dimensional phase space defined by $(Y, \dot{Y}, V)$.

Mostly, we will be interested in the phase space behavior of the tip mass when it is subject to a bi-stable potential with two local minima and one local maximum. Hence, there will be three equilibrium points with two stable points corresponding to the two local minima and one unstable point corresponding to the one local maximum. For such a state to exist, a necessary criterion is that we must choose our system parameters such that $EI(2j-1)^4\frac{\pi^4}{32L^3} + 2c_1 < 0$ and $c_2 > 0$. We are not saying at this point that this will be the sufficient criteria, because of the existence of the additional coupling term ΘV in (5.4). From existing literature [197], it is known that single degree of freedom double well oscillators when subjected to an external forcing such as a harmonic excitation can exhibit rich dynamical behavior with two stable centers corresponding to the two potential wells and one unstable saddle in the middle corresponding to the local energy maximum. Depending on the magnitude of the forcing, the oscillator can exhibit small-amplitude intrawell to large-amplitude interwell or snap-through motions leading to transient or sustained chaos. Since, we are interested in 'free' wave propagation, we do not explicitly consider any external forcing in our system. But, still because of the presence of the electromechanical coupling term, we should be interested in the phase space behavior of our unforced system while still expecting interwell oscillations arising due to large enough initial conditions leading to rich nonlinear phenomena. We take the integer $j = 1$ without loss of generality.

Keeping the flexural rigidity EI untouched/ preserved and simultaneously satisfying the necessary criteria for bi-stability, the distance between the base magnets $d = 2d_h$, the vertical distance between the axis of the base magnets and the axis of the tip magnet d_v, the magnetic field strength at base magnets' surface on its axis B_s and the magnetic field strength at the tip magnet's surface on its axis B_t are chosen accordingly as:

$$d = 2d_h = 39 \text{ mm}, \quad d_v = 32.2 \text{ mm}, \quad B_s = 0.093 \text{ T} \quad B_t = 0.56 \text{ T} \tag{5.8}$$

The coefficients c_0, c_1, c_2 are hence obtained as:

$$\begin{aligned} c_0 &= -0.00133919 \\ c_1 &= -1.69985 \\ c_2 &= 944.64 \end{aligned} \tag{5.9}$$

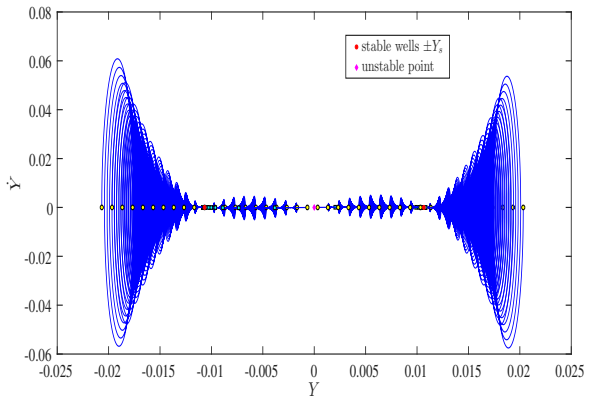
The constant γ_c is evaluated using Eq. (5.7) taking the integer j to be 1. For chosen values of system parameters shown in Table 5.1, γ_c is obtained as $\gamma_c = -1.03 \times 10^{-4}$. The magnetic permeability μ_0 has been taken as $4\pi \times 10^{-7}$ in SI units.

The equilibrium points considering $V = 0$ are obtained as:

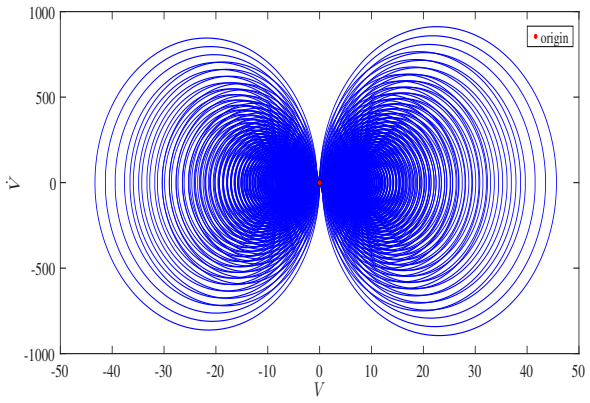
$$Y_s = 0, \qquad Y_s = \pm\sqrt{-\frac{\left(\frac{EI\pi^4}{32L^3} + 2c_1\right)}{4c_2}} \tag{5.10}$$

The phase behavior is shown for two sets of initial conditions of the state space $Y(0), \dot{Y}(0), V(0)$. First, we allow only small initial perturbations of the tip mass displacement from its stable equilibrium points $\pm Y_s$ to study intrawell oscillations. Then, we study the regime of large-amplitude interwell motions by considering the initial perturbations to be significantly large for the tip mass to cross the saddle/ unstable equilibrium point at $Y_s = 0$ at

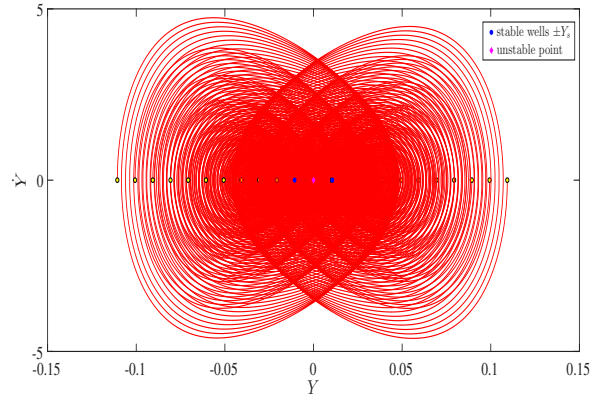
least once. Initial velocity of tip mass and initial voltage are taken to be zero for both cases.



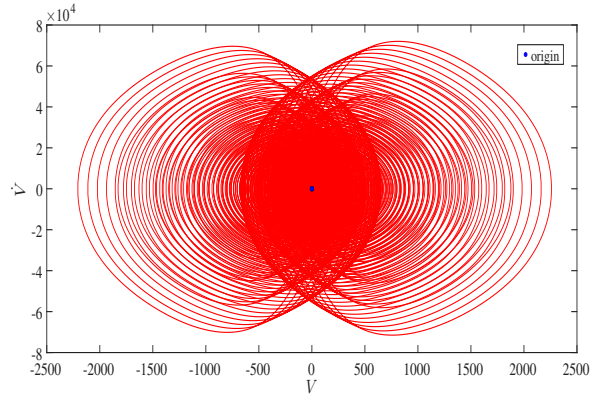
(a) Phase-plane behavior of tip mass $Y(t)$ for small perturbations from stable equilibrium position at $Y_s = 10.7$ mm



(b) Phase-plane behavior of voltage $V(t)$ for small perturbations of the tip mass from stable equilibrium position at $Y_s = 10.7$ mm



(c) Phase-plane behavior of tip mass $Y(t)$ for large enough perturbations from stable equilibrium position resulting in interwell motions



(d) Phase-plane behavior of voltage $V(t)$ for interwell motions of the tip mass

Fig. 5.2: Phase-plane behavior of tip mass $Y(t)$ and voltage $V(t)$ for small intrawell oscillations of the tip mass about its stable equilibrium position and large interwell motions of the tip mass resulting in crossing the unstable saddle in the middle at least once, yellow circles mark starting point of trajectories and cyan squares mark end point of trajectories.

The phase-plane plots in Fig. 5.2 show that the isolated piezomagnetoelastic unit cell is not a conservative bi-stable element, but a dissipative electromechanical oscillator. For small perturbations about the stable equilibria, the trajectories in the $(Y, \dot{Y})$ projection plane spiral toward the nearest well in Fig. 5.2(a), while the corresponding electrical trajectories in the $(V, \dot{V})$ projection plane spiral toward the origin in Fig. 5.2(b). For sufficiently large initial perturbations, the tip mass undergoes transient interwell excursions across the saddle region before ultimately being captured by one of the stable wells, as seen in Fig. 5.2(c), and the associated voltage dynamics again collapse to the origin through larger spiral loops in Fig. 5.2(d). Unlike an uncoupled single degree of freedom conservative bi-stable oscillator, for which one would expect closed intrawell and interwell periodic orbits separated by two homoclinic separatrices of infinite period, the coupling

terms $-\Theta V$ in Eq. (5.4) and $\Theta\dot{Y}$ in Eq. (5.5) continuously transfer mechanical energy into the electrical subsystem and dissipate it through the shunt, so that no closed or homoclinic periodic orbits persist and all projected trajectories are exponentially damped spirals. This is precisely what makes the unit cell a meaningful building block for the periodic chain. Once such nonlinear, bi-stable, energy-converting cells are coupled spatially, one can expect wave-mediated combinations of intrawell confinement, transient snap-through, attenuation and distributed electrical extraction, thereby opening the way to both enhanced energy harvesting potential and richer collective dynamics than in a purely mechanical periodic bi-stable lattice.

5.3 The periodic chain

To arrive at a periodic chain composed of our repeating unit cell discussed in Section 5.2, we consider a one-dimensional array of N such piezomagnetoelastic beam-mass elements connected by coupling the tip mass to adjacent unit cells via horizontal linear springs and a pair of stable negative-inerter modules as shown in Fig. 5.3. The modules are represented at reduced order by a signed two-terminal inertance parameterized by the mass-dimensional scale m_a and the initial architectural tuning angle α, as considered before in Chapter 3. The inerter modules provide an additional means of tuning effective inertia and wave propagation without changing the beam stiffness or magnetic potential. They complement bi-stability in shaping intrawell dispersion and interwell harvesting localization within the admissible parameter range. Electrical extraction remains associated with the piezoelectric resistive loads.

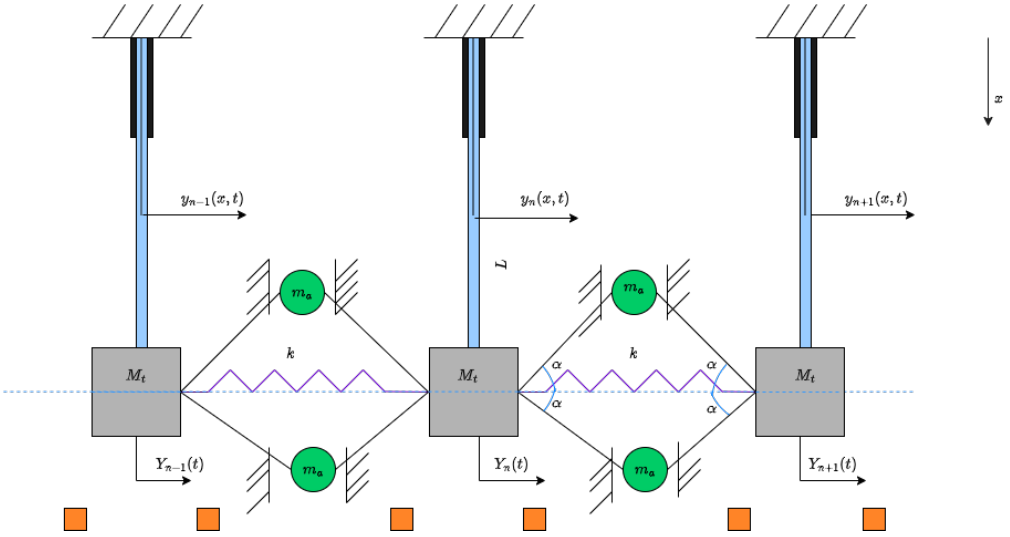


Fig. 5.3: The periodic piezomagnetoelastic chain.

The kinetic energy of the n-th unit cell as shown in Fig. 5.3, arising due to the tip mass M_t is given by

$$T = \frac{1}{2} M_t \dot{Y}_n^{\,2} \tag{5.11}$$

where $Y_n(t)$ is the displacement of the tip mass in the transverse/ horizontal direction in the n-th unit cell.

The potential energy of the n-th unit cell under consideration comprises of the beam's elastic strain energy, the magnetic potential energy due to the two permanent magnets, the elastic potential energy stored in the linear horizontal intercellular springs and the negative of the electrical work done by the piezoelectric patch. The negative inerter contributes to the reduced kinetic energy shown later.

$$U = \frac{1}{2}EI\int_0^L \left(\frac{\partial^2 y_n}{\partial x^2}\right)^2 dx + c_0 + c_1 Y_n^2 + c_2 Y_n^4 + \frac{1}{2}k(Y_n - Y_{n-1})^2 + \frac{1}{2}k(Y_n - Y_{n+1})^2 - W_E \quad (5.12)$$

EI is the flexural rigidity of the beam, c_0, c_1 and c_2 are constant coefficients in the magnetic potential function explained and evaluated in Section 5.2, $y_n = y_n(x,t)$ is the general lateral beam displacement in the n-th unit cell, $Y_n = y_n(L,t)$ is the displacement of the tip mass in the n-th unit cell, k is the stiffness co-efficients of the linear springs, W_E is the electrical work done by the piezoelectric patches. It has been considered that the displacement-curvature relationship of the beam is linear owing to the fact $\frac{Y_s}{L} = \frac{10.7}{96.1} = 0.1 << 1$.

Since we are interested in the first mode-motion of beam displacement, the general lateral displacement at any point in the beam will have identical harmonic time history corresponding to the first natural frequency of vibration of the cantilever beam with tip mass. So, the general lateral displacement $y(x,t)$ can be related to the displacement of the tip mass Y by any admissible function satisfying the geometric boundary conditions at the fixed end of the beam [110].

$$y_n(x,t) = y_n(L,t)\phi(x) = Y_n(t)\phi(x) \quad (5.13)$$

where the admissible function is chosen to be $\phi(x) = 1 - \cos\left((2j-1)\frac{\pi x}{2L}\right)$, j being an integer. It is important to note that it cannot be assumed that $Y_n(t)$ will be a harmonic motion with the lowest natural frequency of an isolated cantilever beam with tip mass because we are imposing additional constraints to the isolated beam-mass system by constructing a periodic chain with intercellular linear spring elements and also the inerters. So, the frequency (ω) of the tip mass $Y_n(t)$ in our periodic system has to be derived following the standard theories of free harmonic wave propagation in periodic structures and in the most generalized case, it will be a function of the wavenumber (μ).

With the chosen $\phi(x)$, the strain energy of the beam can be obtained as

$$\frac{1}{2}EI\int_0^L \left(\frac{\partial^2 y_n}{\partial x^2}\right)^2 dx = \frac{1}{2}EIY_n^2\int_0^L \left(\frac{d^2\phi}{dx^2}\right)^2 dx = \frac{1}{2}EIY_n^2\left(\frac{(2j-1)^4\pi^4}{32L^3}\right) \quad (5.14)$$

The electrical work W_E in the n-th unit cell is derived from the moment produced by a voltage V_n across the piezoelectric layer. The moment is given by $M_\Lambda = \gamma_c V_n(t)$, where γ_c is a constant dependent on the geometry and configuration of the piezoelectric transducer. So, the electrical work can be obtained by multiplying the moment with the curvature of

the beam and is given by

$$\begin{aligned} W_E = \int_0^{L_c} \gamma_c V_n \frac{\partial^2 y_n}{\partial x^2}\, dx =& \gamma_c V_n Y_n \int_0^{L_c} \frac{d^2\phi(x)}{dx^2}\, dx \\ &= \gamma_c V_n Y_n \int_0^{L_c} (2j-1)^2 \frac{\pi^2}{4L^2} \cos\left((2j-1)\frac{\pi x}{2L}\right) dx \\ &= \gamma_c (2j-1)\frac{\pi}{2L} \sin\left((2j-1)\frac{\pi L_c}{2L}\right) V_n Y_n = \Theta Y_n V_n \end{aligned} \tag{5.15}$$

where L_c is the length of the piezoelectric patch and the constant Θ is given by

$$\Theta = \gamma_c (2j-1)\frac{\pi}{2L} \sin\left((2j-1)\frac{\pi L_c}{2L}\right). \tag{5.16}$$

For a bimorph piezoelectric patch, γ_c can be evaluated [107] as

$$\gamma_c = E d_{31} w_c (h + h_c) \tag{5.17}$$

where E is the modulus of elasticity of the beam, h is the thickness of the beam, h_c is the thickness of the piezoelectric patch, w_c is the width of the piezoelectric patch and d_{31} is the piezoelectric constant.

The signed equivalent inertance of each intercellular negative-inerter module is written as

$$b_a = -r_a, \qquad r_a = \frac{m_a}{2}\cot^2\alpha = \frac{m_a \cos^2\alpha}{2\sin^2\alpha} > 0, \tag{5.18}$$

where $b_a < 0$ is the signed inertance and $r_a = -b_a > 0$ is its magnitude. The total reduced kinetic energy of the n-th unit cell is hence obtained as

$$T_{red} = \frac{1}{2} M_t \dot{Y}_n^2 + \frac{1}{2} b_a \left(\dot{Y}_{n+1} - \dot{Y}_n\right)^2. \tag{5.19}$$

Or equivalently as,

$$T_{red} = \frac{1}{2} M_t \dot{Y}_n^2 - \frac{1}{2} r_a \left(\dot{Y}_{n+1} - \dot{Y}_n\right)^2. \tag{5.20}$$

The Lagrangian derivative of the kinetic-energy contribution associated with the n-th unit cell is therefore obtained as

$$\begin{aligned} \frac{d}{dt}\left(\frac{\partial T_{red}}{\partial \dot{Y}_n}\right) &= M_t \ddot{Y}_n + b_a \left(2\ddot{Y}_n - \ddot{Y}_{n-1} - \ddot{Y}_{n+1}\right) \\ &= M_t \ddot{Y}_n - r_a \left(2\ddot{Y}_n - \ddot{Y}_{n-1} - \ddot{Y}_{n+1}\right). \end{aligned} \tag{5.21}$$

The equations of motion governing the n-th unit cell in terms of tip mass displacement for single- mode approximation are hence obtained as:

$$\begin{aligned} M_t \ddot{Y}_n + EI(2j-1)^4 \frac{\pi^4}{32L^3} Y_n + k\left(2Y_n - Y_{n-1} - Y_{n+1}\right) + 2c_1 Y_n + 4c_2 Y_n^3 \\ - \frac{m_a \cos^2\alpha}{2\sin^2\alpha}\left(2\ddot{Y}_n - \ddot{Y}_{n-1} - \ddot{Y}_{n+1}\right) - \Theta V_n = 0 \end{aligned} \tag{5.22}$$

On the electrical side, considering the piezoelectric patches as a capacitor, the electrical governing differential equation remains the same as obtained for the unit cell in Section 5.2:

$$C_p \dot{V}_n + \frac{V_n}{R_l} + \Theta \dot{Y}_n = 0 \tag{5.23}$$

where R_l is the load resistor and C_p is the capacitance of the piezoelectric patches.

5.4 Dispersion characteristics in the linearized regime

5.4.1 Dispersion relation

It is worth mentioning here again that the dispersion analysis and settling-time based energy harvesting characterization in the linearized regime for the piezomagnetoelastic chain considered in this Chapter qualitatively follow from the same analysis used for the linear piezoelectric chain without magnets and inerters considered in Chapter 4. They are retained here to make the analysis in this Chapter self-contained and to signify the quantitative differences arising due to the magnetic potential coefficients and the inerter mass-parameter.

For the linearized regime within one of the two stable wells of the total potential, we do not linearize Eq. (5.22) about the trivial, unstable equilibrium point $Y_n = 0$, but about a chosen stable non-zero equilibrium point Y_s. For the simplest uniform branch, the adjacent unit cells satisfy

$$Y_{n-1} = Y_n = Y_{n+1} = Y_s, \qquad \dot{Y}_n = \ddot{Y}_n = V_n = 0 \tag{5.24}$$

and Eq. (5.22) taking the integer $j = 1$ reduces to

$$\Big(k_{eff} + 2c_1\Big)Y_s + 4c_2 Y_s^3 = 0 \tag{5.25}$$

where $k_{eff} = \frac{EI\pi^4}{32L^3}$. Hence, the equilibrium points are obtained as

$$Y_s = 0, \qquad Y_s = \pm\sqrt{-\frac{\Big(k_{eff} + 2c_1\Big)}{4c_2}} \tag{5.26}$$

The total potential corresponding to the simplest uniform branch can be written as

$$U(Y_n) = \frac{1}{2}\Big(k_{eff} + 2c_1\Big)Y_n^2 + c_2 Y_n^4 \tag{5.27}$$

For the non-zero equilibrium points to be real and stable, the local tangent stiffness at Y_s must satisfy the minimality criterion

$$K_t := \frac{\partial^2 U}{\partial Y_s^2} = k_{eff} + 2c_1 + 12c_2 Y_s^2 > 0 \tag{5.28}$$

Using the non-zero equilibrium points obtained in (5.26) gives

$$K_t = -2\Big(k_{eff} + 2c_1\Big) \tag{5.29}$$

Therefore, for a bi-stable effective net potential with two stable non-zero equilibrium points, it is required that

$$c_2 > 0, \qquad k_{eff} + 2c_1 < 0 \tag{5.30}$$

and in that case the trivial equilibrium point $Y_s = 0$ becomes unstable

We express the net effective displacement as $Y_s + Y_n(t)$, where $Y_n(t)$ denotes a small perturbation about the chosen stable equilibrium point Y_s. For small perturbations $|Y_n| << |Y_s|$, the cubic term in Eq. (5.22) is linearized about Y_s, so that the perturbation

stiffness is modified by the additional term $12c_2Y_s^2$. Assuming a Bloch solution for plane wave propagation in this within-well linearized regime, we can obtain the displacements of the adjacent tip masses in the $n-1$-th and $n+1$-th unit cell as:

$$\begin{aligned} Y_{n+1}(t) &= Y_n(t)e^{i\mu} \\ Y_{n-1}(t) &= Y_n(t)e^{-i\mu} \end{aligned} \tag{5.31}$$

where μ is the non-dimensional wavenumber

Rewriting the voltage V_n in terms of stored charge q_n gives $V_n = R_l\dot{q}_n = \frac{q_n}{C_p}$. Substituting this in the electrical equation (5.23) gives

$$C_pR_l\ddot{q}_n + \frac{q_n}{R_lC_p} + \Theta\dot{Y}_n = 0 \tag{5.32}$$

Using Bloch's solution (5.31) in the governing differential equation of the perturbation about the stable well, taking the integer j to be 1, gives:

$$\left(M_t - \frac{m_a\cos^2\alpha}{\sin^2\alpha}(1-\cos\mu)\right)\ddot{Y}_n + \left(2k(1-\cos\mu) + k_{eff} + 2c_1 + 12c_2Y_s^2\right)Y_n - \Theta\frac{q_n}{C_p} = 0 \tag{5.33}$$

The temporal part of the solution of Eqs. (5.32) and (5.33) is sought in the form [111]:

$$q_n(t) = Qe^{i\omega t} \tag{5.34}$$

where we call ω the frequency of free wave propagation in a colloquial terminology in the horizontal axial direction of the periodic chain and treat it as a book-keeping parameter as of now. By substituting (5.34) in (5.33) gives:

$$\left(M_t - \frac{m_a\cos^2\alpha}{\sin^2\alpha}(1-\cos\mu)\right)\ddot{Y}_n + \left(2k(1-\cos\mu) + k_{eff} + 2c_1 + 12c_2Y_s^2\right)Y_n = \frac{\Theta}{C_p}Qe^{i\omega t} \tag{5.35}$$

Eq. (5.35) can be solved exactly for Y_n, which will comprise of a homogeneous solution and a particular integral and is given by

$$Y_n(t) = Y_0e^{i\omega_0 t} + \frac{\Theta Q}{C_pm_e(\omega_0^2 - \omega^2)}e^{i\omega t} \tag{5.36}$$

where

$$\omega_0 = \sqrt{\frac{\left(2k(1-\cos\mu) + k_{eff} + 2c_1 + 12c_2Y_s^2\right)}{\left(M_t - \frac{m_a\cos^2\alpha}{\sin^2\alpha}(1-\cos\mu)\right)}} \tag{5.37}$$

We introduce the notation

$$m_e = \left(M_t - \frac{m_a\cos^2\alpha}{\sin^2\alpha}(1-\cos\mu)\right) \tag{5.38}$$

Y_0 can be determined from the initial conditions imposed on the perturbation of the tip mass about the chosen stable well

Substituting (5.34) and (5.36) in (5.32) and equating to zero the coefficients of the exponentials, we can obtain the dispersion relation in the within-well linearized regime of

the piezomagnetoelastic chain

$$\left(-\omega^2 C_p R_l Q + \frac{Q}{R_l C_p} + \frac{\Theta^2 i\omega Q}{C_p m_e(\omega_0^2 - \omega^2)} \right) e^{i\omega t} + \left(\Theta i\omega_0 Y_0 \right) e^{i\omega_0 t} = 0 \tag{5.39}$$

Equating the coefficient of $e^{i\omega_0 t}$ to zero in (5.39) gives $Y_0 = 0$, which is quite expected for steady-state Bloch wave propagation within the selected stable potential well.

Equating the coefficient of $e^{i\omega t}$ to zero in (5.39) gives after rearranging terms the dispersion relation $\mu(\omega)$ or $\omega(\mu)$ as:

$$\cos\mu = 1 - \frac{\Big(M_t\omega^2 - k_{eff} - 2c_1 - 12c_2 Y_s^2\Big)\Big(1 - \omega^2(R_l C_p)^2\Big) + \Theta^2 i\omega R_l}{(2k + r_a\omega^2)\Big(1 - \omega^2(R_l C_p)^2\Big)} \tag{5.40}$$

where $r_a = \frac{m_a \cos^2\alpha}{\sin^2\alpha}$ is defined as the negative-inertance factor/magnitude. For the linearized regime within the selected stable well, we plot the dispersion relation obtained in (5.40) in Section 5.4.2. Real parts of the wavenumber μ correspond to propagating waves and imaginary parts correspond to attenuating waves. The parameters of the beam, piezoelectric patches, base and tip magnets are chosen as in Table 5.1. The magnetic

Elastic Beam		**Piezoelectric Patches**	
Parameters	**Values**	**Parameters**	**Values**
ρ	$2700\,\mathrm{kg\,m^{-3}}$	L_c	$30\,\mathrm{mm}$
E	$70\,\mathrm{GPa}$	w_c	$9.3\,\mathrm{mm}$
w	$9.5\,\mathrm{mm}$	h_c	$0.5\,\mathrm{mm}$
h	$0.25\,\mathrm{mm}$	d_{31}	$-210\,\mathrm{pC\,N^{-1}}$
L	$96.1\,\mathrm{mm}$	C_p	$51.4\,\mathrm{nF}$
		R_l	$20\,\mathrm{M\Omega}$
Base Magnets		**Tip Magnet**	
Parameters	**Values**	**Parameters**	**Values**
a	$12.7\,\mathrm{mm}$	a_t	$5\,\mathrm{mm}$
$2b$	$6.35\,\mathrm{mm}$	$2b_t$	$6.35\,\mathrm{mm}$
		M_t	$10\,\mathrm{g}$
		I_t/M_t	$40.87\,\mathrm{mm^2}$

Table 5.1: Parameters used for the piezomagnetoelastic chain model.

permeability μ_0 has been taken as $4\pi \times 10^{-7}$ in SI units.

We would be most likely interested in obtaining our results within a range of the magnetic potential function in terms of tip mass displacement Y_n where it preserves its bi-stable shape with two stable equilibrium positions for $Y_n(t)$ at $Y_n = \pm Y_{magnet}$ and one unstable equilibrium position in the middle at $Y_n = 0$. We also need to ensure that the conditions for existence of two stable non-zero equilibrium points of the tip mass under the net effective potential incorporating the effects from both the beam and the magnets given in (5.30) are satisfied. Hence, the constants c_0, c_1, c_2 and γ_c are taken as evaluated in Section 5.2. In the linearized regime, the dispersion profiles are shown both

with and without the piezoelectric patches. Without the piezoelectric energy harvester, the linearized dispersion relation reduces to:

$$\cos\mu = 1 - \frac{\left(M_t\omega^2 - k_{eff} - 2c_1 - 12c_2Y_s^2\right)}{(2k + r_a\omega^2)} \tag{5.41}$$

The angle α in the initial undeformed equilibrium configuration is taken as $\sin\alpha = 0.5$ throughout this Chapter and in general. For obtaining the dispersion profiles, we adopt the direct procedure, that is, fix the value of the frequency and evaluate the wavenumber by using the linearized dispersion relations (5.40) and (5.41).

5.4.2 Band structure behavior in the linearized regime

We use the dispersion relation obtained with the piezoelectric harvester in (5.40) and without the piezoelectric harvester in (5.41) and plot the dispersion profiles with varying system parameters. Parameter values of the beam, tip magnet, base magnets and piezoelectric harvester are taken as in Table 5.1 unless stated otherwise.

Band structure behavior with the electrical parameters

The ratio of the inerter mass-parameter m_a to the tip mass M_t is taken as $\frac{m_a}{M_t} = 0.5$. The stiffness coefficient of the springs has been chosen to be $k = 0.1k_{eff}$, where $k_{eff} = \frac{EI\pi^4}{32L^3}$.

As the load resistance R_l is increased (with C_p fixed) (Fig. 5.4), the electrical time constant $\tau = R_lC_p$ increases and the piezoelectric shunt transitions from a nearly short-circuit behavior (small τ, voltage quickly leaks through the resistor) towards an open-circuit-like behavior (large τ, charge is retained and the voltage builds up). In the dispersion relation, this change of τ alters both the magnitude and phase of the electromechanical feedback, so that the Bloch wavenumber becomes complex: $Re(\mu)$ identifies propagating pass bands, while $Im(\mu)$ indicates spatially attenuating (stop-band) waves. Physically, the appearance and evolution of $Im(\mu) \neq 0$ with the harvester reflects wave energy being transferred into the electrical domain and dissipated in R_l, whereas increasing τ shifts the frequency range over which this resistive dissipation is most effective and progressively moves the system response toward the limiting (weak-current) behavior where the dispersion approaches that of the structure without electrical extraction. Consequently, tuning R_l (equivalently τ) provides a direct mechanism to control both the location of the attenuation region and the harvesting-induced modification of the band structure.

Fig. 5.4 shows how the Bloch wavenumber changes as the load resistance R_l is increased while all mechanical parameters and the piezoelectric capacitance C_p are kept fixed. Since the electrical time constant $\tau = R_lC_p$ grows with R_l, the shunt circuit transitions from a more short-circuit like condition at small R_l (fast charge leakage through the resistor) toward an open-circuit like condition at large R_l (charge retention and larger voltage buildup). This modifies the frequency-dependent electrical impedance seen by the piezoelectric patches and hence the effective, complex electromechanical feedback acting on the periodic structure. In the dispersion plot, propagating regimes correspond to $Re(\mu)$ (upper half-plane), whereas attenuating regimes are identified by $-|Im(\mu)|$ (lower half-plane). For intermediate resistances (around the values giving $\omega\tau = O(1)$), the electromechanical coupling and resistive dissipation are most effective, producing stronger attenuation

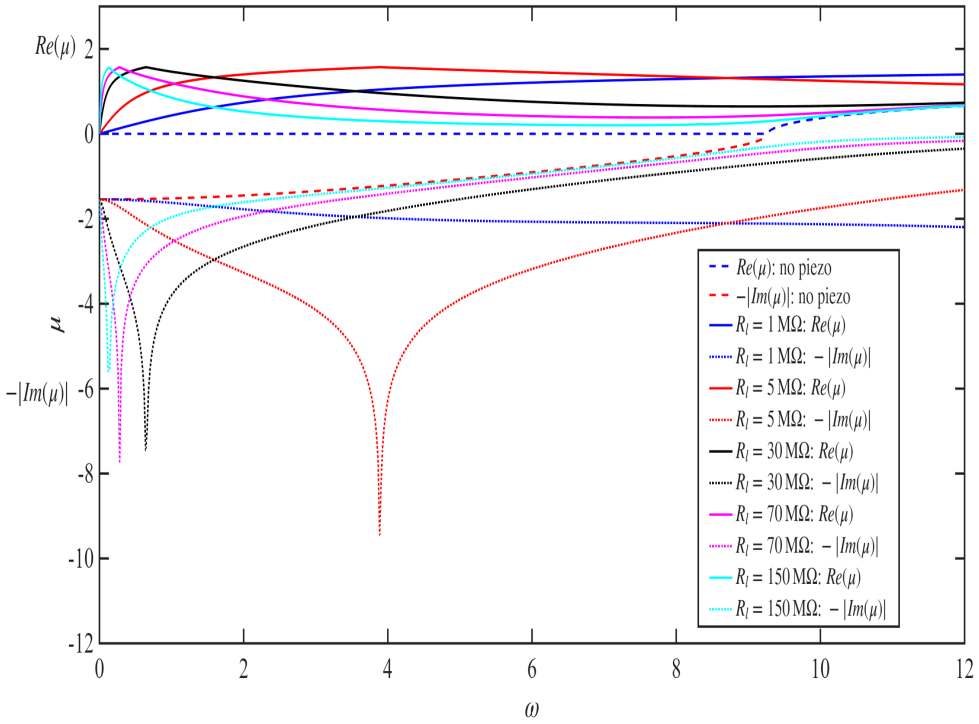


Fig. 5.4: Dispersion profiles obtained in the linearized regime with and without the piezoelectric energy harvester, solid, dashed-dotted lines show the dispersion profiles with the piezoelectric patches and dashed lines show the dispersion profiles without the piezoelectric patches, the dispersion profiles are shown with increasing values of the load resistor R_l keeping the value of the capacitance C_p and all the other parameters fixed as in Table 1, real parts of wavenumber (μ) indicate propagating waves and imaginary parts of wavenumber (μ) indicate attenuating waves, the imaginary components have been reversed in sign only for the purpose of clarity between propagation and attenuation regions which does not alter the physical interpretation, free-wave frequency ω has dimensional units of rad/s.

(larger $|Im(\mu)|$) and a more pronounced modification of the pass-band branches. As R_l is increased further, the electrical current is reduced and the shunt becomes less dissipative; consequently, the harvesting-induced perturbation weakens and the dispersion curves progressively approach the baseline (no piezo) response. Therefore, tuning R_l (equivalently τ) provides a practical knob to shift and shape the attenuation region and to control the extent to which the piezoelectric energy harvester alters the band structure.

It is important to note that increasing the value of the capacitance C_p while keeping the resistance R_l and other parameters fixed will have the same effect on the band structures, and so will be the effect of increasing R_l and C_p simultaneously because all these scenarios will increase the effective electrical time constant τ. Hence, these results are not shown here for redundancy.

Band structure behavior with the mechanical parameters

Next, we will study the effect of varying the stiffness coefficient of the springs (k) and the ratio of the inerter mass-parameter to the tip mass ($\frac{m_a}{M_t}$) on the band structures in the

linearized regime.

Band structure characteristics with varying spring stiffness coefficient First, we keep the mass ratio $(\frac{m_a}{M_t})$ fixed at 0.5 and increase the stiffness coefficient of the horizontal linear springs from $k = 0.5k_{eff}$ to $k = 5k_{eff}$ (Fig. 5.5). Fig. 5.5 summarizes

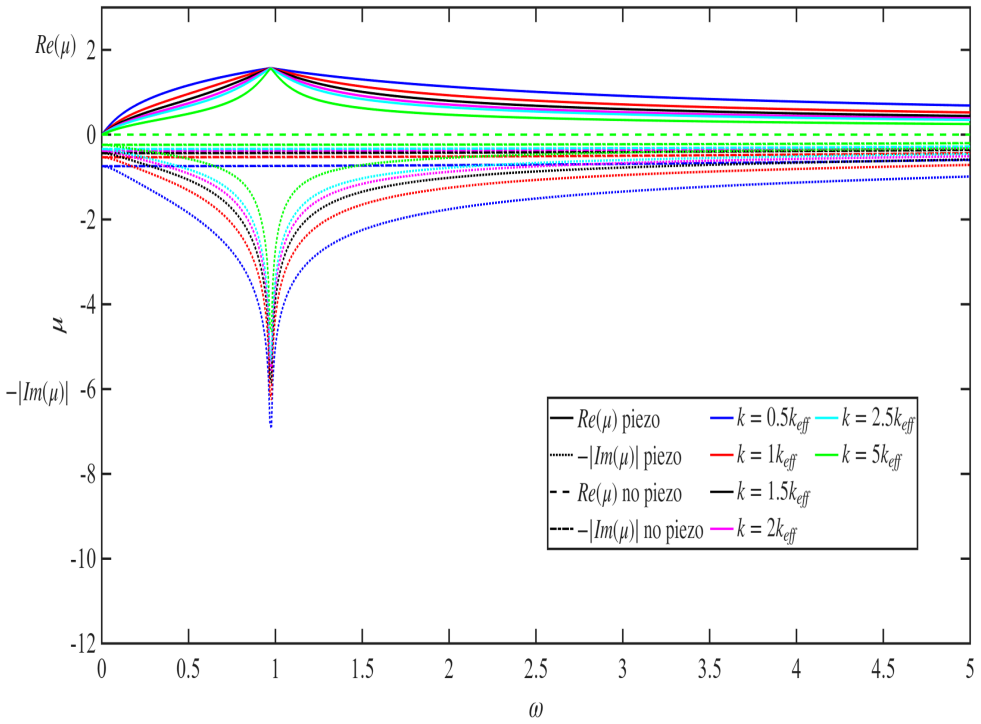


Fig. 5.5: Dispersion profiles obtained in the linearized regime with and without the piezoelectric energy harvester, solid, dotted lines show the dispersion profiles with the piezoelectric patches and dashed, dashed-dotted lines show the dispersion profiles without the piezoelectric patches, the dispersion profiles are shown with increasing values of the spring stiffness coefficient k keeping all the other parameters fixed as in Table 1, real parts of wavenumber (μ) indicate propagating waves and imaginary parts of wavenumber (μ) indicate attenuating waves, the imaginary components have been reversed in sign only for the purpose of clarity between propagation and attenuation regions which does not alter the physical interpretation, free-wave frequency ω has dimensional units of rad/s.

the band structure behavior with increasing values of the spring stiffness coefficient k. We have used continuous and dotted lines for showing the real and imaginary parts of the wavenumber μ respectively with the piezoelectric harvester and dashed and dashed-dotted lines respectively for showing the same without the piezoelectric harvester in Fig. 5.5.

Fig. 5.5 shows that increasing the stiffness coefficient k (from $0.1\,k_{eff}$ to $2.5\,k_{eff}$) effectively makes the unit cell stiffer and reduces how much the internal attachment (tip mass/piezoelectric harvester) can move relative to the beam. When k is small, the connection is compliant, so the attachment can vibrate strongly out of phase with the host structure which enhances scattering and energy exchange, which appears as a pronounced attenuation dip $(-|Im(\mu)|)$ and a more strongly curved $Re(\mu)$ branch. As k increases, the restoring force at the attachment interface becomes stronger and the relative motion is

increasingly constrained within a unit cell and consequently, the repeating unit cell mimics more closely a rigid body type motion and supports wave propagation with reduced phase accumulation per cell. In the dispersion plot this manifests itself as smaller values of $Re(\mu)$ at a given frequency (the $Re(\mu)$ branches shift toward $\mu = 0$ with the peak value remaining unchanged), which is consistent with an increased effective phase velocity and a progressively flatter pass band characteristic. At the same time, the stop band feature becomes narrower and weaker (the minimum of $-|Im(\mu)|$ is less deep), because less energy is temporarily trapped in the internal motion and therefore less energy is available to be dissipated through the coupled electromechanical pathway indicating reduced energy harvesting capability of the piezomagnetoelastic chain. In the limit of large k, the piezoelectric curves approach the no piezo baseline, consistent with the attachment becoming effectively locked to the beam and the harvester having a reduced influence on the band structure. Also, it is observed that in the absence of the piezoelectric harvester, increasing k does not have any effect on the propagating components $Re(\mu)$, but the attenuating or energy dissipating components denoted by $-|Im(\mu)|$ move upward and closer to the horizontal 'no energy transfer' line at $\mu = 0$.

Band structure characteristics with varying inerter mass-parameter The ratio of the inerter mass-parameter to the tip mass ($\frac{m_a}{M_t}$) is varied from 0.5 to 25 (Fig. 5.6) keeping the spring stiffness coefficient fixed at $k = 0.1k_{eff}$. The following sweep is used to characterize the dispersion sensitivity of the signed negative-inertance model over an extended design range. The term *stable negative inerter* applies to the subset of this range for which the complete reduced mass matrix satisfies the required positive-definiteness condition.

Fig. 5.6 summarizes the effect of increasing the normalized negative-inerter design parameter m_a/M_t, with all other parameters held fixed. In the reduced model, the signed inerter coefficient is $b_a = -r_a < 0$, whereas $r_a \propto m_a$ denotes the positive magnitude of the negative inertial coupling. Increasing m_a/M_t therefore strengthens the inertial-reduction effect and decreases the effective Bloch inertia associated with non-uniform intercell motion. At a prescribed harmonic frequency, this reduces the phase accumulation per unit cell, as reflected by the progressive shift of the $\mathrm{Re}(\mu)$ branches toward smaller values of μ, particularly away from the principal resonance region. Since the corresponding phase velocity is proportional to $\omega/\,\mathrm{Re}(\mu)$, this trend indicates a higher effective phase velocity of the propagating component.

The attenuation characteristics are also modified by the negative inertial coupling. Outside the principal resonance-induced stop band, $|Im(\mu)|$ decreases as m_a/M_t increases, so that the plotted $-|Im(\mu)|$ curves move upward toward zero. This indicates weaker evanescent decay per unit cell away from resonance. By contrast, the pronounced attenuation dip remains centred in approximately the same frequency region for all the considered values of m_a/M_t, showing that the location of the dominant electromechanically coupled resonance is comparatively robust, whereas its attenuation strength and broadband influence are tuned through the negative-inertial coupling pathway. The negative inerter does not itself dissipate energy; rather, it reshapes the effective inertia and phase characteristics of the wave field, thereby modifying how the periodic and piezoelectric dynamics distribute propagation and attenuation across the frequency range.

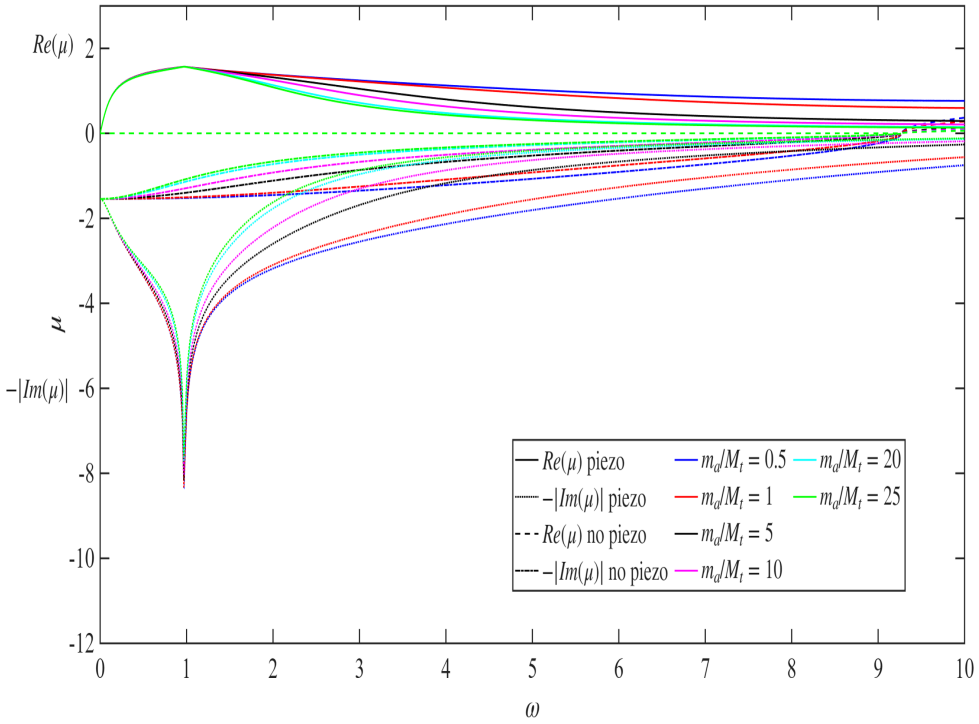


Fig. 5.6: Dispersion profiles obtained in the linearized regime with and without the piezoelectric energy harvester, solid, dotted lines show the dispersion profiles with the piezoelectric patches and dashed, dashed-dotted lines show the dispersion profiles without the piezoelectric patches, the dispersion profiles are shown with increasing values of the mass ratio $\frac{m_a}{M_t}$ keeping all the other parameters fixed as in Table 1, real parts of wavenumber (μ) indicate propagating waves and imaginary parts of wavenumber (μ) indicate attenuating waves, the imaginary components have been reversed in sign only for the purpose of clarity between propagation and attenuation regions which does not alter the physical interpretation, free-wave frequency ω has dimensional units of rad/s.

5.4.3 Summary of dispersion behavior in the linearized regime

In Section 5.4.1 and Section 5.4.2 we have derived and evaluated the linearized dispersion relation of the periodic piezomagnetoelastic chain by combining the mechanical governing equation with the electrical shunt dynamics of the piezoelectric patches. In the presence of the harvester, the dispersion relation (5.40) yields a generally complex Bloch wavenumber $\mu(\omega)$ due to the frequency-dependent electromechanical feedback introduced by the term proportional to $\Theta^2 i\omega R_l$, whereas in the absence of the harvester the relation reduces to the purely mechanical form (5.41). Consequently, $Re(\mu)$ identifies the propagating (pass-band) component and $Im(\mu)$ identifies evanescent/attenuating behavior (stop-band component), and the comparison between the 'piezo' and 'no-piezo' curves provides a direct measure of how strongly the electrical subsystem perturbs wave propagation.

From an energy-harvesting perspective, the key implication of the linear band structure results is that the regions where the piezoelectric patches induce larger attenuation (larger $|Im(\mu)|$ relative to the no piezo case) correspond to frequency ranges in which mechanical wave energy is more effectively transferred into the electrical domain and dissipated through the resistive load. In particular, tuning the electrical time constant

$\tau = R_l C_p$ shifts and reshapes the attenuation features because τ controls the phase and magnitude of the shunt response; this suggests that the harvested power can be enhanced by choosing R_l (or C_p) such that the dominant wave propagation frequencies fall in the range where the piezo-induced attenuation is strongest (typically when $\omega\tau = O(1)$). At very small or very large τ, the shunt tends toward the limiting short-/open-circuit like behaviors and the dispersion approaches the no piezo response, indicating weaker electrical extraction.

The mechanical tuning results further demonstrate that the unit-cell parameters govern both wave propagation and the distribution of mechanical deformation available for piezoelectric conversion. Increasing the coupling stiffness k constrains the relative motion between neighboring cells and causes the piezoelectric dispersion curves to approach the no-piezo baseline, indicating a weaker electromechanical modification of the band structure. By contrast, increasing the normalized negative-inerter mass parameter m_a/M_t increases the magnitude $r_a \propto m_a$ of the signed inertial coupling $b_a = -r_a < 0$ and therefore reduces the effective Bloch inertia associated with non-uniform intercell motion. This inertial-reduction effect modifies the phase accumulation, effective propagation speed, and the strength and breadth of the attenuation features without itself dissipating mechanical energy. These trends imply an inherent trade-off for distributed harvesting in a finite chain. Strong piezoelectrically induced attenuation can promote local transfer of mechanical energy into the electrical domain near a dominant operating frequency, but it can also restrict wave penetration and thereby reduce the contribution of patches located farther downstream. The linearized dispersion analysis therefore provides practical guidance for the joint selection of the electrical parameters (R_l, C_p) and mechanical parameters $(k, m_a/M_t)$, so that the piezoelectrically induced attenuation peaks and relevant band-edge regions are positioned near the targeted free-wave frequencies, while the negative-inertance magnitude remains within the admissible range of the complete reduced mass matrix. In this way, the design can balance localized electrical extraction against the spatial distribution of harvested energy along the chain.

5.5 Energy harvested in the linearized regime through free wave propagation

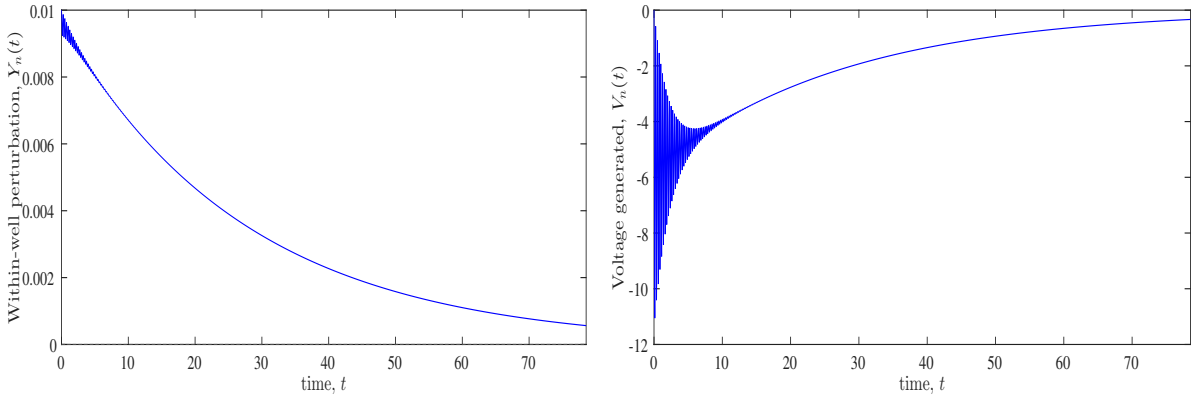
The average power harvested by the piezoelectric patch over one time period of free wave frequency ω is calculated as:

$$P_{ave} = \frac{\omega}{2\pi} \int_0^{\frac{2\pi}{\omega}} \frac{V_n^2(t)}{R_l}\, dt \tag{5.42}$$

To obtain $V_n(t)$ in the regime of Bloch-wave propagation, we numerically integrate equations (5.23) and (5.33) in the time-domain using the fourth-order Runge-Kutta (ode45) algorithm in Matlab after rewriting $V_n = \frac{q_n}{C_p} = R_l \dot{q}_n$. We resort to convert the charge equation back to voltage while performing the time-domain integration because equation (5.32) represents a lossless second-order oscillator in q_n which when coupled to the second-order mechanical DOF (5.33) through Θ, the combined electromechanical system can develop an unstable pair of eigenvalues, i.e. behaving like a negative damping or active feedback and hence causing the system response to blow up numerically in time.

This will not be suitable to capture the attenuation/ decay of spatial waves resulting in the harvested power through the piezoelectric patch via numerical simulations.

To calculate the wavenumber μ for a given free wave frequency ω, we use the linearized dispersion relation derived in (5.40). Since the imaginary part of the wavenumber μ is accountable for mechanical energy dissipation manifesting in the harvested electrical power, we ignore the real part of μ. For complex $\mu = \alpha + i\beta$, we take $\cos\mu = \cos i\beta = \cosh\beta$. We set the value of the free wave frequency ω and evaluate α and β using (5.40) and run our time-domain simulation for 100 cycles of the free wave frequency and compute the power using (5.42) over a cycle when the initial oscillatory mechanical transients induced due to the initial displacement/ velocity conditions imposed on the tip mass and hence the initial oscillatory electrical transients generated in the piezoelectric patch/ harvester die out completely resulting in V_n to decay or grow respectively along a smooth envelope and the magnitude of the voltage, $|V_n(t)|$ becomes the largest irrespective of sign (because the power harvested depends on V_n^2) to obtain the maximum steady-state power. In an example plot shown in Fig. 5.7, with an input frequency value of $\omega = 8$, this seems to happen approximately at time $t = t_s \approx 20$ seconds from an apparent visual glance at Fig. 5.7(b). A small initial perturbation of $Y_n(0) = Y_0 = 0.01, \dot{Y}_n(0) = 0$ has been and will be henceforth imposed on the tip mass to generate free wave motion in the periodic system in the linearized regime within the stable potential well. In a general scenario, we will use a spring stiffness value of $k = 0.1k_{eff}$, where $k_{eff} = \frac{EI\pi^4}{32L^3}$ and an inerter mass-parameter value of $m_a = 0.5M_t$ and other parameter values from Table 5.1. Fig. 5.7 is an example plot that depicts the transient voltage response of the shunted



(a) Tip mass displacement $Y_n(t)$ from stable equilibrium position in the linearized regime

(b) Voltage generated $V_n(t)$ in the linearized regime

Fig. 5.7: Time-domain responses in the linearized regime showing the tip mass displacement $Y_n(t)$ from the stable equilibrium point at $+Y_s$ as obtained in (5.26) and voltage generated in the piezoelectric patch $V_n(t)$ for a representative n-th unit cell, for an initial perturbation on the tip mass as $Y_n(0) = 0.01, \dot{Y}_n(0) = 0$ from the stable equilibrium position at $+Y_s$ and with values of system parameters chosen as in Table 5.1.

piezoelectric patch when the chain is released from an initial tip displacement with zero initial charge/voltage. As soon as the tip mass begins to move, the electromechanical coupling converts the mechanical velocity into an electrical response through the RC shunt relation (5.23), so V_n departs from zero once $\dot{Y}_n \neq 0$. The initial sign of the voltage

is set by our sign conventions and the negative d_{31} embedded in Θ, but it does not affect the harvested energy because the electrical power scales with $\frac{V_n^2}{R_l}$. The oscillatory nature of $V_n(t)$ reflects the underlying coupled electromechanical vibration, while its decaying envelope indicates that the stored mechanical energy is progressively transferred to the electrical domain and dissipated in the resistor. After a sufficient amount of time, the decay is dominated by the electrical time constant $\tau = R_l C_p$. Using $\cos\mu = \cosh\beta$ with $\mu = \alpha + i\beta$ from (5.40) effectively imposes a purely evanescent (stopband) Bloch condition, modifying the effective inertia/stiffness in the mechanical equation via $1 - \cos\mu < 0$ and thereby capturing, in a single representative cell's time-domain simulation, the enhanced attenuation or energy-extraction behavior associated with the bandgap.

5.6 Dependence of maximum steady-state power on free wave frequency

As mentioned before in Chapter 4, by free-wave frequency, we refer to the characteristic frequency associated with free wave propagation generated solely by initial conditions in the absence of any sustained external forcing or base excitation. Therefore, ω should not be interpreted as an independently prescribed excitation frequency. Instead, it is used as a dispersion-based book-keeping parameter that parameterizes the admissible free-wave components supported by the chosen structural, magnetic, inertial, and electrical properties of the chain. In practice, sweeping ω is equivalent to scanning the corresponding family of system designs through the dispersion relation, since the associated wavenumber, effective inertia, effective stiffness, and harvested power are all determined by the coupled system parameters. Once a maximum-power condition is imposed later in Section 5.7.1, the optimum value $\omega = \omega_e$ is no longer arbitrary, but emerges from the design parameters and the imposed initial state. In the nonlinear regime, this interpretation is further amplitude-dependent, because the initial perturbation fixes the intrawell oscillation amplitude and thereby modifies the nonlinear dispersion branch on which the corresponding free-wave frequency is evaluated.

The free wave frequency ω (which we consider as a book-keeping parameter, again re-emphasizing the fact that it has to be and will be prescribed essentially by accordingly choosing the values of the system design parameters) is swept over a range of values and the power harvested over a cycle when initial oscillatory transients generated due to the initial conditions imposed on the tip mass die out completely and voltage generated is maximum in magnitude, is evaluated and plotted with ω. We use a value of spring stiffness coefficient of $k = 0.1k_{eff}$, inerter mass-parameter value of $m_a = 0.5M_t$ and keep the values of the other parameters fixed as defined in Table 5.1. We also impose two more conditions for practical feasibility:

- $m_e(\mu) = \left(M_t - \frac{m_a \cos^2\alpha}{\sin^2\alpha}(1 - \cos\mu) \right) \neq 0$
- $K(\mu) = \left(2k(1 - \cos\mu) + k_{eff} + 2c_1 + 12c_2 Y_s^2 \right) > 0$ from equation (5.33).

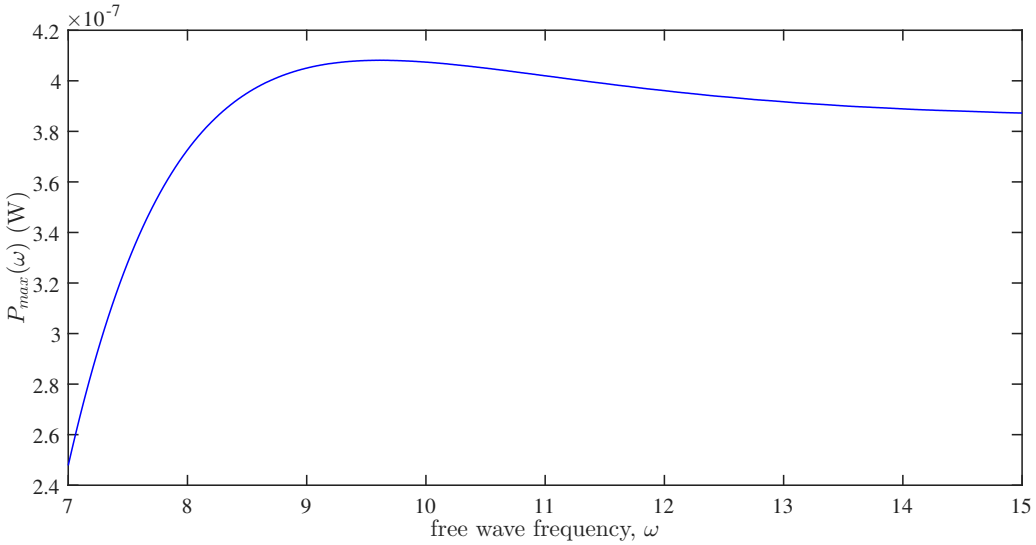


Fig. 5.8: Power harvested in the linearized regime over the cycle of maximum steady-state voltage amplitude plotted with free wave frequency ω for an initial perturbation on the tip mass as $Y_n(0) = 0.01, \dot{Y}_n(0) = 0$ from the stable equilibrium position.

Fig. 5.8 shows the power harvested in the linearized regime over the cycle of maximum steady-state voltage amplitude from free wave motion through our chosen piezomagnetoelastic periodic chain for a range of free wave frequencies ω with initial conditions for the tip mass chosen the same as in Fig. 5.7. It is observed that the maximum steady-state power or in other words, the maximum steady-state energy is harvested in the linearized regime through the piezoelectric patch from free wave motion through our system at a particular value of frequency ω (which happens to be approximately around $\omega \approx 9.5$ in Fig. 5.8), while keeping the structural and electrical parameters of the system fixed. We denote this frequency corresponding to maximum harvested energy/ power in the steady state as $\omega = \omega_e \approx 9.5$ for our chosen system parameters.

To generate the curve depicting the dependence of maximum steady-state power on non-dimensional frequency ω, we have extracted the voltage over one time period/ cycle of our colloquially used free wave frequency ω after a certain settling time when the initial oscillatory transients die out and the voltage $\tilde{V}_n(\tau)$ evolves along a smooth envelope. Later, we will show in (5.7.1) that there is instead a more systematic and consistent method to choose the time period of this cycle based on the system eigenvalues in the intrawell linearized regime.

As of now, we have used a value of the settling time as $t_s = 20$ seconds from our visual approximation from Fig. 5.7(b) which was obtained by setting $\omega = 8$ which lies within the range of ω swept in Fig. 5.8. We have used this same value of visually approximated settling time to obtain the power vs frequency curve shown in Fig. 5.8, for every input frequency ω over the sweeping interval chosen. Later, we will propose a systematic analytical approach in Section 5.7.3 to derive a compact closed-form expression for this settling time which we will denote by $t_s(\omega)$ in terms of the input free wave frequency ω or in other words the system parameters. We will also show that the optimum frequency value $\omega = \omega_e$ corresponding to the peak power and the magnitude of the peak power harvested in the steady-state regime denoted by the isolated peak in Fig. 5.8 are both

dependent on this settling time $t_s(\omega)$.

Note: One feature noteworthy here of this piezomagnetoeastic periodic harvester-model in contrary to the piezoelectric model discussed in Chapter 4 is that in the piezoelectric model, the optimum free wave frequency/peak power location was independent and robust to the precise settling time value chosen while the peak power magnitude depended on this value. But for the proposed piezomagnetoelastic model developed in this Chapter, both the peak power location and magnitude are dependent on the value of this settling time chosen even in the linearized intrawell regime.

5.7 An analytical approach to characterize harvested power in the linearized regime

5.7.1 Analytical framework in the time-domain to find optimum frequency for maximum steady-state power

Modal expansion of state space vector

In the linear regime, we can convert Eqs. (5.23) and (5.33) to an equivalent state space form $\mathbf{A}\dot{\mathbf{y}} + \mathbf{B}\mathbf{y} = \mathbf{0}$ by choosing an appropriate state vector $\mathbf{y} = \begin{Bmatrix} Y_n(t) \\ \dot{Y}_n(t) \\ V_n(t) \end{Bmatrix}$. The matrices $\mathbf{A}$ and $\mathbf{B}$ are obtained as:

$$\mathbf{A} = \begin{bmatrix} 1 & 0 & 0 \\ 0 & m_e(\mu) & 0 \\ 0 & 0 & C_p \end{bmatrix}, \mathbf{B} = \begin{bmatrix} 0 & -1 & 0 \\ K(\mu) & 0 & -\Theta \\ 0 & \Theta & \frac{1}{R_l} \end{bmatrix} \tag{5.43}$$

where $m_e(\mu)$ and $K(\mu)$ have already been defined in Section 5.6.

We use the same logic as in Section 5.6, that we use the imaginary part of wavenumber μ from (5.40) which is responsible for wave attenuation/ energy dissipation responsible in energy being harvested by the piezoelectric patch. So, we take $\cos\mu = \cos(\alpha + i\beta) \approx \cosh\beta$. Since we take $\cos\mu$ to be real, our $m_e(\mu)$ and $K(\mu)$ will also be real and so will be matrices $\mathbf{A}$ and $\mathbf{B}$.

The state space equation with matrices defined in (5.43) can be converted into an eigenvalue problem $\dot{\mathbf{y}} = \mathbf{S}\mathbf{y}$ where $\mathbf{S} = -\mathbf{A}^{-1}\mathbf{B}$. Assuming a solution of the form $\mathbf{y} = \mathbf{y}_0 e^{\lambda t}$, gives the standard eigenvalue problem $\mathbf{S}\mathbf{y}_0 = \lambda\mathbf{y}_0$. Setting the determinant $|\mathbf{S} - \lambda I| = 0$ for non-trivial solutions of $\mathbf{y}_0$, we get the characteristic polynomial in terms of λ as:

$$\lambda^3 + a\lambda^2 + b\lambda + c = 0 \tag{5.44}$$

where $a = \frac{1}{R_l C_p}, b = \frac{K(\mu)}{m_e(\mu)} + \frac{\Theta^2}{m_e(\mu)C_p}, c = \frac{K(\mu)}{m_e R_l C_p}$. For convenience, we denote these coefficients by physically meaninngful lumped quantities as:

$$\tau = R_l C_p, \omega_m^2 = \frac{K(\mu)}{m_e(\mu)}, \kappa = \frac{\Theta^2}{m_e(\mu)C_p} \tag{5.45}$$

By applying Cardano's formula for cubic equations, solving (5.44) gives the roots λ as:

$$\lambda_l = 2\sqrt{-\frac{p}{3}}\cos\left(\frac{1}{3}\arccos\left(\frac{3q}{2p}\sqrt{-\frac{3}{p}}\right) - \frac{2\pi l}{3}\right) - \frac{1}{3\tau}, \qquad l = 1,2,3 \tag{5.46}$$

where $p = (\omega_m^2 + \kappa) - \frac{1}{3\tau^2}, \quad q = \frac{2}{27\tau^3} + \frac{2\omega_m^2 - \kappa}{3\tau}$. For all three real roots of λ, we should choose our system parameters such that $p < 0$. Once we find the eigenvalues λ_l, we can find the eigenvectors $v_l, \quad l = 0,1,2$ by substituting λ_l in the eigenvalue problem. In the linear regime, using modal superposition, the state vector $\mathbf{y}(t)$ can always be written as:

$$\mathbf{y}(t) = \begin{Bmatrix} Y_n(t) \\ \dot{Y}_n(t) \\ V_n(t) \end{Bmatrix} = c_1 v_1 e^{\lambda_1 t} + c_2 v_2 e^{\lambda_2 t} + c_3 v_3 e^{\lambda_3 t} \tag{5.47}$$

where $c_1,\ c_2,\ c_3$ are constants which can be determined from the initial conditions or initial state $\mathbf{y}(0) = \mathbf{y}_0$ by inverting the eigenvector matrix $\mathbf{V} = [v_1 \quad v_2 \quad v_3]$, whose columns are the eigenvectors $v_l, \quad l = 1,2,3$. If the eigenvalues of $\mathbf{S}$ are distinct, which is the most generalized case, then the eigenvectors v_l will always be linearly independent which means that the eigenvector matrix constructed by using those eigenvectors as its columns will always be non-singular and hence invertible. So, in the most generalized case, we can always find out the constant coefficients $c_1,\ c_2,\ c_3$ by choosing our desired non-zero initial conditions or initial state of the system.

The eigenvalues and hence the eigenvectors will be dependent on the system parameters and the wavenumber μ related to free wave propagation through our system in the linearized regime. Here, we have posed a general eigenvalue problem for free response of linear systems whereas in the next section Section 5.7.1, we will show how the book-keeping parameter ω comes into the picture through the stiffness term $K\Big(\mu(\omega)\Big)$ or equivalently $\mathbf{B}(\omega)$ in the regime of free wave propagation through linear periodic systems.

Step-by-step analytical formulation for obtaining maximum steady-state power

Using the Bloch reduction and writing $V_n = q_n/C_p$, the linearized governing equations can be written as

$$m_e(\mu)\,\ddot{Y}_n(t) + K(\mu)\,Y_n(t) - \Theta\,V_n(t) = 0 \tag{5.48}$$

$$C_p\,\dot{V}_n(t) + \frac{1}{R_l}V_n(t) + \Theta\,\dot{Y}_n(t) = 0 \tag{5.49}$$

where

$$m_e(\mu) = M_t - r_a\big(1 - \cos\mu\big) \tag{5.50}$$

$$K(\mu) = 2k\big(1 - \cos\mu\big) + k_{eff} + 2c_1 + 12c_2 Y_s^2 \tag{5.51}$$

For each prescribed free-wave frequency ω, compute $\mu(\omega)$ from the linearized dispersion relation (5.40), and then treat $\cos\mu$ (hence m_e and K) as frequency-dependent through $\mu(\omega)$:

$$\cos\mu(\omega) = 1 - \frac{\Big(M_t\omega^2 - k_{eff} - 2c_1 - 12c_2Y_s^2\Big)\Big(1 - \omega^2(R_lC_p)^2\Big) + \Theta^2\, i\omega R_l}{\Big(2k + r_a\omega^2\Big)\Big(1 - \omega^2(R_lC_p)^2\Big)} \tag{5.52}$$

For 'purely-evanescent' approximation used in Section 5.5, rewrite $\cos\mu$ as $\cosh\beta$ with $\beta = |Im(\mu)|$. Hence, define β in closed-form as $\beta = sgn * \left|Im\left\{\arccos\big(\chi(\omega)\big)\right\}\right| = sgn * \left|Im\left(\arccos\left[1-\frac{\left(M_t\omega^2-\frac{EI\pi^4}{32L^3}-2c_1-12c_2Y_s^2\right)\left(1-\omega^2(R_lC_p)^2\right)+\Theta^2 i\omega R_l}{(2k+r_a\omega^2)\left(1-\omega^2(R_lC_p)^2\right)}\right]\right)\right|$ from (5.40), with the sgn function defined as $sgn = \text{sgn}\left[Re\left(1-\frac{\left(M_t\omega^2-\frac{EI\pi^4}{32L^3}-2c_1-12c_2Y_s^2\right)\left(1-\omega^2(R_lC_p)^2\right)+\Theta^2 i\omega R_l}{(2k+r_a\omega^2)\left(1-\omega^2(R_lC_p)^2\right)}\right)\right]$, if the argument inside square brackets is $\neq 0$, or $sgn = 1$ when the argument inside square brackets is 0.

Choose the state vector

$$\mathbf{y}(t) = \begin{bmatrix} y_1(t) \\ y_2(t) \\ y_3(t) \end{bmatrix} = \begin{bmatrix} Y_n(t) \\ \dot{Y}_n(t) \\ V_n(t) \end{bmatrix} \tag{5.53}$$

Then (5.48)–(5.49) are equivalent to

$$A(\omega)\,\dot{\mathbf{y}}(t) + B(\omega)\,\mathbf{y}(t) = \mathbf{0} \tag{5.54}$$

with

$$A(\omega) = \begin{bmatrix} 1 & 0 & 0 \\ 0 & m_e(\omega) & 0 \\ 0 & 0 & C_p \end{bmatrix}, \qquad B(\omega) = \begin{bmatrix} 0 & -1 & 0 \\ K(\omega) & 0 & -\Theta \\ 0 & \Theta & 1/R_l \end{bmatrix} \tag{5.55}$$

If $m_e(\omega) \neq 0$ and $C_p > 0$, define the standard state matrix

$$\dot{\mathbf{y}}(t) = S(\omega)\,\mathbf{y}(t), \qquad S(\omega) = -A(\omega)^{-1}B(\omega) = \begin{bmatrix} 0 & 1 & 0 \\ -\dfrac{K(\omega)}{m_e(\omega)} & 0 & \dfrac{\Theta}{m_e(\omega)} \\ 0 & -\dfrac{\Theta}{C_p} & -\dfrac{1}{R_lC_p} \end{bmatrix} \tag{5.56}$$

Let $(\lambda_i, \mathbf{v}_i, \mathbf{w}_i)$, $i = 1, 2, 3$, be the right/left eigen-triples of $S(\omega)$:

$$S(\omega)\mathbf{v}_i(\omega) = \lambda_i(\omega)\mathbf{v}_i(\omega), \qquad \mathbf{w}_i(\omega)^{\mathsf{T}}S(\omega) = \lambda_i(\omega)\mathbf{w}_i(\omega)^{\mathsf{T}}, \qquad \mathbf{w}_i^{\mathsf{T}}\mathbf{v}_j = \delta_{ij} \tag{5.57}$$

Then for initial condition $\mathbf{y}(0) = \mathbf{y}_0$,

$$\mathbf{y}(t) = \sum_{i=1}^{3}\left(\mathbf{w}_i^{\mathsf{T}}\mathbf{y}_0\right)\mathbf{v}_i\,e^{\lambda_i t} \tag{5.58}$$

The voltage is the third component:

$$V_n(t) = \mathbf{e}_3^{\mathsf{T}}\mathbf{y}(t) = \sum_{i=1}^{3} c_i(\omega)\,e^{\lambda_i(\omega)t}, \qquad c_i(\omega) = \left(\mathbf{e}_3^{\mathsf{T}}\mathbf{v}_i(\omega)\right)\left(\mathbf{w}_i(\omega)^{\mathsf{T}}\mathbf{y}_0\right) \tag{5.59}$$

where $\mathbf{e}_3 = [0\ 0\ 1]^{\mathsf{T}}$.

Over a single wave period $T(\omega) = 2\pi/\omega$, starting at time t_s,

$$P_{ave}(t_s, \omega) = \frac{1}{R_l\,T(\omega)}\int_{t_s}^{t_s+T(\omega)} V_n(t)^2\,dt \tag{5.60}$$

Substituting (5.59) gives the closed-form double-sum:

$$P_{ave}(t_s,\omega)=\frac{1}{R_l\,T}\sum_{i=1}^{3}\sum_{j=1}^{3}\frac{c_ic_j\,e^{(\lambda_i+\lambda_j)t_s}\Big(e^{(\lambda_i+\lambda_j)T}-1\Big)}{\lambda_i+\lambda_j},\qquad T=\frac{2\pi}{\omega}\tag{5.61}$$

Optimality condition for peak-power frequency. Define $t_0(\omega)$ as an interior maximizer of $P_{ave}(t_s,\omega)$ in the post-transient regime. A necessary condition for obtaining the maximum steady-state power is

$$E(t_0,\omega):=\frac{\partial P_{ave}}{\partial t_0}(t_s,\omega)=0\tag{5.62}$$

The peak-power frequency ω_e (peak of $\bar{P}$ after optimizing over t_0) satisfies

$$F(t_0(\omega),\omega):=\frac{\partial P_{ave}}{\partial\omega}\Big(t_0(\omega),\omega\Big)=0\tag{5.63}$$

Let, $T=\frac{2\pi}{\omega}$, $B_{ij}(\omega)=\lambda_i(\omega)+\lambda_j(\omega)$, $B'_{ij}(\omega)=\lambda'_i(\omega)+\lambda'_j(\omega)$ and denote $c'_i=dc_i/d\omega$, $\lambda'_i=d\lambda_i/d\omega$. Then the condition $F=0$ can be written as

$$0=F(t_0,\omega)=\underbrace{e^{B_{11}t_0}\,\mathcal{G}_{11}}_{(1,1)}+2\underbrace{e^{B_{12}t_0}\,\mathcal{G}_{12}}_{(1,2)}+2\underbrace{e^{B_{13}t_0}\,\mathcal{G}_{13}}_{(1,3)}+\underbrace{e^{B_{22}t_0}\,\mathcal{G}_{22}}_{(2,2)}+2\underbrace{e^{B_{23}t_0}\,\mathcal{G}_{23}}_{(2,3)}+\underbrace{e^{B_{33}t_0}\,\mathcal{G}_{33}}_{(3,3)}\tag{5.64}$$

where, for each pair (i,j),

$$\begin{aligned}\mathcal{G}_{ij}=&\big(c'_ic_j+c_ic'_j\big)\,\frac{e^{B_{ij}T}-1}{B_{ij}}\;+\;c_ic_j\,t_0\,B'_{ij}\,\frac{e^{B_{ij}T}-1}{B_{ij}}\;+\;c_ic_j\left(\frac{e^{B_{ij}T}(B_{ij}T-1)+1}{B_{ij}^2}\right)B'_{ij}\\&+\;\frac{1}{\omega}\,c_ic_j\,\frac{e^{B_{ij}T}-1}{B_{ij}}\;-\;\frac{T}{\omega}\,c_ic_j\,e^{B_{ij}T}\end{aligned}\tag{5.65}$$

Substitute $B_{ij}=\lambda_i+\lambda_j$ explicitly. For instance, $B_{12}=\lambda_1+\lambda_2$, $\implies \frac{e^{B_{12}T}-1}{B_{12}}=\frac{e^{(\lambda_1+\lambda_2)T}-1}{\lambda_1+\lambda_2}$

Applying this substitution to all $\mathcal{G}_{ij}$ in (5.64) gives an explicit transcendental equation in terms of $\{\lambda_i(\omega),\lambda'_i(\omega),c_i(\omega),c'_i(\omega)\}$, the location t_0 for maximum steady-state power, and $T=2\pi/\omega$. Solving this transcendental equation gives the value for ω and hence $t_0(\omega)$ in terms of known or designed system parameters, so that they do not remain arbitrary external inputs or book-keeping parameters henceforth and provide a design/ operating range of our system parameters to obtain maximum harvested power through free wave motion in a steady state. The only thing remaining is to establish the same for the settling time $t_s(\omega)$ in terms of system parameters which we will derive in Section 5.7.3.

As stated, the final optimality condition obtained from (5.59)–(5.64) is transcendental in nature. This is expected because the harvested-power expression contains modal coefficients, eigenvalues, and exponential terms, all of which depend implicitly on the free-wave frequency through the coupled electromechanical dispersion relation. Therefore, the resulting condition should not be interpreted as an elementary closed-form formula for the optimum frequency. Rather, it provides a mathematically tractable residual whose roots correspond to stationary values of the averaged harvested power. The physical interpretation of this result is that the optimum harvested power is governed by the combined influence of the electromechanical eigenstructure, the decay of the modal response, and the selected post-transient averaging interval. The eigenvalues determine the decay

rate and oscillatory content of the response, whereas the modal coefficients determine how strongly each mode contributes to the voltage generated across the load resistance. Consequently, the transcendental form of the optimality condition arises naturally from retaining the complete state-space and eigenvalue dependence of the coupled system. Although this makes the analytical expression relatively dense, it also preserves the full parameter dependence required for a systematic optimization of the harvested energy.

Such transcendental equations can be solved using standard numerical root-finding or optimization techniques, including the Newton–Raphson method, secant method, bisection method, Brent's method, fixed-point iteration, continuation methods, or derivative-free optimization algorithms. In the present study, the final optimality condition is evaluated numerically in Matlab, and the corresponding optimum frequency and maximum averaged harvested power are obtained from the numerical solution of the derived transcendental equation.

In the intrawell linearized regime, for each fixed free-wave parameter ω, the reduced electromechanical model remains a Linear Time Invariant (LTI) system and the actual oscillatory content of the post-transient response is governed by the dominant complex-conjugate poles of the state matrix $S(\omega)$, which we write as $s_{2,3}(\omega) = -\sigma_{\text{osc}}(\omega) \pm i\omega_d(\omega)$. Therefore, although ω enters the Bloch reduction through the effective coefficients $m_e(\omega)$ and $K(\omega)$, the cycle over which the steady-state harvested power is evaluated is chosen from the damped modal period $T_d(\omega) = 2\pi/\omega_d(\omega)$ rather than from the book-keeping period $2\pi/\omega$. Accordingly, after estimating the transient-settling time either from a visual approximation or later from a systematic derivation (as shown in (5.7.3), we evaluate the post-transient power by sliding a window of length $T_d(\omega)$ over the response and defining

$$P_{ave}(t_0, \omega) = \frac{1}{R_l T_d(\omega)} \int_{t_0}^{t_0+T_d(\omega)} V_n^2(t)\, dt \tag{5.66}$$

with the maximum steady-state power obtained as

$$P_{max}(\omega) = \max_{t_0 \geq t_s(\omega)} P_{ave}(t_0, \omega) \tag{5.67}$$

This refinement makes the time-domain power metric consistent with the actual oscillatory transient observed in $V_n(t)$ and removes the inconsistency that arises when the averaging window is prescribed from ω while the post-transient cycle is in fact controlled by $\omega_d(\omega)$

5.7.2 An alternative analytical approach in the Laplace domain to find maximum steady-state power and the corresponding optimum frequency and the extent of its validity

Transfer function/ frequency response evaluation

Let the Laplace transforms of displacement and voltage be denoted by

$$\mathcal{L}\{Y_n(t)\} = Y_n(s) \qquad \mathcal{L}\{V_n(t)\} = V_n(s) \tag{5.68}$$

Using standard identities

$$\mathcal{L}\{\dot{Y}_n\} = sY_n(s) - Y_n(0) \tag{5.69}$$

$$\mathcal{L}\{\ddot{Y}_n\} = s^2Y_n(s) - sY_n(0) - \dot{Y}_n(0) \tag{5.70}$$

$$\mathcal{L}\{\dot{V}_n\} = sV_n(s) - V_n(0) \tag{5.71}$$

Applying $\mathcal{L}\{\cdot\}$ to (5.48)-(5.49) gives the algebraic system

$$\left(m_e s^2 + K\right) Y_n(s) - \Theta V_n(s) = m_e \left(sY_n(0) + \dot{Y}_n(0)\right) \tag{5.72}$$

$$\Theta s\, Y_n(s) + \left(C_p s + \frac{1}{R_l}\right) V_n(s) = C_p V_n(0) + \Theta Y_n(0) \tag{5.73}$$

Equivalently in matrix form we obtain

$$\underbrace{\begin{bmatrix} m_e s^2 + K & -\Theta \\ \Theta s & C_p s + \dfrac{1}{R_l} \end{bmatrix}}_{\mathbf{D}(s;\mu)} \begin{bmatrix} Y_n(s) \\ V_n(s) \end{bmatrix} = \begin{bmatrix} m_e \left(sY_n(0) + \dot{Y}_n(0)\right) \\ C_p V_n(0) + \Theta Y_n(0) \end{bmatrix} \tag{5.74}$$

By Cramer's rule, we define the common denominator, $\Delta(s;\mu) = (m_e s^2 + K)\left(C_p s + \frac{1}{R_l}\right) + \Theta^2 s$. Then the voltage in the Laplace domain is obtained as:

$$V_n(s) = \frac{(m_e s^2 + K)\left(C_p V_n(0) + \Theta Y_n(0)\right) - \Theta s\, m_e \left(sY_n(0) + \dot{Y}_n(0)\right)}{\Delta(s;\mu)} \tag{5.75}$$

For the free response initial conditions used throughout: $Y_n(0) = Y_0, \dot{Y}_n(0) = 0, V_n(0) = 0$, the expression in (5.75) simplifies exactly to

$$V_n(s) = \frac{\Theta\, K(\mu)\, Y_0}{\Delta(s;\mu)} \tag{5.76}$$

Defining the complex frequency-axis voltage $\widehat{V}_n(\omega) \equiv V_n(i\omega)$, we get

$$\widehat{V}_n(\omega) = \frac{\Theta K(\omega)\, Y_0}{\left(i\omega C_p + \frac{1}{R_l}\right)\left(K(\omega) - m_e(\omega)\omega^2\right) + i\omega\Theta^2} \tag{5.77}$$

Using the one-period average power definition, the harmonic-amplitude form is

$$P(\omega) = \frac{1}{2R_l} \left|\widehat{V}_n(\omega)\right|^2 \tag{5.78}$$

Substituting the expression for $\widehat{V}_n(\omega)$ gives

$$P(\omega) = \frac{1}{2R_l} \left| \frac{\Theta K(\omega)\, Y_0}{\left(i\omega C_p + \frac{1}{R_l}\right)\left(K(\omega) - m_e(\omega)\omega^2\right) + i\omega\Theta^2} \right|^2 \tag{5.79}$$

Let $N(\omega) \equiv \Theta K(\omega)\, Y_0, D(\omega) \equiv \left(i\omega C_p + \frac{1}{R_l}\right)\left(K(\omega) - m_e(\omega)\omega^2\right) + i\omega\Theta^2$. Then the expression for power is obtained as

$$P(\omega) = \frac{1}{2R_l} \left| \frac{N(\omega)}{D(\omega)} \right|^2 \tag{5.80}$$

The condition for obtaining maximum power is set in the conventional form as:

$$\frac{dP(\omega)}{d\omega} = 0 \quad \Longleftrightarrow \quad Re\left\{\frac{N'(\omega)}{N(\omega)} - \frac{D'(\omega)}{D(\omega)}\right\} = 0 \tag{5.81}$$

Since $N'(\omega)/N(\omega) = K'(\omega)/K(\omega)$, we only need $D'(\omega)$, Introducing

$$Q(\omega) \equiv K(\omega) - m_e(\omega)\omega^2 \tag{5.82}$$

We get

$$D(\omega) = \Big(i\omega C_p + \frac{1}{R_l}\Big)Q(\omega) + i\omega\Theta^2 \tag{5.83}$$

$$D'(\omega) = iC_p\,Q(\omega) + \Big(i\omega C_p + \frac{1}{R_l}\Big)Q'(\omega) + i\Theta^2 \tag{5.84}$$

where $Q'(\omega) = K'(\omega) - m_e'(\omega)\omega^2 - 2m_e(\omega)\omega$. Finally, $K'(\omega)$ and $m_e'(\omega)$ follow from introducing the notation $\chi(\omega) = \cos\mu(\omega)$ and using the frequency-dependent relations (5.50) and (5.51) as :

$$\begin{aligned} K'(\omega) &= -2k\,\chi'(\omega) \\ m_e'(\omega) &= r_a\,\chi'(\omega) \end{aligned} \tag{5.85}$$

Now from dispersion relation (5.52), it can be seen that $\chi(\omega) = \cos\mu(\omega)$ is a complex number with non-zero real and imaginary parts in the most generalized case. Since while working in the Laplace domain, we cannot have complex coefficients of variables, we use our previous logic that we are interested only in the imaginary component of the wavenumber μ which is responsible for wave attenuation and hence manifestation of the harvested energy. Hence, we take $\cos\mu(\omega) = \cosh\beta(\omega)$, as done in Section 5.7.1.

Therefore, the frequency-dependent effective mass and stiffness can be written as

$$m_e(\omega) = M_t - r_a\,(1 - \cosh\beta(\omega)) \qquad K(\omega) = 2k\,(1 - \cosh\beta(\omega)) + k_{eff} + 2c_1 \tag{5.86}$$

Their derivatives follow by the chain rule

$$\frac{d}{d\omega}\cosh\beta(\omega) = \sinh\beta(\omega)\,\beta'(\omega) \tag{5.87}$$

so that we obtain

$$K'(\omega) = -2k\,\sinh\beta(\omega)\,\beta'(\omega) \qquad m_e'(\omega) = r_a\,\sinh\beta(\omega)\,\beta'(\omega) \tag{5.88}$$

Hence,

$$Q'(\omega) = -\left(2k + r_a\omega^2\right)\sinh\beta(\omega)\,\beta'(\omega) - 2m_e(\omega)\omega \tag{5.89}$$

Substituting the above expressions into the stationary condition (5.81) gives the scalar equation for the optimum free-wave frequency $\omega = \omega_e$ as:

$$Re\left\{\frac{-2k\,\sinh\beta(\omega)\,\beta'(\omega)}{K(\omega)} - \frac{iC_p\,Q(\omega) + \left(i\omega C_p + \frac{1}{R_l}\right)Q'(\omega) + i\Theta^2}{\left(i\omega C_p + \frac{1}{R_l}\right)Q(\omega) + i\omega\Theta^2}\right\} = 0 \tag{5.90}$$

where

$$Q(\omega) = K(\omega) - m_e(\omega)\omega^2 \tag{5.91}$$

and

$$K(\omega) = 2k\,(1 - \cosh\beta(\omega)) + k_{eff} + 2c_1 \qquad m_e(\omega) = M_t - r_a\,(1 - \cosh\beta(\omega)) \tag{5.92}$$

together with the feasibility constraints

$$\omega > 0, \qquad m_e(\omega) \neq 0, \qquad K(\omega) > 0 \tag{5.93}$$

And in practice as mentioned before, $\beta(\omega)$ is evaluated from

$$\beta(\omega) = \left|Im\left\{\arccos\big(\chi(\omega)\big)\right\}\right| \tag{5.94}$$

where $\chi(\omega) = 1 - \dfrac{\left(M_t\omega^2 - k_{eff} - 2c_1 - 12c_2Y_s^2\right)\left(1-\omega^2(R_lC_p)^2\right) + \Theta^2 i\omega R_l}{(2k + r_a\omega^2)\left(1-\omega^2(R_lC_p)^2\right)}$. $\beta'(\omega)$ can be obtained numerically (finite differences) or by analytic differentiation of $\mu(\omega) = \arccos(\chi(\omega))$

$$\mu'(\omega) = -\frac{\chi'(\omega)}{\sqrt{1-\chi(\omega)^2}} \qquad \beta'(\omega) = \operatorname{sgn}(Im\{\mu(\omega)\})\,Im\{\mu'(\omega)\} \tag{5.95}$$

Extent of validity of the Laplacian framework and possible advantages

Remark on Laplace-domain versus time-domain optima As discussed before in Chapter 4, in the Laplace-domain framework, we evaluate the voltage in the complex-frequency domain as $V_n(s)$ and obtain a frequency-response magnitude by restricting to the imaginary axis, $s = i\omega$, which leads to a closed-form power estimate $P(\omega) = \frac{|V_n(i\omega)|^2}{2R_l}$.

This is useful because it enables an analytical prediction of the attainable (peak) power level without explicit time stepping and it reveals how the electrical and mechanical parameters enter the power expression. However, maximizing $|V_n(i\omega)|$ is a purely frequency-domain criterion that does not enforce the same time-domain constraint used in our definition of P_{max} in Section 5.5 and Section 5.7.1, where the power is computed over the one-period window that achieves the largest post-transient average after a prescribed steady-time threshold $t \geq t_0$ when the displacement and consequently voltage evolve along a smooth envelope. In the present free-response setting, $V_n(t)$ is a superposition of damped modal contributions, so the cycle that yields the largest voltage magnitude after transients depends not only on frequency content but also on modal decay rates and on the chosen steady-time window. Consequently, the Laplace-domain maximizer obtained directly from $|V_n(i\omega)|$ can reproduce the correct peak power magnitude while predicting an 'optimal' ω that is shifted relative to the time-domain optimum defined with the post-transient windowing rule. To obtain an optimal frequency that is consistent with the deterministic time-domain metric, the Laplace-domain solution must be mapped back to $V_n(t)$ via an inverse Laplace transform or an equivalent modal reconstruction, after which the same t_0 based windowing constraint can be enforced during the optimization.

Fig. 5.9 again shows this disadvantage of the Laplacian approach in predicting the true optimum frequency requirement of the system to generate maximum steady-state power. However, the Laplacian framework provides an excellent approach to obtain an approximate close-form expression for the settling time $t_s(\omega)$ in terms of the system parameters without having to actually evaluate the roots of the cubic characteristic polynomial (5.44) of the coupled electromechanical system, which we will show in the next Section 5.7.3, where we will use the concept of settling time in a sort of inverse Laplacian framework to

enforce the time constraint mentioned previously in Section 5.6 and Section 5.7.1.

5.7.3 An approximate analytical approach to characterize the settling time t_s mentioned in Section 5.7.1

As we have mentioned before in Section 5.7.1 and Section 5.5, we intend to extract the voltage at a time when the initial oscillatory transients die out and the magnitude of the voltage generated in the harvester $|V_n(t)|$ is maximum. Finding an exact closed-form solution for this settling time $t_s(\omega)$ might be challenging. So, we use an approximate approach to evaluate the expression for this time instant. We use the example time-domain response of the tip mass $Y_n(t)$ shown in Fig. 5.7(a), which seems to be a superposition of a smooth exponentially decaying function in time and an exponentially decaying function in time with initial transients/ oscillatory components which die out eventually. Hence, a suitable time-domain approximation for the tip mass displacement $Y_n(t)$ from the stable equilibrium position at Y_s can be assumed to be of the form:

$$Y_n(t) \approx Ae^{-st} + Be^{\left(-\sigma \pm i\omega_d\right)t} \tag{5.96}$$

Now, once we have an idea about the approximate closed-form behavior of the tip mass Y_n in the time-domain, we use the concept of 'settling time' for Linear Time Invariant (LTI) systems to evaluate the time after which the transients finally settle on a smooth envelope. We can also make this suitable ansatz that the time after which the initial oscillatory transients die out in the displacement $Y_n(t)$ is close to the same time after which the initial transients die out in the voltage $V_n(t)$ and $V_n(t)$ grows along a smooth envelope from a negative value towards zero or in other words $|V_n(t)|$ decays along a smooth envelope from a positive value towards zero as shown in Fig. 5.7(b). Since we are interested in the harvested power which depends on $|V_n(t)|$, this seems to be an ansatz which is worthwhile.

Then, we go back to our dispersion relation in the linearized regime given by (5.52) and the closed-form definition posed for $\cos\mu = \cosh\beta$ in Section 5.7.1. So, in essence, defining our wavenumber dependent parameter $\cos\mu$ boils down to evaluating the $\cos^{-1}$ of an imaginary number in the form of $a+ib$, where a and b are real. In our case, we can explicitly write

$$a = 1 - \frac{M_t\omega^2 - k_{eff} - 2c_1 - 12c_2Y_s^2}{2k + r_a\omega^2}, b = -\frac{\Theta^2\omega R_l}{(2k + r_a\omega^2)(1-\omega^2\tau^2)} \tag{5.97}$$

where $k_{eff} = \frac{EI\pi^4}{32L^3}$, $\tau = R_lC_p$ is the electrical time constant of the harvester. When $|a| < 1$, then $\cos^{-1}(z) = \cos^{-1}(a+ib)$ is analytic at $z = a$ and for small value of $|b|$, specifically for $|b| < 1-|a|$, we can expand the function $\cos^{-1}(z)$ around $z = a$ in a Taylor series in terms of b by retaining upto cubic terms as:

$$\cos^{-1}(z) \approx \cos^{-1}(a+ib) = \cos^{-1}(a) - i\frac{b}{\sqrt{1-a^2}} + \frac{ab^2}{2(1-a^2)^{\frac{3}{2}}} + i\frac{(1+2a^2)b^3}{6(1-a^2)^{\frac{5}{2}}} \tag{5.98}$$

Then, we can separate the imaginary part of $\cos^{-1}(a+ib)$ as:

$$Im\Big(\cos^{-1}(a+ib)\Big) \approx -\frac{b}{\sqrt{1-a^2}} + \frac{(1+2a^2)b^3}{6(1-a^2)^{\frac{5}{2}}} \tag{5.99}$$

Where we retain upto cubic terms in b. Evaluating the sgn function remains a trivial task because it boils down to evaluating the sign of a real function of real variables given by $sgn = \text{sgn}\left(1 - \frac{M_t\omega^2 - k_{eff} - 2c_1 - 12c_2Y_s^2}{2k + r_a\omega^2}\right)$. Then our real $\cos\mu$ takes the form:

$$\cos\mu(\omega) = \cosh\beta(\omega) \approx \cosh\left(sgn * \left| -\frac{b(\omega)}{\sqrt{1-a(\omega)^2}} + \frac{(1+2a(\omega)^2)b(\omega)^3}{6(1-a(\omega)^2)^{\frac{5}{2}}} \right|\right) \tag{5.100}$$

This provides a compact approximation for the real-valued attenuation parameter needed in the settling-time estimate.

Concept of 'settling time' adapted to the free-decay voltage

For each fixed free-wave frequency ω, the linearized electromechanical model defines a linear time-invariant (LTI) system, whose free response $V_n(t)$ can be written as a superposition of modal exponentials

$$V_n(t;\omega) = \sum_j A_j(\omega)\, e^{s_j(\omega)\, t} \tag{5.101}$$

where $\{s_j(\omega)\}$ are the poles (equivalently, eigenvalues) of the linearized system and the coefficients $A_j(\omega)$ depend on the initial conditions

In standard control theory for Linear Time Invariant (LTI) systems, if the dominant transient is governed by an underdamped complex-conjugate pair

$$s_{2,3}(\omega) = -\sigma(\omega) \pm i\,\omega_d(\omega) \tag{5.102}$$

Then the oscillatory envelope decays approximately as $e^{-\sigma(\omega)t}$, and the settling time to a prescribed tolerance ϵ is estimated by

$$t_s(\omega) \approx \frac{\ln(1/\epsilon)}{\sigma(\omega)} \tag{5.103}$$

Common choices for the tolerance are $\epsilon = 0.02$ (2% criterion) giving $t_s \approx 4/\sigma$ and $\epsilon = 0.01$ (1% criterion) giving $t_s \approx 4.6/\sigma$

In our free-decay setting, the final value of $V_n(t)$ is zero, and the practical meaning of 'transients have settled' is that the oscillatory components have decayed below a chosen tolerance so that $V_n(t)$ evolves along a smooth envelope. Accordingly, we define an ω-dependent transient-decay time as:

$$t_s(\omega) \approx \frac{\ln(1/\epsilon)}{\sigma_{\text{osc}}(\omega)} \tag{5.104}$$

where $\sigma_{\text{osc}}(\omega)$ is the decay rate associated with the oscillatory (complex-conjugate) pole pair of the system This choice targets the decay of oscillations rather than the slowest real pole, because the latter may control very long-time tail behavior without necessarily governing when the voltage envelope becomes visually smooth over one period.

Explicit parameter-level approximation for $\sigma_{\text{osc}}(\omega)$ and $t_s(\omega)$ and comparison with numerical results

From the Laplace-domain formulation in Section 5.7.2, the transient decay is governed by the roots of the characteristic denominator

$$\Delta(s;\omega) = \big(m_e(\omega)s^2 + K(\omega)\big)\Big(C_p s + \frac{1}{R_l}\Big) + \Theta^2 s \tag{5.105}$$

Expanding Δ yields a cubic polynomial

$$m_e(\omega)C_p\, s^3 + \frac{m_e(\omega)}{R_l}\, s^2 + \big(K(\omega)C_p + \Theta^2\big)s + \frac{K(\omega)}{R_l} = 0 \tag{5.106}$$

Introducing the electrical time constant and two convenient normalized parameters as done earlier in Section 5.7.1,

$$\tau = R_l C_p \qquad \omega_m^2(\omega) = \frac{K(\omega)}{m_e(\omega)} \qquad \kappa(\omega) = \frac{\Theta^2}{m_e(\omega)C_p}$$

the characteristic equation can be written as

$$s^3 + \frac{1}{\tau}s^2 + \big(\omega_m^2(\omega) + \kappa(\omega)\big)s + \frac{\omega_m^2(\omega)}{\tau} = 0 \tag{5.107}$$

In the common regime where the roots separate into one predominantly real slow pole and one underdamped complex-conjugate pair, a useful approximation for the slow real pole is obtained by balancing the last two terms in (5.107) as:

$$s_r(\omega) \approx -\frac{\omega_m^2(\omega)}{\omega_m^2(\omega) + \kappa(\omega)}\,\frac{1}{\tau}$$

Using the sum of roots relation for the cubic, the real part of the complex pair then satisfies, considering the fact that for stable bounded solution in time, the real part of the complex conjugate pair should be negative:

$$-2\,\sigma_{\text{osc}}(\omega) + s_r(\omega) \approx -\frac{1}{\tau} \implies 2\,\sigma_{\text{osc}}(\omega) \approx s_r(\omega) + \frac{1}{\tau} \implies \sigma_{\text{osc}}(\omega) \approx \frac{1}{2\tau}\,\frac{\kappa(\omega)}{\omega_m^2(\omega) + \kappa(\omega)} \tag{5.108}$$

Substituting back $\tau = R_l C_p$, $\omega_m^2 = K/m_e$, and $\kappa = \Theta^2/(m_e C_p)$ in (5.108) gives a particularly compact ratio

$$\frac{\kappa(\omega)}{\omega_m^2(\omega) + \kappa(\omega)} = \frac{\Theta^2}{K(\omega)C_p + \Theta^2}$$

Hence, an explicit decay-rate estimate is $\sigma_{\text{osc}}(\omega) \approx \frac{1}{2R_l C_p}\,\frac{\Theta^2}{K(\omega)C_p+\Theta^2}$ and the corresponding transient-decay time becomes:

$$t_s(\omega) \approx \frac{\ln(1/\epsilon)}{\sigma_{\text{osc}}(\omega)} \approx 2R_l C_p\,\frac{K(\omega)C_p + \Theta^2}{\Theta^2}\,\ln\Big(\frac{1}{\epsilon}\Big) \tag{5.109}$$

Taking the most common choice for the tolerance value as $\epsilon = 1\% = 0.01$ gives the final explicit expression for the optimum time $t_s(\omega)$ as:

$$t_s(\omega) = 9.2\,\tau\,\frac{K(\omega)C_p + \Theta^2}{\Theta^2} \tag{5.110}$$

In our dispersion-based parameterization, the effective stiffness and mass depend on the

attenuation parameter $\beta(\omega)$ through

$$K(\omega) = 2k\big(1 - \cosh(\beta(\omega))\big) + k_{eff} + 2c_1 + 12c_2Y_s^2 \qquad m_e(\omega) = M_t - r_a\big(1 - \cosh(\beta(\omega))\big)$$

where $\cosh\beta(\omega)$ is obtained from the approximate relation derived in (5.100). The expression derived in (5.110) provides an explicit, parameter-level approximation for $t_s(\omega)$ which we have defined as the settling time to extract the voltage to compute the maximum harvested power for a particular value of the frequency in Section 5.7.1 (Eq. (5.60)).

As a check that our approximated procedure matches effectively with direct numerical time-domain (ode45) simulations, we use our approximate closed-form expression derived in (5.110) to evaluate the optimum settling time for an input value of free wave frequency set to $\omega = 8$, the same frequency value used to obtain the time-domain response $Y_n(t)$ and $V_n(t)$ in Fig. 5.7. Our closed-form expression gives a value for the optimum time t_s as:

$$t_s = 9.83338 \approx 10 \text{ seconds} \tag{5.111}$$

This value agrees quite well with the time taken for the tip mass displacement to settle to a smooth envelope as shown in Fig. 5.7(a). The analytical estimate is approximately 50% below the visually identified value of $t_s \approx 20$ seconds used in Section 5.5, which is expected given the conservative nature of the visual approximation. Both values lie well within the 80 seconds simulation window in Fig. 5.7.

We can hence use this generalized closed-form expression for $t_s(\omega)$ to compute the maximum harvested power for each input frequency ω by using the analytical definition in (5.60). This closes the gap that remained in linking back the last remaining book-keeping parameter $t_s(\omega)$ to the inherent system design parameters. We have already done the same in (5.7.1) for the other two book-keeping parameters, which were ω and the time period of the cycle $T_d(\omega)$ over which we intend to average the maximum power in the post-transient regime after t_s.

In a special scenario of our periodic chain, with no permanent base magnets and inerter mechanisms, and the tip mass made of a non-magnetic material, the periodic model reduces to a simple linear piezoelectric chain as considered before in Chapter 4. In that case, our settling-time analytical approximation in the linearized regime still remains valid for the coupled linear electromechanical system with similar qualitative time-domain behavior of tip mass and voltage. The wavenumber (or frequency) dependent stiffness will just reduce to $K(\omega) = 2k\big(1 - \cosh(\beta(\omega))\big) + k_{eff}$, and the effective mass m_e reduces to just $m_e = M_t$. β can be obtained from the dispersion relation (5.40) by putting $c_1 = c_2 = r_a = 0$. The same approximate formula obtained in (5.110) can then be applied as is.

Applicability and limitations of the 'settling time' concept

The 'settling time' estimate is applicable for our case because, for each fixed ω, the linearized dynamics define an LTI system and the voltage response is a linear combination of modal exponentials whose decay rates are dictated by the poles $s_j(\omega)$ Consequently, a settling-time scale based on the dominant oscillatory decay rate $\sigma_{\text{osc}}(\omega)$ provides a principled approximation for the time at which the oscillatory transients become small and the voltage evolves along a smooth envelope

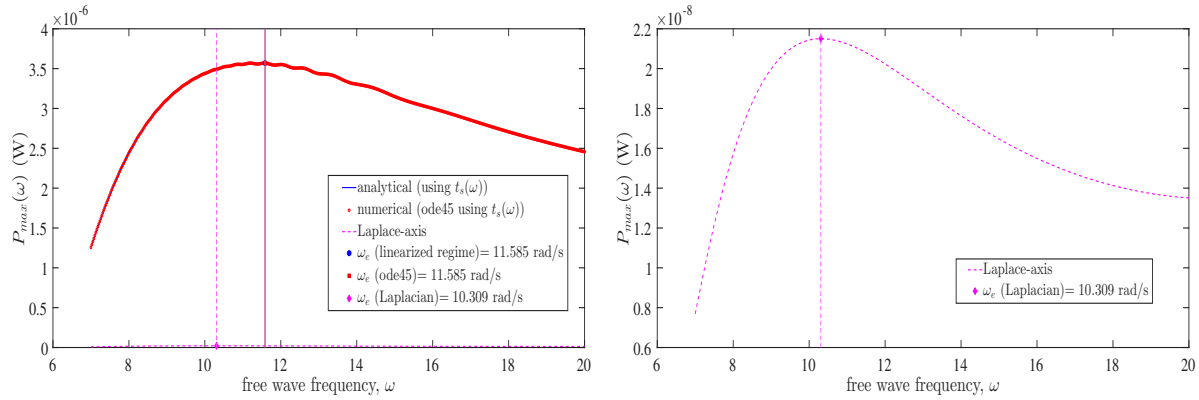
Two practical limitations should be noted:

- Firstly, sweeping ω produces a family of LTI systems because $\beta(\omega)$ (and hence $K(\omega)$ and $m_e(\omega)$) varies with ω, so the identity of the dominant pole pair may change across the sweep.

- Secondly, when the poles are not well separated (e.g. near repeated roots, near stability boundaries, or near singular electrical factors), a single exponential envelope approximation becomes less accurate and the settling time may be better estimated directly from the computed pole set $\{s_j(\omega)\}$ rather than from a closed-form approximation.

5.7.4 Comparison of theoretical power with numerical time-domain integration

We use same initial conditions for both the analytical and numerical methods for the tip mass i.e. $Y_n(0) = 0.01$, $\dot{Y}_n(0) = 0$ and zero initial voltage $V_n(0) = 0$ which comes quite obviously considering our primary goal which is to generate/ build up voltage and hence power harvesting the energy from free wave motion through our system. The spring stiffness coefficient and the inerter mass-parameter are chosen as $k = 0.1k_{eff}$ and $m_a = 0.5M_t$. Other parameters are chosen as in Table 5.1.



(a) Analytical time-domain estimate and Laplace prediction versus direct numerical integration

(b) Laplace-axis prediction (zoomed in)

Fig. 5.9: Comparison of analytical time-domain estimate, numerical integration, and Laplace-axis power prediction using $t_s(\omega)$ as calculated from (5.110), for the chosen parameter set, $t_s(\omega)$ varies from 9.69 to 10.14 s over the plotted frequency range, optimum frequency $\omega = \omega_e$ is marked at the peak power amplitude.

Fig. 5.9 shows the comparison between the analytically and numerically obtained maximum steady state power's variation with the free wave frequency ω. The value of $t_s(\omega)$ as obtained from (5.110) is used for both the analytical formulation derived in Section 5.7.1 and time-domain simulations using ode45. To calculate power directly in the Laplace domain $P(\omega) = |V(i\omega)|^2/(2R_l)$, without using any time-constraint, the formulation derived in Section 5.7.2 has been employed.

The excellent agreement between the analytical time-domain curve and the ode45 results in Fig. 5.9(a) confirms that the proposed time-domain framework reproduces both

the peak magnitude (3.569416×10^{-6} W) and the peak location (optimum frequency $\omega_e = 11.5852$ rad/s) when the same power-extraction rule i.e. one-period averaging over $T_d(\omega)$ after $t_s(\omega)$ as calculated/evaluated from (5.110) is enforced. In contrast, the Laplace-axis curve (zoomed in Fig. 5.9(b)) predicts a different optimum frequency $\omega_e = 10.3086$ rad/s (as calculated from (5.90)) and, in general, a different attainable peak level, which is 2.150071×10^{-8} W. This discrepancy reflects the limitation discussed in Section 5.7.2. Evaluating $V(s)$ on the imaginary axis implicitly treats the response as a purely harmonic steady-state frequency response, whereas the quantity plotted in the time domain is a windowed maximum power extracted from a free decay transient after the mechanical modes have sufficiently settled. Because this windowed criterion depends on decay rates (real parts of eigenvalues), modal interference, and the finite-time envelope evolution of $V_n(t)$, it is not fully captured by $s = i\omega$ alone. Consequently, the direct Laplace-axis formulation remains useful for rapid analytical magnitude estimates, settling time formulation and trend studies, but recovering an optimum frequency consistent with the deterministic time-domain metric requires reconstructing $V_n(t)$, e.g. via inverse Laplace/eigen-expansion and applying the same $t_s(\omega)$-based power criterion.

5.8 General strongly nonlinear regime – Intrawell motions of the tip mass

We now consider the piezomagnetoelastic periodic chain in its general nonlinear regime where the tip mass is allowed to undergo sufficiently large amplitudes of motion and hence the cubic term Y_n^3 becomes dominant. Since in our proposed periodic model, even in the strongly nonlinear regime, the nonlinearities are confined within a unit cell and the intercellular coupling springs are linear, we assume a Bloch-consistent harmonic approximation [14, 201] for the tip mass displacement in the regime of free wave propagation in the form:

$$Y_n(t) = \left(\sum_{m=1}^{M} A_m \cos\left[m(\mu.\mathbf{n} - \omega t)\right] + B_m \sin\left[m(\mu.\mathbf{n} - \omega t)\right] \right) \tag{5.112}$$

where $\mu.\mathbf{n} = \mu_1 n_1 + \mu_2 n_2$ is the inner product of the non-dimensional wavenumber vector with the directional vector of the general 2-D periodic lattice. M represents the number of harmonics considered. A_m and B_m are the unknown harmonic coefficients to be determined from the initial conditions. Since ours is a one-dimensional periodic system, $\mu.\mathbf{n} = \mu_1 n_1 + \mu_2 n_2$ simplifies to μn with n being the index of the repeating unit cell. Without loss of generality, we can choose the representative unit cell to be at $n = 0$, then the adjacent unit cells will have indices of -1 and $+1$. and μn reduces to $\pm\mu$.

We characterize free wave propagation when the tip mass is subject to a bi-stable magnetic potential function with two local minima and one local maxima. Choosing the distance between the magnets $d = 2d_h$, the vertical distance between the tip magnet's and base magnets' axis d_v and the field strength B_t at tip magnet's surface accordingly will result in a bi-stable magnetic potential well in terms of tip mass displacement Y_n corresponding to two stable and one unstable equilibrium position as discussed in Section 5.4.1 and associated values of the constant coefficients in the magnetic potential function. Henceforth, for generalization throughout the nonlinear analysis, we will represent these coefficients as $2c_1 = a_1$ and $4c_2 = a_2$. Rewriting (5.22) and taking the integer

$j = 1$ without loss of generality gives the equation of motion in the general strongly nonlinear regime as:

$$\begin{aligned} M_t\ddot{Y}_n + k_{eff}Y_n + k\Big(2Y_n - Y_{n-1} - Y_{n+1}\Big) + a_1Y_n + a_2Y_n^3 \\ - \frac{m_a\cos^2\alpha}{2\sin^2\alpha}\Big(2\ddot{Y}_n - \ddot{Y}_{n-1} - \ddot{Y}_{n+1}\Big) - \Theta V_n = 0 \end{aligned} \tag{5.113}$$

5.8.1 Amplitude-dependent dispersion relation within a potential well

To characterize free wave motion within one of the two stable wells of the total potential of the tip mass, we first determine the static equilibrium from the simplest uniform branch as done previously for the linearized regime in Section 5.4.1. We now introduce the intrawell perturbation variable for the generalized strongly nonlinear regime as

$$Y_n(t) = Y_s + u_n(t) \tag{5.114}$$

Substituting (5.114) into (5.113) and equating to zero the collective terms responsible for satisfying the fixed point criteria gives

$$M_t\ddot{u}_n + K_tu_n + k\left(2u_n - u_{n-1} - u_{n+1}\right) + 3a_2Y_su_n^2 + a_2u_n^3 - \frac{r_a}{2}\left(2\ddot{u}_n - \ddot{u}_{n-1} - \ddot{u}_{n+1}\right) - \Theta V_n = 0 \tag{5.115}$$

where

$$r_a = \frac{m_a\cos^2\alpha}{\sin^2\alpha} \tag{5.116}$$

To allow oscillations around a non-zero mean inside the potential well, we augment the harmonic expansion (5.112) with a zero harmonic and express the perturbation from the stable equilibrium position in the Bloch-consistent harmonic expansion form as:

$$u_n(t) = U_0 + \sum_{m=1}^{M}\left[A_m\cos m(\mu n - \omega t) + B_m\sin m(\mu n - \omega t)\right] \tag{5.117}$$

Restricting to the zero harmonic and the first harmonic for small-amplitude intrawell oscillations gives

$$u_n(t) \approx U_0 + A_1\cos(\mu n - \omega t) + B_1\sin(\mu n - \omega t) = U_0 + R\cos(\mu n - \omega t - \phi) \tag{5.118}$$

where

$$R = \sqrt{A_1^2 + B_1^2} \tag{5.119}$$

Using the first harmonic truncation with zero harmonic addition, the quadratic and cubic displacement terms in (5.115) are approximated by retaining only the constant and fundamental-harmonic components:

$$u_n^2(t) \approx \left(U_0^2 + \frac{R^2}{2}\right) + 2U_0R\cos(\mu n - \omega t - \phi) \tag{5.120}$$

$$u_n^3(t) \approx \left(U_0^3 + \frac{3}{2}U_0R^2\right) + \left(3U_0^2R + \frac{3}{4}R^3\right)\cos(\mu n - \omega t - \phi) \tag{5.121}$$

The electrical equation (5.23) is linear in voltage $V_n(t)$. Therefore, the zero harmonic gives

$$V_0 = 0 \tag{5.122}$$

while the first harmonic satisfies

$$\hat{V}_1 = \frac{i\omega\Theta}{\frac{1}{R_l} - i\omega C_p}\,\hat{U}_1 \tag{5.123}$$

The zero harmonic component U_0 after substituting Eqs. (5.118),(5.120),(5.121) in Eq. (5.115) yields the zero harmonic balance equation

$$K_t U_0 + 3a_2 Y_s \left(U_0^2 + \frac{R^2}{2}\right) + a_2 \left(U_0^3 + \frac{3}{2} U_0 R^2\right) = 0 \tag{5.124}$$

The fundamental component gives

$$\left[K_t + 2k(1-\cos\mu) - \omega^2\big(M_t - r_a(1-\cos\mu)\big) - \frac{i\omega\Theta^2}{\frac{1}{R_l} - i\omega C_p} + 6a_2 Y_s U_0 + 3a_2 U_0^2 + \frac{3}{4} a_2 R^2\right]\hat{U}_1 = 0 \tag{5.125}$$

For a non-trivial first harmonic, $\hat{U}_1 \neq 0$, Eq. (5.125) gives the amplitude-dependent dispersion relation within the selected potential well:

$$\cos\mu = 1 - \frac{M_t\omega^2 - K_t - 6a_2 Y_s U_0 - 3a_2 U_0^2 - \frac{3}{4} a_2 R^2 + \frac{i\omega\Theta^2}{\frac{1}{R_l} - i\omega C_p}}{2k + r_a\omega^2} \tag{5.126}$$

This gives the amplitude-dependent dispersion relationship inside a static potential well in the general strongly nonlinear regime. It differs from the zero-mean relation by the appearance of the zero-harmonic correction U_0 and the equilibrium shift Y_s, both of which arise from the asymmetry of the local oscillation about the non-zero stable equilibrium.

For the representative unit cell, we can take $n = 0$ without loss of generality. Then, the initial conditions are imposed on the perturbation u_n as

$$u_n(0) = \epsilon, \qquad \dot{u}_n(0) = \dot{Y}_n(0) \tag{5.127}$$

where $\epsilon = Y_n(0) - Y_s$. From (5.118), the corresponding amplitude is

$$R = \sqrt{(\epsilon - U_0)^2 + \left(\frac{\dot{Y}_n(0)}{\omega}\right)^2} \tag{5.128}$$

If the initial velocity is zero, then

$$R = |\epsilon - U_0| \tag{5.129}$$

Small-amplitude approximation: If R is sufficiently small, then $U_0 = O(R^2)$. Neglecting U_0^2 and U_0^3 in (5.124) gives

$$U_0 \approx -\frac{3a_2 Y_s}{2K_t} R^2 \tag{5.130}$$

and substituting this in (5.126) and using the expression for the stable equilibrium point

Y_s as obtained in (5.26) yields the reduced local approximation

$$\cos\mu \approx 1 - \frac{M_t\omega^2 - K_t + \frac{15}{4}a_2R^2 + \dfrac{i\omega\Theta^2}{\frac{1}{R_l} - i\omega C_p}}{2k + r_a\omega^2} \tag{5.131}$$

This can be rationalized further to:

$$\cos\mu \approx 1 - \frac{\left(M_t\omega^2 - K_t + \frac{15}{4}a_2R^2\right)(1+\omega^2\tau_e^2) + i\omega\Theta^2R_l\,(1+i\omega\tau_e)}{(2k + r_a\omega^2)\,(1+\omega^2\tau_e^2)}. \tag{5.132}$$

where $\tau_e = R_lC_p$ is the electrical time constant.

5.8.2 Time-domain response and energy harvested in the strongly nonlinear regime.

In the strongly nonlinear regime, we characterize the system response, i.e., tip mass displacement and voltage generated for intrawell oscillations of the tip mass within the potential well centered at $Y_n = +Y_s$.

We obtain the time-domain response via a continuation method to find the converged nonlinear dispersion branch $\mu(\omega)$ for a desired target value of ω. For small amplitudes within a local potential well, we use the dispersion relation obtained in (5.126). It is worthwhile to note here that assuming our nonlinear model described by (5.115, 5.23) even for small-amplitude oscillations in the vicinity of the stable equilibrium point $+Y_s$ will exhibit the same qualitative behavior as our linearized model described by (5.33, 5.23) will be erroneous, since $+Y_s$ is a center. In the vicinity of a center, we cannot make any prediction on the qualitative behavior of our nonlinear model based on the linearized model's dynamic response [197]. Since our system is symmetric in the static equilibrium for the simplest uniform branch, it is reasonable to assume that considering the potential well centred at $Y_n = -Y_s$ will yield the same characteristics in terms of time-domain response and energy harvesting potential.

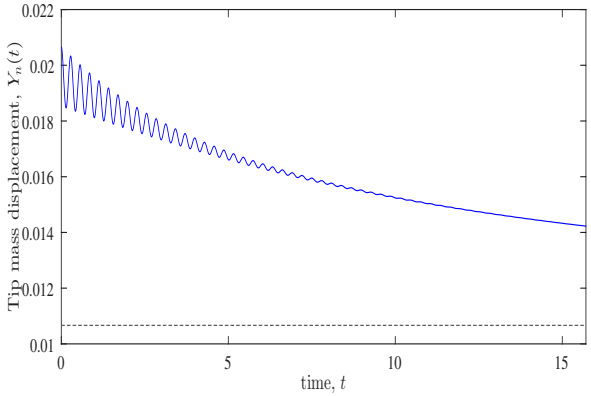
Small-amplitude intrawell oscillations about a stable center

To obtain the small-amplitude intrawell response in the general strongly nonlinear regime, we construct the nonlinear Bloch branch by continuation in the book-keeping parameter ω starting from a low-amplitude seed point within the same stable potential well. At each continuation step, the previously converged values of the zero-harmonic correction U_0 and the Bloch wavenumber μ are used as predictor values, and are then corrected by solving the zero-harmonic balance equation (5.124) together with the amplitude-dependent dispersion relation (5.126), while updating the oscillation amplitude R from the imposed initial perturbation about the equilibrium position at $+Y_s$. As an initial guess for the zero-harmonic component U_0, we use the small amplitude approximation in (5.130). This predictor-corrector procedure ensures that the solution remains on the same intrawell nonlinear branch, avoids spurious jumps to neighboring roots of the algebraic system, and provides a converged branch $\mu(\omega)$ which is then used in the direct time-domain integration of the governing equations (5.115, 5.23) for the representative unit cell.

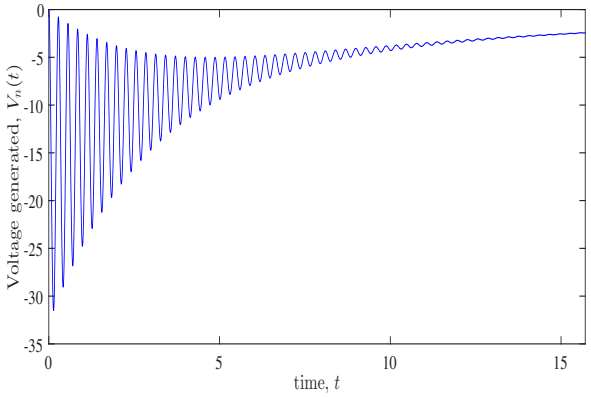
We use the same purely evanescent Bloch wave approximation for the wavenumber μ as $\cos\mu = sgn * \cosh\beta$, where $\beta = |Im(\mu)|$ and the sgn function defined as $sgn = \mathrm{sgn}(\cos\mu)$,

where $\cos\mu$ is given by the amplitude-dependent dispersion relation in (5.132). Since for strictly intrawell oscillations, we do not want to enter the negative-stiffness region, we impose a feasibility constraint on the net wavenumber-dependent effective stiffness as $K(\mu) = K_t + 2k(1-\cos\mu) > 0$ for the general strongly nonlinear regime.

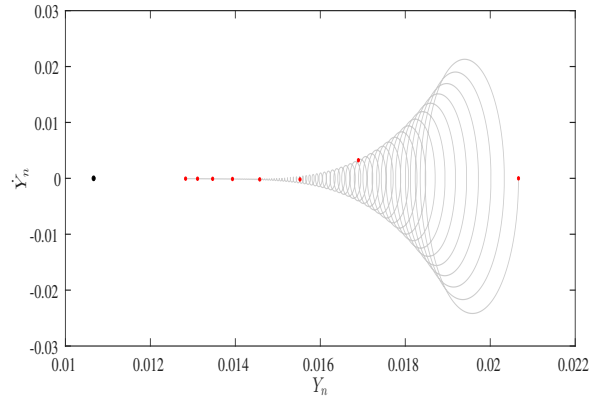
Time-domain response of tip mass displacement for intrawell oscillations and voltage generated



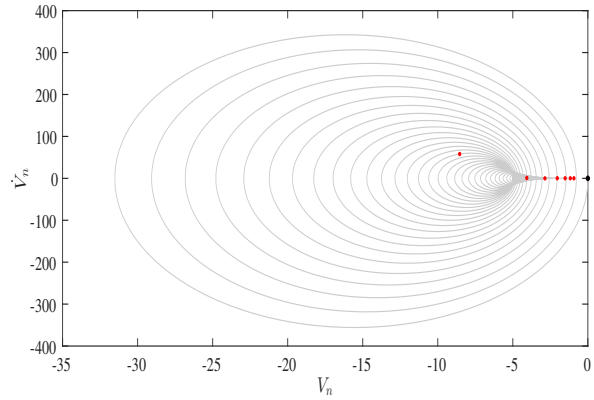
(a) Tip mass displacement $Y_n(t)$, the horizontal dashed line showing the stable equilibrium position $+Y_s$



(b) Voltage generated $V_n(t)$



(c) Phase portrait of tip mass with the Poincare points, the black dot showing the stable equilibrium point $\left(Y_n(0), \dot{Y}_n(0)\right) = (+Y_s, 0)$



(d) Phase portrait of generated voltage with the Poincare points, the black dot showing the initial voltage $\left(V_n(0), \dot{V}_n(0)\right) = (0, 0)$

Fig. 5.10: Time-domain responses and phase portraits showing the tip mass displacement $Y_n(t)$ and voltage generated $V_n(t)$ for intrawell oscillations in the strongly nonlinear regime for a representative n-th unit cell, for an initial perturbation on the tip mass as $Y_n(0) = 0.01, \dot{Y}_n(0) = 0$ from the stable equilibrium position at $Y_s = +0.0107$, $k = 0.1k_{eff}$, $m_a = 0.5M_t$, and with values of system parameters chosen as in Table 5.1.

Fig. 5.10 shows the time-domain response and Poincare maps of the tip mass and voltage generated for the single harmonic dispersion relation in the strongly nonlinear regime (5.132) with a target value of free wave frequency $\omega = 20$ and spring stiffness

and inerter mass-parameter chosen to be the same as in the linearized regime, i.e., $k = 0.1k_{eff}$, $m_a = 0.5M_t$. To generate the Poincare maps for our unforced system, we plot the points evaluated in the phase space $Y_n(t)$, $\dot{Y}_n(t)$ and $V_n(t)$, $\dot{V}_n(t)$ whenever time t is an integer multiple of $\frac{2\pi}{\omega_n}$, where

$$\omega_n = \sqrt{\frac{K(\mu)}{M_t - r_a(1 - \cos\mu)}} \tag{5.133}$$

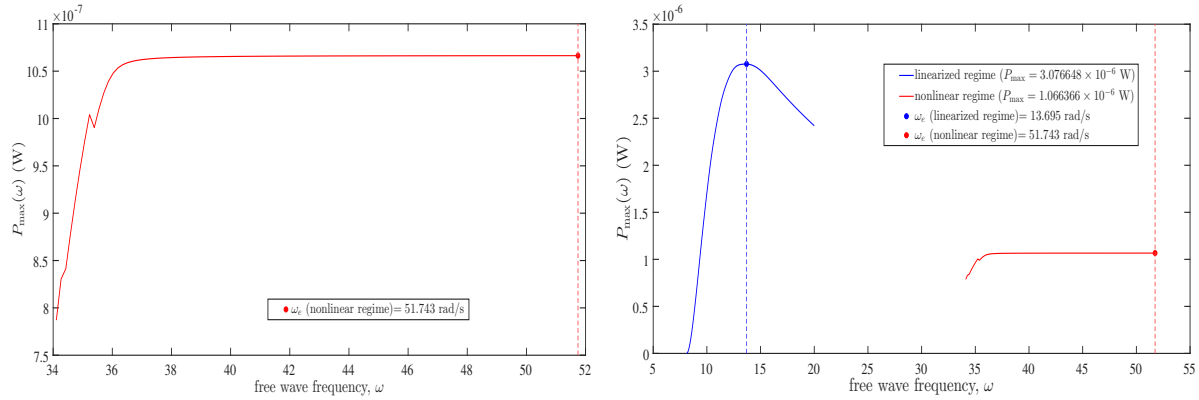
with $\cos\mu$ obtained from the dispersion relation in (5.132).

The tip mass still remains in the potential well at $Y_s = +0.0107$ for the chosen initial perturbation as is evident from Fig. 5.10(a) and the Poincare map in Fig. 5.10(c). The time-domain responses show similar behavior qualitatively with that in the linearized regime in Fig. 5.7 obtained with the same initial perturbation on the tip mass. Though the feasibility constraint to obtain stable transient oscillatory behavior has shifted the input free wave frequency value required from $\omega = 8$ to $\omega = 20$. Later, we will see what this implies in terms of system design parameters in terms of enhanced energy harvesting potential when compared to the linearized model.

Once we get an idea of the dynamic behavior related to intrawell oscillations in the strongly nonlinear regime, we evaluate the maximum power harvested in the steady state as a function of the free wave frequency, considered again as a book-keeping parameter as of now. Since in the general strongly nonlinear regime even for small-amplitude intrawell oscillations, we cannot pose any reduced eigenvalue problem, our previously introduced concept of settling time and hence optimal power constraint criterion cannot be set up in a closed-form in terms of the book-keeping parameter (more colloquially called free wave frequency). Hence, we use the settling time formula derived in (5.110) in the linearized regime to evaluate the maximum steady-state power harvested. We choose the same initial perturbation on the tip mass from the stable equilibrium position at $Y_s = 0.0107$ to generate intrawell oscillations in the strongly nonlinear regime shown in Fig. 5.10(a), as was used for the linearized regime in Fig. 5.7(a), i.e. $u_n(0) = 0.01 \implies Y_n(0) = Y_s + u_n(0) = 0.0207$, $\dot{Y}_n(0) = \dot{u}_n(0) = 0$.

Enhanced energy harvesting potential in terms of design implications

Fig. 5.11(a) shows that, once the intrawell nonlinear branch is evaluated under the admissibility constraints of bounded effective mass and positive effective stiffness, the harvested power no longer exhibits the narrow resonant-type optimum characteristic of the linearized baseline, but instead rises from the low-frequency end of the admissible branch and then approaches a broad quasi-saturated plateau over the remainder of the feasible frequency range. By contrast, Fig. 5.11(b) shows that, for the same structural choice $k = k_{eff}$ and $m_a = 0.1M_t$, the linearized intrawell response attains a distinct optimum at $\omega_e = 13.695$ and then decreases as ω is increased further. The strongly nonlinear regime therefore transforms the response from a sharply tuned operating point into a much wider near-optimal operating band while still maintaining a comparable maximum power magnitude. As it can be seen from the comparison in Fig. 5.11(b), the maximum power harvested for intrawell oscillations in the nonlinear regime is 1.07×10^{-6} W, while the maximum power harvested in the linearized regime is 3.08×10^{-6} W. In the context of enhanced vibration energy harvesting, this is a significant outcome because it indicates that the nonlinear



(a) Power harvested in the general strongly nonlinear intrawell regime ($k = k_{eff}$, $m_a = 0.1M_t$)

(b) Comparison between power harvested in the linearized and nonlinear intrawell regimes ($k = k_{eff}$, $m_a = 0.1M_t$)

Fig. 5.11: Comparison between power harvested in the general strongly nonlinear regime for intrawell oscillations within the stable potential well at $Y_n = +Y_s$ and power harvested in the linearized regime for the same small initial perturbation around the stable equilibrium point at $Y_n = +Y_s$.

piezomagnetoelastic chain can sustain almost constant maximum harvested power, very close to the nonlinear branch's own saturation level, over a substantially broader range of free-wave frequencies, rather than only in the immediate neighborhood of one isolated optimum. However, when the maximum power magnitude is compared, the nonlinear branch shows approximately a three-fold reduction with respect to thelinearized branch. The principal nonlinear benefit is therefore the broader quasi-saturated region close to the nonlinear branch's own maximum, not preservation or enhancement of the sharper linearized peak. This is a bandwidth–peak power trade-off: the appropriate design choice depends on whether peak output or a wider useful operating range is the priority. The broadened plateau alone does not establish a greater total harvested energy for an arbitrary transient input.

In the present implementation, the post-transient extraction window used for the nonlinear intrawell branch (shown in red in Fig. 5.11) is anchored to the linearized baseline through the settling-time estimate developed earlier. Specifically, we take a constant value $t_s = 10.015$, obtained from (5.110) by evaluating the linearized framework at the optimum frequency $\omega = 13.695$ corresponding to the peak power of the linearized blue power curve in Fig. 5.11(b), which has been obtained by using the settling-time formula $t_s(\omega)$ derived in Eq. (5.110) for every swept free-wave frequency ω. In this sense, the linearized intrawell model provides the reference settling-time scale with which the general nonlinear response is evaluated. The resulting red plateau in Fig. 5.11(a) or Fig. 5.11(b) should therefore not be interpreted as an artifact of premature power extraction, but rather as a genuine consequence of the strongly nonlinear branch structure. Equally importantly, this broad nonlinear operating window is obtained while satisfying all admissibility conditions imposed on the reduced branch, so that the response remains inside the selected potential well and does not enter the effective negative-stiffness regime. The broadened high-power band is thus realized without relying on inverted-stiffness dynamics or un-

bounded growth, and remains fully consistent with passive energy harvesting from stable intrawell oscillations.

From a design perspective, the nonlinear plateau admits a direct inverse-map interpretation. The free-wave frequency ω remains a book-keeping parameter, but it is one that is determined implicitly by the structural, inertial, magnetic, and electrical properties of the chain through the corresponding dispersion relation. Consequently, the much wider admissible frequency interval in Fig. 5.11(b) translates directly into a wider set of realizable system-parameter combinations that can deliver essentially saturated harvested power at comparable magnitudes with the linearized regime. This is especially important in the present case because the broadened nonlinear operating regime is obtained simultaneously with an increased/ improved stiffness-to-weight ratio of the static unit cell, achieved here by increasing the spring stiffness from $k = 0.1k_{eff}$ to $k = k_{eff}$ while reducing the inerter-module's mass-parameter from $m_a = 0.5M_t$ to $m_a = 0.1M_t$. Such a shift toward higher stiffness and lower initial auxiliary/design inertia is always desirable in real structural design, since it reduces inertial penalty and material usage while preserving a wide high-performance harvesting window. At the same time, the nonlinearities shift the admissible operating range to higher values of the book-keeping frequency when compared to the linearized baseline, so that the ω-axis itself serves as an inverse design map for selecting improved, wider ranges of system parameters for which high harvested power, intrawell stability, and positive effective stiffness are achieved simultaneously.

5.9 General strongly nonlinear regime – Interwell motions of the tip mass, related wave profile and localized energy harvesting

5.9.1 Quantitative justification for single-mode reduction to study interwell fronts and associated harvesting within the parameter space considered

For the present dimensional parameters listed in Table 5.1, the beam mass is

$$m_b = \rho L w h = 0.616 \text{ g}$$

whereas the attached tip mass is $M_t = 10$ g. The tip mass is therefore approximately 16.2 times larger than the beam mass, so the dominant inertia is concentrated at the tip. Within the admissible mode family used in the reduction, the modal bending stiffness is

$$k_j = EI(2j-1)^4 \frac{\pi^4}{32L^3}$$

Thus, the second-mode stiffness is $k_2/k_1 = 3^4 = 81$. The corresponding bare beam–tip-mass frequencies are

$$\omega_1 = \sqrt{\frac{k_1}{M_t}} = 17.23 \text{ rad s}^{-1}, \ \omega_2 = \sqrt{\frac{k_2}{M_t}} = 155.10 \text{ rad s}^{-1}$$

Including the local magnetic tangent stiffness at $Y = Y_e$ gives approximately

$$\omega_{1,\tan} = 9.27 \text{ rad s}^{-1}, \qquad \omega_{2,\tan} = 154.42 \text{ rad s}^{-1}$$

The second flexural mode therefore remains more than an order of magnitude above the characteristic frequency associated with the front-induced response and the averaging scale used for interwell harvesting analysis in this Section. In addition, the selected potential well displacement satisfies $Y_e/L = 0.1$. (Note: To avoid confusion between the partial derivative of displacement Y with respect to the continuous spatial variable s, which is conventionally denoted by Y_s, throughout the interwell harvesting section, the stable equilibria on either side of the saddle will be denoted by Y_e.) These estimates support use of the first generalized coordinate for the coherent, tip-dominated transition-front dynamics. They do not exclude localized higher-mode excitation during the earliest and most abrupt part of snap-through. A multimode beam model would be required to resolve such short-time details.

The relevant dynamical scales for assessing higher-mode participation are the local first-mode time scale $T_1 = 2\pi/\omega_{1,\tan}$ and the front-passage time $T_f = W/c$ where W and c are the front width and front velocity as will be discussed later in Section 5.9.2. Equivalently, the characteristic response rates are $\omega_{1,\tan}$ and c/W, and the single-mode reduction requires the appreciable response spectrum to remain well separated from the second flexural frequency,

$$\max\left\{\omega_{1,\tan}, \frac{c}{W}\right\} \ll \omega_{2,\tan}$$

For the selected parameters, $\omega_{1,\tan}/\omega_{2,\tan} \simeq 0.060$, while the fitted front-passage rate c/W is smaller still. This frequency-separation criterion is the primary dynamical check on the single-mode approximation. The additional condition $Y_e/L \ll 1$ is a complementary geometric check on the assumed beam kinematics and the neglect of large axial motion; it does not by itself guarantee modal separation.

5.9.2 Continuum limit of the discrete piezomagnetoelastic chain

Long-wavelength limit and inherent dissipative dynamics

We start from the exact discrete equations of motion for the representative n-th unit cell of the periodic piezomagnetoelastic chain shown in Fig. 5.3 with the integer taken as $j = 1$ without loss of generality:

$$\begin{aligned} M_t\ddot{Y}_n + k_{eff}Y_n + k\Big(2Y_n - Y_{n-1} - Y_{n+1}\Big) + 2c_1Y_n \\ +4c_2Y_n^3 - r_a\Big(2\ddot{Y}_n - \ddot{Y}_{n-1} - \ddot{Y}_{n+1}\Big) - \Theta V_n = 0 \end{aligned} \tag{5.134}$$

$$C_p\dot{V}_n + \frac{V_n}{R_l} + \Theta\dot{Y}_n = 0 \tag{5.135}$$

where

$$k_{eff} = \frac{EI\pi^4}{32L^3}, \qquad r_a = \frac{m_a\cos^2\alpha}{2\sin^2\alpha} \tag{5.136}$$

and r_a is defined as the negative-inertance factor.

For long wavelength limit we transform the discrete chain to a continuum model by taking the following assumptions:

1. The periodic chain is uniform, with constant cell spacing ℓ between the centres of adjacent tip masses.

2. The displacement and voltage vary smoothly from cell to cell, so that the wavelength of the propagating disturbance is large enough compared to the cell spacing, i.e. $\ell/\lambda \ll 1$

The discrete variables can therefore be represented by smooth continuum fields

$$Y_n(t) \to Y(s,t), \qquad V_n(t) \to V(s,t), \qquad s = n\ell \tag{5.137}$$

For the periodic chain, the governing physics is more naturally organized by a small set of dimensionless groups than by the dimensional values in (5.8) alone. A convenient set is the scaled well-separation parameter $\beta = (Y_e/L)^2 = -(k_{eff} + 2c_1)/(4c_2L^2)$, which measures the strength of the bi-stability relative to the beam length, the normalized inertance factor $\mu_a = r_a/M_t = m_a \cos^2\alpha/(2M_t \sin^2\alpha)$, the electromechanical time-scale ratio $\tau = (R_l C_p)\sqrt{k/M_t}$, comparing electrical relaxation to the characteristic mechanical time, and the long-wave parameter $\varepsilon_\ell = \ell/\lambda \ll 1$. In this form, interwell nonlinear effects become possible when $\beta > 0$, inertance effects become appreciable when μ_a is not negligible, and electromechanical modulation becomes important when $\tau = O(1)$. The dimensional choice previously in (5.8) can hence be viewed as a representative operating point within the regime $\beta > 0$, $Y_e/L \ll 1$, and $\varepsilon_\ell \ll 1$, so that the unit cell is symmetrically bi-stable, the static well displacement remains small compared with the beam length and is therefore compatible with the single-mode reduction, and the subsequent chain analysis is carried out in the moderate inertial-coupling, broad-front regime relevant to the localized harvesting mechanism studied here.

For the transition-front solution, the natural long-wave parameter is more specifically

$$\varepsilon_\ell = \frac{\ell}{W}, \tag{5.138}$$

where W is the front width. Since a spatial derivative of order m scales as W^{-m}, the ratio between the $O(\ell^4)$ and $O(\ell^2)$ nearest-neighbor corrections scales as

$$\frac{\ell^2}{12W^2} = \frac{\varepsilon_\ell^2}{12}. \tag{5.139}$$

For the fitted front used later in the numerical comparison, $W/\ell = 3.717$, giving an estimated relative fourth-order correction of 0.006. This provides an a posteriori check of the leading long-wavelength truncation for the chosen parameter set.

Taylor series expansions are retained up to $O(\ell^4)$ to preserve the leading dispersive corrections. The corresponding long-wave approximation truncated at $O(\ell^2)$ is then obtained as a special case. Using Taylor series expansion about the point $s = n\ell$, we write the tip mass displacement of adjacent unit cells as:

$$\begin{aligned} Y_{n\pm1}(t) = Y(s \pm \ell, t) = Y \pm \ell Y_s + \frac{\ell^2}{2} Y_{ss} \pm \frac{\ell^3}{6} Y_{sss} \\ + \frac{\ell^4}{24} Y_{ssss} + O(\ell^5) \end{aligned} \tag{5.140}$$

and similarly

$$\begin{aligned} \ddot{Y}_{n\pm1}(t) = Y_{tt}(s \pm \ell, t) = Y_{tt} \pm \ell Y_{stt} + \frac{\ell^2}{2} Y_{sstt} \pm \frac{\ell^3}{6} Y_{ssstt} \\ + \frac{\ell^4}{24} Y_{sssstt} + O(\ell^5) \end{aligned} \tag{5.141}$$

where subscripts denote partial differentiation with respect to the corresponding variables.

Hence, the discrete nearest-neighbor combinations become

$$2Y_n - Y_{n-1} - Y_{n+1} = -\ell^2 Y_{ss} - \frac{\ell^4}{12} Y_{ssss} + O(\ell^6) \tag{5.142}$$

and

$$2\ddot{Y}_n - \ddot{Y}_{n-1} - \ddot{Y}_{n+1} = -\ell^2 Y_{sstt} - \frac{\ell^4}{12} Y_{ssstt} + O(\ell^6) \tag{5.143}$$

Substituting (5.142) and (5.143) into (5.134), the continuum limit of the mechanical equation is obtained as

$$\begin{aligned} M_t Y_{tt} + r_a \ell^2 Y_{sstt} + \frac{r_a \ell^4}{12} Y_{ssstt} - k\ell^2 Y_{ss} - \frac{k\ell^4}{12} Y_{ssss} \\ + \big(k_{eff} + 2c_1\big) Y + 4c_2 Y^3 - \Theta V = 0 \end{aligned} \tag{5.144}$$

Since the electrical equation (5.135) contains no intercellular coupling terms, its continuum counterpart retains the same local form

$$C_p V_t + \frac{V}{R_l} + \Theta Y_t = 0 \tag{5.145}$$

Hence, the continuum electromechanical model corresponding to the discrete chain is given by Eqs. (5.144) and (5.145). Eq. (5.144) may be interpreted as a generalized nonlinear dispersive Klein–Gordon/Boussinesq type equation with additional mixed spatio-temporal inertia terms induced by the inertial coupling, and locally coupled to the electrical field $V(s,t)$.

If only the leading long-wavelength terms are retained, i.e. neglecting $O(\ell^4)$ corrections, then (5.144) reduces to

$$\begin{aligned} M_t Y_{tt} + r_a \ell^2 Y_{sstt} - k\ell^2 Y_{ss} + \big(k_{eff} + 2c_1\big) Y \\ + 4c_2 Y^3 - \Theta V = 0 \end{aligned} \tag{5.146}$$

together with

$$C_p V_t + \frac{V}{R_l} + \Theta Y_t = 0 \tag{5.147}$$

Eqs. (5.144)–(5.147) provide the continuum limit, long-wavelength approximation for analyzing large-amplitude interwell wave motion, including transition fronts and soliton-like wave propagation, in the strongly nonlinear piezomagnetoelastic chain. Eq. (5.146) gives us a nonlinear regularized wave equation, with an underlying hyperbolic Klein–Gordon core, in terms of displacement variable $Y(s,t)$ and involving an electromechanical coupling paremeter Θ, considering that the intercellular springs are of a hardening nature with $k > 0$.

In its exact form, we seek traveling wave solutions of the strongly nonlinear equation (5.146) in the form

$$Y(s,t) = Y(s - vt) = Y(z) \tag{5.148}$$

where v is the velocity of wave propagation in the periodic chain and $z = s - vt$ being a reduced variable. Substituting (5.148) in (5.146) and (5.147) gives

$$\begin{aligned} (M_t v^2 - k\ell^2) Y_{zz} + r_a \ell^2 v^2 Y_{zzzz} + \big(k_{eff} + 2c_1\big) Y \\ + 4c_2 Y^3 - \Theta V = 0 \end{aligned} \tag{5.149}$$

$$vC_pV_z - \frac{V}{R_l} + v\Theta Y_z = 0 \tag{5.150}$$

For convenience, we introduce the notation

$$A_v = M_t v^2 - k\ell^2, B_v = r_a \ell^2 v^2, a_0 = k_{eff} + 2c_1, b_0 = 4c_2 \tag{5.151}$$

Then Eq. (5.149) takes the compact form

$$B_v Y_{zzzz} + A_v Y_{zz} + a_0 Y + b_0 Y^3 - \Theta V = 0 \tag{5.152}$$

Although the direct first integral does not exist for (5.152) unlike a conventional φ^4 problem [202] because of the existence of the fourth order leading term in derivative of z induced by our choice of the inertially coupled model and the existence of the coupling term ΘV representing distributed electrical dissipation, multiplying Eq. (5.152) by Y_z still yields a useful pseudo-energy balance. Indeed, we obtain

$$B_v Y_{zzzz} Y_z + A_v Y_{zz} Y_z + a_0 Y Y_z + b_0 Y^3 Y_z - \Theta V Y_z = 0 \tag{5.153}$$

The first four terms can be written as total derivatives with respect to z as

$$A_v Y_{zz} Y_z = \frac{d}{dz}\left(\frac{A_v}{2} Y_z^2\right) \tag{5.154}$$

$$a_0 Y Y_z = \frac{d}{dz}\left(\frac{a_0}{2} Y^2\right) \tag{5.155}$$

$$b_0 Y^3 Y_z = \frac{d}{dz}\left(\frac{b_0}{4} Y^4\right) \tag{5.156}$$

$$B_v Y_{zzzz} Y_z = \frac{d}{dz}\left[B_v\left(Y_{zzz} Y_z - \frac{1}{2} Y_{zz}^2\right)\right] \tag{5.157}$$

Hence, we obtain

$$\begin{aligned} \frac{d}{dz}\Bigg[&\frac{A_v}{2} Y_z^2 + B_v\left(Y_{zzz} Y_z - \frac{1}{2} Y_{zz}^2\right) \\ &+ \frac{a_0}{2} Y^2 + \frac{b_0}{4} Y^4\Bigg] - \Theta V Y_z = 0 \end{aligned} \tag{5.158}$$

The coupling term can be re-expressed by using the traveling-wave electrical equation (5.150). From

$$v\Theta Y_z = \frac{V}{R_l} - vC_pV_z \tag{5.159}$$

it follows that

$$-\Theta V Y_z = -\frac{V^2}{vR_l} + C_p V V_z = -\frac{V^2}{vR_l} + \frac{d}{dz}\left(\frac{C_p}{2} V^2\right) \tag{5.160}$$

Substituting (5.160) into (5.158) gives the pseudo-energy balance law

$$\begin{aligned} \frac{d}{dz}\Bigg[&\frac{A_v}{2} Y_z^2 + B_v\Big(Y_{zzz} Y_z - \frac{1}{2} Y_{zz}^2\Big) + \frac{a_0}{2} Y^2 \\ &+ \frac{b_0}{4} Y^4 + \frac{C_p}{2} V^2\Bigg] = \frac{V^2}{vR_l} \end{aligned} \tag{5.161}$$

for a traveling wave propagating with $v > 0$ in the positive (considered left to right) axial direction of the periodic chain. This balance law immediately shows that an exact nontrivial constant-speed passive heteroclinic front between two symmetric energy wells is not admissible. Suppose that the wave propagating medium extends to $\pm\infty$ and that in an initial state all the tip masses are at their initial positive static equilibrium position $+Y_e$ and after the wave has propagated through the chain, all the tip masses have snapped to their other negative stable equilibrium branch at $-Y_e$. Without loss of generality and using appropriate normalization, the bi-stable potential well can always be chosen to be symmetrically oriented around the unstable local maxima in the middle at $Y = 0$. Also, assuming that energy harvesting through the piezoelectric harvester is achievable only during wave propagation and not before or after it, considering the dissipative electromechanical nature of the system dynamics, we obtain:

$$Y(-\infty) = +Y_e, \qquad Y(+\infty) = -Y_e \tag{5.162}$$

with

$$Y_z,\, Y_{zz},\, Y_{zzz},\, V \to 0 \qquad \text{as} \qquad z \to \pm\infty \tag{5.163}$$

and where Y_e is one of the two stable non-zero equilibria of the symmetric double-well potential. Integrating (5.161) over the whole real line yields

$$\left[\frac{a_0}{2}Y^2 + \frac{b_0}{4}Y^4\right]_{-\infty}^{+\infty} = \frac{1}{vR_l}\int_{-\infty}^{\infty} V^2(z)\,dz \tag{5.164}$$

Since the two wells of the symmetric bi-stable potential have equal energy, the left hand side of Eq. (5.164) goes to zero identically, whereas the right hand side is non-negative and is strictly positive unless $V \equiv 0$. Therefore, a nontrivial exact constant-speed heteroclinic front connecting the two equal wells cannot exist in the passive electromechanical chain. In other words, the relevant interwell wavefront in our system is not an exact conservative kink, but a decelerating or modulated transition front, unless an asymmetry between the wells or an additional external energy supply is introduced.

To characterize admissible traveling-wave tails, we can linearize the coupled traveling-wave system about one of the stable equilibria $Y_e = \pm\sqrt{-\frac{\left(k_{eff}+2c_1\right)}{4c_2}}$. Writing

$$Y(z) = Y_e + \eta(z), \quad V(z) = \nu(z), \quad |\eta| \ll 1, \quad |\nu| \ll 1 \tag{5.165}$$

and introducing the local tangent stiffness

$$K_t = k_{eff} + 2c_1 + 12c_2Y_e^2 \tag{5.166}$$

gives the linearized traveling-wave equations

$$B_v\eta_{zzzz} + A_v\eta_{zz} + K_t\eta - \Theta\nu = 0 \tag{5.167}$$

$$vC_p\nu_z - \frac{\nu}{R_l} + v\Theta\eta_z = 0 \tag{5.168}$$

Seeking normal-mode solutions of the form

$$\eta(z) = \hat{\eta}e^{\lambda z}, \qquad \nu(z) = \hat{\nu}e^{\lambda z} \tag{5.169}$$

leads to the algebraic system

$$\left(B_v\lambda^4 + A_v\lambda^2 + K_t\right)\hat{\eta} - \Theta\hat{\nu} = 0 \tag{5.170}$$

$$v\Theta\lambda\hat{\eta} + \left(vC_p\lambda - \frac{1}{R_l}\right)\hat{\nu} = 0 \tag{5.171}$$

and therefore the spatial characteristic equation

$$\left(B_v\lambda^4 + A_v\lambda^2 + K_t\right)\left(vC_p\lambda - \frac{1}{R_l}\right) + v\Theta^2\lambda = 0 \tag{5.172}$$

Eq. (5.172) determines the spatial eigenvalues of the traveling-wave system and hence classifies whether the front tails are monotone or oscillatory and whether localized front-type profiles are admissible for a given wave speed v and parameter set. Here, spatial eigenvalue refers to exponential evolution with respect to the co-moving spatial coordinate $z = s - vt$. The mode $e^{\lambda z}$ grows or decays in space in that frame. A localized front requires roots with $\mathrm{Re}\,\lambda < 0$ for decay as $z \to +\infty$ and roots with $\mathrm{Re}\,\lambda > 0$ for decay as $z \to -\infty$. Real nonzero roots produce monotone exponential tails, whereas complex roots with nonzero real part produce oscillatory decaying tails. Roots with $\mathrm{Re}\,\lambda = 0$ do not decay and therefore do not generate localized tails. In particular, $\lambda = 0$ is not a root in the present finite-load problem because substitution into equation (5.172) gives $-K_t/R_l \neq 0$ for $K_t > 0$ and $0 < R_l << \infty$.

Analytical leading-order wave profile

In our electromechanically damped chain, the large-amplitude interwell traveling-wave problem is naturally reformulated as a non-conservative spatial dynamical system with distributed electrical dissipation, rather than as a conservative quadrature problem or more specifically called a φ^4 problem in field theory as considered in [38] or other existing literature. So, since an exact constant-speed front does not exist for our dissipative periodic chain, we make a slowly modulated front ansatz for the traveling wave. We therefore consider a slowly modulated interwell front connecting the two stable branches

$$Y_e = \pm\sqrt{-\frac{a_0}{b_0}} = \pm\sqrt{-\frac{k_{eff} + 2c_1}{4c_2}} \tag{5.173}$$

where $a_0 = k_{eff} + 2c_1$ and $b_0 = 4c_2$, and seek a right-running front in the form

$$Y(s,t) \approx Y_K(\xi)\,, \qquad V(s,t) \approx V_K(\xi)\,, \qquad \xi = \frac{s - X(t)}{W(t)} \tag{5.174}$$

where $X(t)$ is the front center, $c(t) = \dot{X}(t)$ is the instantaneous front speed, and $W(t)$ is the slowly varying front width. We assume that the front modulation is slow in the sense that

$$\frac{\dot{W}}{c} = O(\varepsilon_m), \qquad \frac{W\ddot{X}}{c^2} = O(\varepsilon_m), \qquad \frac{W\ddot{W}}{c^2} = O(\varepsilon_m) \qquad 0 < \varepsilon_m \ll 1 \tag{5.175}$$

Using (5.174), the reduced variable satisfies

$$\xi_s = \frac{1}{W}, \qquad \xi_t = -\frac{c + \dot{W}\,\xi}{W} \tag{5.176}$$

Hence, to leading order in the slow-modulation parameter ε_m, we obtain

$$Y_t = -\frac{c}{W}Y_K' + O(\varepsilon_m) \tag{5.177}$$

$$Y_{tt} = \frac{c^2}{W^2} Y_K'' + O(\varepsilon_m) \tag{5.178}$$

$$Y_{ss} = \frac{1}{W^2} Y_K'' \tag{5.179}$$

$$Y_{sstt} = \frac{c^2}{W^4} Y_K^{(4)} + O(\varepsilon_m) \tag{5.180}$$

and similarly

$$V_t = -\frac{c}{W} V_K' + O(\varepsilon_m) \tag{5.181}$$

where prime now denotes differentiation with respect to ξ.

Substituting (5.177)–(5.181) into the leading-order continuum equations (5.146) and (5.147), and neglecting terms of order $O(\varepsilon_m)$, gives the quasi-steady profile equations

$$\frac{r_a \ell^2 c^2}{W^4} Y_K^{(4)} + \frac{M_t c^2 - k\ell^2}{W^2} Y_K'' + a_0 Y_K + b_0 Y_K^3 - \Theta V_K = 0 \tag{5.182}$$

$$-\frac{c C_p}{W} V_K' + \frac{V_K}{R_l} - \frac{c\Theta}{W} Y_K' = 0 \tag{5.183}$$

For a broad front, $W \gg \ell$, the fourth-order dispersive term in (5.182) is asymptotically smaller than the second-order term, while in the weak electromechanical-coupling limit the front shape is determined at leading order by the mechanical balance

$$\frac{M_t c^2 - k\ell^2}{W^2} Y_K'' + a_0 Y_K + b_0 Y_K^3 = 0 \tag{5.184}$$

Since $a_0 < 0$ and $b_0 > 0$ in the bi-stable regime, equation (5.184) admits the φ^4-type kink profile [202] given by

$$Y_K(\xi) = Y_e \tanh \xi \tag{5.185}$$

provided the width-speed relation

$$W^2 = \frac{2\big(M_t c^2 - k\ell^2\big)}{a_0} = \frac{2\big(k\ell^2 - M_t c^2\big)}{|a_0|} \tag{5.186}$$

is satisfied. Since $a_0 < 0$, the requirement $W^2 > 0$ yields the subsonic condition for the wave speed.

$$c^2 < \frac{k\ell^2}{M_t} \tag{5.187}$$

Thus, in the broad-front regime, the theoretical front is a slowly modulated φ^4 kink whose width depends on the instantaneous propagation speed through (5.186). Substituting (5.185) into (5.183) gives the slaved voltage profile

$$V_K' - \Gamma V_K = -\frac{\Theta}{C_p} Y_K' \tag{5.188}$$

with

$$\Gamma = \frac{W}{c R_l C_p} \tag{5.189}$$

Since

$$Y_K'(\xi) = Y_e \operatorname{sech}^2 \xi \tag{5.190}$$

the formal solution of (5.188) is

$$V_K(\xi) = e^{\Gamma\xi}\left[C_V - \frac{\Theta Y_e}{C_p}\int_{\xi_0}^{\xi} e^{-\Gamma\eta}\,\mathrm{sech}^2\,\eta\,d\eta\right] \tag{5.191}$$

where C_V is a constant of integration determined by the asymptotic condition imposed on the traveling front. By choosing an appropriate boundedness condition as $\xi \to +\infty$, the exponentially growing homogeneous part represented by $e^{\Gamma\xi}C_V$ can always be removed for a stable voltage solution.

Eqs. (5.185), (5.186), and (5.191) define the leading-order theoretical interwell wavefront in the electromechanically damped chain. The front is therefore not an exact conservative kink of fixed speed, but a quasi-steady topological front whose shape is inherited from the underlying bi-stable mechanical potential while its speed, width, and electrical signature are modulated by the electromechanical extraction and the inertial coupling.

A reduced evolution law for the front modulation may now be obtained by combining the pseudo-energy balance (5.161) with the modulated-front ansatz (5.174). Introducing the front energy functional

$$\begin{aligned}\mathcal{E}_f[c,W] = \int_{-\infty}^{\infty}\Bigg[&\frac{M_t c^2}{2W}\big(Y_K'\big)^2 + \frac{r_a\ell^2c^2}{2W^3}\big(Y_K''\big)^2 + \frac{k\ell^2}{2W}\big(Y_K'\big)^2\\ &+W\left(\frac{a_0}{2}Y_K^2 + \frac{b_0}{4}Y_K^4 - \frac{a_0}{2}Y_e^2 - \frac{b_0}{4}Y_e^4\right) + \frac{C_pW}{2}V_K^2\Bigg]\,d\xi\end{aligned} \tag{5.192}$$

the leading-order electromechanical energy balance takes the form

$$\frac{d}{dt}\mathcal{E}_f[c(t),W(t)] = -\frac{W(t)}{R_l}\int_{-\infty}^{\infty} V_K^2(\xi;c,W)\,d\xi \tag{5.193}$$

Hence, after substituting the width-speed relation (5.186), one obtains the reduced modulation equation

$$\frac{d\mathcal{E}_f}{dc}\,\dot{c} = -\frac{W(c)}{R_l}\int_{-\infty}^{\infty} V_K^2(\xi;c)\,d\xi \tag{5.194}$$

which shows that the passive electrical extraction necessarily decelerates the interwell front as it propagates through the chain. Therefore, the large-amplitude interwell solitary response in the present electromechanical system is more accurately described as a slowly modulated or decelerating topological front rather than as an exact conservative soliton of constant speed.

It is useful to emphasize that the propagating object studied here is not a conservative one-parameter soliton family parameterized by a freely varying amplitude. In the present bi-stable chain, the front connects the two stable branches $\pm Y_e$, so its jump amplitude is set primarily by the well separation, whereas the dynamically relevant quantities are its instantaneous width and propagation speed. For this reason, the reduced theory naturally yields the width-speed relation in (5.186), together with the modulation law in Eq. (5.194), rather than a unique amplitude-speed law of conservative soliton type. This distinction is a direct consequence of the passive electromechanical dissipation. As the front transfers mechanical energy into the electrical circuit, its speed cannot remain uniform during propagation, even though its kink-like interwell structure is preserved to leading order. The objective of this interwell study is therefore not a full dynamical tax-

onomy of solitary waves, but the characterization of the front structure most relevant to energy conversion. In that sense, the asymptotic comparison already adopted is the natural analytical reference for the present system. In the broad front limit the mechanical core reduces to the φ^4-type kink profile in (5.185), while the departures from the conservative φ^4 setting are precisely the physically important ingredients here, namely inertance-induced higher order dispersion and electromechanical dissipation.

5.9.3 Parametric plotting to compare with numerical results

Wave fronts

For comparison of our theoretical model to numerical simulations (Fig. 5.12), we consider a finite chain consisting of 100 unit cells with both ends free at all times. We consider all the masses in the chain to be at the initial static equilibrium position within the potential well at $Y = +Y_e$. We impose on the first mass in the chain a velocity sufficiently high for it to snap to its other stable branch at $Y = -Y_e$ to generate free wave motion in the chain in its interwell regime. The spring stiffness is considered to be $k = k_{eff}$ and the inerter mass-parameter is considered to be $m_a = 0.1M_t$ with other parameter values chosen as in Table 5.1. The simulation is run for 80 seconds using the explicit RK4 `ode45` solver in Matlab.

The numerical model is the original finite discrete system, equations (5.134) and (5.135), integrated simultaneously in time-domain for $n = 1, \ldots, N$ where $N = 100$ and the continuum equations are used only for the analytical approximation. All numerical finite-chain integrations used in the comparison plots were computed with tolerance values of `RelTol`$= 10^{-10}$ and `AbsTol`$= 10^{-10}$. The finite size can influence late-time reflected waves and the tails near the free boundaries. For the representative case, $L_{\text{chain}} = (N-1)\ell = 99\ell$ and $W = 3.717\ell$, so the chain contains approximately 26.6 front widths. The analytical comparisons are therefore restricted to intervals for which the primary front core remains in the chain interior. Reflected and end-generated components are retained in the exact finite-chain simulation but are not part of the infinite-domain front approximation.

It is important in this scenario to distinguish the absence of sustained forcing from the absence of supplied energy. The velocity imposed on the first mass is a prescribed initial-value trigger that supplies the finite energy required to cross the magnetic potential barrier. Once the initial state has been specified, however, the finite chain evolves autonomously, with no time-dependent external force or base excitation. Let

$$\mathbf{Y} = (Y_1, \ldots, Y_N)^{\mathrm{T}}$$

and let $\mathbf{L}_f$ denote the free-end discrete nearest-neighbor Laplacian. The inertially coupled mass matrix is

$$\mathbf{M}_f = M_t\mathbf{I} - r_a\mathbf{L}_f$$

The mechanical and electrically stored energies of the finite chain are given by

$$\begin{aligned}\mathcal{E}_{\mathrm{m}}(t) = \frac{1}{2}\dot{\mathbf{Y}}^{\mathrm{T}}\mathbf{M}_f\dot{\mathbf{Y}} + \sum_{n=1}^{N}\left(\frac{a_0}{2}Y_n^2 + c_2Y_n^4\right) \\ + \frac{k}{2}\sum_{n=1}^{N-1}(Y_{n+1}-Y_n)^2\end{aligned} \tag{5.195}$$

and

$$\mathcal{E}_{\mathrm{e}}(t) = \frac{C_p}{2}\sum_{n=1}^{N}V_n^2(t) \tag{5.196}$$

where $a_0 = k_{eff} + 2c_1$. Multiplication of the discrete mechanical equations (5.134) by $\dot{Y}_n$ and of the electrical equations (5.135) by V_n, followed by summation over the chain, gives

$$\frac{d}{dt}\left(\mathcal{E}_{\mathrm{m}} + \mathcal{E}_{\mathrm{e}}\right) = -\sum_{n=1}^{N}\frac{V_n^2}{R_l} \tag{5.197}$$

Consequently, the total energy delivered to the electrical loads or in other words the harvested energy is obtained as

$$E_{\mathrm{harv}}(t) = \int_0^t \sum_{n=1}^{N}\frac{V_n^2(\tau)}{R_l}\,d\tau \tag{5.198}$$

The reference equilibrium energy is

$$\mathcal{E}_{\mathrm{eq}} = N\left(\frac{a_0}{2}Y_e^2 + c_2Y_e^4\right) \tag{5.199}$$

corresponding to all masses at $+Y_e$, with zero velocity and voltage. The initial excess supplied energy is therefore

$$E_{\mathrm{in}} = \mathcal{E}_{\mathrm{m}}(0) + \mathcal{E}_{\mathrm{e}}(0) - \mathcal{E}_{\mathrm{eq}} \tag{5.200}$$

For the present initial condition, in which only the first mass at the free end has velocity v_0, this reduces to

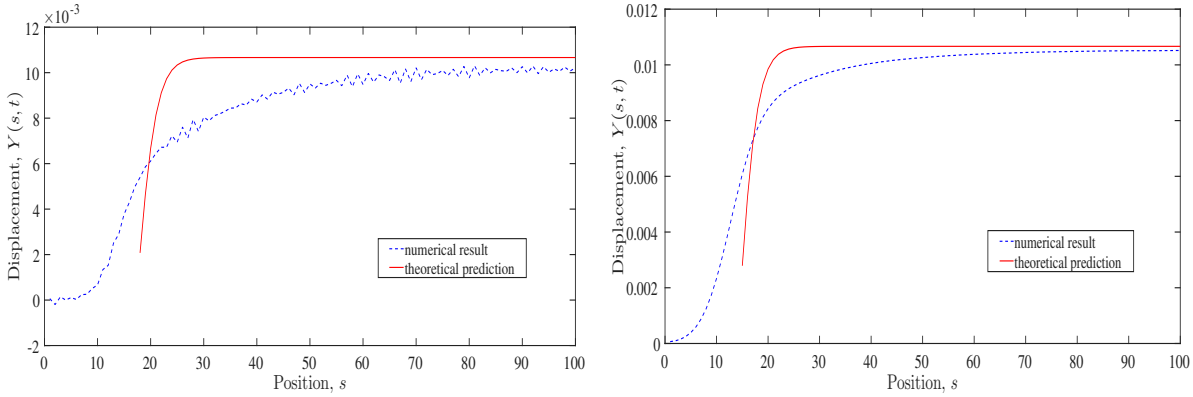
$$E_{\mathrm{in}} = \frac{1}{2}(M_t - r_a)v_0^2 \tag{5.201}$$

With $v_0 = 40\ \mathrm{m\,s^{-1}}$, the initial supplied energy is $E_{\mathrm{in}} = 6.80$ J. At the end of the 80 s simulation, the corresponding values of harvested energy and conversion ratio were obtained as

$$E_{\mathrm{harv}} = 6.799\ \mathrm{J}, \qquad \eta_E = \frac{E_{\mathrm{harv}}}{E_{\mathrm{in}}} = 0.999,$$

with a relative energy-balance residual of 5.945×10^{-6}. Because the resistive loads are the only irreversible loss mechanism included in the model, η_E is an idealized model-level conversion ratio rather than a prediction of the efficiency of a practical harvester containing mechanical, dielectric, and power-electronic losses.

The small perturbations in the numerical solution with respect to the theoretical prediction in Fig. 5.12(a) are caused due to discreteness effects [203]. The numerical front appears broader than the leading theoretical core because the discrete solution contains lattice-scale dispersion, radiated wavetrains, electromechanical feedback on the front



(a) Tip mass displacement in each unit cell plotted with unit-cell index n along the chain taken at time $t = 30$ seconds

(b) Tip mass displacement in each unit cell plotted with unit-cell index n along the chain taken at time $t = 50$ seconds

Fig. 5.12: Comparison of the theoretically predicted wavefront with numerically determined wave profile, for plotting the wave profile across the chain snapshots are taken at $t = 30$ seconds and $t = 50$ seconds (for parameters: $\ell = 1$, left-boundary scaled coordinates $\xi_L(t = 30 \text{ seconds}) = -4.3759$ and $\xi_L(t = 50 \text{ seconds}) = -3.4983$ which are alignment shifts associated with the two snapshot times and not additional physical parameters of the model, $Y_e = 0.0107$).

shape, and slow variation of its speed and width. These effects are omitted from the broad-front, weak-coupling φ^4 approximation. The theoretical profile is therefore intended to describe the coherent front core rather than the complete finite-chain waveform. Moreover, the theoretical far-field values are asymptotic infinite-domain equilibria, whereas the curves in Fig. 5.12 are finite-time snapshots. Small precursor waves, residual intrawell oscillations, and free-end effects consequently make the numerical value near $s = 100$ differ slightly from Y_e at the reported times.

For our dissipative chain, the propagating wave should be interpreted not as an exact conservative soliton, but as a kink-like, slowly modulated transition front which approaches asymptotically in time the leading order core captured by the reduced φ^4 type profile derived in Section 5.9.2. In contrast to conservative bi-stable chains considered previously, the present piezomagnetoelastic chain is intrinsically dissipative due to the electromechanical shunt, and therefore the large-amplitude interwell wave is not expected to evolve into an exact constant-speed heteroclinic soliton that switches the chain permanently from one stable branch to the other. Instead, the numerical results show a transient topological like front which induces barrier crossing and propagates through the chain (Fig. 5.12(a)), but leaves behind a decaying relaxation tail as energy is continuously extracted into the electrical domain. In this sense, the relevant nonlinear wave object in the present system is a damped or quasi-solitonic transition front rather than a conservative soliton. For this reason, the long integration window (Fig. 5.12(b)) is retained to characterize the full dissipative evolution and energy conversion process, whereas the front profile comparison with theory is performed at an earlier time snapshot, when the front core is still in the interior of the chain and before the post-front relaxation has collapsed the excited cells back toward the neighborhood of the saddle at $Y = 0$.

Throughout this section we intentionally restrict attention to the primary front regime,

namely to time windows for which the interwell front remains in the interior of the chain and the core dynamics are not governed by interactions with waves reflected from the boundaries. Accordingly, front-front and front-reflection collision dynamics are not pursued here, since the present work is concerned with the enhanced and spatially localized energy harvesting generated by the primary dissipative transition front.

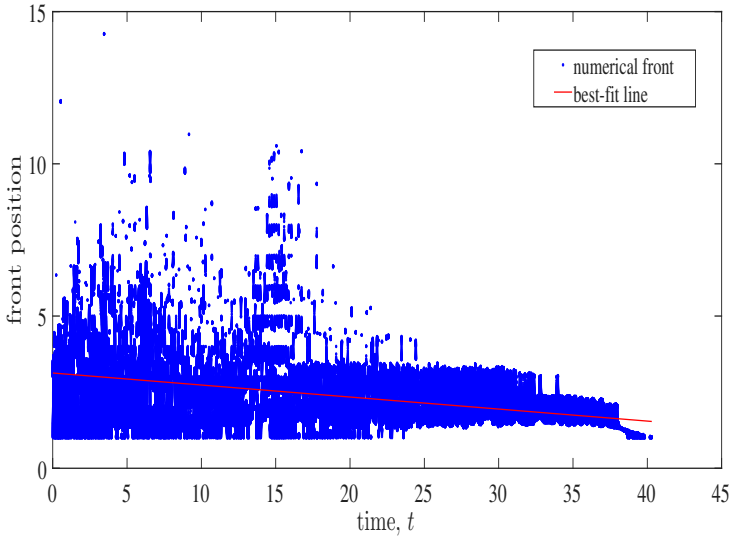


Fig. 5.13: Transition-front position vs time, extracted from the numerical $Y = 0$ crossing. The red line shows the least-squares fit used to estimate the representative averaged propagation speed.

The front position shown in Fig. 5.13, is extracted from the finite-chain simulation as the interpolated spatial location at which the displacement crosses the saddle value $Y = 0$, separating the switched branch behind the front from the unswitched branch ahead of it. The resulting trajectory is not interpreted as an exact constant-speed characteristic. Rather, its scatter and departure from an ideal straight line are consistent with the dissipative, slowly modulated nature of the interwell transition front. The blue points in Fig. 5.13 are raw deterministic front-position samples, not ensemble data. No ensemble averaging and no temporal averaging are applied to the plotted points. Their scatter reflects discrete cell switching and fast local oscillations superposed on the slowly varying front. The red line is a least-squares fit over the selected primary-front interval and its slope is used as a representative average propagation speed in the leading-order quasi-steady profile.

The preservation of a kink-like core at the two time-snapshots in Fig. 5.12, together with the gradual nonlinearity of the front-position trajectory in Fig. 5.13, provides a consistency check for slow modulation of the front speed and width. We do not interpret these observations as a pointwise validation of the complete reduced modulation equation for $c(t)$ and $W(t)$.

For a direct comparison of the numerical wave profile with the theoretical leading-order solution obtained in (5.185) satisfying the width-speed relation in (5.186), a least-squares fit to a substantial interior portion of the primary-front trajectory, before boundary effects become significant, is used to obtain a representative propagation speed as mentioned before. This fitted trajectory is shown by the red line in Fig. 5.13. Substituting this averaged

speed in the theoretical solution shows a good agreement in the asymptotic limit with the numerical wave profile as shown in Fig. 5.12, which confirms the adequacy of the theoretical leading-order prediction. This fitted, averaged propagation speed obtained from the numerical front will also be used for the voltage and power comparison henceforth.

We now compare the theoretical voltage model obtained in equation (5.191) to numerical simulations. Since the direct numerical voltage obtained from the finite nonlinear chain contains fast carrier oscillations, local radiative contributions, and boundary-reflected components superposed on the coherent electromechanical signal generated by the propagating front, a pointwise comparison with the reduced theoretical voltage profile is not insightful. For this reason, we compare the theoretical prediction with the envelope of the numerical voltage, which filters out the rapidly oscillating carrier content and retains the slowly varying front-induced amplitude that is captured by the asymptotic traveling-wave theory.

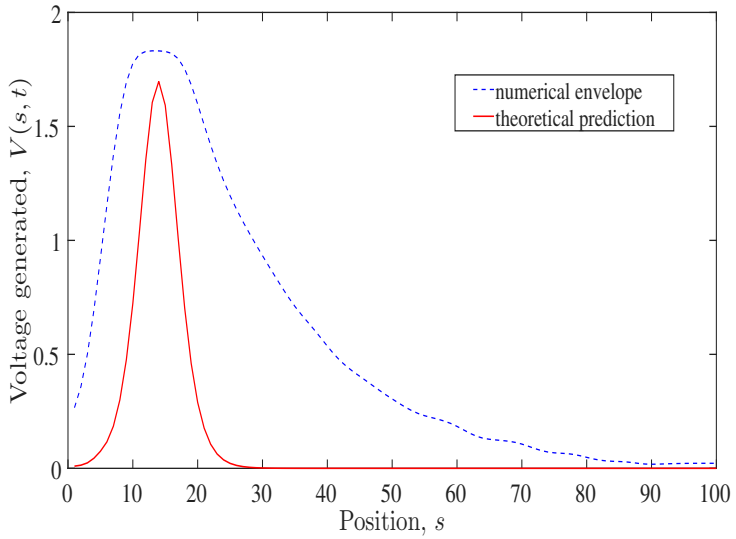


Fig. 5.14: Comparison of the theoretically predicted voltage model with numerically determined voltage envelope (for parameters $\ell = 1$, $\xi_0 = -3.4983$, $Y_e = 0.0107$), for plotting the voltage profile across the chain a snapshot is taken at $t = 50$ seconds.

For comparison of the theoretical voltage front with numerical finite-chain results (Fig. 5.14), Eq. (5.188) was not evaluated directly through its formal integral representation because, over a finite comparison window, the factor $e^{\Gamma\xi}$ in the closed-form solution (5.191) can become numerically ill-conditioned when $\Gamma > 0$, thereby amplifying round-off and producing spurious overflow or underflow even though the physically relevant bounded solution remains finite. To avoid this practical difficulty in finite models, we imposed the boundedness condition in the far-field asymptotic state ahead of the propagating front and solved Eq. (5.188) backward in ξ by a backward Euler marching scheme. This procedure is numerically stable for the present first-order linear equation, preserves the decaying character of the bounded voltage solution, and yields a compact front-localized profile that can be compared directly with the envelope of the numerical voltage. In this way, the theoretical voltage prediction captures the coherent electromechanical signature of the interwell front without contamination from the exponentially ill-conditioned homogeneous contribution.

The slightly apparent deviation of the numerical envelope from the equilibrium voltage $V = 0$ near $s = 100$ in Fig. 5.14 is a finite-time, finite-chain effect rather than a nonzero electrical equilibrium. The free-end region contains small precursor and reflected wave components, and the finite electrical time constant $R_l C_p$ preserves voltage for a short interval after local mechanical motion. These contributions decay under the electrical equation so that $V_n \to 0$ as $t \to \infty$. The theoretical profile instead imposes $V \to 0$ in the infinite-domain far-field state, and the comparison is intended primarily for the interior front-generated voltage signature.

Energy harvested through free wave propagation

Building on the front profile and voltage envelope comparisons in Section 5.9.3, we quantify the harvested output directly from the electrical response of each unit cell. For the finite-chain simulation, the numerical voltage history $V_n(t)$ obtained from the direct time integration is converted to the instantaneous electrical power $p_n(t) = V_n^2(t)/R_l$. The harvested energy over one observation window of duration $T = 2\pi/\omega_T$ is then defined as

$$E_n(t_0) = \int_{t_0}^{t_0+T} \frac{V_n^2(t)}{R_l}\, dt$$

where $\omega_T = \sqrt{\frac{K_t}{M_t}}$ is a frequency defined from the local tangent stiffness $K_t = k_{eff} + 2c_1 + 12c_2 Y_e^2$ and the corresponding average power is obtained as $\bar{P}_n(t_0) = E_n(t_0)/T$. The post-transient harvested output at the n-th cell is taken as the maximum of this one-cycle average over all admissible windows with $t_0 \geq t_s$ where t_s is a wait time based on observations. The theoretical counterpart is constructed exactly the same manner, except that the full voltage signal is replaced by the composite front envelope prediction obtained in Section 5.9.3 from the bounded front core solution together with the post-front RC tail. Thus,

$$E_n(t_0) = \int_{t_0}^{t_0+T} \frac{V_{n,}^2(t)}{R_l}\, dt, \qquad \bar{P}_n(t_0) = \frac{E_n(t_0)}{T}$$

and the same maximization over $t_0 \geq t_s$ is used to compare theory and numerical simulation on a cell-by-cell basis.

To present the results in a physically transparent and unit-independent manner, the averaged powers are reported in scaled form by using the natural voltage scale $V_0 = |\Theta Y_e/C_p|$ associated with the interwell front and the corresponding natural power scale $P_0 = V_0^2/R_l$. The plotted quantity is therefore the average scaled power $\tilde{P} = \bar{P}/P_0$. This normalization removes the trivial dependence on the absolute voltage level and resistor value, and highlights instead how efficiently the propagating nonlinear front redistributes harvestable electrical output along the chain.

The resulting comparison in Fig. 5.15 shows that the harvested output is strongly localized over a finite set of cells (roughly between cell number 10 and 20 for numerical simulations) reached by the primary interwell front and then decays downstream. The reduced envelope-based theory reproduces this localization and subsequent attenuation in a qualitatively consistent manner, while the numerical curve remains broader and larger in magnitude because it still contains carrier-scale oscillations, radiative wavetrains, and finite-chain effects that are intentionally averaged out in the slowly modulated theoretical description. Since, to obtain the harvested power, the voltage is squared and the

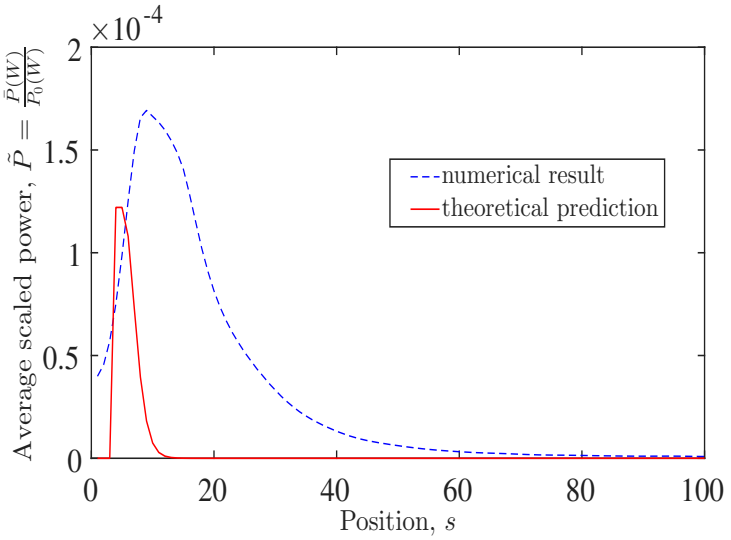


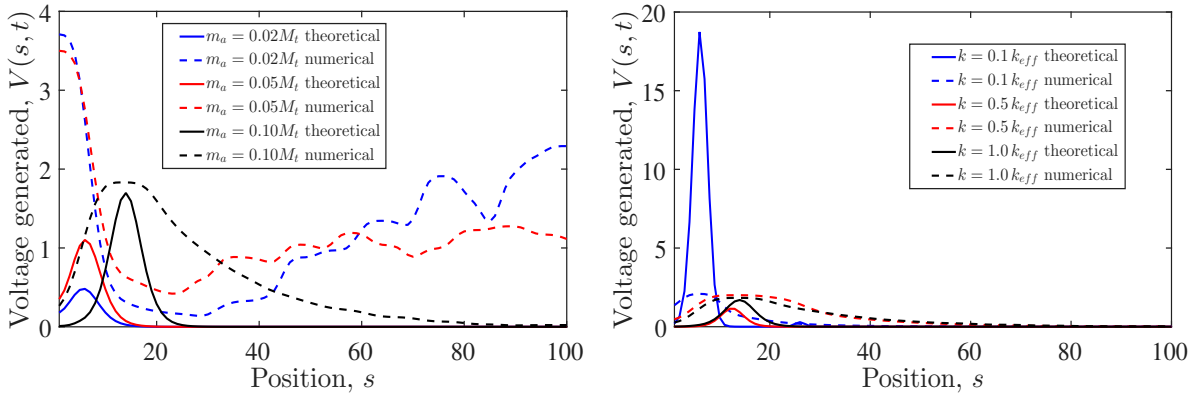
Fig. 5.15: Comparison of theoretically predicted average power with numerically obtained power profile (for parameters $\ell = 1$, $Y_e = 0.0107$), for obtaining the power profile across the chain a cycle averaging is used after an initial wait time of $t_s = 50$ seconds, the actual harvested power is scaled by a factor of $P_0 = \frac{\Theta^2 Y_e^2}{C_p^2 R_l}$.

resulting cycle average is maximized over admissible post-transient windows, differences in the voltage history comparison can be magnified in the final power profile comparison. The differences delimit the validity of the approximation: the theory retains the broad, slowly modulated coherent front and its post-front RC memory and accordingly, the reduced model is intended for the interior broad-front regime, away from strong boundary interactions and parameter ranges in which the front width or electrical memory length approaches the unit-cell spacing.

Parameter sweep for voltage profile comparison and selection of the best combination for discussing advantages later

We now vary some useful system parameters like the inerter mass-parameter m_a, the coupling spring stiffness k and the load resistance R_l to compare the theoretical voltage prediction and the numerical results and choose the combination of these parameters which gives the strongest localized voltage profile and the least disagreement between the theoretical model and numerical simulations to discuss possible advantages of our proposed model later in Section 5.9.4.

The parameter sweeps in Fig. 5.16 and Fig. 5.17 are used to identify a representative design point that combines a large and spatially localized electrical response with reliable reduced-order prediction. Since the cell-wise harvested power is constructed from V_n^2/R_l, agreement between the theoretical and numerical voltage envelopes provides a direct test of whether the reduced model can predict the location and spatial extent of the corresponding power concentration. Fig. 5.16(a) shows that, for $m_a = 0.02M_t$ and $0.05M_t$, the numerical response contains a large component near the initially disturbed boundary together with appreciable distributed and radiative content further along the chain. These contributions are not described by the single coherent-front ansatz and should not be



(a) Comparison of theoretical voltage profile with numerical simulations for varying inerter mass-parameter m_a keeping the coupling spring stiffness constant at $k = k_{eff}$.

(b) Comparison of theoretical voltage profile with numerical simulations for varying coupling spring stiffness k keeping the inerter mass-parameter constant at $m_a = 0.1M_t$.

Fig. 5.16: Comparison of the theoretically predicted voltage model with numerically determined voltage envelope for different inerter mass-parameters and coupling spring stiffness values, for plotting the voltage profile across the chain snapshot is taken at $t = 50$ seconds (for parameter: $\ell = 1$), load resistance is kept fixed at $R_l = 20$ MΩ.

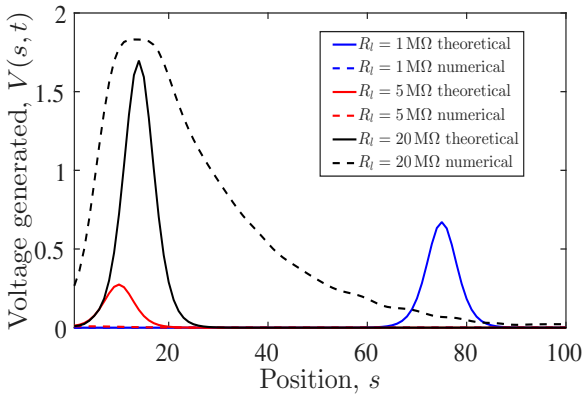


Fig. 5.17: Comparison of the theoretically predicted voltage model with numerically determined voltage envelope for varying values of load resistance R_l keeping the inerter mass-parameter constant at $m_a = 0.1M_t$ and coupling spring stiffness constant at $k = k_{eff}$ (for parameter $\ell = 1$), for plotting the voltage profile across the chain a snapshot is taken at $t = 50$ seconds.

interpreted as superior front-mediated localization merely because the boundary voltage is large. In contrast, $m_a = 0.1M_t$ produces a dominant interior voltage peak followed by a systematic spatial decay, with the theoretical model reproducing its position, magnitude, and overall localization most effectively. Moderate inerter mass therefore reorganizes the response into the coherent front-mediated structure relevant to localized harvesting.

The coupling-stiffness sweep in Fig. 5.16(b) similarly favors $k = k_{eff}$. For $k = 0.1k_{eff}$, the theory predicts an unrealistically sharp and large voltage peak. From $W^2 = 2(k\ell^2 - M_t c^2)/|a_0|$, reducing k drives the predicted front width toward the unit-cell scale, so that the broad-front condition $W \gg \ell$ and the long-wavelength approximation cease to be well

satisfied; discreteness, higher-order spatial corrections, and radiated wave components then become significant. The agreement improves at $k = 0.5k_{eff}$ and is strongest at $k = k_{eff}$, where the front remains sufficiently smooth while retaining a high localized voltage and hence power output.

Finally, Fig. 5.17 shows that the low-resistance cases $R_l = 1$ MΩ and 5 MΩ rapidly discharge the piezoelectric capacitance. Their electrical memory length $L_{\mathrm{RC}} = cR_lC_p$ can become comparable to or smaller than the cell spacing, making the voltage signature short-lived and sensitive to discrete and fast transient components that are excluded from the quasi-steady envelope model. At $R_l = 20$ MΩ, the front-generated voltage is retained for sufficiently long to produce the largest reliably predicted localized output among the tested loads, and the theoretical and numerical profiles agree closely in peak location and spatial decay. Consequently, the combination

$$m_a = 0.1M_t, \quad k = k_{eff}, \quad R_l = 20 \text{ M}\Omega \tag{5.202}$$

is adopted in Section 5.9.4 as the best joint operating point within the sampled parameter ranges. This selection is not asserted to be a global optimum over the continuous parameter space. Rather, it gives the strongest combination of front-mediated voltage and hence power localization and theoretical predictability among the cases considered. Once a representative front speed is supplied, the reduced model can therefore be used as an inexpensive parameter-screening tool, while the observed discrepancies at very low m_a, low k, and low R_l delineate the regimes in which full discrete simulations remain necessary.

5.9.4 Advantages over a linear model with no magnets or inerters

We now explore possible advantages in terms of energy harvesting with our chosen bi-stable, inertially coupled piezomagnetoelastic chain over a linear piezoelectric harvester with no magnets and inerters. For numerical time-integration purposes using `ode45`, in both the linear and nonlinear periodic models, we choose a finite chain with 100 unit cells free at both ends and apply on the first mass the same initial displacement and velocity. Considering our chosen bi-stable periodic chain, the initial velocity is taken to be sufficiently high so that the first mass snaps from its initial stable branch at $+Y_e$ to the other stable branch at $-Y_e$ in order to generate transient solitary waves in the chain.

Fig. 5.18 shows the clear advantage of energy harvesting through free wave propagation with the chosen bi-stable, inertially coupled piezomagnetoelastic model over a linear piezoelectric harvester with no inerters. While the piezomagnetoelastic harvester produces strongly localized energy distribution among the unit cells, the linear harvester without inerters creates an energy profile which is spatially delocalized and almost equally distributed among the unit cells and of much lower magnitude.

To establish an improved design route in terms of localized energy harvesting, starting from the linear baseline model with no inerters, we compare our chosen model with

1. A linear piezoelectric chain with inerters.

2. A bi-stable piezomagnetoelastic chain with no inerters.

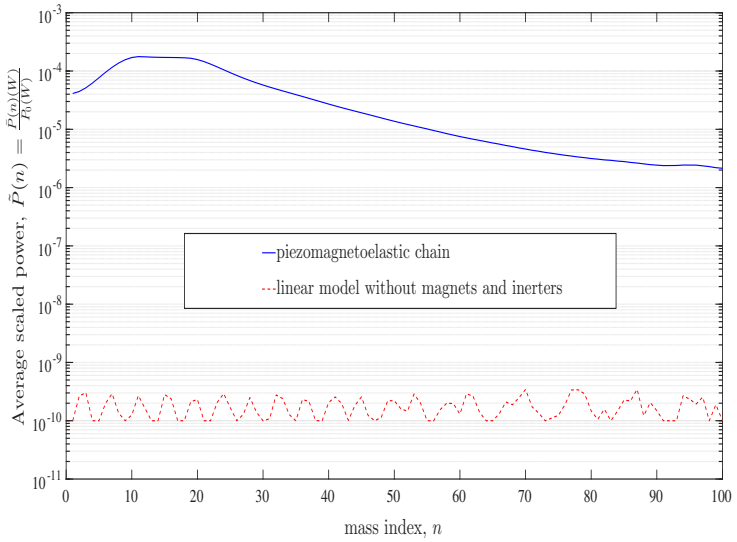


Fig. 5.18: Comparison of power harvested vs mass index n of the nonlinear, inertially coupled piezomagnetoelastic chain with a linear piezoelectric chain with no inerters and magnets, the power plots have been generated numerically for a finite chain of $n = 100$ unit cells with same initial conditions imposed on the first mass for both the cases, a semi-logarithmic y axis has been chosen for better visual comparison.

Linear chain with inerters

As a first step away from the linear baseline, it is natural to introduce inerters while retaining a linear piezoelectric chain. This modification changes the effective inertia and dispersive character of the system, but the corresponding harvested-power profile remains almost spatially uniform and several orders of magnitude smaller than that of the chosen piezomagnetoelastic chain as can be seen in Fig. 5.19, showing that inerter-contribution alone does not create a strong mechanism for energy localization. Moreover, since increasing the inerter mass beyond $m_a = 0.1M_t$ leads to divergence instabilities in the voltage response for our chosen model in the interwell snap-through regime, further improvement cannot be pursued safely by simply increasing the inertance magnitude level. The linear inertially coupled chain should therefore be viewed as a useful intermediate benchmark, but not as a practically sufficient design for enhanced localized energy harvesting.

Bi-stable chain with no inerters

With the useful level of inertial coupling bounded by voltage stability, the next systematic design step would be to introduce magnetic nonlinearity and hence bi-stability. The comparison with the bi-stable chain without inerters in Fig. 5.20 shows that the addition of magnets produces the dominant increase in harvesting performance, lifting the response from the weak linear regime to a much stronger wave-mediated electrical output. However, without inertial coupling mechanism, the harvested power remains more broadly redistributed along the chain, with a less sharply concentrated spatial profile than in the fully inertially coupled bi-stable/nonlinear model. This establishes a clear design pathway for enhanced, localized energy harvesting. Inertial coupling alone proves to be insufficient, while adding bi-stability provides the main enhancement in harvested energy,

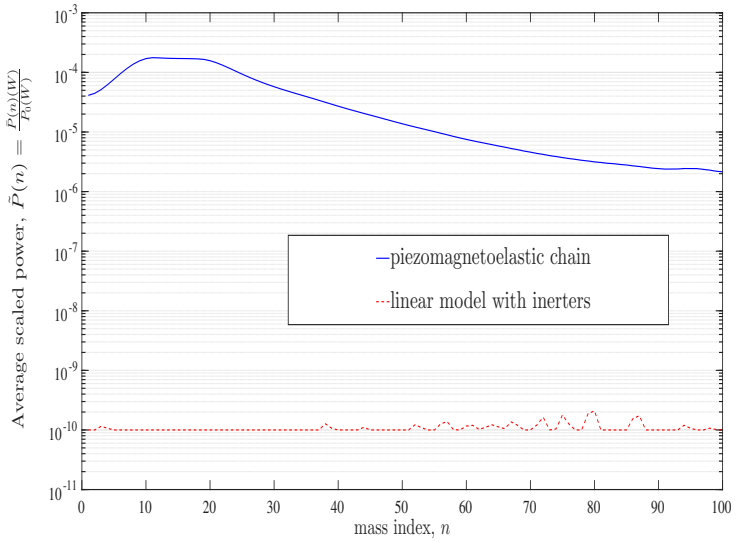


Fig. 5.19: Comparison of power harvested vs mass index n of the nonlinear, inertially coupled piezomagnetoelastic chain with a linear piezoelectric chain with inerters and without magnets, the power plots have been generated numerically for a finite chain of $n = 100$ unit cells with same initial conditions imposed on the first mass for both the cases, a semi-logarithmic y axis has been chosen for better visual comparison.

and the combination of bi-stability with moderate inertance magnitude gives the most practically useful outcome by coupling substantial electrical output with strong spatial localization.

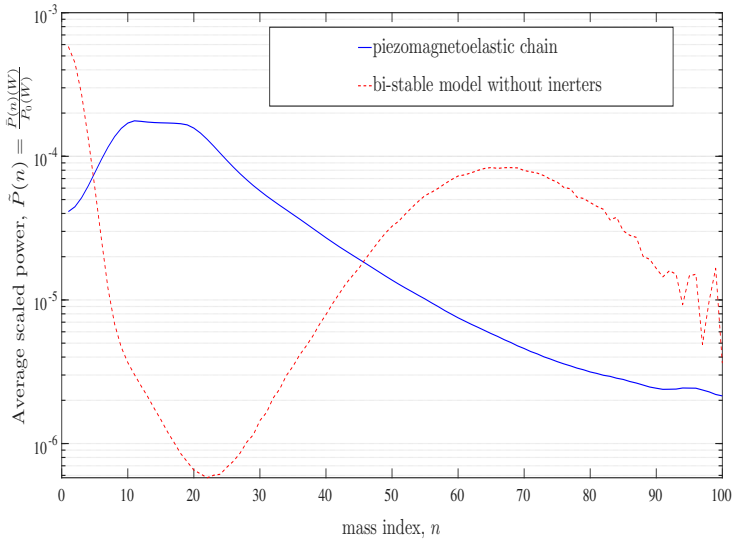


Fig. 5.20: Comparison of power harvested vs mass index n of the bi-stable, inertially coupled piezomagnetoelastic chain with a bi-stable piezomagnetoelastic chain without inerters, the power plots have been generated numerically for a finite chain of $n = 100$ unit cells with same initial conditions imposed on the first mass for both the cases, a semi-logarithmic y axis has been chosen for better visual comparison.

5.9.5 Discussion of interwell energy harvesting

Viewed as a systematic design route, the results identify a clear progression from the linear piezoelectric chain to the bi-stable inertially coupled piezomagnetoelastic architecture. The linear baseline without magnets and inerters produces a weak and essentially delocalized electrical response. Introducing inerters while retaining linearity modifies the effective inertia and dispersive character of the chain, but does not by itself generate an efficient localization mechanism for harvesting. The resulting power remains several orders of magnitude smaller than that of the nonlinear chain and is distributed almost uniformly across the cells. Moreover, because the voltage response becomes unstable when the inerter mass-parameter is increased beyond $m_a = 0.1M_t$ for our chosen model, inertial coupling alone does not provide an open-ended route for performance enhancement. The next physically meaningful step is therefore the introduction of magnetic nonlinearity leading to bi-stability, which activates interwell dynamics and produces the dominant increase in harvestable electrical output relative to the classical linear harvester.

The fully coupled model combines these ingredients in their most useful form. In the bi-stable chain without inerters, the harvested energy is substantially enhanced, but it remains comparatively broad in space. Moderate inertial coupling then plays a more selective role. Rather than merely increasing the overall response level, it reorganizes the nonlinear wave-mediated electromechanical conversion into a markedly sharper and more localized harvesting pattern. From a practical perspective, this is the main advantage of the chosen architecture. The localization of harvestable energy is not imposed through defect engineering, graded parameter landscapes, or a separate design stage dedicated to trapping a transition wave at a prescribed site. Moreover, although a finite initial disturbance is used to nucleate the front in the finite-chain simulations, the subsequent localization does not rely on sustained or resonance-tuned excitation, nor on an impulse protocol tailored to pin or arrest the wave at a prescribed location. Instead, it emerges intrinsically from the unforced coupled action of magnetic bi-stability, electromechanical dissipation, and moderate inertial coupling during free wave propagation. In this sense, the proposed chain provides a conceptually simpler and potentially more robust pathway to high local power density than a linear piezoelectric harvester, while also clarifying that the decisive design improvement is not inertial coupling in isolation, but inertial coupling used in concert with nonlinear bi-stability.

5.10 Concluding remarks

This Chapter has proposed an inertially coupled nonlinear piezomagnetoelastic chain as a physically realizable framework for harvesting energy from transient free waves, rather than from a prescribed sustained external excitation. Starting from a dissipative bi-stable unit cell, we showed that electromechanical coupling fundamentally alters the phase space structure of the isolated element and turns it into an energy converting building block for a periodic medium capable of attenuation and distributed electrical extraction. On this basis, a reduced electromechanical model was developed for the chain and analyzed in both the linearized intrawell and strongly nonlinear intrawell regimes.

In the linearized regime, the combination of Bloch reduction with a settling-time-aware power metric provided a predictive analytical framework for identifying the maximum

steady-state harvested power and the associated free-wave operating frequency directly from the coupled structural, magnetic, inertial, and electrical parameters, with validation against numerical time-domain simulations. In the strongly nonlinear intrawell regime, the amplitude-dependent dispersion analysis and time-domain evaluation revealed that magnetic bi-stability and inertial coupling do not simply increase an isolated harvesting peak, but instead, they transform a sharply tuned linear operating point into a broad quasi-saturated band of near optimal performance over a much wider free wave frequency interval. Importantly, this enhancement is achieved within stable intrawell oscillations, without relying on negative-stiffness induced divergence, and is accompanied by an improved stiffness-to-weight ratio through stiffer coupling and lower initial auxiliary/design inertia.

We have also shown localized energy harvesting in the piezomagnetoelastic chain in the regime of free interwell wave propagation generated by sufficiently large initial conditions without the need for sustained external forcing. Starting from the discrete chain model and its long-wavelength continuum approximation, we have showed that the relevant propagating structure in the passive electromechanical system is not an exact conservative soliton, but a slowly modulated φ^4 type interwell front whose propagation is intrinsically altered by electrical energy extraction. This led to closed-form leading order descriptions of the front profile, the slaved voltage field, and the corresponding front modulation law. We have used direct numerical simulations of a discrete finite chain to show good qualitative agreement with the asymptotic predictions for the front shape, voltage envelope, and spatial distribution of harvested power.

Our study in the interwell regime fills a clear gap between three strands of existing literature that have largely remained separate, namely nonlinear piezoelectric and piezomagnetoelastic energy harvesters, transition-wave dynamics in multistable lattices, and inerter-based wave tailoring. In contrast to earlier frameworks that emphasize either externally forced unit-cell harvesters or mechanically focused transition wave phenomena, the present work provides an analytically tractable electromechanical description of wave mediated energy conversion in an extended bi-stable chain with inertial coupling. Equally importantly, the results identify a systematic design route toward improved harvesting performance. The linear piezoelectric baseline produces weak and spatially delocalized output and adding inerters alone modifies the dispersive character of the chain but does not create efficient localization and is practically limited by voltage divergence beyond moderate inertance magnitudes. Hence, introducing magnetic bi-stability provides the dominant increase in harvestable electrical output, and the combination of bi-stability with moderate inertial coupling yields the most effective overall architecture by coupling substantial output with sharply localized harvesting.

From the standpoint of novelty and practical impact, our results highlight that strong spatial concentration of harvestable energy can emerge intrinsically from the coupled action of magnetic bi-stability, inertial coupling, and electromechanical dissipation during free wave propagation. In the proposed architecture, localization does not need to be imposed through defect engineering, graded trapping landscapes, or a separate parameter design stage dedicated to pinning or arresting a transition wave, nor does it rely on resonance tuning around a prescribed excitation frequency. The localized electrical response is instead a natural consequence of the nonlinear transient dynamics of the harvester itself. This establishes a conceptually simpler and potentially more robust pathway to high local

power density than conventional linear piezoelectric harvesters, and advances the state of the art by showing how passive nonlinear wave transport can be harnessed, in a mathematically transparent manner, for enhanced and spatially localized energy harvesting in architected nonlinear metamaterials.

The next work in Chapter 6 will extend this free-wave energy harvesting framework in nonlinear piezomagnetoelastic chains to nonlinear piezomagnetoelastic chains with mass-diatomic repeating unit cells, where the mass contrast will be shown to produce richer bandgap and enhanced harvesting behavior.

Chapter 6

Energy harvesting capacity of diatomic inertially coupled nonlinear piezomagnetoelastic chains

The free-wave energy harvesting framework developed for nonlinear piezomagnetoelastic chains in Chapter 5 is now extended to mass-diatomic nonlinear chains, retaining the inerters and bi-stable magnetic effects. It is anticipated that this mass contrast in the repeating unit cell may give rise to richer dispersion and hence enhanced energy harvesting characteristics.

6.1 The mass-diatomic unit-cell model

6.1.1 Equations of motion

As a repeating building block for our periodic chain, we choose a diatomic, piezomagnetoelastic unit-cell model comprising of two inverted, vertical cantilever beams of length L with tip mass at the free end and piezoelectric patches attached at the base near the fixed end. The tip masses are subject to a magnetic potential of two permanent repelling magnets placed symmetrically on both sides of each beam near the free end with their north poles facing upward. A schematic diagram of the unit cell is shown in Fig. 6.1 with the dimensions labeled. The two beams are considered to be identical in all respect with width w, thickness h, and length L. The beam material is considered to be isotropic with density ρ and modulus of elasticity E. The diatomicity of the model arises from the difference of the tip masses labeled as M_1 and M_2. The two tip masses in the unit cell are coupled to each other by a linear horizontal spring of stiffness k and a pair of stable negative-inerter mechanisms, as considered before in Chapter 5, with mass-dimensional design parameter m_a and initial design angle α of the rigid links with the horizontal axis. The two tip masses are also considered to be made up of a magnetic material and of identical geometric parameters a_t and $2b_t$ as shown in Fig. 6.1. B_t denotes the magnetic field strength at either tip magnet's surface and B_s denotes the magnetic field strength at the permanent base magnets' surface on its axis.

Each of the two permanent magnet pairs placed on either side of both the beams is considered to have a radius a in the horizontal direction and length $2b$ in the vertical direction.

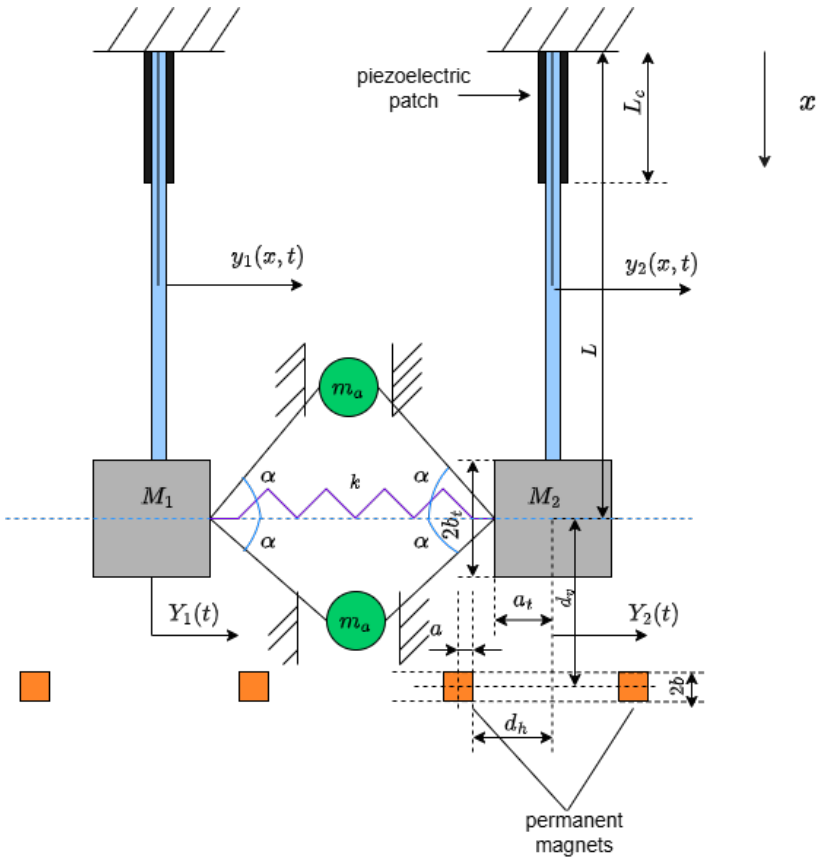


Fig. 6.1: The repeating diatomic piezomagnetoelastic unit-cell model.

The vertical distance between the center of the tip mass and the center of base magnets is denoted as d_v and the horizontal distance between the center of the tip mass and the center of either magnet is denoted as d_h. Piezoelectric patches are placed in a bimorph 31 configuration near the fixed end of each beam for electrical energy harvesting from free wave motion through the final assembled periodic chain. The piezoelectric patches in the beams are considered to be identical in all respects with the same capacitance C_p, load resistor R_l, same piezoelectric constant γ_c, and the same length L_c.

The equations of motion of the two degree of freedom unit cell in terms of beam tip mass displacements for single-mode approximation can be obtained easily using the monoatomic model in Chapter 5 as a reference as:

$$M_1\ddot{Y}_1 + EI(2j-1)^4\frac{\pi^4}{32L^3}Y_1 + k\Big(Y_1 - Y_2\Big) + 2c_1Y_1 + 4c_2Y_1^3 - \frac{m_a\cos^2\alpha}{2\sin^2\alpha}\Big(\ddot{Y}_1 - \ddot{Y}_2\Big) - \Theta V_1 = 0 \tag{6.1}$$

$$M_2\ddot{Y}_2 + EI(2j-1)^4\frac{\pi^4}{32L^3}Y_2 + k\Big(Y_2 - Y_1\Big) + 2c_1Y_2 + 4c_2Y_2^3 - \frac{m_a\cos^2\alpha}{2\sin^2\alpha}\Big(\ddot{Y}_2 - \ddot{Y}_1\Big) - \Theta V_2 = 0 \tag{6.2}$$

where c_1, c_2 are the magnetic coefficients arising from the two permanent magnets. The magnetic potential function has been considered in accordance with the Moon-Holmes model [106] with a suitable fourth-order truncation without loss of generality for our present objective.

On the electrical side, considering the piezoelectric patches as a capacitor, the electrical

governing differential equations can be obtained as:

$$C_p\dot{V}_1 + \frac{V_1}{R_l} + \Theta\dot{Y}_1 = 0 \tag{6.3}$$

$$C_p\dot{V}_2 + \frac{V_2}{R_l} + \Theta\dot{Y}_2 = 0 \tag{6.4}$$

Where V_1, V_2 represent the voltages generated.

The single-mode reduction for beam displacement, as discussed before in Chapter 4 and Chapter 5, is intended as a leading-order description of the unit cell in the tip mass dominated regime considered here. It is expected to remain appropriate so long as the response is governed predominantly by the fundamental flexural mode, i.e., when the dynamics are controlled by the global tip motion rather than by short-wavelength bending of the beam. The approximation may lose quantitative accuracy when snap-through becomes sufficiently abrupt to generate appreciable higher-mode content, strong curvature localization develops near the clamp, or the relevant time scales approach those of the higher flexural modes. In this sense, the present formulation should be viewed as a reduced model for the collective intrawell wave dynamics and harvesting trends, rather than as a full structural representation of all beam modes. In the next Section 6.1.2, it will be shown that for our chosen symmetric bi-stable magnetic potential design, the distance from the unstable equilibrium point in the middle to the stable equilibrium points on either side of each mass will be sufficiently small compared to the length of the beam ($Y_s/L = \pm 0.1$) for neglecting large axial beam motion and nonlinear strain-curvature relations.

6.1.2 Phase plane behavior

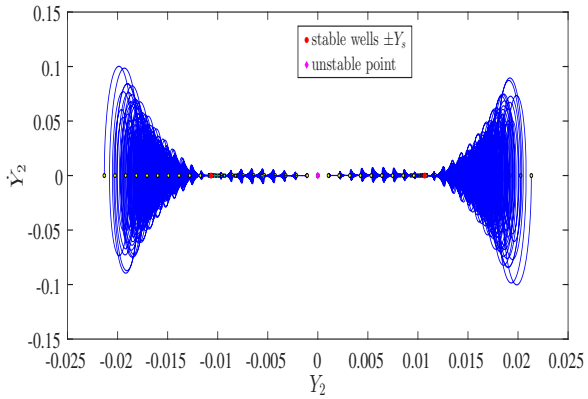
We investigate the phase-plane behavior of the diatomic piezomagnetoelastic unit cell introduced in Section 6.1.1 for a general case with the masses $M_1 \neq M_2$ and the limiting case with masses $M_1 = M_2$ which renders the diatomic cell to a simple monoatomic one. We choose the magnetic coefficients c_1, c_2 such that the magnetic potential landscape, without the coupling spring and the effective beam potential, is itself double-well. For each case, we report the displacement and voltage phase-plane behavior where the phase plane is defined by taking a two-dimensional projection of the actual six-dimensional phase space. For displacements this two-dimensional projection is taken on a plane defined by $[Y, \dot{Y}]$ and for voltages it is defined by $[V, \dot{V}]$. Since we will be interested in a bi-stable double-well shaped magnetic potential, the parameters d_h, d_v, B_s, B_t are chosen accordingly which results in the coefficient values $c_1 = -1.69985$, $c_2 = 944.64$. Detailed expressions for the coefficients in terms of the magnetic parameters have been provided previously in Chapter 5 alongwith the table for other system parameters, which are kept fixed throughout this Chapter without loss of generality. The initial angle of inclination of the inerter module's rigid links with the horizontal axis will be taken as $\sin\alpha = 0.5$ throughout.

We take representative mass ratios $m_a = 0.1M_1$, $M_2 = 0.5M_1$, M_1, and coupling spring stiffness $k = 0.1K_b$, where $K_b = \frac{EI\pi^4}{32L^3}$ is defined as the effective contribution from beam stiffness for single-mode approximation taking the integer $j = 1$ without loss of generality. The value of mass M_1 is taken the same as the tip mass M_t in Chapter 5, Table 5.1, i.e, $M_1 = 10$ g. For each mass ratio M_2/M_1, we report the phase-plane behavior for:

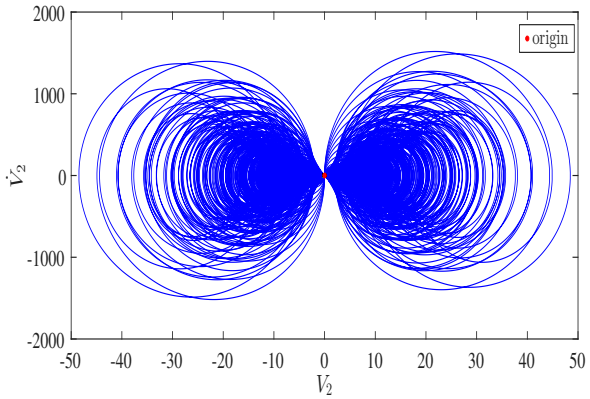
1. small-amplitude intrawell motions of the masses from their initial stable uniform branch.

2. large-amplitude interwell motions of the masses resulting from large initial displacements.

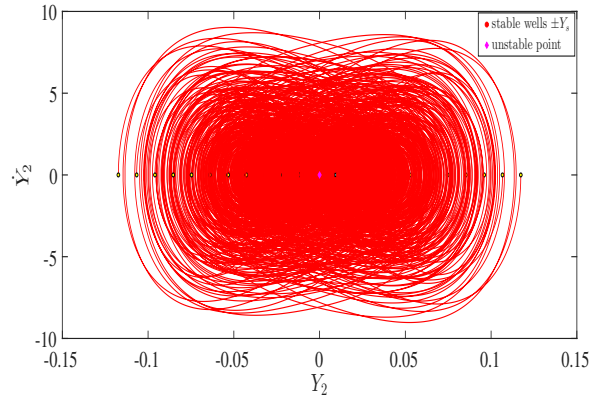
The two masses Y_1, Y_2 and the voltages V_1, V_2 show identical qualitative behavior, so we choose to report one of them as a representative study.



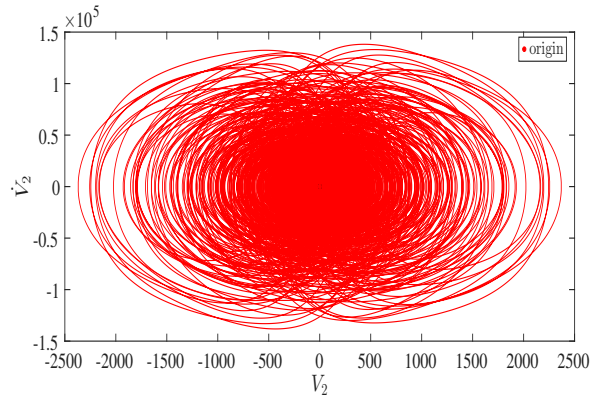
(a) Phase-plane behavior of tip mass $Y(t)$ for small perturbations from stable equilibrium position at $Y_s = 10.7$ mm



(b) Phase-plane behavior of voltage $V(t)$ for small perturbations of the tip mass from stable equilibrium position at $Y_s = 10.7$ mm



(c) Phase-plane behavior of tip mass $Y(t)$ for large perturbations from stable equilibrium position at $Y_s = 10.7$ mm

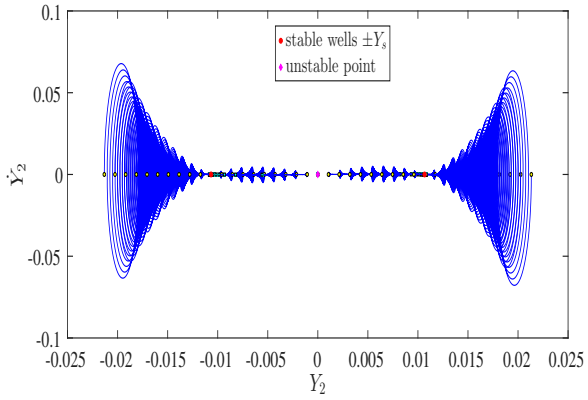


(d) Phase-plane behavior of voltage $V(t)$ for large perturbations of the tip mass from stable equilibrium position at $Y_s = 10.7$ mm

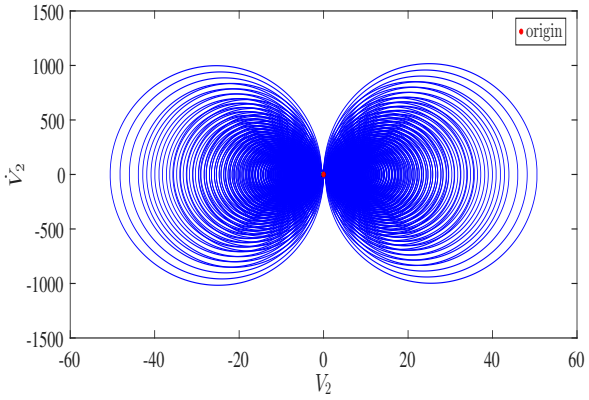
Fig. 6.2: Phase-plane behavior of tip mass $Y(t)$ and voltage $V(t)$ for small intrawell and large interwell motions of the tip mass about its stable equilibrium position, yellow circles mark starting point of trajectories and cyan squares mark end point of trajectories, mass ratio $M_2/M_1 = 0.5$.

Fig. 6.2 shows the phase-plane response of the mass-diatomic unit cell for $M_2/M_1 = 0.5$. For small perturbations, the mechanical trajectories form damped intrawell spirals about the stable equilibrium, while the voltage phase-plane trajectories decay toward the electrical origin because of the resistive load. For large perturbations, the trajectories leave the local well and form damped quasi-homoclinic interwell loops before eventually

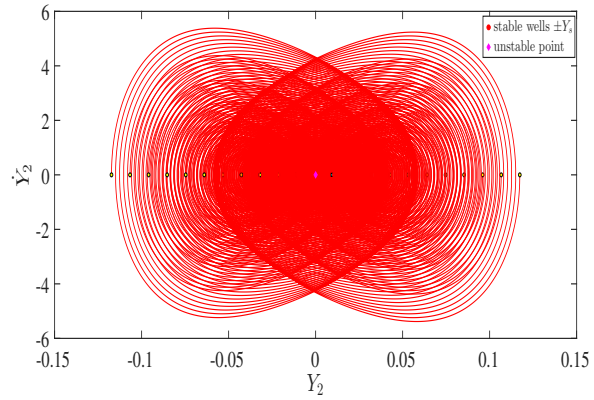
settling due to electromechanical dissipation. The mass diatomicity introduces two distinct inertial time scales in the unit cell, so the projected phase portraits contain a nested structure: one set of visible damped spirals and quasi-homoclinic loops is accompanied by another hidden set associated with the second sublattice response. Thus, the qualitative bi-stable dynamics of the piezomagnetoelastic harvester are preserved, but the mass contrast enriches the phase-plane structure through coupled acoustic-like and optical-like unit-cell motion.



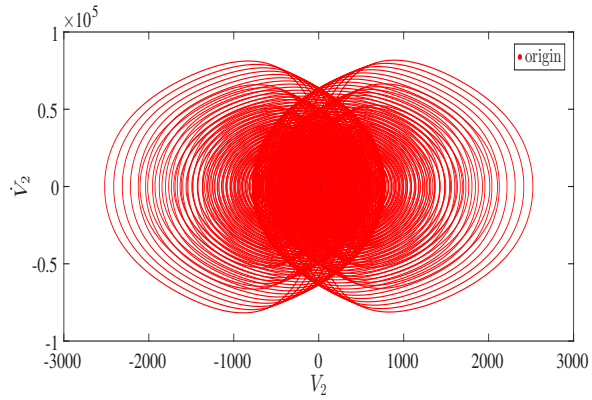
(a) Phase-plane behavior of tip mass $Y(t)$ for small perturbations from stable equilibrium position at $Y_s = 10.7$ mm



(b) Phase-plane behavior of voltage $V(t)$ for small perturbations of the tip mass from stable equilibrium position at $Y_s = 10.7$ mm



(c) Phase-plane behavior of tip mass $Y(t)$ for large perturbations from stable equilibrium position at $Y_s = 10.7$ mm



(d) Phase-plane behavior of voltage $V(t)$ for large perturbations of the tip mass from stable equilibrium position at $Y_s = 10.7$ mm

Fig. 6.3: Phase-plane behavior of tip mass $Y(t)$ and voltage $V(t)$ for small intrawell and large interwell motions of the tip mass about its stable equilibrium position, yellow circles mark starting point of trajectories and cyan squares mark end point of trajectories, mass ratio $M_2/M_1 = 1$.

Fig. 6.3 shows the limiting case $M_2/M_1 = 1$, where the two sublattices become dynamically identical. In this limit, the hidden nested phase-plane structure observed in the diatomic case collapses into a single visible set of damped intrawell spirals for small perturbations and a single set of damped quasi-homoclinic interwell orbits for large perturbations. The voltage phase portraits similarly reduce to one dominant dissipative

electrical response converging toward the origin. This monoatomic phase-plane behavior has been reported before in Chapter 5. Therefore, the monoatomic limit confirms that the underlying nonlinear bi-stable mechanism remains the same, while the additional hidden spirals and hidden quasi-homoclinic loops in Fig. 6.2 arise specifically from mass diatomicity and the resulting coupled two-mass unit-cell dynamics.

6.2 Linearized dispersion behavior for the mass-diatomic chain

6.2.1 Dispersion relation

To arrive at an one-dimensional periodic chain comprising of our diatomic piezomagnetoelastic unit-cell model considered in Section 6.1, we consider N such arrays of unit cells coupled by horizontal linear springs and a pair of stable negative-inerter units as shown in Fig. 6.4. The linear bending stiffness contribution of each beam is denoted by

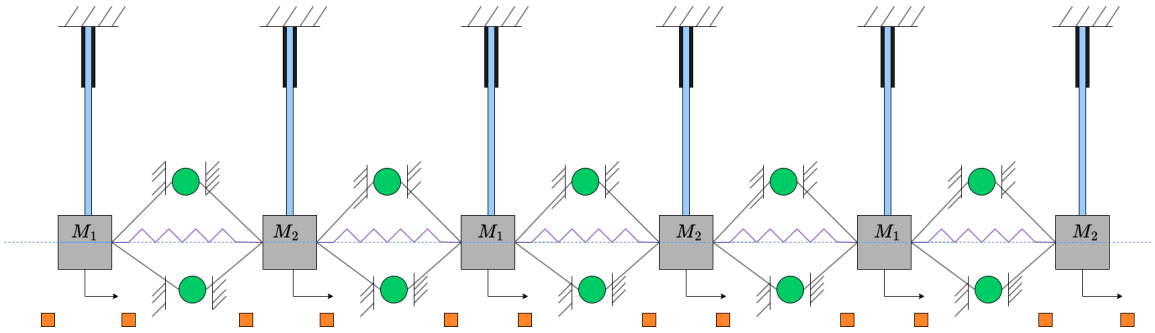


Fig. 6.4: The periodic diatomic chain.

$$K_b = EI\frac{\pi^4}{32L^3} \tag{6.5}$$

For the n-th representative unit cell of an infinite periodic chain ($N \to \infty$), the two generalized coordinates are denoted by $Y_{1,n}(t)$ and $Y_{2,n}(t)$, where the tip masses associated with the two sublattices are M_1 and M_2, respectively. The only source of diatomicity is $M_1 \neq M_2$. All springs have identical stiffness k, and all inerters have identical coefficient $r_a = \frac{m_a \cos^2\alpha}{2\sin^2\alpha}$. The periodic-chain extension of (6.1)-(6.4) is hence obtained as:

$$\begin{aligned} &M_1\ddot{Y}_{1,n} + K_bY_{1,n} + k\left(2Y_{1,n} - Y_{2,n} - Y_{2,n-1}\right) + 2c_1Y_{1,n} + 4c_2Y_{1,n}^3 \\ &\quad - r_a\left[\left(\ddot{Y}_{1,n} - \ddot{Y}_{2,n}\right) + \left(\ddot{Y}_{1,n} - \ddot{Y}_{2,n-1}\right)\right] - \Theta V_{1,n} = 0 \end{aligned} \tag{6.6a}$$

$$\begin{aligned} &M_2\ddot{Y}_{2,n} + K_bY_{2,n} + k\left(2Y_{2,n} - Y_{1,n} - Y_{1,n+1}\right) + 2c_1Y_{2,n} + 4c_2Y_{2,n}^3 \\ &\quad - r_a\left[\left(\ddot{Y}_{2,n} - \ddot{Y}_{1,n}\right) + \left(\ddot{Y}_{2,n} - \ddot{Y}_{1,n+1}\right)\right] - \Theta V_{2,n} = 0 \end{aligned} \tag{6.6b}$$

$$C_p\dot{V}_{1,n} + \frac{V_{1,n}}{R_l} + \Theta\dot{Y}_{1,n} = 0 \tag{6.6c}$$

$$C_p\dot{V}_{2,n} + \frac{V_{2,n}}{R_l} + \Theta\dot{Y}_{2,n} = 0 \tag{6.6d}$$

The simplest uniform equilibrium branch is obtained by taking all cells and both sublattices to have the same static displacement Y_s and zero voltage

$$Y_{1,n} = Y_{2,n} = Y_s \tag{6.7a}$$
$$V_{1,n} = V_{2,n} = 0 \tag{6.7b}$$
$$\dot{Y}_{1,n} = \dot{Y}_{2,n} = \ddot{Y}_{1,n} = \ddot{Y}_{2,n} = 0 \tag{6.7c}$$

Substitution of Eq. (6.7) into Eq. (6.6) gives the uniform-branch equilibrium condition

$$(K_b + 2c_1)\, Y_s + 4c_2 Y_s^3 = 0 \tag{6.8}$$

For the common bi-stable configuration, the two non-zero stable equilibria are

$$Y_s^{\pm} = \pm\sqrt{-\frac{K_b + 2c_1}{4c_2}} \tag{6.9}$$

The derivation below is valid for either stable root Y_s. The perturbations about the selected stable uniform branch are introduced as

$$Y_{1,n} = Y_s + u_{1,n} \tag{6.10a}$$
$$Y_{2,n} = Y_s + u_{2,n} \tag{6.10b}$$
$$V_{1,n} = v_{1,n} \tag{6.10c}$$
$$V_{2,n} = v_{2,n} \tag{6.10d}$$

The tangent stiffness of each piezomagnetoelastic oscillator about the selected stable equilibrium is

$$K_s = K_b + 2c_1 + 12c_2 Y_s^2 \tag{6.11}$$

Keeping only the terms linear in $u_{1,n}$, $u_{2,n}$, $v_{1,n}$, and $v_{2,n}$ gives

$$\begin{aligned} &M_1\ddot{u}_{1,n} + K_s u_{1,n} + k\,(2u_{1,n} - u_{2,n} - u_{2,n-1}) \\ &\quad - r_a\,[(\ddot{u}_{1,n} - \ddot{u}_{2,n}) + (\ddot{u}_{1,n} - \ddot{u}_{2,n-1})] - \Theta v_{1,n} = 0 \end{aligned} \tag{6.12a}$$
$$\begin{aligned} &M_2\ddot{u}_{2,n} + K_s u_{2,n} + k\,(2u_{2,n} - u_{1,n} - u_{1,n+1}) \\ &\quad - r_a\,[(\ddot{u}_{2,n} - \ddot{u}_{1,n}) + (\ddot{u}_{2,n} - \ddot{u}_{1,n+1})] - \Theta v_{2,n} = 0 \end{aligned} \tag{6.12b}$$
$$C_p\dot{v}_{1,n} + \frac{v_{1,n}}{R_l} + \Theta\dot{u}_{1,n} = 0 \tag{6.12c}$$
$$C_p\dot{v}_{2,n} + \frac{v_{2,n}}{R_l} + \Theta\dot{u}_{2,n} = 0 \tag{6.12d}$$

The conductance of the load resistance is introduced as

$$G_l = \frac{1}{R_l} \tag{6.13}$$

The spatial Bloch reduction is written as

$$\begin{bmatrix} u_{1,n}(t) \\ u_{2,n}(t) \end{bmatrix} = \mathbf{u}(t)e^{in\mu} \tag{6.14a}$$
$$\begin{bmatrix} v_{1,n}(t) \\ v_{2,n}(t) \end{bmatrix} = \mathbf{v}(t)e^{in\mu} \tag{6.14b}$$

where μ is the non-dimensional Bloch wavenumber. Substituting Eq. (6.14) into Eq. (6.12) gives the Bloch-reduced electromechanical equations

$$\mathbf{M}_\mu \ddot{\mathbf{u}} + \mathbf{K}_\mu \mathbf{u} - \Theta \mathbf{v} = \mathbf{0} \tag{6.15a}$$

$$C_p \dot{\mathbf{v}} + G_l \mathbf{v} + \Theta \dot{\mathbf{u}} = \mathbf{0} \tag{6.15b}$$

The Bloch-reduced mass matrix is hence obtained as:

$$\mathbf{M}_\mu = \begin{bmatrix} M_1 - 2r_a & r_a\left(1 + e^{-i\mu}\right) \\ r_a\left(1 + e^{i\mu}\right) & M_2 - 2r_a \end{bmatrix} \tag{6.16}$$

The Bloch-reduced stiffness matrix is given by

$$\mathbf{K}_\mu = \begin{bmatrix} K_s + 2k & -k\left(1 + e^{-i\mu}\right) \\ -k\left(1 + e^{i\mu}\right) & K_s + 2k \end{bmatrix} \tag{6.17}$$

The state vector is defined as

$$\mathbf{x} = \begin{bmatrix} \mathbf{u} \\ \dot{\mathbf{u}} \\ \mathbf{v} \end{bmatrix} \tag{6.18}$$

Using Eq. (6.18), Eq. (6.15) is rewritten in first-order state-space form as

$$\dot{\mathbf{x}} = \mathbf{A}_\mu \mathbf{x} \tag{6.19}$$

where the Bloch state matrix is

$$\mathbf{A}_\mu = \begin{bmatrix} \mathbf{0}_2 & \mathbf{I}_2 & \mathbf{0}_2 \\ -\mathbf{M}_\mu^{-1}\mathbf{K}_\mu & \mathbf{0}_2 & \Theta\mathbf{M}_\mu^{-1} \\ \mathbf{0}_2 & -\dfrac{\Theta}{C_p}\mathbf{I}_2 & -\dfrac{G_l}{C_p}\mathbf{I}_2 \end{bmatrix} \tag{6.20}$$

The state-space normal mode is assumed in the form

$$\mathbf{x}(t) = \boldsymbol{\phi} e^{st} \tag{6.21}$$

Substitution of Eq. (6.21) into Eq. (6.19) gives the eigenvalue problem

$$\left(s\mathbf{I} - \mathbf{A}_\mu\right)\boldsymbol{\phi} = \mathbf{0} \tag{6.22}$$

Therefore, for non-trivial $\boldsymbol{\phi}$, the state-space dispersion relation is obtained as

$$\det\left(s\mathbf{I} - \mathbf{A}_\mu\right) = 0 \tag{6.23}$$

An equivalent reduced form of Eq. (6.23) is obtained by partitioning the eigenvector as

$$\boldsymbol{\phi} = \begin{bmatrix} \mathbf{U} \\ s\mathbf{U} \\ \boldsymbol{\Phi} \end{bmatrix} \tag{6.24}$$

The mechanical and electrical parts of the eigenvalue problem are then

$$\left(s^2\mathbf{M}_\mu + \mathbf{K}_\mu\right)\mathbf{U} - \Theta\boldsymbol{\Phi} = \mathbf{0} \tag{6.25a}$$

$$\left(C_p s + G_l\right)\boldsymbol{\Phi} + \Theta s\mathbf{U} = \mathbf{0} \tag{6.25b}$$

From Eq. (6.25b), the voltage eigenvector is

$$\boldsymbol{\Phi} = -\frac{\Theta s}{C_p s + G_l}\mathbf{U} \tag{6.26}$$

Substitution of Eq. (6.26) into Eq. (6.25a) gives

$$\left[s^2\mathbf{M}_\mu + \mathbf{K}_\mu + \frac{\Theta^2 s}{C_p s + G_l}\mathbf{I}_2\right]\mathbf{U} = \mathbf{0} \tag{6.27}$$

The reduced determinant form of the dispersion relation is therefore

$$\det\left[s^2\mathbf{M}_\mu + \mathbf{K}_\mu + \frac{\Theta^2 s}{C_p s + G_l}\mathbf{I}_2\right] = 0 \tag{6.28}$$

Introducing

$$\Gamma(s) = C_p s + G_l \tag{6.29}$$

Eq. (6.28) can be written in polynomial determinant form as

$$\det\left[\Gamma(s)\left(s^2\mathbf{M}_\mu + \mathbf{K}_\mu\right) + \Theta^2 s\mathbf{I}_2\right] = 0 \tag{6.30}$$

Using Eqs. (6.16) and (6.17), Eq. (6.30) gives the explicit state-space dispersion relation

$$\begin{aligned}\Delta(s,\mu) = &\left\{\Gamma(s)\left[(M_1 - 2r_a)\,s^2 + K_s + 2k\right] + \Theta^2 s\right\}\left\{\Gamma(s)\left[(M_2 - 2r_a)\,s^2 + K_s + 2k\right] + \Theta^2 s\right\} \\ &- 4\Gamma^2(s)\left(r_a s^2 - k\right)^2 \cos^2\left(\frac{\mu}{2}\right) = 0\end{aligned} \tag{6.31}$$

For the direct computation of the dispersion branches, the Bloch wavenumber is prescribed as a real parameter

$$\mu \in [0, \pi] \tag{6.32}$$

The corresponding Bloch factor appearing in the characteristic equation is written as

$$\mathcal{C}_\mu = \cos^2\left(\frac{\mu}{2}\right) \tag{6.33}$$

Starting from the polynomial state-space characteristic equation in Eq. (6.31), the dispersion relation for fixed μ is obtained by solving

$$\begin{aligned}\Delta(s,\mu) = &\left\{\Gamma(s)\left[(M_1 - 2r_a)\,s^2 + K_s + 2k\right] + \Theta^2 s\right\}\left\{\Gamma(s)\left[(M_2 - 2r_a)\,s^2 + K_s + 2k\right] + \Theta^2 s\right\} \\ &- 4\Gamma^2(s)\left(r_a s^2 - k\right)^2 \mathcal{C}_\mu = 0\end{aligned} \tag{6.34}$$

where

$$\Gamma(s) = C_p s + G_l \tag{6.35}$$

For compactness, the following quantities are introduced

$$m_1 = M_1 - 2r_a \tag{6.36a}$$
$$m_2 = M_2 - 2r_a \tag{6.36b}$$
$$A_s = K_s + 2k \tag{6.36c}$$
$$B_s = C_p A_s + \Theta^2 \tag{6.36d}$$

Using Eq. (6.36), Eq. (6.34) can be expanded as

$$\Delta(s,\mu) = \sum_{\ell=0}^{6} p_\ell(\mu) s^\ell = 0 \tag{6.37}$$

The polynomial coefficients are

$$p_6 = C_p^2 \left(m_1 m_2 - 4 r_a^2 \mathcal{C}_\mu\right) \tag{6.38a}$$
$$p_5 = 2 C_p G_l \left(m_1 m_2 - 4 r_a^2 \mathcal{C}_\mu\right) \tag{6.38b}$$
$$p_4 = C_p B_s \left(m_1 + m_2\right) + G_l^2 m_1 m_2 - 4 G_l^2 r_a^2 \mathcal{C}_\mu + 8 C_p^2 r_a k \mathcal{C}_\mu \tag{6.38c}$$
$$p_3 = G_l \left(m_1 + m_2\right) \left(2 C_p A_s + \Theta^2\right) + 16 C_p G_l r_a k \mathcal{C}_\mu \tag{6.38d}$$
$$p_2 = G_l^2 A_s \left(m_1 + m_2\right) + B_s^2 - 4 C_p^2 k^2 \mathcal{C}_\mu + 8 G_l^2 r_a k \mathcal{C}_\mu \tag{6.38e}$$
$$p_1 = 2 G_l A_s B_s - 8 C_p G_l k^2 \mathcal{C}_\mu \tag{6.38f}$$
$$p_0 = G_l^2 A_s^2 - 4 G_l^2 k^2 \mathcal{C}_\mu \tag{6.38g}$$

The roots of Eq. (6.37) are denoted by

$$\mathcal{S}(\mu) = \{s_q(\mu) : \Delta(s_q, \mu) = 0,\ q = 1, 2, \ldots, 6\} \tag{6.39}$$

Each root is interpreted as a temporal state-space eigenvalue of the form

$$s_q(\mu) = -\sigma_q(\mu) + i\omega_q(\mu) \tag{6.40}$$

where $\sigma_q(\mu)$ is the modal decay rate and $\omega_q(\mu)$ is the damped modal frequency. The modal frequencies are then extracted from their imaginary parts as

$$\omega_q(\mu) = \mathrm{Im}\left[s_q(\mu)\right] \tag{6.41}$$

The positive-frequency oscillatory roots are collected as

$$\mathcal{S}_+(\mu) = \{s_q(\mu) \in \mathcal{S}(\mu) : \omega_q(\mu) > 0\} \tag{6.42}$$

If an electrical-dominant root is present in $\mathcal{S}_+(\mu)$, it is discarded by using the mechanical participation factor of the corresponding state-space eigenvector. For the eigenvector

$$\boldsymbol{\phi}_q = \begin{bmatrix} \mathbf{U}_q \\ s_q \mathbf{U}_q \\ \boldsymbol{\Phi}_q \end{bmatrix} \tag{6.43}$$

the mechanical participation factor is defined as

$$\eta_q^m = \frac{\|\mathbf{U}_q\|^2 + \|s_q \mathbf{U}_q\|^2}{\|\mathbf{U}_q\|^2 + \|s_q \mathbf{U}_q\|^2 + \|\boldsymbol{\Phi}_q\|^2} \tag{6.44}$$

The electrical-dominant roots are eliminated by imposing a lower bound on the mechanical participation factor. A positive-frequency root is retained as mechanically admissible only if

$$\eta_q^m \geq \eta_{\min}^m \tag{6.45}$$

where $\eta_{\min}^m$ is a prescribed tolerance.

The two electromechanical dispersion branches are then obtained by selecting the two mechanically dominant roots in $\mathcal{S}_+(\mu)$ and ordering them by increasing damped frequency

$$0 < \mathrm{Im}\left[s_L(\mu)\right] \leq \mathrm{Im}\left[s_U(\mu)\right] \tag{6.46}$$

The lower and upper branch frequencies are then

$$\omega_L(\mu) = \mathrm{Im}\left[s_L(\mu)\right] \tag{6.47a}$$
$$\omega_U(\mu) = \mathrm{Im}\left[s_U(\mu)\right] \tag{6.47b}$$

The corresponding temporal decay rates are

$$\sigma_L(\mu) = -\operatorname{Re}\left[s_L(\mu)\right] \tag{6.48a}$$
$$\sigma_U(\mu) = -\operatorname{Re}\left[s_U(\mu)\right] \tag{6.48b}$$

In the conservative mechanical limit, the piezoelectric coupling is removed by setting

$$\Theta = 0 \tag{6.49}$$

The electrical roots then decouple from the mechanical roots, and the mechanical part of Eq. (6.34) reduces to

$$\left(m_1 s^2 + A_s\right)\left(m_2 s^2 + A_s\right) - 4\left(r_a s^2 - k\right)^2 \mathcal{C}_\mu = 0 \tag{6.50}$$

For the conservative case, the temporal eigenvalue is purely imaginary and can be written as

$$s = \mathrm{i}\omega \tag{6.51}$$

Substitution of Eq. (6.51) into Eq. (6.50) gives

$$\left(A_s - m_1\omega^2\right)\left(A_s - m_2\omega^2\right) - 4\left(k + r_a\omega^2\right)^2 \mathcal{C}_\mu = 0 \tag{6.52}$$

Introducing

$$\Omega = \omega^2 \tag{6.53}$$

Eq. (6.52) becomes

$$a_2(\mu)\Omega^2 + a_1(\mu)\Omega + a_0(\mu) = 0 \tag{6.54}$$

where

$$a_2(\mu) = m_1 m_2 - 4r_a^2 \mathcal{C}_\mu \tag{6.55a}$$
$$a_1(\mu) = -A_s\left(m_1 + m_2\right) - 8kr_a\mathcal{C}_\mu \tag{6.55b}$$
$$a_0(\mu) = A_s^2 - 4k^2\mathcal{C}_\mu \tag{6.55c}$$

The two conservative mechanical solutions are

$$\Omega_\pm(\mu) = \frac{-a_1(\mu) \pm \sqrt{a_1^2(\mu) - 4a_2(\mu)a_0(\mu)}}{2a_2(\mu)} \tag{6.56}$$

The conservative lower and upper branch frequencies are obtained from the positive real values of $\Omega_\pm(\mu)$

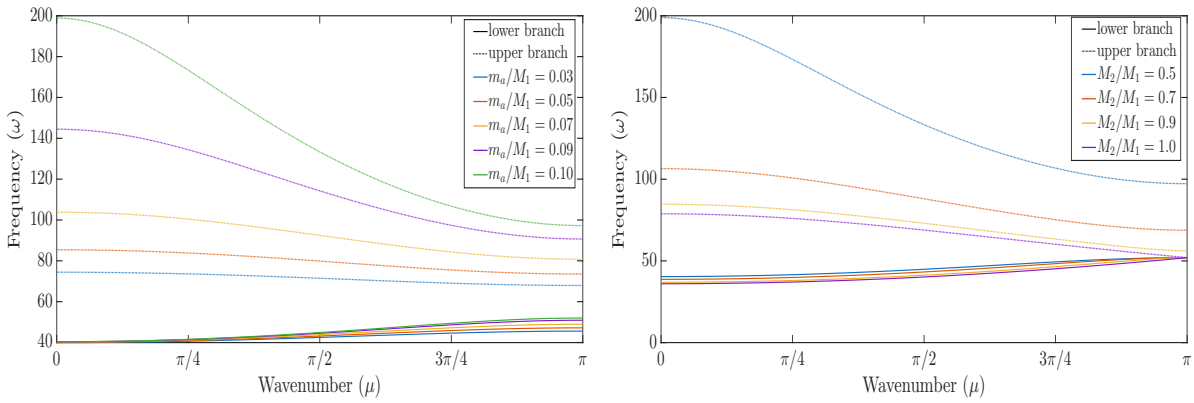
$$\omega_L^0(\mu) = \min\left[\sqrt{\Omega_+(\mu)}, \sqrt{\Omega_-(\mu)}\right] \tag{6.57a}$$
$$\omega_U^0(\mu) = \max\left[\sqrt{\Omega_+(\mu)}, \sqrt{\Omega_-(\mu)}\right] \tag{6.57b}$$

6.2.2 Bandstructure behavior with system parameters

The dispersion relations obtained with the piezoelectric harvesters are plotted with varying system parameters taking the initial angle α as $\sin\alpha = 0.5$.

Dispersion profiles with varying mass ratios

We plot the dispersion profiles while varying both the inerter mass-parameter ratio m_a/M_1 and the principal mass ratio M_2/M_1 with the spring stiffness kept fixed at $k = K_b$.



(a) Dispersion branches plotted with varying inerter mass ratio m_a/M_1 with the principal mass ratio kept fixed at $M_2/M_1 = 0.5$

(b) Dispersion branches plotted with varying principal mass ratio M_2/M_1 with the inerter mass ratio kept fixed at $m_a/M_1 = 0.1$

Fig. 6.5: Linearized dispersion branches plotted with varying mass ratios m_a/M_1 and M_2/M_1 with coupling spring stiffness kept fixed at $k = K_b$, solid curves represent lower acoustic-like branch and dotted curves represent upper optical-like branch.

Fig. 6.5(a) shows the dispersion branches for different inerter mass ratios m_a/M_1 while keeping the principal mass ratio fixed at $M_2/M_1 = 0.5$. The lower branch remains confined to a relatively narrow frequency range and increases mildly with the wavenumber, whereas the upper branch is strongly shifted upward as m_a/M_1 is increased. This indicates that the inertial-coupling mechanism affects the optical-like branch much more significantly than the acoustic-like branch, because the former is associated with stronger relative motion between neighboring masses. Consequently, increasing m_a/M_1 enlarges the frequency separation between the lower and upper branches and broadens the diatomic bandgap. The trend demonstrates that, within the positive definite effective inertia range, inertial coupling can be used as an effective tuning parameter for controlling the location and width of the acoustic–optical separation.

Fig. 6.5(b) shows the dispersion branches for different principal mass ratios M_2/M_1 while keeping the inerter mass ratio fixed at $m_a/M_1 = 0.1$. The largest branch separation occurs for the smallest value of M_2/M_1, where the mass contrast between the two sublattices is strongest. As M_2/M_1 increases, the upper branch moves downward and the gap between the lower and upper branches progressively decreases. This behavior confirms that the observed bandgap is primarily generated by mass diatomicity. When M_2/M_1 approaches unity, the two masses in the unit cell become dynamically identical, and the true mass-diatomic gap tends to collapse into the folded monoatomic dispersion representation. Thus M_2/M_1 ratio provides a direct means of tuning the acoustic–optical bandgap, while m_a/M_1 provides an additional inertance factor-based control over the branch locations.

Dispersion profiles with varying spring stiffness

Fig. 6.6 shows the piezoelectric dispersion branches for varying coupling spring stiffness ratios k/K_b, while keeping the mass ratios fixed at $m_a/M_1 = 0.1$ and $M_2/M_1 = 0.5$. Increasing k/K_b shifts both the lower and upper branches upward, since a stronger coupling

spring increases the effective restoring force of the periodic chain. However, the upward shift is observed in both branches in a broadly similar manner, so the frequency separation between the lower and upper branches does not change significantly. Therefore, unlike the inerter mass ratio or the principal mass ratio, the coupling stiffness does not strongly tune the effective acoustic–optical bandgap for the present parameter range. This indicates that k behaves as an almost neutral parameter from the viewpoint of bandgap-based attenuation and energy harvesting, although it still affects the absolute frequency range over which the branches appear.

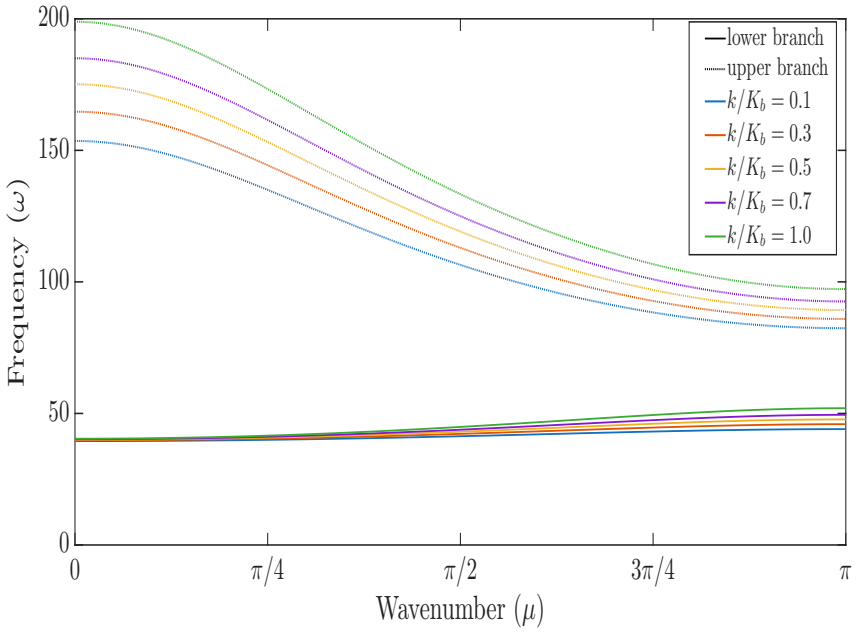


Fig. 6.6: Linearized dispersion branches plotted with varying coupling spring stiffness k with mass ratios kept fixed at $m_a/M_1 = 0.1$ and $M_2/M_1 = 0.5$, solid curves represent lower acoustic-like branch and dotted curves represent upper optical-like branch.

6.3 Energy harvesting in the linearized regime

6.3.1 Harvesting formulation

In the linearized regime, the energy harvesting response is evaluated about the stable uniform branch with the tangent stiffness defined as in Section 6.2.1. The voltage vector is extracted from the state vector defined in Section 6.2.1 using

$$\mathbf{v}(t) = \mathbf{C}_v \mathbf{x}_\mu(t) \tag{6.58}$$

where

$$\mathbf{C}_v = \begin{bmatrix} \mathbf{0}_2 & \mathbf{0}_2 & \mathbf{I}_2 \end{bmatrix} \tag{6.59}$$

All harvested power and energy quantities are interpreted per representative unit cell. For the complex Bloch-amplitude representation, the cycle-averaged harvested power per unit cell is

$$p_h(t;\mu) = \frac{G_l}{2} \mathbf{v}^H(t)\mathbf{v}(t) \tag{6.60}$$

Using Eq. (6.58), Eq. (6.60) becomes

$$p_h(t;\mu) = \frac{G_l}{2}\mathbf{x}_\mu^H(t)\mathbf{C}_v^H\mathbf{C}_v\mathbf{x}_\mu(t) \tag{6.61}$$

The harvested energy per unit cell over the time interval $[0, T]$ is

$$e_h(T;\mu) = \int_0^T p_h(t;\mu)\,dt \tag{6.62}$$

For a Bloch-reduced initial condition $\mathbf{x}_\mu(0) = \mathbf{x}_{\mu,0}$, the free response is

$$\mathbf{x}_\mu(t) = e^{\mathbf{A}_\mu t}\mathbf{x}_{\mu,0} \tag{6.63}$$

Substitution of Eq. (6.63) into Eq. (6.62) gives

$$e_h(T;\mu) = \frac{G_l}{2}\int_0^T \mathbf{x}_{\mu,0}^H e^{\mathbf{A}_\mu^H t}\mathbf{C}_v^H\mathbf{C}_v e^{\mathbf{A}_\mu t}\mathbf{x}_{\mu,0}\,dt \tag{6.64}$$

The same expression can be written using the finite-time harvesting Gramian

$$e_h(T;\mu) = \mathbf{x}_{\mu,0}^H\mathbf{W}_h(T;\mu)\mathbf{x}_{\mu,0} \tag{6.65}$$

where

$$\mathbf{W}_h(T;\mu) = \frac{G_l}{2}\int_0^T e^{\mathbf{A}_\mu^H t}\mathbf{C}_v^H\mathbf{C}_v e^{\mathbf{A}_\mu t}\,dt \tag{6.66}$$

The initial stored electromechanical energy per representative unit cell is defined as

$$e_0(\mu) = \frac{1}{4}\dot{\mathbf{u}}_0^H\mathbf{M}_\mu\dot{\mathbf{u}}_0 + \frac{1}{4}\mathbf{u}_0^H\mathbf{K}_\mu\mathbf{u}_0 + \frac{1}{4}C_p\mathbf{v}_0^H\mathbf{v}_0 \tag{6.67}$$

For initially uncharged piezoelectric circuits,

$$\mathbf{v}_0 = \mathbf{0} \tag{6.68}$$

The normalized harvested energy per representative unit cell is then

$$\eta_h(T;\mu) = \frac{e_h(T;\mu)}{e_0(\mu)} \tag{6.69}$$

The average harvested power over $[0, T]$ is

$$\overline{p}_h(T;\mu) = \frac{e_h(T;\mu)}{T} \tag{6.70}$$

The branch-wise harvesting response is obtained from the Bloch state-space eigenvalue problem

$$(s\mathbf{I} - \mathbf{A}_\mu)\,\boldsymbol{\phi} = \mathbf{0} \tag{6.71}$$

The eigenvalue associated with dispersion branch b is written as

$$s_b(\mu) = -\sigma_b(\mu) + i\omega_b(\mu) \tag{6.72}$$

where

$$b \in \{L, U\} \tag{6.73}$$

The corresponding right eigenvector is partitioned as

$$\boldsymbol{\phi}_b(\mu) = \begin{bmatrix} \mathbf{U}_b(\mu) \\ s_b(\mu)\mathbf{U}_b(\mu) \\ \boldsymbol{\Phi}_b(\mu) \end{bmatrix} \tag{6.74}$$

where

$$\mathbf{U}_b(\mu) = \begin{bmatrix} U_{1,b}(\mu) \\ U_{2,b}(\mu) \end{bmatrix} \tag{6.75a}$$

$$\mathbf{\Phi}_b(\mu) = \begin{bmatrix} \Phi_{1,b}(\mu) \\ \Phi_{2,b}(\mu) \end{bmatrix} \tag{6.75b}$$

A branch-pure Bloch free wave in the representative unit cell is written as

$$\mathbf{x}_\mu^{(b)}(t) = a_b \boldsymbol{\phi}_b(\mu) e^{s_b(\mu)t} \tag{6.76}$$

The modal amplitude a_b is determined from the Bloch-reduced initial condition. If $\boldsymbol{\psi}_b(\mu)$ is the corresponding left eigenvector, then

$$a_b = \frac{\boldsymbol{\psi}_b^H(\mu)\mathbf{x}_{\mu,0}}{\boldsymbol{\psi}_b^H(\mu)\boldsymbol{\phi}_b(\mu)} \tag{6.77}$$

The voltage components associated with branch b are

$$v_1^{(b)}(t) = a_b \Phi_{1,b}(\mu) e^{s_b(\mu)t} \tag{6.78a}$$

$$v_2^{(b)}(t) = a_b \Phi_{2,b}(\mu) e^{s_b(\mu)t} \tag{6.78b}$$

The cycle-averaged harvested power per representative unit cell associated with branch b at time t over a local pseudo-cycle defined by $T_b = \frac{2\pi}{\omega_b}$, assuming a slowly varying envelope, is hence obtained as

$$\overline{p}_{h,b}(t;\mu) = \frac{|a_b|^2}{2R_l}\left[|\Phi_{1,b}(\mu)|^2 + |\Phi_{2,b}(\mu)|^2\right] e^{-2\sigma_b(\mu)t} \tag{6.79}$$

The harvested energy per representative unit cell from branch b over $[0, T]$, where T is a time window chosen by us is thus obtained as

$$e_{h,b}(T;\mu) = \frac{\overline{p}_{h,b}^0(\mu)}{2\sigma_b(\mu)}\left[1 - e^{-2\sigma_b(\mu)T}\right] \tag{6.80}$$

where $\overline{p}_{h,b}^0(\mu) = \frac{|a_b|^2}{2R_l}\left[|\Phi_{1,b}(\mu)|^2 + |\Phi_{2,b}(\mu)|^2\right]$. Since in our dissipative electromechanical chain, in the linearized regime, the displacements settle down to the initial stable uniform branch, the harnessed voltage and hence the harvested energy decay eventually to zero. The infinite-time branch-wise harvested energy per representative unit cell is hence given by

$$e_{h,b}^\infty(\mu) = \frac{\overline{p}_{h,b}^0(\mu)}{2\sigma_b(\mu)} \tag{6.81}$$

The branch-wise settling time is defined as the time required for the response along that branch to get rid of the initial oscillatory transients represented by $\mathrm{i}\omega_b$ and settle on a smooth decaying envelope within a specified tolerance of ϵ and is obtained in a general form from controls theory of Linear Time Invariant (LTI) systems as done before in Chapters 4 and 5 as:

$$t_{s,b}(\mu) = \frac{\ln(1/\epsilon)}{\sigma_b(\mu)} \tag{6.82}$$

The damped modal oscillation period associated with branch b is defined as

$$T_b(\mu) = \frac{2\pi}{\omega_b(\mu)} \tag{6.83}$$

The exact physical voltage response of the r-th harvester in the representative unit cell is obtained from the real part of the complex modal voltage response as

$$v_{r,\mathrm{phys}}^{(b)}(t;\mu) = \mathrm{Re}\left[a_b \Phi_{r,b}(\mu) e^{s_b(\mu)t}\right], \qquad r = 1, 2 \tag{6.84}$$

The exact instantaneous harvested power per representative unit cell is therefore

$$p_{h,b}(t;\mu) = \frac{1}{R_l} \sum_{r=1}^{2} \left[v_{r,\mathrm{phys}}^{(b)}(t;\mu)\right]^2 \tag{6.85}$$

For compactness, the following voltage-amplitude measures are introduced

$$S_b(\mu) = |\Phi_{1,b}(\mu)|^2 + |\Phi_{2,b}(\mu)|^2 \tag{6.86a}$$

$$Q_b(\mu) = \Phi_{1,b}^2(\mu) + \Phi_{2,b}^2(\mu) \tag{6.86b}$$

Using $s_b(\mu) = -\sigma_b(\mu) + i\omega_b(\mu)$, Eq. (6.85) can be written as

$$p_{h,b}(t;\mu) = \frac{e^{-2\sigma_b(\mu)t}}{2R_l} \left\{|a_b|^2 S_b(\mu) + \mathrm{Re}\left[a_b^2 Q_b(\mu) e^{2i\omega_b(\mu)t}\right]\right\} \tag{6.87}$$

The harvested energy in a post-settling oscillation window starting at t_0 is defined as

$$e_{h,b}^{w}(t_0;\mu) = \int_{t_0}^{t_0+T_b(\mu)} p_{h,b}(t;\mu)\, dt \tag{6.88}$$

Substitution of Eq. (6.87) into Eq. (6.88) gives

$$\begin{aligned} e_{h,b}^{w}(t_0;\mu) = {} & \frac{|a_b|^2 S_b(\mu)}{2R_l} \frac{e^{-2\sigma_b(\mu)t_0} - e^{-2\sigma_b(\mu)[t_0+T_b(\mu)]}}{2\sigma_b(\mu)} \\ & + \frac{1}{2R_l}\,\mathrm{Re}\left[a_b^2 Q_b(\mu) \frac{e^{\lambda_b(\mu)[t_0+T_b(\mu)]} - e^{\lambda_b(\mu)t_0}}{\lambda_b(\mu)}\right] \end{aligned} \tag{6.89}$$

where

$$\lambda_b(\mu) = -2\sigma_b(\mu) + 2i\omega_b(\mu) \tag{6.90}$$

The corresponding post-settling window-averaged harvested power is

$$\overline{p}_{h,b}^{w}(t_0;\mu) = \frac{e_{h,b}^{w}(t_0;\mu)}{T_b(\mu)} \tag{6.91}$$

Following the settling-time based procedure, the first post-settling window is obtained by setting

$$t_0 = t_{s,b}(\mu) \tag{6.92}$$

Thus, the first post-settling harvested energy and power are introduced as

$$e_{h,b}^{\mathrm{ps}}(\mu) = e_{h,b}^{w}\left(t_{s,b}(\mu);\mu\right) \tag{6.93a}$$

$$\overline{p}_{h,b}^{\mathrm{ps}}(\mu) = \overline{p}_{h,b}^{w}\left(t_{s,b}(\mu);\mu\right) \tag{6.93b}$$

If the maximum post-settling harvested power is to be searched over multiple oscillation windows, the admissible window indices are defined as

$$\mathcal{M}_b(\mu) = \{m \in \mathbb{N}_0 : t_{s,b}(\mu) + (m+1)\, T_b(\mu) \le T_f\} \tag{6.94}$$

where T_f is the final observation time. The optimal post-settling window index is then

$$m_b^*(\mu) = \underset{m \in \mathcal{M}_b(\mu)}{\arg\max}\, \overline{p}_{h,b}^{w}\left(t_{s,b}(\mu) + mT_b(\mu);\mu\right) \tag{6.95}$$

The maximum post-settling harvested power for branch b is

$$\overline{p}_{h,b}^{\max}(\mu) = \overline{p}_{h,b}^{w}\left(t_{s,b}(\mu) + m_b^*(\mu)T_b(\mu);\mu\right) \tag{6.96}$$

The corresponding harvested energy in the optimal post-settling window is

$$e_{h,b}^{\max}(\mu) = e_{h,b}^{w}\left(t_{s,b}(\mu) + m_b^*(\mu)T_b(\mu);\mu\right) \tag{6.97}$$

The normalized harvested energy in the optimal post-settling window is

$$\eta_{h,b}^{\max}(\mu) = \frac{e_{h,b}^{\max}(\mu)}{e_{0,b}(\mu)} \tag{6.98}$$

The optimal linearized Bloch free-wave harvesting condition is then obtained by maximizing the post-settling harvested power over the lower and upper branches and over the first Brillouin zone

$$(b^*, \mu^*) = \underset{b\in\{L,U\},\ \mu\in[0,\pi]}{\arg\max}\ \overline{p}_{h,b}^{\max}(\mu) \tag{6.99}$$

The corresponding optimal operating frequency can then be obtained from the dispersion branches defined in Section 6.2 as

$$\omega^* = \omega_{b^*}(\mu^*) \tag{6.100}$$

For a Bloch-reduced initial condition that excites both branches, the exact harvested energy per representative unit cell is evaluated from Eq. (6.64). When the lower and upper branch frequencies are sufficiently separated, the harvested energy can be approximated as

$$e_h(T;\mu) \approx e_{h,L}(T;\mu) + e_{h,U}(T;\mu) \tag{6.101}$$

In the no-piezo limit,

$$\Theta = 0 \tag{6.102}$$

the voltage response vanishes as

$$\mathbf{\Phi}_b(\mu) = \mathbf{0} \tag{6.103}$$

Therefore,

$$\overline{p}_{h,b}^{0}(\mu) = 0 \tag{6.104a}$$

$$e_{h,b}(T;\mu) = 0 \tag{6.104b}$$

$$\eta_{h,b}^{s}(\mu) = 0 \tag{6.104c}$$

Thus, in the linearized Bloch-reduced regime, the conservative no-piezo branches provide the reference wave dynamics, whereas the piezoelectric branches quantify electromechanical energy conversion through the voltage amplitudes, modal decay rates, and branch-wise harvested energy per representative unit cell.

6.3.2 Power variation with wavenumber

We investigate how the harvested maximum steady-state power obtained using the formulation presented in Section 6.3.1 varies with the wavenumber μ in the linearized regime.

In the linearized regime, the dispersion branches and the associated bandgaps are intrinsic properties of the Bloch-reduced electromechanical eigenvalue problem and are therefore determined solely by the system matrices and the Bloch wavenumber μ, not by

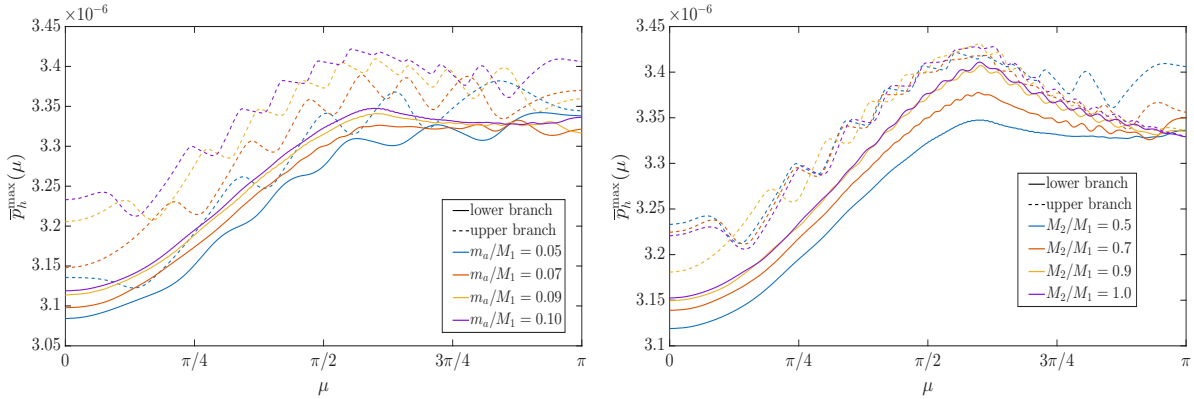
the chosen initial conditions. In contrast, the harvested power obtained from the post-settling formulation depends explicitly on the initial perturbation through its projection onto the complex Bloch eigenvectors, since the initial state fixes the modal distribution, the relative excitation levels of the lower and upper branches, and the resulting interference between the corresponding modal contributions. Consequently, different initial perturbations can produce markedly different power curves even though the underlying dispersion structure remains unchanged. We choose a representative set of initial conditions on the perturbations of the masses M_1 and M_2 given by $[u_1(0), u_2(0)] = [+Y_s, +Y_s]$ and consider the initial velocities and voltages to be zero. This simplest set of initial displacement perturbations seems to produce a peak-like harvested power characteristic related to both the dispersion branches at a particular value of wavenumber and hence free wave frequency.

As per our formulation developed in Section 6.3.1 to characterize maximum harvested power in the sense of steady state for our inherently dissipative system when the system dynamics loses its initial oscillatory transients and evolves along a smooth envelope, we define the two power branches as:

- Lower branch–After computing the lower dispersion branch frequency $\omega_L(\mu)$ from Section 6.2, the post-settling power is evaluated over one-period windows of length $T_L(\mu) = \frac{2\pi}{\omega_L(\mu)}$.
- Upper branch–After computing the upper dispersion branch frequency $\omega_U(\mu)$ from Section 6.2, the post-settling power is evaluated over one-period windows of length $T_U(\mu) = \frac{2\pi}{\omega_U(\mu)}$.

Harvested power behavior with mass ratio

First, we vary the inerter mass ratio m_a/M_1 and the principal mass ratio M_2/M_1 keeping the coupling spring stiffness fixed at $k = 0.1K_b$.



(a) Power vs wavenumber μ plotted with varying inerter mass ratio m_a/M_1 with the principal mass ratio kept fixed at $M_2/M_1 = 0.5$

(b) Power vs wavenumber μ plotted with varying principal mass ratio M_2/M_1 with the inerter mass ratio kept fixed at $m_a/M_1 = 0.1$

Fig. 6.7: Power vs wavenumber μ in the linearized regime plotted with varying mass ratios m_a/M_1 and M_2/M_1 with coupling spring stiffness kept fixed at $k = 0.1K_b$, solid curves represent lower branch and dotted curves represent upper branch.

Fig. 6.7(a) shows the post-settling harvested power as a function of the Bloch wavenumber μ in the linearized regime for different inerter mass ratios m_a/M_1, while keeping $M_2/M_1 = 0.5$. Both the lower branch period and upper branch period power curves increase from the long-wavelength region and attain their highest values in the intermediate wavenumber range, approximately around the middle of the Brillouin zone. Increasing m_a/M_1 within the positive-definite inertia range generally raises the harvested power level and modifies the location and sharpness of the peak, indicating that negative-inertance magnitude improves the electromechanical energy-transfer capability by enhancing the relative-motion contribution between the two sublattices. The upper branch period curves exhibit stronger local undulations, which is expected because the upper branch is more sensitive to the relative acceleration mechanism and to the mixed modal content generated by the imposed initial perturbation. It can also be seen that within the positive-definite effective inertia range $m_a/M_1 \leq 0.1$, higher values of the inerter mass-parameter produce an intermediate power peak within the Brillouin zone $0 < \mu < \pi$, whereas lower values of inerter mass-parameter produce a power characteristic that tends to attain a maximum value at the right edge of the Brillouin zone at $\mu = \pi$. This certainly provides a design advantage for higher negative-inertance magnitudes compared to lower, because the edges of the Brillouin zone being sensitive to Bragg reflection, boundary conditions and structural perturbations, an intermediate power peak is always more desirable than a maxima at the zone boundaries.

Fig. 6.7(b) shows the corresponding variation of harvested power in the linearized regime with the principal mass ratio M_2/M_1, while keeping $m_a/M_1 = 0.1$. The power curves again show a clear rise from $\mu = 0$ toward an intermediate wavenumber peak, followed by a gradual reduction toward the Brillouin-zone boundary. Compared with the inerter mass ratio, the principal mass ratio changes the power curves more moderately for the present parameter range, although increasing M_2/M_1 shifts the relative levels of the lower and upper branch responses. One direct correlation with the band structure behavior is noticeable immediately, which is with M_2/M_1 increasing from 0.5 to 1 where the unit cell loses its diatomicity and the two masses get close to being identical, the lower and the upper power branches also approach each other. These observations collectively indicate that the harvested power is influenced not only by the band structure but also by how the prescribed initial perturbation projects onto the complex Bloch eigenvectors of the two branches. Thus, while M_2/M_1 controls the mass-diatomic splitting, the most effective harvesting response occurs when the modal voltage participation and the initial condition-induced modal distribution are favorably aligned in the intermediate wavenumber region. Also, it can be noticed that a sharper contrast between the masses, i.e. a larger degree of diatomicity represented by values of M_2/M_1 significantly smaller than 1, within the positive-definite effective inertia range, produces a power characteristic that increases to a maximum optimal and tends to remain fairly saturated at that value henceforth for the remaining admissible wavenumber range, whereas values of M_2/M_1 closer to 1 tend to produce a power curve which decays from a maximum value towards comparatively lower magnitudes. Since high and almost-saturated power harvesting is an improved design objective, using a diatomic model tends to offer this significant advantage over a monoatomic version of the chain.

Harvested power behavior with coupling spring stiffness

We now keep the inerter mass ratio and the principal mass ratio fixed at $m_a/M_1 = 0.1$ and $M_2/M_1 = 0.5$ and plot the power vs wavenumber behavior with varying coupling spring stiffness k.

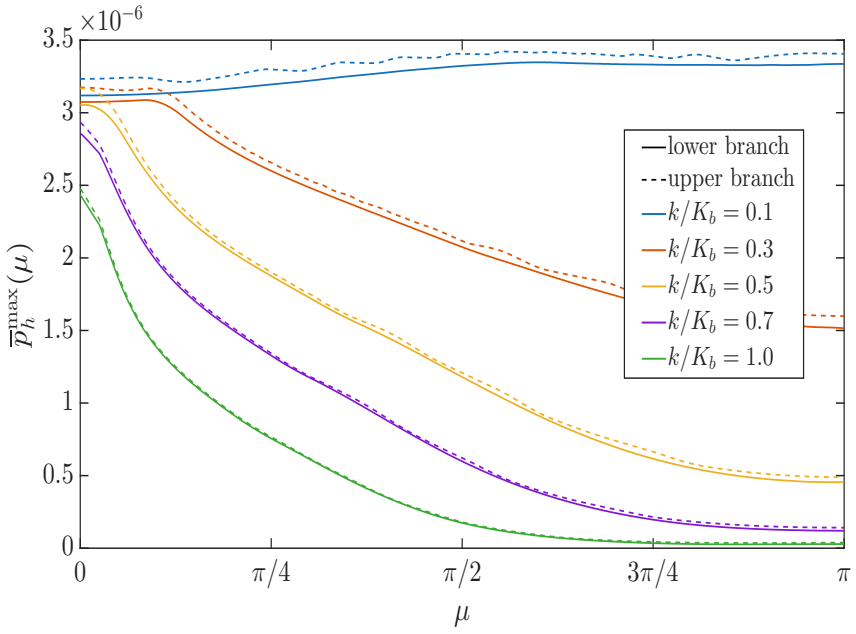


Fig. 6.8: Power vs wavenumber μ in the linearized regime plotted with varying coupling spring stiffness k with mass ratios kept fixed at $m_a/M_1 = 0.1$ and $M_2/M_1 = 0.5$, solid curves represent lower branch and dashed curves represent upper branch.

Fig. 6.8 shows that the coupling stiffness has a strong influence on the post-settling harvested power characteristic, even though its effect on the band structure is comparatively neutral. As was observed in Fig. 6.6, increasing k/K_b shifts both the lower acoustic-like and upper optical-like branches upward in a similar manner, so the effective separation between the two branches and hence the associated bandgap do not change significantly. However, the harvested-power curves in Fig. 6.8 show that increasing k/K_b progressively suppresses the power level over most of the Brillouin zone, especially away from the long-wavelength limit. This indicates that although the coupling stiffness does not act as a strong bandgap-tuning parameter, it modifies the modal response and the voltage-producing deformation amplitudes associated with the imposed initial perturbation. For larger k/K_b, the stronger coupling makes the sublattice motion more constrained and reduces the effective electromechanical response over the intermediate and high-wavenumber regions, leading to a rapid decay of harvested power with μ. Thus, from the harvesting viewpoint, a relatively low coupling stiffness is more favorable for maintaining high post-settling power over a broader wavenumber range atleast in the linearized regime. Also, one more noticeable feature is that increasing k/K_b brings the two power branches closer with the branches almost merging with each other, when the coupling stiffness gets equal/ comparable to the onsite effective structural stiffness K_b.

6.4 General strongly nonlinear regime

6.4.1 Long-wavelength continuum limit of the diatomic chain for studying snap-through transition fronts

Starting from the exact discrete equations of motion in Eqs. (6.6a)–(6.6d), the local nonlinear restoring force of each piezomagnetoelastic oscillator is written as

$$\mathcal{F}(Y) = (K_b + 2c_1)\, Y + 4c_2 Y^3 \tag{6.105}$$

For simplicity, we consider all masses in the chain, i.e., nearest neighbor masses in a unit cell and adjacent masses in adjacent unit cells, to be located at an equal spacing from each other. Let ℓ denote this equal distance of adjacent masses of the homogeneous diatomic chain. In the long-wavelength limit, the two sublattice displacements and voltages are represented by smooth fields

$$Y_{1,n}(t) \to Y_1(s,t), \qquad V_{1,n}(t) \to V_1(s,t) \tag{6.106a}$$

$$Y_{2,n}(t) \to Y_2(s,t), \qquad V_{2,n}(t) \to V_2(s,t) \tag{6.106b}$$

$s = m\ell$ denoting the position variable along the axial direction of the periodic chain where m is the mass index. The neighboring sublattice fields are expanded in Taylor series about the corresponding mass location considering the mass in a particular governing equation of motion as a reference position. Hence, we get

$$Y_{2,n} + Y_{2,n-1} = 2Y_2 + \ell^2 Y_{2,ss} + \mathcal{O}(\ell^4) \tag{6.107a}$$

$$Y_{1,n} + Y_{1,n+1} = 2Y_1 + \ell^2 Y_{1,ss} + \mathcal{O}(\ell^4) \tag{6.107b}$$

The same expansion is used for the acceleration fields. Retaining terms up to $\mathcal{O}(\ell^2)$ for long-wavelength limit $\ell/\lambda << 1$, gives the two-field nonlinear continuum model

$$M_1 Y_{1,tt} + \mathcal{F}(Y_1) + k\left[2(Y_1 - Y_2) - \ell^2 Y_{2,ss}\right] - r_a\left[2(Y_{1,tt} - Y_{2,tt}) - \ell^2 Y_{2,sstt}\right] - \Theta V_1 = 0 \tag{6.108a}$$

$$M_2 Y_{2,tt} + \mathcal{F}(Y_2) + k\left[2(Y_2 - Y_1) - \ell^2 Y_{1,ss}\right] - r_a\left[2(Y_{2,tt} - Y_{1,tt}) - \ell^2 Y_{1,sstt}\right] - \Theta V_2 = 0 \tag{6.108b}$$

$$C_p V_{1,t} + G_l V_1 + \Theta Y_{1,t} = 0 \tag{6.108c}$$

$$C_p V_{2,t} + G_l V_2 + \Theta Y_{2,t} = 0 \tag{6.108d}$$

where

$$G_l = \frac{1}{R_l} \tag{6.109}$$

To expose the acoustic-like and optical-like continuum fields, the mean and contrast variables are introduced as

$$Y = \frac{Y_1 + Y_2}{2}, \qquad Z = \frac{Y_1 - Y_2}{2} \tag{6.110a}$$

$$V = \frac{V_1 + V_2}{2}, \qquad W_e = \frac{V_1 - V_2}{2} \tag{6.110b}$$

The total and difference masses are defined as

$$M_\Sigma = M_1 + M_2, \qquad M_\Delta = M_1 - M_2 \tag{6.111}$$

The nonlinear force combinations are then defined as

$$\mathcal{F}_+(Y,Z) = \mathcal{F}(Y+Z) + \mathcal{F}(Y-Z) \tag{6.112a}$$
$$\mathcal{F}_-(Y,Z) = \mathcal{F}(Y+Z) - \mathcal{F}(Y-Z) \tag{6.112b}$$

Using Eqs. (6.110)–(6.112), the continuum equations become

$$\frac{M_\Sigma}{2}Y_{tt} + \frac{M_\Delta}{2}Z_{tt} + \frac{1}{2}\mathcal{F}_+(Y,Z) - k\ell^2 Y_{ss} + r_a\ell^2 Y_{sstt} - \Theta V = 0 \tag{6.113a}$$
$$\frac{M_\Delta}{2}Y_{tt} + \left(\frac{M_\Sigma}{2} - 4r_a\right)Z_{tt} + \frac{1}{2}\mathcal{F}_-(Y,Z) + 4kZ + k\ell^2 Z_{ss} - r_a\ell^2 Z_{sstt} - \Theta W_e = 0 \tag{6.113b}$$
$$C_p V_t + G_l V + \Theta Y_t = 0 \tag{6.113c}$$
$$C_p W_{e,t} + G_l W_e + \Theta Z_t = 0 \tag{6.113d}$$

For explicit nonlinear calculations, the force combinations can be written as

$$\mathcal{F}_+(Y,Z) = 2(K_b + 2c_1)Y + 8c_2Y^3 + 24c_2YZ^2 \tag{6.114a}$$
$$\mathcal{F}_-(Y,Z) = 2(K_b + 2c_1)Z + 24c_2Y^2Z + 8c_2Z^3 \tag{6.114b}$$

Eqs. (6.113) provide the long-wavelength analytical framework for the mass-diatomic piezomagnetoelastic chain. The field $Y(x,t)$ represents the acoustic-like mean motion, while $Z(x,t)$ represents the optical-like internal contrast motion generated by the diatomicity. The harvested power density per representative continuum unit cell is

$$p_h(x,t) = \frac{V_1^2 + V_2^2}{R_l} = \frac{2}{R_l}\left[V^2 + W_e^2\right] \tag{6.115}$$

6.4.2 Analytical leading-order transition fronts

For interwell front calculations in the strongly nonlinear regime, the continuum fields may be reduced using a traveling coordinate ξ with the leading traveling-front representation

$$Y(s,t) = \mathcal{Y}(\xi), \qquad Z(s,t) = \mathcal{Z}(\xi) \tag{6.116a}$$
$$V(s,t) = \mathcal{V}(\xi), \qquad W_e(s,t) = \mathcal{W}_e(\xi) \tag{6.116b}$$

This representation converts Eq. (6.113) into a coupled acoustic–optical front system with piezoelectric voltage fields slaved through Eqs. (6.113c) and (6.113d). The slowly modulated front coordinate is now introduced as

$$\xi = \frac{s - X(t)}{W(t)} \tag{6.117}$$

where

$$c(t) = \dot{X}(t) \tag{6.118}$$

Here $X(t)$ is the instantaneous front center, $c(t)$ is the instantaneous front speed, and $W(t)$ is the slowly varying front width. The slowly modulated front ansatz is written as

$$Y(s,t) = \mathcal{Y}(\xi), \qquad Z(s,t) = \mathcal{Z}(\xi) \tag{6.119a}$$
$$V(s,t) = \mathcal{V}(\xi), \qquad W_e(s,t) = \mathcal{W}_e(\xi) \tag{6.119b}$$

The slow front modulation conditions are imposed as

$$\frac{\dot{W}}{c} = O(\epsilon_m), \qquad \frac{W\ddot{X}}{c^2} = O(\epsilon_m), \qquad \frac{W\ddot{W}}{c^2} = O(\epsilon_m), \qquad 0 < \epsilon_m \ll 1 \tag{6.120}$$

Using Eq. (6.117), the reduced coordinate satisfies

$$\xi_s = \frac{1}{W}, \qquad \xi_t = -\frac{c + \dot{W}\xi}{W} \tag{6.121}$$

For the front core $|\xi| = O(1)$, Eq. (6.120) gives the leading-order derivative rules

$$\mathcal{A}_t = -\frac{c}{W}\mathcal{A}' + O(\epsilon_m), \qquad \mathcal{A}_{tt} = \frac{c^2}{W^2}\mathcal{A}'' + O(\epsilon_m) \tag{6.122a}$$

$$\mathcal{A}_{ss} = \frac{1}{W^2}\mathcal{A}'', \qquad \mathcal{A}_{sstt} = \frac{c^2}{W^4}\mathcal{A}^{(4)} + O(\epsilon_m) \tag{6.122b}$$

where $\mathcal{A} \in \{\mathcal{Y}, \mathcal{Z}\}$ and the prime denotes differentiation with respect to ξ. Similarly, the voltage fields satisfy

$$V_t = -\frac{c}{W}\mathcal{V}' + O(\epsilon_m) \tag{6.123a}$$

$$W_{e,t} = -\frac{c}{W}\mathcal{W}_e' + O(\epsilon_m) \tag{6.123b}$$

Substitution of Eqs. (6.122) and (6.123) into the long-wavelength continuum equations gives the leading-order frozen-time front system

$$\frac{r_a \ell^2 c^2}{W^4}\mathcal{Y}^{(4)} + \frac{M_\Sigma c^2 - 2k\ell^2}{2W^2}\mathcal{Y}'' + \frac{M_\Delta c^2}{2W^2}\mathcal{Z}'' + \frac{1}{2}\mathcal{F}_+(\mathcal{Y}, \mathcal{Z}) - \Theta\mathcal{V} = 0 \tag{6.124a}$$

$$-\frac{r_a \ell^2 c^2}{W^4}\mathcal{Z}^{(4)} + \frac{M_\Delta c^2}{2W^2}\mathcal{Y}'' + \frac{(M_\Sigma - 8r_a)\,c^2 + 2k\ell^2}{2W^2}\mathcal{Z}'' + \frac{1}{2}\mathcal{F}_-(\mathcal{Y}, \mathcal{Z}) + 4k\mathcal{Z} - \Theta\mathcal{W}_e = 0 \tag{6.124b}$$

$$-\frac{cC_p}{W}\mathcal{V}' + G_l\mathcal{V} - \frac{c\Theta}{W}\mathcal{Y}' = 0 \tag{6.124c}$$

$$-\frac{cC_p}{W}\mathcal{W}_e' + G_l\mathcal{W}_e - \frac{c\Theta}{W}\mathcal{Z}' = 0 \tag{6.124d}$$

The nonlinear force combinations are evaluated along the front as

$$\mathcal{F}_+(\mathcal{Y}, \mathcal{Z}) = 2(K_b + 2c_1)\mathcal{Y} + 8c_2\mathcal{Y}^3 + 24c_2\mathcal{Y}\mathcal{Z}^2 \tag{6.125a}$$

$$\mathcal{F}_-(\mathcal{Y}, \mathcal{Z}) = 2(K_b + 2c_1)\mathcal{Z} + 24c_2\mathcal{Y}^2\mathcal{Z} + 8c_2\mathcal{Z}^3 \tag{6.125b}$$

The voltage equations may equivalently be written in slaved first-order form as

$$\mathcal{V}' - \frac{G_l W}{cC_p}\mathcal{V} = -\frac{\Theta}{C_p}\mathcal{Y}' \tag{6.126a}$$

$$\mathcal{W}_e' - \frac{G_l W}{cC_p}\mathcal{W}_e = -\frac{\Theta}{C_p}\mathcal{Z}' \tag{6.126b}$$

For an interwell front connecting the two stable uniform branches, the leading boundary conditions are

$$\mathcal{Y}(-\infty) = -Y_s, \qquad \mathcal{Y}(+\infty) = Y_s \tag{6.127a}$$

$$\mathcal{Z}(-\infty) = 0, \qquad \mathcal{Z}(+\infty) = 0 \tag{6.127b}$$

$$\mathcal{Y}'(\pm\infty) = \mathcal{Z}'(\pm\infty) = 0, \qquad \mathcal{Y}''(\pm\infty) = \mathcal{Z}''(\pm\infty) = 0 \tag{6.127c}$$

$$\mathcal{V}(\pm\infty) = 0, \qquad \mathcal{W}_e(\pm\infty) = 0 \tag{6.127d}$$

To obtain a leading-order analytical front, the transition is assumed to be acoustic-dominant, with the optical-like contrast field appearing as a correction to the mean front.

The bi-stable stiffness parameter is defined as

$$a = K_b + 2c_1 \tag{6.128}$$

with

$$Y_s = \sqrt{-\frac{a}{4c_2}} \tag{6.129}$$

The dominant acoustic-like front is obtained by setting

$$\mathcal{Z} = 0 \tag{6.130}$$

and neglecting the piezoelectric back-action and the higher-order dispersive correction in Eq. (6.124a). This gives

$$\frac{M_\Sigma c^2 - 2k\ell^2}{2W^2}\mathcal{Y}_0'' + a\mathcal{Y}_0 + 4c_2\mathcal{Y}_0^3 = 0 \tag{6.131}$$

A heteroclinic transition satisfying Eq. (6.127a) is hence obtained as

$$\mathcal{Y}_0(\xi) = Y_s \tanh\xi \tag{6.132}$$

provided that the instantaneous front width satisfies

$$W^2(t) = \frac{2k\ell^2 - M_\Sigma c^2(t)}{-a} \tag{6.133}$$

which requires

$$2k\ell^2 > M_\Sigma c^2(t) \tag{6.134}$$

The optical-like correction is then introduced as

$$\mathcal{Y}(\xi) = \mathcal{Y}_0(\xi), \qquad \mathcal{Z}(\xi) = \mathcal{Z}_1(\xi), \qquad |\mathcal{Z}_1| \ll |\mathcal{Y}_0| \tag{6.135}$$

Retaining terms linear in $\mathcal{Z}_1$ in Eq. (6.124b), while neglecting the higher-order fourth-derivative correction, gives the second-order inhomogeneous equation

$$D_Z\mathcal{Z}_1'' + \left[4k + a + 12c_2\mathcal{Y}_0^2(\xi)\right]\mathcal{Z}_1 = -\frac{M_\Delta c^2}{2W^2}\mathcal{Y}_0'' \tag{6.136}$$

where

$$D_Z = \frac{(M_\Sigma - 8r_a)c^2 + 2k\ell^2}{2W^2} \tag{6.137}$$

Using Eq. (6.132), Eq. (6.136) becomes

$$D_Z\mathcal{Z}_1'' + \left[4k - 2a + 3a\ \mathrm{sech}^2\,\xi\right]\mathcal{Z}_1 = \frac{M_\Delta c^2 Y_s}{W^2}\,\mathrm{sech}^2\,\xi\,\tanh\xi \tag{6.138}$$

The optical correction is solved subject to the localized front conditions

$$\mathcal{Z}_1(-\infty) = 0, \qquad \mathcal{Z}_1(+\infty) = 0, \qquad \mathcal{Z}_1'(\pm\infty) = 0 \tag{6.139}$$

Since the forcing term in the r.h.s of Eq. (6.138) is odd in ξ, the localized correction is also considered to be odd

$$\mathcal{Z}_1(-\xi) = -\mathcal{Z}_1(\xi) \tag{6.140}$$

At each frozen value of the slowly varying quantities $c(t)$ and $W(t)$, the optical correction may be written directly using the Green's function of the linearized optical operator. Defining

$$\mathcal{L}_Z = D_Z\frac{d^2}{d\xi^2} + Q_Z(\xi) \tag{6.141}$$

with

$$D_Z = \frac{(M_\Sigma - 8r_a)c^2 + 2k\ell^2}{2W^2} \tag{6.142a}$$

$$Q_Z(\xi) = 4k - 2a + 3a\ \mathrm{sech}^2\,\xi \tag{6.142b}$$

the inhomogeneous optical-correction equation is written as

$$\mathcal{L}_Z \mathcal{Z}_1 = S_Z(\xi) \tag{6.143}$$

where

$$S_Z(\xi) = \frac{M_\Delta c^2 Y_s}{W^2}\,\mathrm{sech}^2\,\xi\ \tanh\xi \tag{6.144}$$

Let $G_Z(\xi,\eta)$ be the Green's function satisfying

$$\mathcal{L}_Z G_Z(\xi,\eta) = \delta(\xi - \eta) \tag{6.145}$$

with the localized boundary condition

$$G_Z(\xi,\eta) \to 0 \qquad \text{as} \qquad \xi \to \pm\infty \tag{6.146}$$

Then the optical correction is obtained as

$$\mathcal{Z}_1(\xi) = \int_{-\infty}^{\infty} G_Z(\xi,\eta) S_Z(\eta)\, d\eta \tag{6.147}$$

or, equivalently,

$$\mathcal{Z}_1(\xi) = \frac{M_\Delta c^2 Y_s}{W^2} \int_{-\infty}^{\infty} G_Z(\xi,\eta)\,\mathrm{sech}^2\,\eta\ \tanh\eta\, d\eta \tag{6.148}$$

The leading-order diatomic transition fronts on the two sublattices are therefore obtained as

$$Y_1(s,t) \simeq Y_s \tanh\left(\frac{s - X(t)}{W(t)}\right) + \mathcal{Z}_1\left(\frac{s - X(t)}{W(t)}\right) \tag{6.149a}$$

$$Y_2(s,t) \simeq Y_s \tanh\left(\frac{s - X(t)}{W(t)}\right) - \mathcal{Z}_1\left(\frac{s - X(t)}{W(t)}\right) \tag{6.149b}$$

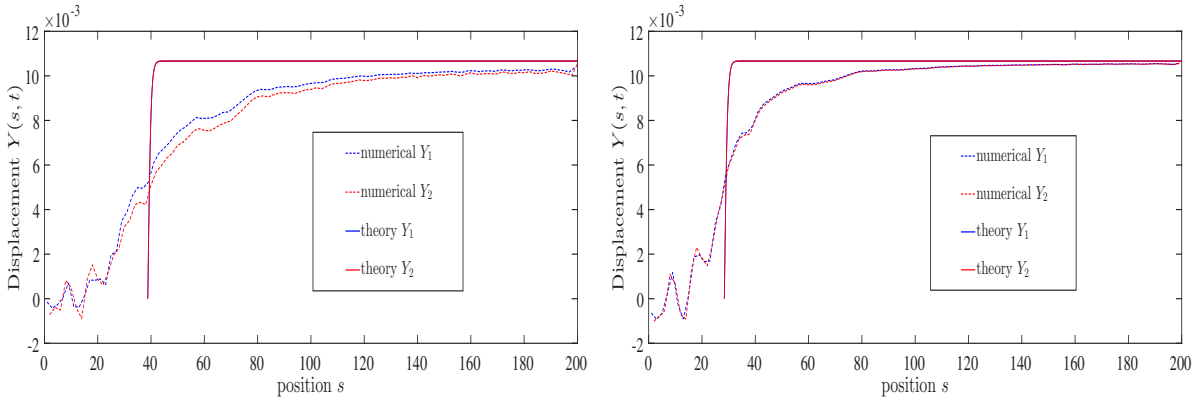
When $M_\Delta = 0$, the forcing term in Eq. (6.138) goes to zero and the leading-order front reduces to the purely acoustic-like transition $\mathcal{Z}_1 = 0$. Substituting the leading-order transition front solutions obtained in (6.149) back in Eqs. (6.113c, 6.113d), we can obtain the slaved voltage profiles V and W_e for an acoustic-dominant transition.

The exact in-phase and out-of-phase similar Nonlinear Normal Mode (NNM) reductions are not invariant manifolds/ subspaces for the mass-diatomic front system when $M_1 \neq M_2$. An exact in-phase front would require $Y_1 = Y_2$, or equivalently $\mathcal{Z} = 0$. From Eq. (6.126b), this also gives $\mathcal{W}_e = 0$ under the localized voltage boundary condition. However, substituting $\mathcal{Z} = 0$ and $\mathcal{W}_e = 0$ into the optical-like equation (6.124b) leaves the residual coupling term $(M_\Delta c^2/2W^2)\mathcal{Y}'' = 0$. Hence, for a general diatomic chain with $M_\Delta \neq 0$, a nontrivial acoustic-like transition front with $\mathcal{Y}'' \neq 0$ cannot remain exactly in phase. Similarly, an exact out-of-phase front would require $Y_1 = -Y_2$, or $\mathcal{Y} = 0$. From Eq. (6.126a), this also gives $\mathcal{V} = 0$, while Eq. (6.124a) reduces to $(M_\Delta c^2/2W^2)\mathcal{Z}'' = 0$ because $\mathcal{F}_+(0,\mathcal{Z}) = 0$ from Eq. (6.125a). Thus, for $M_\Delta \neq 0$, a nontrivial optical-like transition front with $\mathcal{Z}'' \neq 0$ also cannot exist as an exact out-of-phase similar NNM. Therefore, the nonlinear transition waves in the mass-diatomic chain must generally be

interpreted as nonsimilar acoustic–optical fronts, with one field dominant and the other appearing as a coupled correction.

6.4.3 Comparison of theoretical leading-order wavefronts with numerical simulations

To compare the leading-order analytical wavefronts with direct numerical simulations, we consider a finite chain comprising of 100 diatomic unit cells with free boundaries at both ends. Initially, all the masses in the chain are at their uniform stable branch $+Y_s$. We apply to the first unit cell in the chain an initial velocity sufficiently high for both the masses M_1 and M_2 to snap to their other stable uniform branch at $Y_1 = Y_2 = -Y_s$. The initial voltages are kept at zero. The finite chain is simulated for 80 seconds using the explicit RK4 `ode45` solver in Matlab. Mass ratios are kept at $m_a/M_1 = 0.1$ and $M_2/M_1 = 0.5$. From our harvested-power behavior for the linearized model (Fig. 6.8) we observed that as the coupling spring stiffness increases from $k = 0.1K_b$ to the limiting case of $k = K_b$, the optimum wavenumber for maximum post-settling harvested power shifts more and more towards the left edge of the Brillouin zone at $\mu = 0$ and in the limiting case, the maximum post-settling power corresponds to standing-wave solutions with $\mu = 0$. Since we are more interested in energy harvesting from propagating transient waves, for the general strongly nonlinear regime, we will focus our attention on the value of coupling spring stiffness which is expected to produce an optimum in an intermediate-to-high wavenumber range $0 < \mu < \pi$. Hence for presenting general transition wavefronts or power behavior, we will take the coupling spring stiffness to be $k = 0.1K_b$.



(a) Tip mass displacement in each unit cell plotted with mass index m or position s along the chain taken at time $t = 30$ seconds

(b) Tip mass displacement in each unit cell plotted with mass index m or position s along the chain taken at time $t = 50$ seconds

Fig. 6.9: Comparison of the theoretically predicted wavefront with numerically determined wave profile, for plotting the wave profile across the chain snapshots are taken at $t = 30$ seconds and $t = 50$ seconds (for parameters: $\ell = 1$, left-boundary scaled coordinates $\xi_L(t = 30 \text{ seconds}) = -32.151$ and $\xi_L(t = 50 \text{ seconds}) = -23.305$ which are alignment shifts associated with the two snapshot times and not additional physical parameters of the model, $Y_s = 0.0107$), the theoretical curves are shown only over the coherent front-core region in $\xi = (s - X(t))/W(t)$, while the numerical profiles are retained over the full plotted chain.

Fig. 6.9 shows the comparison between the theoretical leading-order wavefronts obtained in Section 6.4.2 and direct numerical time-domain simulations of the finite chain at time snapshots of $t = 30$, 50 seconds. The small perturbations in the numerical results with respect to the theoretical prediction are caused due to discreteness effects. For our dissipative chain, the propagating wave should be interpreted not as an exact conservative soliton, but as a kink-like, slowly modulated transition front which approaches asymptotically in time the leading order core captured by the reduced φ^4 type profile derived in Section 6.4.2. In contrast to conservative bi-stable chains considered previously, the present piezomagnetoelastic chain is intrinsically dissipative due to the electromechanical shunt, and therefore the large-amplitude interwell wave is not expected to evolve into an exact constant-speed heteroclinic soliton that switches the chain permanently from one stable branch to the other. Instead, the numerical results show a transient topological like front which induces barrier crossing and propagates through the chain (Fig. 6.9(a)), but leaves behind a decaying relaxation tail as energy is continuously extracted into the electrical domain. In this sense, the relevant nonlinear wave object in the present system is a damped or quasi-solitonic transition front rather than a conservative soliton. For this reason, the long integration window (Fig. 6.9(b)) is retained to characterize the full dissipative evolution and energy conversion process, whereas the front profile comparison with theory is performed at an earlier time snapshot, when the front core is still in the interior of the chain and before the post-front relaxation has collapsed the excited cells back toward the neighborhood of the saddle at $Y_1 = Y_2 = 0$.

We intentionally restrict attention to the primary front regime, namely to time windows for which the interwell front remains in the interior of the chain and the core dynamics are not governed by interactions with waves reflected from the boundaries. For a direct comparison of the numerical wave profile with the theoretical leading-order solution obtained in (6.149), a least-squares fit to a substantial interior portion of the primary-front trajectory obtained from numerical simulations of the finite chain, before boundary effects become significant, is used to obtain a representative propagation speed. Substituting this averaged speed in the theoretical solution shows a good agreement in the asymptotic limit with the numerical wave profile as shown in Fig. 6.9, which confirms that the theoretical leading-order prediction can capture the transient wavefront behavior to a considerable extent.

6.4.4 Bloch-consistent Harmonic Balance Method

To compute amplitude-dependent nonlinear dispersion branches, the motion is expanded about the stable uniform branch as

$$Y_{r,n}(t) = Y_s + q_{r,n}(t), \qquad r = 1, 2 \tag{6.150}$$

A Bloch-consistent nonlinear harmonic expansion is then introduced as

$$q_{r,n}(t) = \sum_{m=-H}^{H} Q_{r,m} e^{im(n\mu - \Omega t)} \tag{6.151a}$$

$$V_{r,n}(t) = \sum_{m=-H}^{H} \Phi_{r,m} e^{im(n\mu - \Omega t)} \tag{6.151b}$$

where the realness conditions are

$$Q_{r,-m} = Q_{r,m}^*, \qquad \Phi_{r,-m} = \Phi_{r,m}^* \tag{6.152}$$

For the cubic magnetic nonlinearity, a third-harmonic truncation is used in the leading nonlinear calculation

$$H = 3 \tag{6.153}$$

The nonlinear restoring force about the stable branch is written as

$$\mathcal{R}(q) = \mathcal{F}(Y_s + q) - \mathcal{F}(Y_s) = K_s q + 12 c_2 Y_s q^2 + 4 c_2 q^3 \tag{6.154}$$

where

$$K_s = K_b + 2c_1 + 12 c_2 Y_s^2 \tag{6.155}$$

The m-th harmonic coefficient of $\mathcal{R}(q_{r,n})$ is denoted by

$$\mathcal{N}_{r,m} = K_s Q_{r,m} + 12 c_2 Y_s \left[q_r^2\right]_m + 4 c_2 \left[q_r^3\right]_m \tag{6.156}$$

with the convolution coefficients

$$\left[q_r^2\right]_m = \sum_{p=-H}^{H} Q_{r,p} Q_{r,m-p} \tag{6.157a}$$

$$\left[q_r^3\right]_m = \sum_{p=-H}^{H} \sum_{q=-H}^{H} Q_{r,p} Q_{r,q} Q_{r,m-p-q} \tag{6.157b}$$

where coefficients outside the retained harmonic range are set to zero. Substitution of Eq. (6.151) into the exact discrete equations gives, for each retained harmonic $m = -H, \ldots, H$, the mechanical harmonic-balance residuals

$$\mathcal{N}_{1,m} + \left[2k - m^2\Omega^2(M_1 - 2r_a)\right] Q_{1,m} - \left(k + r_a m^2 \Omega^2\right)\left(1 + e^{-im\mu}\right) Q_{2,m} - \Theta \Phi_{1,m} = 0 \tag{6.158a}$$

$$\mathcal{N}_{2,m} + \left[2k - m^2\Omega^2(M_2 - 2r_a)\right] Q_{2,m} - \left(k + r_a m^2 \Omega^2\right)\left(1 + e^{im\mu}\right) Q_{1,m} - \Theta \Phi_{2,m} = 0 \tag{6.158b}$$

The electrical harmonic-balance residuals are

$$\left(G_l - im\Omega C_p\right) \Phi_{r,m} - im\Omega\Theta Q_{r,m} = 0, \qquad r = 1, 2 \tag{6.159}$$

Eqs. (6.158) and (6.159) define the nonlinear algebraic system

$$\mathbf{R}_{\mathrm{HB}}\left(\mathbf{Q}, \mathbf{\Phi}, \Omega; \mu, A\right) = \mathbf{0} \tag{6.160}$$

where $\mathbf{Q}$ and $\mathbf{\Phi}$ collect all retained mechanical and voltage harmonics. To close the autonomous nonlinear eigenproblem, the fundamental mechanical amplitude and phase are normalized by

$$|Q_{1,1}|^2 + |Q_{2,1}|^2 = A^2 \tag{6.161a}$$

$$\mathrm{Im}(Q_{1,1}) = 0 \tag{6.161b}$$

For a prescribed pair (μ, A), the nonlinear lower and upper Bloch branches are obtained by solving Eq. (6.160) together with Eq. (6.161) and continuing the solutions from the corresponding linear Bloch eigenvectors:

$$\Omega = \Omega_b(\mu, A), \qquad b \in \{L, U\} \tag{6.162}$$

The conservative nonlinear backbone is recovered by setting $G_l = 0$ in Eq. (6.159), while retaining $G_l \neq 0$ gives the corresponding electromechanically damped harmonic-balance residual used for harvesting-oriented continuation. The dispersion branches for the strongly nonlinear regime are evaluated numerically for every fixed pair μ, A with the wavenumber μ being restricted to the irreducible Brillouin zone (IBZ) $\mu \in [0, \pi]$.

6.4.5 Nonlinear dispersion branches

Just like we did for the linearized regime, we plot the the amplitude-dependent dispersion characteristics $\Omega(\mu)$ for different system parameters in the general strongly nonlinear regime obtained from the Bloch-consistent Harmonic Balance method proposed in Section 6.4.4. We use a fairly high initial perturbation on the displacements Y_1 and Y_2 from their initial stable branches at $[+Y_s, +Y_s]$ to characterize the general strongly nonlinear behavior without any small-motion approximation. Hence we provide a further perturbation on the masses M_1 and M_2 as $[+2Y_s, +2Y_s]$ from their initial stable configuration.

For the nonlinear harmonic-balance evaluation, a short-circuit condition is used only to obtain a conservative reference backbone for the diatomic lattice. This choice removes the resistive electrical dissipation from the nonlinear periodic-branch computation and therefore allows the amplitude-dependent lower and upper branches to be represented by real frequencies. The resulting branches are not interpreted as the complete dissipative electromechanical response of the harvester, but rather, they provide a clean baseline for identifying how the cubic magnetic nonlinearity modifies the linearized band structure. This is useful because the expected hardening effect can be isolated clearly before introducing the additional complications associated with decay, post-settling response, and harvested-power evaluation.

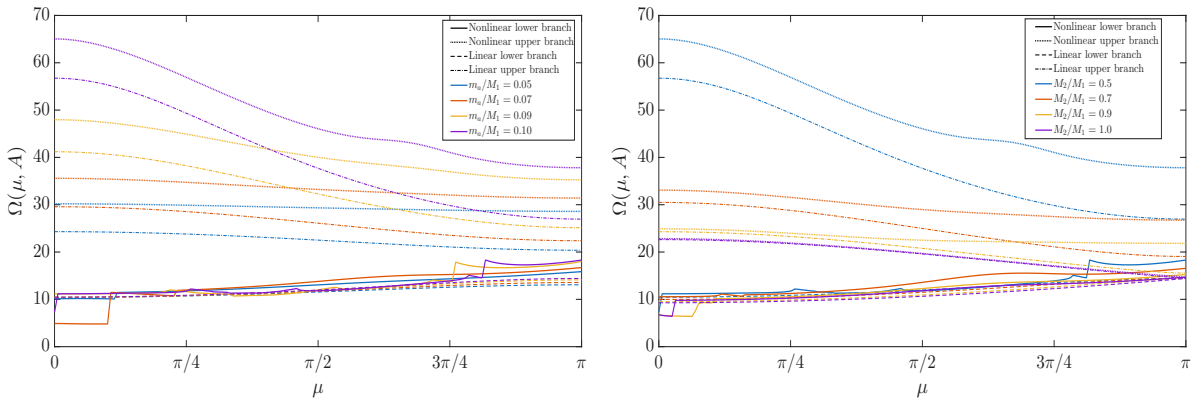
Nonlinear dispersion behavior with varying mass ratios

We vary the mass ratios m_a/M_1 and M_2/M_1, keeping the coupling spring stiffness fixed at $k = 0.1K_b$ and plot the dispersion profiles.

Fig. 6.10 compares the nonlinear harmonic-balance branches with the corresponding linearized branches. In both Fig. 6.10(a) and Fig. 6.10(b), the nonlinear lower and upper branches are shifted upward relative to their linear counterparts, confirming the hardening character of the cubic magnetic restoring force about the stable branch. Fig. 6.10(a) shows that increasing m_a/M_1 modifies the branch locations, with the upper optical-like branch being more sensitive because it is associated with stronger relative motion and therefore stronger participation of the stable negative-inerter mechanism. Fig. 6.10(b) shows that increasing M_2/M_1 reduces the mass contrast between the two sublattices and consequently decreases the acoustic–optical separation. The results collectively demonstrate that the nonlinear backbone curves preserve the qualitative diatomic branch structure of the linearized model while shifting the branches upward in frequency due to the hardening nonlinearity.

Nonlinear dispersion behavior with varying spring stiffness

We then vary the coupling spring stiffness k keeping the inerter and principal mass ratios fixed at $m_a/M_1 = 0.1$ and $M_2/M_1 = 0.5$ respectively.



(a) Nonlinear dispersion branches plotted with varying inerter mass ratio m_a/M_1 with the principal mass ratio kept fixed at $M_2/M_1 = 0.5$

(b) Nonlinear dispersion branches plotted with varying principal mass ratio M_2/M_1 with the inerter mass ratio kept fixed at $m_a/M_1 = 0.1$

Fig. 6.10: Nonlinear dispersion branches plotted with varying mass ratios m_a/M_1 and M_2/M_1, solid curves represent lower nonlinear branch and dotted curves represent upper nonlinear branch, dashed and dashed-dotted curves represent the lower and upper linearized branches to provide the baseline reference.

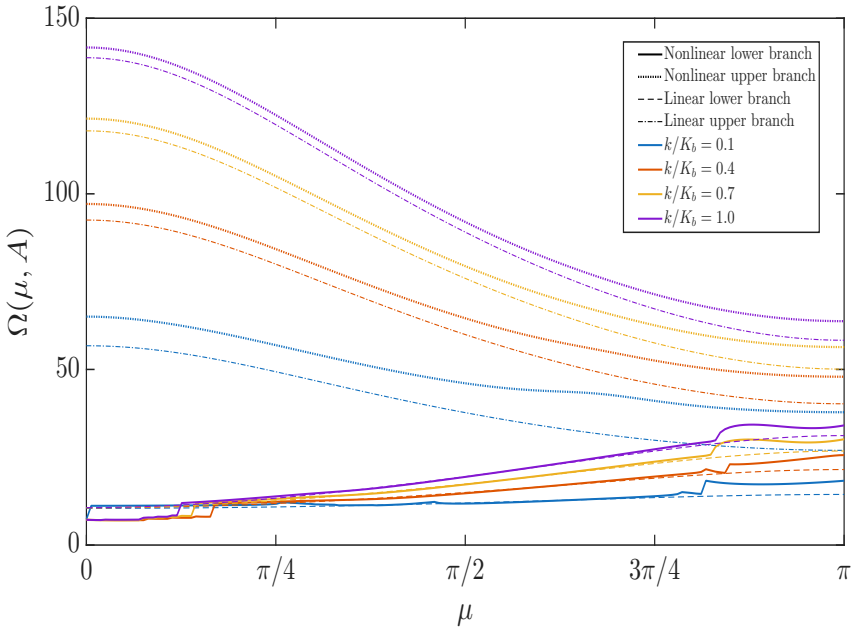


Fig. 6.11: Nonlinear dispersion branches plotted with varying coupling spring stiffness k with mass ratios kept fixed at $m_a/M_1 = 0.1$ and $M_2/M_1 = 0.5$, solid curves represent lower nonlinear branch and dotted curves represent upper nonlinear branch, dashed and dashed-dotted curves represent the lower and upper linearized branches to provide the baseline reference.

Fig. 6.11 shows the effect of the coupling spring stiffness on the short-circuit nonlinear backbone branches, with $m_a/M_1 = 0.1$ and $M_2/M_1 = 0.5$ kept fixed. Increasing k/K_b shifts both the nonlinear lower and upper branches upward, indicating that stronger coupling increases the effective stiffness of the diatomic lattice. The upward shift is more

visible for the upper optical-like branch because this branch contains stronger relative motion between neighboring masses and is therefore more directly affected by the coupling spring. The corresponding linearized branches are also shown as reference curves, and the nonlinear branches remain shifted upward relative to them, confirming the hardening contribution of the cubic piezomagnetoelastic nonlinearity. Overall, the results indicate that the coupling stiffness mainly changes the absolute frequency levels of the nonlinear branches, while preserving the qualitative acoustic-like and optical-like branch structure of the diatomic chain.

6.4.6 Energy harvested in the general nonlinear regime

We use the same post-settling maximum harvested power framework formulated in Section 5.5 and plot the harvested power with wavenumber μ varying from 0 to π. In the nonlinear regime, the post-settling harvested power is characterized as a continuation of the linearized formulation in Section 6.3.1, with the linear branch frequency $\omega_b(\mu)$ replaced by the amplitude-dependent nonlinear frequency $\Omega_b(\mu, A)$ obtained from the Bloch-consistent harmonic balance formulation in Section 6.4.4. For a prescribed amplitude A fixed through Eq. (6.161a), the nonlinear branch solution provides the harmonic coefficients $Q_{r,m}^{(b)}(\mu, A)$ and the branch frequency $\Omega_b(\mu, A)$, where $b \in \{L, U\}$. Although the short-circuit backbone is used to obtain a conservative reference nonlinear dispersion branch, the finite-load voltage response used for harvesting can be reconstructed in post-processing from the electrical harmonic relation in Eq. (6.159) as

$$\Phi_{r,m}^{(b)} = \frac{im\Omega_b\Theta}{G_l - im\Omega_b C_p} Q_{r,m}^{(b)}, \qquad m = 1, \dots, H, \qquad r = 1, 2 \tag{6.163}$$

The corresponding physical voltage signal over one representative unit cell is then written as

$$v_{r,\mathrm{phys}}^{(b)}(t; \mu, A) = \mathrm{Re}\left[\sum_{m=1}^{H} \Phi_{r,m}^{(b)}(\mu, A) e^{-im\Omega_b(\mu,A)t} + \mathrm{c.c.}\right] \tag{6.164}$$

where c.c. denotes complex conjugate. The nonlinear pseudo-period associated with branch b is defined as

$$T_b^{\mathrm{NL}}(\mu, A) = \frac{2\pi}{\Omega_b(\mu, A)} \tag{6.165}$$

Following the same post-settling window idea used in Eqs. (6.88)–(6.96), the branch-wise nonlinear average harvested power over a post-settling window beginning at t_0 is evaluated as

$$\overline{p}_{h,b}^{w,\mathrm{NL}}(t_0; \mu, A) = \frac{1}{R_l T_b^{\mathrm{NL}}} \int_{t_0}^{t_0 + T_b^{\mathrm{NL}}} \sum_{r=1}^{2} \left[v_{r,\mathrm{phys}}^{(b)}(t; \mu, A)\right]^2 dt \tag{6.166}$$

Here t_0 is chosen after the initial transient response has settled onto the nonlinear branch envelope. In the numerical implementation, this post-settling starting time $t_{s,b}^{\mathrm{NL}}$ is obtained as an approximation using the same tolerance-based procedure used in the linearized regime, but the averaging period is now the nonlinear pseudo-period in Eq. (6.165). The maximum post-settling nonlinear harvested power is then defined as

$$\overline{p}_{h,b}^{\max,\mathrm{NL}}(\mu, A) = \max_{m \in \mathcal{M}_b^{\mathrm{NL}}} \overline{p}_{h,b}^{w,\mathrm{NL}}\left(t_{s,b}^{\mathrm{NL}} + mT_b^{\mathrm{NL}}; \mu, A\right) \tag{6.167}$$

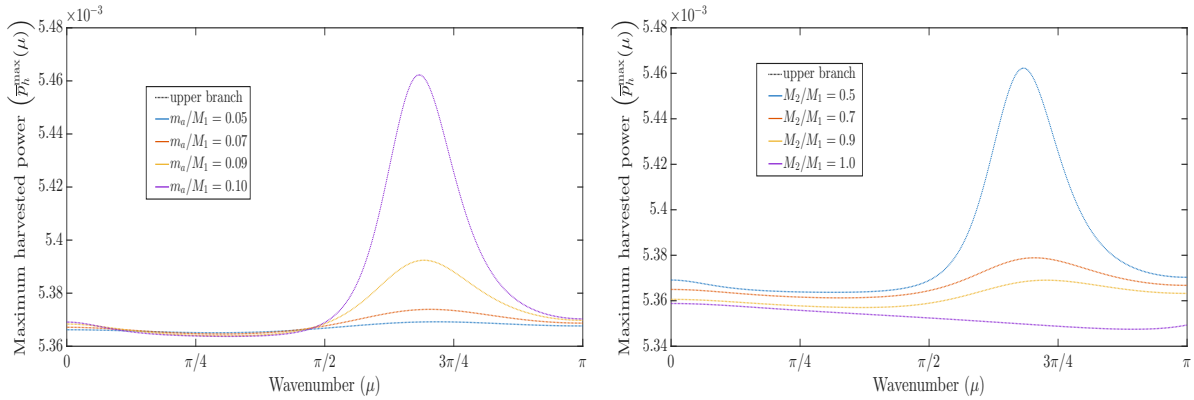
where $\mathcal{M}_b^{\mathrm{NL}}$ denotes the admissible set of post-settling averaging windows within the selected observation time. Finally, the nonlinear harvesting optimum is obtained by maximizing over the two nonlinear branches and over the first Brillouin zone as

$$(b^*, \mu^*) = \underset{b\in\{L,U\},\ \mu\in[0,\pi]}{\arg\max}\ \overline{p}_{h,b}^{\max,\mathrm{NL}}(\mu, A), \qquad \Omega^* = \Omega_{b^*}(\mu^*, A) \tag{6.168}$$

Thus, the nonlinear harvesting calculation uses the harmonic-balance backbone to determine the amplitude-dependent branch period, while the harvested power is evaluated from the finite-load voltage response over post-settling windows, in direct analogy with the linearized formulation developed in Section 6.3.1.

Harvested power behavior with mass ratios

Like we did for the linearized model, we now investigate the maximum post-settling harvested power vs wavenumber μ with $\mu \in [0, \pi]$ for different mass ratios m_a/M_1 and M_2/M_1 with the coupling spring stiffness kept fixed at $k = 0.1K_b$. In the nonlinear HB calculation, only the upper-branch harvested-power curve is reported, because the lower nonlinear branch exhibits multivalued fixed-amplitude continuation features in the present parameter range, whereas the upper branch provides a smooth nonlinear continuation. The two power branches follow the same definition posed in Section 6.3.2. As a sufficiently large initial displacement to observe pronounced effects of the strong nonlinearity, we perturb the masses M_1 and M_2 by $[2Y_s,\ 2Y_s]$ from their initial stable uniform configuration $[Y_s,\ Y_s]$, with the initial velocities and voltages kept at 0.



(a) Power vs wavenumber μ plotted with varying inerter mass ratio m_a/M_1 with the principal mass ratio kept fixed at $M_2/M_1 = 0.5$

(b) Power vs wavenumber μ plotted with varying principal mass ratio M_2/M_1 with the inerter mass ratio kept fixed at $m_a/M_1 = 0.1$

Fig. 6.12: Power vs wavenumber μ in the general strongly nonlinear regime plotted with varying mass ratios m_a/M_1 and M_2/M_1, coupling spring stiffness is kept fixed at $k = 0.1K_b$.

Fig. 6.12 shows the variation of the nonlinear HB harvested-power branches with the inerter mass ratio and the principal mass ratio. Compared with the linearized power trends in Fig. 6.7, the nonlinear regime produces substantially larger harvested-power magnitudes (approximately 10^2 times larger) over the admissible wavenumber range, confirming that the large-amplitude piezomagnetoelastic response significantly enhances the voltage-

producing motion. In Fig. 6.12(a), the highest power level is obtained for $m_a/M_1 = 0.1$, indicating that the increasing negative-inertance effect improves nonlinear energy conversion within the admissible positive-definite inertia range considered here. In Fig. 6.12(b), the strongest response occurs for $M_2/M_1 = 0.5$, where the mass contrast and hence the diatomic acoustic–optical separation within the positive-definite inertia range are most pronounced. Therefore, the parameter pair $m_a/M_1 = 0.1$ and $M_2/M_1 = 0.5$ provides a favorable nonlinear harvesting configuration for the subsequent direct comparison with the linearized model in Section 6.5.

Harvested power behavior with spring stiffness

Now, we keep the mass ratios fixed at $m_a/M_1 = 0.1$ and $M_2/M_1 = 0.5$ and report the harvested power vs wavenumber behavior with varying coupling spring stiffness k. Initial conditions are taken to be the same as considered before for varying mass ratios.

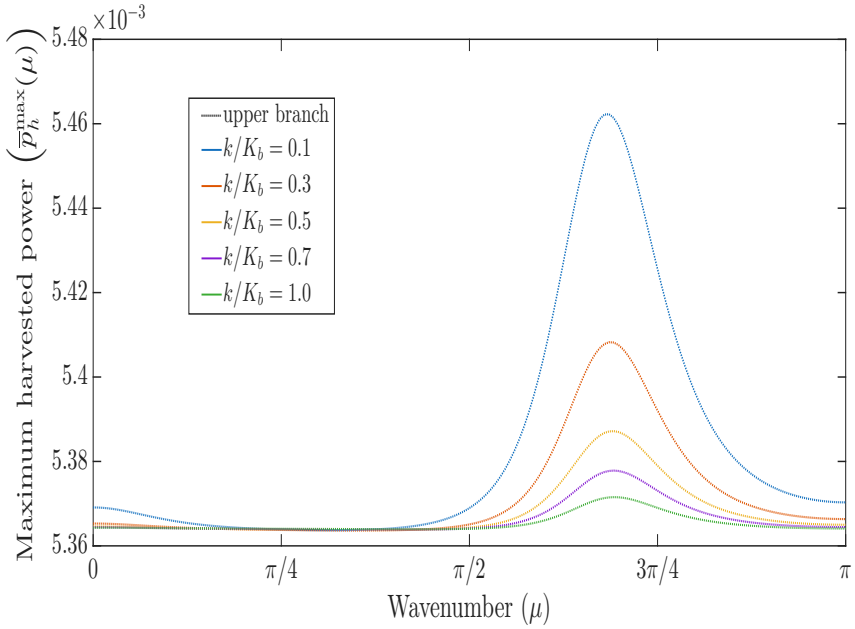


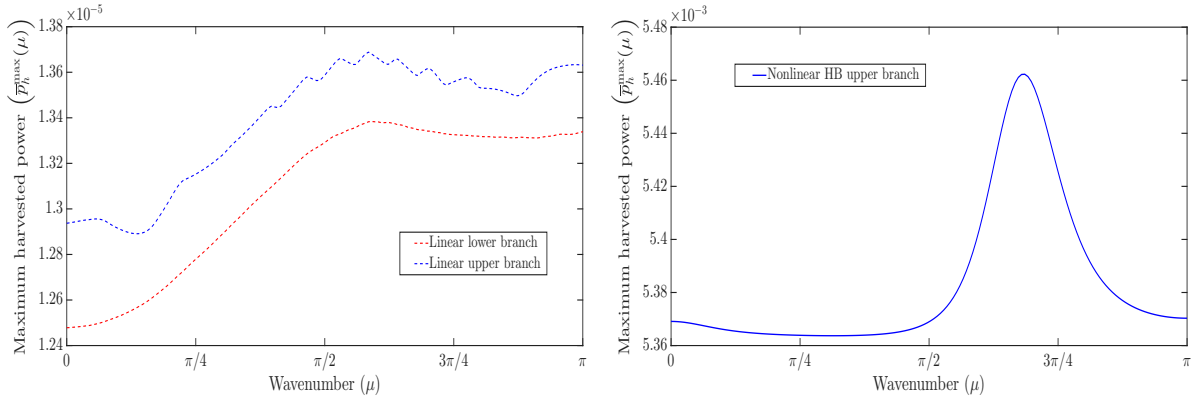
Fig. 6.13: Power vs wavenumber μ in the general strongly nonlinear regime plotted with varying coupling spring stiffness with mass ratios kept fixed at $m_a/M_1 = 0.1$ and $M_2/M_1 = 0.5$.

Fig. 6.13 shows the nonlinear harvested-power response for different coupling stiffness ratios while keeping $m_a/M_1 = 0.1$ and $M_2/M_1 = 0.5$ fixed. In contrast to the linearized stiffness-dependent power behavior in Fig. 6.8, the nonlinear HB response remains at a much globally larger power scale (approximately 10^2 times larger), but the magnitude is progressively reduced as k/K_b is increased. The largest nonlinear power is obtained for the weakest coupling considered, $k = 0.1K_b$, which suggests that relatively soft inter-mass coupling allows larger voltage-producing deformation amplitudes in the strongly nonlinear regime. Combining this result with Fig. 6.12(a) and Fig. 6.12(b), the parameter set $k = 0.1K_b$, $M_2 = 0.5M_1$, and $m_a = 0.1M_1$ can be regarded as an optimum representative configuration for highlighting the enhanced nonlinear harvesting advantage over the corresponding linearized model in the subsequent comparison in Section 6.5.

6.5 Enhanced energy harvesting potential of the strongly nonlinear model

6.5.1 Advantages of using the strongly nonlinear diatomic model over the linearized one

To investigate harvesting advantages offered by the exact nonlinear periodic model in the strongly nonlinear regime, we compare the harvested-power characteristics obtained from the nonlinear HB formulation with those obtained from state-space formulation for the linearized model over the admissible wavenumber range $\mu \in [0, \pi]$. For consistent comparisons, the same representative initial displacement perturbation level is used in both cases. The masses M_1 and M_2 are perturbed by $[2Y_s, 2Y_s]$ from the stable uniform configuration $[Y_s, Y_s]$, while the initial velocities and voltages are taken to be zero. The comparison is performed for the representative parameter set $m_a/M_1 = 0.1$, $M_2/M_1 = 0.5$, and $k = 0.1K_b$. In the nonlinear HB calculation, only the upper-branch harvested-power curve is reported in the compact comparison because the lower nonlinear branch exhibits multivalued fixed-amplitude continuation features in the present parameter range, whereas the upper branch provides a smooth nonlinear continuation suitable for comparison with the corresponding linearized response. Since the linearized upper branch gives larger harvested power for all $\mu \in [0, \pi]$ than the linearized lower branch for this parameter set, as shown in Fig. 6.14(a), using the upper linearized branch as a baseline provides a conservative reference for assessing the enhancement achieved by the exact nonlinear harvester model.



(a) Power vs wavenumber μ using the linearized model

(b) Power vs wavenumber μ using the exact nonlinear model

Fig. 6.14: Comparison of energy harvested using the exact nonlinear model against the linearized model for the same general set of initial displacement conditions on the unit-cell masses with initial velocities and voltages chosen to be 0.

Fig. 6.14(a) shows that the linearized model produces a localized harvested-power optimum with respect to the Bloch wavenumber μ for both the branches with the lower branch lying below the upper branch. The harvested power increases toward an optimal wavenumber and then decreases away from this point, indicating that the linearized response is strongly dependent on the spectral location of the excited wave component.

In contrast, Fig. 6.14(b) shows that the nonlinear HB-based model produces a much larger harvested-power level (approximately 10^2 times larger) over the same admissible wavenumber range and for the same initial displacements. The nonlinear curve is not strictly flat. It also exhibits a distinct local peak in the intermediate-to-high wavenumber region. However, the relative variation of the nonlinear power over μ is comparatively modest, because the response remains at a globally enhanced level when compared to the linearized model even away from the optimum. Thus, the nonlinear model does not merely shift the optimal operating point to higher wavenumbers, but changes the harvesting landscape by producing a high-power response over a broader portion of the Brillouin zone. The shift of the nonlinear optimum toward a higher wavenumber indicates that the general large-amplitude piezomagnetoelastic response favors shorter-wavelength components of the transient free wave, which are not predicted as the most effective harvesting components by the linearized model. From a design perspective, this means that exploiting the nonlinear regime can move the optimal harvesting condition to a different spectral region while simultaneously increasing the attainable power level, thereby providing an additional tuning mechanism beyond the linear band-structure design.

The comparison in Fig. 6.14 highlights the design advantage of exploiting the exact nonlinear dynamics rather than relying only on the linearized approximation. The linearized model is valuable for identifying branch structure, bandgap formation, and the first estimate of favorable harvesting frequencies, but it describes only the small-amplitude response about the stable branch. Once the large-amplitude piezomagnetoelastic nonlinearity is activated, the hardening nonlinear backbone alters the branch frequencies and increases the voltage-producing capability associated with the free wave. As a result, the nonlinear regime can provide both a substantially higher harvested power level globally even away from the local optimum and therefore a less sharply tuned response with respect to μ. This is particularly important for transient free waves, whose spectral content is distributed over a range of wavenumbers rather than concentrated at a single optimally tuned value. One more significant advantage of the nonlinear model is that in practical ambient harvesting environments, where disturbances can be arbitrarily large and intermittent, the linearized model due to the constraints of small-displacement formulation predicts a power curve which is not necessarily smooth over the Brillouin zone as can be seen in Fig. 6.14(a), whereas the nonlinear model formulated for general initial displacement perturbations without any small-amplitude approximation can still generate a sufficiently smooth power curve over the same wavenumber range.

6.5.2 Validation of the strongly nonlinear model against direct numerical simulations

To validate the nonlinear harmonic balance (HB) harvested-power prediction, we perform direct numerical simulations of a finite periodic chain comprising of 100 diatomic unit cells and the boundary conditions at both ends wrapped onto each other, using the same wavenumber-dependent branch initial conditions that are used in the HB calculation [201]. For each admissible Bloch wavenumber μ, the HB solution obtained from Eq. (6.160) provides the branch frequency $\Omega_b(\mu, A)$ and the corresponding harmonic coefficients $Q^{(b)}_{r,m}(\mu, A)$ and $\Phi^{(b)}_{r,m}(\mu, A)$. These coefficients are then used to initialize the finite chain with the same nonlinear Bloch wave shape, including the associated displacement,

velocity, and voltage fields, rather than exciting the chain by a localized impulse. The exact nonlinear discrete equations are then integrated in time using `ode45`, and the harvested power is evaluated directly from the simulated voltages over one nonlinear branch period. This comparison ensures that the numerical simulation and the HB model correspond to the same branch, same wavenumber, and same amplitude, so that the validation assesses the accuracy of the HB harvested-power formulation itself rather than the spectral distribution produced by a particular transient excitation.

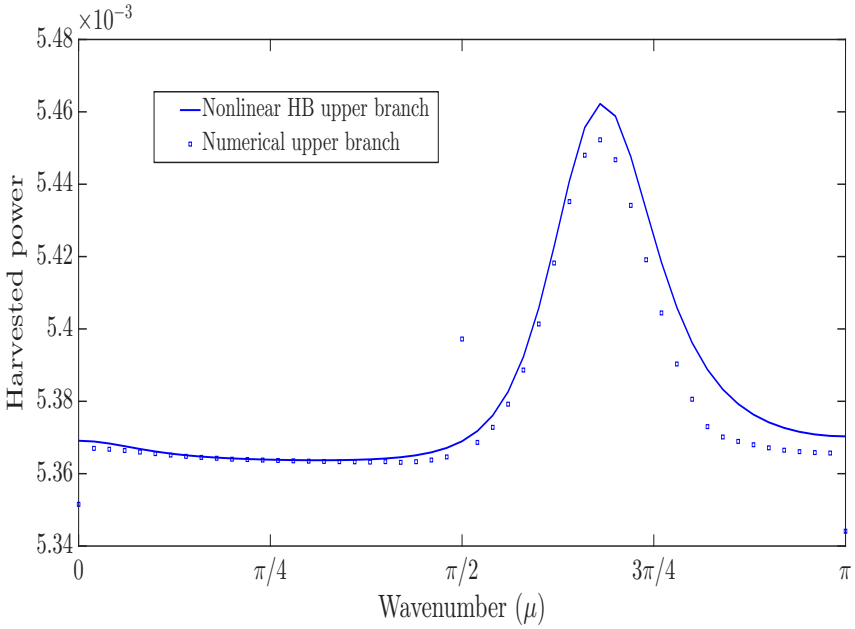


Fig. 6.15: Comparison of the harvested power upper branch between the nonlinear HB model and direct numerical simulations of a finite periodic chain comprising of 100 diatomic unit cells for the same representative system parameters used in Section 6.5.1.

Fig. 6.15 shows a considerably good agreement between the HB power branch with direct time-domain integrations, which confirms the validation of the proposed Bloch-consistent HB framework for the strongly nonlinear model in a general regime of moderately large-amplitude motions. This validation closes the objective of the present Chapter in proving the effectiveness of using the proposed diatomic, inertially coupled, nonlinear piezomagnetoelastic periodic chain model for enhanced energy harvesting over linear/ linearized models.

6.6 Concluding remarks

This work presented a mass-diatomic nonlinear piezomagnetoelastic chain as a tunable platform for enhanced energy harvesting from transient free-wave motion. Starting from the exact discrete electromechanical equations of motion, a Bloch-reduced state-space formulation was developed in the linearized regime about the stable uniform branch. The resulting damped electromechanical dispersion problem naturally produced two mechanically dominant branches associated with the acoustic-like and optical-like motions of the

diatomic unit cell. The analysis showed that the principal mass ratio M_2/M_1 directly controls the mass-diatomic acoustic–optical separation, while the inerter mass ratio m_a/M_1 provides an additional mechanism for shifting the branch locations and broadening the effective bandgap within the admissible positive-definite inertia range. In contrast, the coupling stiffness k mainly shifts the absolute frequency levels of the branches and has a comparatively weaker influence on the effective bandgap width, although it significantly affects the harvested-power response through the modal voltage participation and the initial condition induced modal distribution.

A post-settling harvested-power framework was developed to quantify energy harvesting in the linearized dissipative regime. Since the electromechanical chain is inherently dissipative, the harvested response was evaluated over pseudo-periodic post-settling windows defined by the damped branch frequencies. This formulation showed that the harvested power is not determined by the band structure alone, but also by the projection of the initial perturbation onto the complex Bloch eigenvectors and by the corresponding voltage participation of the two branches. The parametric studies demonstrated that the diatomic chain can produce clear peak-like power characteristics in the intermediate-wavenumber region, and that inertance magnitude and mass contrast can be used to tune these peaks. The results also showed that although strong coupling may not significantly alter the bandgap, it can suppress the harvested power over a large part of the Brillouin zone, highlighting the need to optimize energy harvesting using both band-structure and power-response criteria.

The strongly nonlinear regime was investigated through two complementary analytical routes. First, a long-wavelength continuum reduction was derived in terms of mean and contrast fields, which exposed the acoustic-like and optical-like components of the nonlinear diatomic transition dynamics. This formulation showed that exact in-phase and out-of-phase similar nonlinear normal mode reductions are not generally invariant for the mass-diatomic chain when $M_1 \neq M_2$. Consequently, the nonlinear transition waves must be interpreted as nonsimilar acoustic–optical fronts, where a dominant acoustic-like transition is accompanied by an optical-like correction generated by the mass contrast. A leading-order analytical front solution was obtained by combining the dominant acoustic-like φ^4 transition with a linear inhomogeneous optical-correction problem. Secondly, a Bloch-consistent harmonic balance formulation was developed to compute amplitude-dependent nonlinear dispersion branches. The short-circuit harmonic balance branches were used as conservative nonlinear backbone references, allowing the hardening effect of the cubic magnetic nonlinearity to be isolated clearly.

The nonlinear harvested-power comparison further demonstrated the central advantage of using the exact nonlinear model. The linearized regime predicts a well-defined optimal wavenumber, but the harvested power remains relatively small and further decreases away from that optimum. In the nonlinear regime, the HB-based formulation shows a much higher harvested-power level and a broader globally elevated response over the Brillouin zone, although the nonlinear power still exhibited a clear peak rather than remaining perfectly saturated. This refined observation supports the main objective of this Chapter that the combination of mass diatomicity and piezomagnetoelastic nonlinearity enhances the harvesting potential by combining richer branch and bandgap behavior with large-amplitude nonlinear energy conversion. Therefore, the nonlinear diatomic chain offers a more effective and robust design pathway for harvesting energy from transient free

waves than what would be inferred from the linearized model alone.

Finite-chain numerical studies were then used to validate the analytical leading-order wavefronts and harmonic balance (HB) power formulations. The first set of finite-chain simulations demonstrated the propagation of nonlinear transition fronts under localized snap-through excitation. The other set of finite-chain simulations, initialized using the same wavenumber-dependent nonlinear Bloch wave shapes as the harmonic-balance model, provided a direct branch-wise validation of the nonlinear harvested-power formulation. These validations clarify the distinction between intrinsic branch-wise harvesting potential and the actual spectral distribution produced by a localized transient excitation. Overall, this Chapter establishes a systematic framework linking linear bandgaps, nonlinear backbone branches, transition fronts, and post-settling energy harvesting in diatomic nonlinear piezomagnetoelastic chains.

Few extensions can naturally follow from this study. Firstly, the present one-dimensional framework can be generalized to two- and three-dimensional diatomic or multiatomic piezomagnetoelastic lattices, where richer directional bandgaps, anisotropic wave propagation, and topological or defect-guided energy localization may be exploited for enhanced harvesting. Secondly, experimental validation of the proposed diatomic chain would be valuable for assessing the practical influence of fabrication tolerances, magnetic-field nonlinearities, inerter-mechanism realization, and circuit losses. Thirdly, the present single-mode beam approximation can be extended to include multi-mode contributions from each piezomagnetoelastic beam, which may be important when higher-frequency branch interactions, multimodal internal resonances, or broadband transient excitations are present. These directions would further strengthen the design framework for nonlinear periodic energy harvesters operating under realistic transient wave environments and are kept as a future work.

Chapter 7

Conclusion and future outlook

7.1 Summary

This Thesis has investigated tunable bandgap behavior and energy harvesting characteristics in nonlinear periodic structures. The central aim has been to connect two bodies of work that have often been treated separately: nonlinear wave propagation in periodic media and electromechanical energy harvesting from realistic transient disturbances. Classical periodic structures provide bandgaps, attenuation zones, and wave-filtering effects, but their response is usually fixed once the unit-cell geometry and material parameters are chosen. Conventional piezoelectric harvesters, on the other hand, can convert mechanical energy into electrical energy, but are often most effective only near a prescribed resonance or under sustained external excitation. The work presented here addresses the gaps identified in Chapter 1 and Chapter 2: the absence of a unified framework that proceeds from nonlinear bandgap manipulation, to free-wave power prediction, to nonlinear broadband enhancement, and finally to spatially localized harvesting through transition fronts.

The first part of the Thesis, Chapter 3, considered a bi-stable, inertially coupled periodic chain with coupled horizontal–vertical dynamics. The chosen unit cell combines geometric bi-stability, stable negative-inertance effects, and inter-cell periodic coupling, thereby creating a system whose wave behavior is richer than that of a purely linear periodic chain or a simpler single degree of freedom bi-stable lattice. The phase-plane analysis of the isolated unit cell showed that the vertical bi-stable mass preserves unforced intrawell and interwell dynamical behavior even when coupled to orthogonal horizontal degrees of freedom. This motivated the use of the unit cell as a building block for nonlinear metamaterials.

A major methodological contribution of Chapter 3 was the development of an Amplitude-Locked, Inverse-method-Guided, multi-harmonic Nonlinear framework, referred to as ALIGN. This framework combines weakly nonlinear asymptotic analysis, multi-harmonic harmonic balance, robust branch tracking, and inverse time-domain validation. It was developed specifically to handle the difficulties that arise in strongly nonlinear discrete periodic structures with non-polynomial and non-integrable geometric nonlinearities. The framework makes it possible to compute amplitude-dependent Bloch dispersion branches, track them across near-degeneracies and branch-merging regions, and validate the resulting nonlinear dispersion predictions against finite-chain simulations. The analysis also identified physically admissible mass-ratio regimes of the proposed architecture, including critical

stability thresholds for the inerters and neighboring-mass parameters, and showed that mass-ratio tuning provides a systematic route for bandgap manipulation. In the strongly nonlinear regime, the nominal three-branch structure of the unit cell often collapses into two dominant propagating branches because of modal redistribution between the horizontal and vertical degrees of freedom. Thus, the first part of the Thesis established the wave-propagation foundation required for the subsequent energy-harvesting studies.

The second part of the Thesis, Chapter 4, introduced energy harvesting from transient free waves in a linear piezoelectric periodic chain. This chapter deliberately began with a linear electromechanical setting so that the role of periodic dispersion, attenuation, and electrical dissipation could be isolated before introducing additional nonlinearities. The key idea was to replace sustained harmonic forcing by initial condition-driven free wave propagation. This is important because many practical disturbances in structural systems are intermittent, impulsive, or spatially distributed, rather than externally prescribed sinusoidal loads.

The main contribution of Chapter 4 was the formulation of a settling-time-aware harvested-power metric. By combining Bloch-reduced electromechanical dynamics, closed-form time-domain response, and a physically motivated post-transient averaging window, the chapter derived a systematic criterion for evaluating maximum steady-state harvested power from a decaying free response. The settling time $\tau_s(\omega)$ identifies when the voltage response has moved beyond the initial transient and can be used consistently for one-period power averaging. This converts free-wave decay from a merely observed transient phenomenon into a design variable. It also produces an inverse map from structural and electrical parameters to an optimum free-wave frequency ω_e, without requiring resonance tuning against an externally imposed forcing frequency. The results showed that the location of the optimum frequency is robust with respect to the precise settling-time choice, while the magnitude of the peak harvested power remains sensitive to the post-settling extraction window. This chapter therefore established the baseline analytical link between wave propagation and energy conversion.

The third part of the Thesis, Chapter 5, extended this free-wave harvesting framework to an inertially coupled nonlinear piezomagnetoelastic chain. In this model, magnetic bi-stability realizes a double-well potential in a physically simpler beam-based architecture, while inertial coupling modifies the effective inertia and wave-transmission characteristics of the periodic chain. The analysis was carried out first in the linearized intrawell regime and then in the general strongly nonlinear regime. In the linearized regime, the same settling-time-aware power concept from Chapter 4 was generalized to include magnetic, inertial, structural, and electrical parameters. This yielded analytical predictions for optimum harvested power and optimum operating frequency, validated against numerical time-domain integrations.

The strongly nonlinear intrawell analysis showed that the role of magnetic bi-stability and inerters is not merely to raise a single isolated power peak. Instead, the nonlinear chain can broaden the high-performance region into a wide quasi-saturated band of near-optimal harvesting over a much larger free-wave frequency interval. Importantly, this enhancement was obtained while maintaining stable intrawell motion, rather than relying on negative-stiffness-induced divergence or unbounded response. This result directly fills the gap between nonlinear amplitude-dependent dispersion and practical electromechanical power extraction: the nonlinear dispersion structure becomes a mechanism for

broadening the useful harvesting regime.

The interwell analysis in Chapter 5 provided a second harvesting mechanism based on localized transition fronts. For sufficiently large initial conditions, the bi-stable chain supports interwell propagation in which the relevant object is not an exact conservative soliton, but a slowly modulated φ^4-type front altered by electromechanical dissipation. The continuum approximation produced leading-order descriptions of the front profile, the slaved voltage field, and the corresponding harvested-power envelope. Numerical simulations of finite chains showed qualitative agreement with the predicted front shape, voltage envelope, and spatial power localization. This result is significant because it shows that localized harvesting can emerge intrinsically from the coupled nonlinear dynamics of magnetic bi-stability, inerter-effects, and piezoelectric dissipation. It does not need to be imposed through defects, graded traps, or an externally engineered wave-arresting protocol.

The final part of the Thesis, Chapter 6, introduced mass diatomicity into the nonlinear piezomagnetoelastic chain. This created a richer branch structure while preserving a physically realizable unit-cell architecture. The linearized analysis showed the emergence of acoustic-like and optical-like branches, together with bandgaps and wavenumber-dependent power characteristics that depend on mass contrast, inertance factor, coupling stiffness, and the modal projection of the initial perturbation. This clarified that band-structure information alone is not sufficient for harvesting design; a designer must also account for voltage participation, modal decay, and how the initial disturbance excites the electromechanical branches.

In the strongly nonlinear regime, Chapter 6 developed a continuum description in terms of mean and contrast fields and showed that exact in-phase and out-of-phase similar nonlinear normal-mode reductions are not generally invariant when the two masses are unequal. The nonlinear transition front must therefore be understood as a nonsimilar acoustic–optical front: a dominant acoustic-like transition accompanied by an optical-like correction generated by mass contrast. A Bloch-consistent harmonic-balance formulation was then used to compute nonlinear backbone branches and harvested power in the large-amplitude regime. The nonlinear model produced a substantially higher and more globally elevated harvested-power response across the Brillouin zone than the linearized model, with the enhancement approaching two orders of magnitude for the cases studied. Finite-chain simulations provided validation of both the leading-order snap-through transition-front description and the branch-wise nonlinear power formulation. Overall, the diatomic extension established a systematic framework linking linear bandgaps, nonlinear backbone branches, transition fronts, and post-settling energy harvesting.

Taken together, the Thesis shows that nonlinear periodic structures can be designed not only to block, transmit, or redirect waves, but also to convert wave energy into useful electrical output under transient free propagation. The main design philosophy emerging from the work is that bandgap manipulation, attenuation, nonlinear branch shaping, and harvesting should not be treated as separate objectives. Instead, they can be integrated into a single wave-mediated electromechanical design framework.

7.2 How the Thesis fills the literature gap

The Introduction identified several limitations in the existing literature. Firstly, much of the classical work on periodic media and mechanical metamaterials focuses on fixed band structures determined by geometry, material contrast, or local resonance. Although these structures can be effective for filtering and attenuation, their performance is often not intrinsically adaptive to wave amplitude or transient conditions. The present work addresses this limitation by developing nonlinear periodic systems whose dispersion and bandgap behavior depend on mass ratios, inertial-coupling parameters, bi-stability, and wave amplitude. The ALIGN framework in Chapter 3 provides a practical way to analyze this class of strongly nonlinear structures without reducing them to overly simplified polynomial models.

Secondly, the literature on bi-stable structures and the literature on inerters have often developed in parallel. Bi-stability is known to produce snap-through, interwell transitions, and amplitude-dependent dynamics, while inertial coupling is known to reshape effective inertia and create low/high-frequency attenuation. The present work combines these mechanisms in a single periodic setting. The resulting structures exhibit critical stability thresholds, branch merging, modal redistribution, and tunable bandgaps. Thus, the work fills the gap between bi-stable wave tailoring and inerter-induced metamaterial design. Instead of conventional inertial amplifiers which have been employed extensively in existing literature, this work shifts focus to stable negative-inerters and sets thresholds for these types of inerters in terms of their inherent design parameters before proposing and exploiting them in nonlinear periodic models to obtain desirable energy harvesting designs and tunable dispersion behavior predictable via inexpensive semi-analytical algorithms.

Thirdly, classical vibration energy harvesting often relies on sustained forcing or resonance tuning. This is restrictive for realistic structural environments where disturbances are intermittent, impulsive, or spatially distributed. The settling-time formulation in Chapter 4 fills this gap by developing a harvesting metric based on free-wave propagation generated solely by initial conditions. The optimum harvesting frequency is obtained from the intrinsic electromechanical dynamics of the periodic chain rather than from an externally prescribed forcing frequency. This makes the framework more naturally suited to transient vibration environments.

Fourth, nonlinear and multistable harvesters are often studied as isolated oscillators, while phononic and metamaterial harvesters often emphasize energy guiding, trapping, or defect-based concentration. The work in Chapter 5 fills the gap between these viewpoints by treating the harvester as an extended nonlinear periodic medium. Energy conversion is not an add-on to a waveguide; it is part of the inherent free-wave dynamics. In the intrawell regime, nonlinear dispersion broadens the useful harvesting band. In the interwell regime, transition-front propagation spatially localizes the harvestable electrical output. This provides a unified picture of broadband and spatially localized harvesting in the same physical architecture.

Finally, the diatomic extension in Chapter 6 fills a further gap by showing how mass contrast and nonlinear piezomagnetoelasticity can be used together to enrich branch structure and improve harvesting capacity. The results show that mass-diatomicity does more than create an acoustic–optical band structure: in the nonlinear electromechanical setting,

it changes the front dynamics, modal participation, and branch-wise power extraction. This creates an additional design handle for transient free-wave harvesters.

7.3 Research contributions

The main contributions of this Thesis can be summarized as follows.

1. A bi-stable, negative-inertance induced unit cell with coupled horizontal–vertical dynamics was proposed and analyzed as a building block for nonlinear periodic structures. The unit cell preserves rich intrawell and interwell dynamics while also supporting inertial coupling through a mechanically realizable linkage.

2. A general semi-analytical framework, ALIGN, was developed for strongly nonlinear discrete periodic structures. The framework combines asymptotic analysis, multi-harmonic harmonic balance, branch tracking, amplitude-locked inverse method validation, and nonlinear stability diagnostics. It is applicable to systems with non-polynomial and non-integrable geometric nonlinearities.

3. The weakly and strongly nonlinear dispersion behavior of a bi-stable, inertially coupled periodic chain was characterized. The analysis identified physically admissible mass-ratio thresholds, systematic bandgap trends, and nonlinear modal redistribution leading to dominant branch merging.

4. A settling-time-aware framework was introduced for energy harvesting from transient free waves in a linear piezoelectric periodic chain. This framework links Bloch dispersion, attenuation, closed-form time response, and one-period post-settling power extraction.

5. A physically motivated optimum free-wave harvesting frequency was defined without assuming sustained harmonic excitation. The corresponding maximum steady-state power was shown to depend on the post-transient voltage envelope and settling-time criterion, thereby providing an internally consistent free-decay harvesting metric.

6. The settling-time idea was extended to inertially coupled nonlinear piezomagnetoelastic chains. In the strongly nonlinear intrawell regime, magnetic bi-stability and stable negative-inertance effects were shown to broaden the useful high-power harvesting region into a quasi-saturated band of near-optimal performance achieved simultaneously with an improved/ increased stiffness-to-weight ratio.

7. Spatially localized energy harvesting from interwell transition fronts was demonstrated in a dissipative piezomagnetoelastic periodic chain. The relevant propagating structure was identified as a slowly modulated φ^4-type front rather than an exact conservative soliton, and leading-order analytical descriptions were derived for the front profile, voltage envelope, and harvested-power distribution.

8. A systematic design comparison was established between a linear piezoelectric chain, a linear inertially coupled chain, a bi-stable chain without inertial coupling/inerters, and the fully coupled bi-stable-inertial piezomagnetoelastic chain. This comparison

showed that magnetic bi-stability provides the dominant increase in harvestable output, while moderate inertance factor sharpens spatial localization.

9. A mass-diatomic nonlinear piezomagnetoelastic chain was formulated and analyzed. The work showed how acoustic-like and optical-like branches, mass contrast, inertial coupling-effects, and nonlinear electromechanical coupling jointly affect bandgaps and harvested power.

10. In the strongly nonlinear diatomic regime, the transition front was shown to be a nonsimilar acoustic–optical structure rather than a purely in-phase or out-of-phase nonlinear normal mode. A leading-order front model and harmonic-balance branch formulation were developed and validated numerically.

11. Across the Thesis, finite-chain simulations were used to connect the analytical and semi-analytical models to direct time-domain behavior. These simulations clarified the distinction between intrinsic branch-wise harvesting potential and the actual response generated by localized transient excitation.

7.4 Novelty and impact

The novelty of this work lies in bringing together the rich aspects of structural dynamics, nonlinear vibrations, wave propagation in periodic structures, and vibration energy harvesting in a single, comprehensive, and analytically tractable framework. The work shows that free wave propagation in suitably engineered nonlinear periodic structures can be exploited at the inherent dynamics-level itself without the necessary requirements of sustained external forcing and defect or sophisticated grading-based architecture. The unified framework proposed and developed in this work exploits the effects of nonlinearity and inertial-coupling mechanisms in periodic structures for tunable bandgap engineering and desirable energy harvesting characteristics under ambient environments where the intermittent and abrupt disturbances are better modeled as initial conditions rather than well-designed, sustained forcing.

The impact of the research is moderately big in a broader context. It opens the pathway for optimal design of self-powered systems which can harvest energy from ambient structural vibrations. Few practical applications can include, though not limited to, generation of electrical energy in aeroplane cabins from wing-vibrations during long flights, structural vibration monitoring of suspension bridges under ambient vibration environments, wave filtering and vibration suppression through suitably engineered nonlinear periodic architectures, vibration isolation and localized energy extraction via transduction in a selected region of a practical engineering or medical device.

Relative to narrowly tuned resonant harvesting, the expected gains are a wider useful operating range and greater spatial concentration of electrical output under transient disturbances, rather than a universal increase in peak power. The large nonlinear-to-linear gains reported in Chapter 6 are model-specific comparisons, not measured gains over existing devices. Practical improvements in usable energy or sensor duty cycle would require matched-input experiments accounting for device size and mechanical, dielectric and circuit losses.

7.5 Recommendations for future work

The results presented in this Thesis open several natural directions for future research.

7.5.1 Experimental realization and validation

The most direct next step is experimental validation of the proposed nonlinear periodic harvesters. A laboratory prototype of the piezomagnetoelastic chain would make it possible to assess the practical influence of magnetic field imperfections, finite beam flexibility, fabrication tolerances, bearing friction, patch bonding, circuit losses, and imperfect inertial linkages. Experimental tests would also clarify how robust the predicted broadband intrawell harvesting and spatially localized interwell harvesting remain under non-ideal boundary conditions and realistic initial disturbances.

7.5.2 Improved nonlinear time-domain validation

The ALIGN framework uses amplitude-locked inverse-method simulations to validate nonlinear harmonic-balance branches. However, in strongly nonlinear regimes, small changes in initial conditions, boundary reflections, and nonlinear modal interactions can move finite-chain responses away from the computed periodic Bloch orbit. Future work should improve the mapping between multi-harmonic harmonic balance coefficients and finite-chain initial conditions. This includes replacing RMS-based amplitude targeting by more exact energy matching or modal projection-based initialization schemes. Further nonlinear Floquet and Lyapunov analyses could also be used to map stable, weakly unstable, quasiperiodic, and chaotic propagation regimes.

7.5.3 Multimode beam and higher-dimensional electromechanical models

The present beam-based piezomagnetoelastic models use reduced single-mode descriptions. This is appropriate for the low frequency regimes emphasized here, but higher-frequency branch interactions, broadband excitation, and multimodal internal resonances may require richer structural models. Future work should include multimode beam expansions, finite-element beam models, and distributed piezoelectric coupling. This would make it possible to test whether the nonlinear broadening and localized harvesting mechanisms persist when higher bending modes and more realistic strain distributions are included.

7.5.4 Two and three-dimensional nonlinear harvesting lattices

Another important extension is to generalize the one-dimensional chains to two- and three-dimensional nonlinear piezomagnetoelastic lattices. Higher dimensional systems would allow directional bandgaps, anisotropic group velocity, wave beaming, topological edge transport, and defect-guided localization to be combined with electromechanical harvesting. This would extend the present framework from axial transient free waves to spatially distributed wave packets and multidirectional impacts, which are more representative of realistic structural environments.

7.5.5 Circuit design and adaptive electrical interfaces

The present work uses simple resistive harvesting circuits to expose the fundamental electromechanical mechanisms. Future work should investigate nonlinear, adaptive, and synchronized electrical interfaces. Examples include switch-based harvesting circuits, active or semi-active shunts, impedance-tuned circuits, and distributed electrical networks coupled across unit cells. Such circuits may enhance the voltage response, control the effective electrical damping, and improve the trade-off between wave attenuation and harvested power.

7.5.6 Optimization, uncertainty, and design maps

The analytical and semi-analytical tools developed in this Thesis can be used to build high-dimensional design maps. Future studies should formulate optimization problems in which the objective is not only maximum harvested power, but also bandwidth, localization length, robustness to parameter uncertainty, stability of the nonlinear branch, and manufacturability. Sensitivity analysis and uncertainty quantification would be especially important for magnetic systems, where small geometric variations can change the double-well landscape and therefore the interwell transition dynamics.

7.5.7 General transient and stochastic excitation environments

The present studies emphasize initial condition-driven free waves and localized snap-through type disturbances. A broader future direction is to study general transient and stochastic excitation environments. Real structural disturbances may contain broadband spectra, repeated impulses, moving loads, or random excitations. Extending the settling-time and post-transient power framework to these settings would help determine when the free-wave optimum, nonlinear broadband plateau, and localized transition-front harvesting mechanisms remain effective.

7.6 Final remarks

The central outcome of this Thesis is a design framework in which nonlinear free wave propagation and energy harvesting are treated as one coupled problem. Bandgaps, attenuation, modal redistribution, transition fronts, voltage generation, and post-settling power extraction are all linked through the same structural and electromechanical parameters. The resulting systems are not merely vibration filters with attached harvesters, nor isolated harvesters placed in a periodic host. They are nonlinear electromechanical metamaterials in which wave tailoring and energy conversion occur together.

By combining geometric and magnetic bi-stability, suitably chosen inerter-effects, piezoelectric coupling, settling-time-aware power prediction, and mass-diatomic branch engineering, this Thesis demonstrates several routes toward passive structures that can guide, attenuate, localize, and harvest transient wave energy. These results provide a foundation for future self-powered sensing and vibration-control systems that operate not under idealized sustained forcing, but under the intermittent free-wave disturbances that arise naturally in engineering structures.

Journal Publications

1. A. Bhattacharyya, S. Adhikari, Bandgap manipulation through a bi-stable inertially amplified strongly nonlinear periodic chain. International Journal of Non-Linear Mechanics 187 (2026) 105364 (based on Chapter 3).

2. A. Bhattacharyya, S. Adhikari, Energy harvesting from transient free waves in a piezoelectric periodic chain: a settling-time approach. Journal of Physics D: Applied Physics 59(23) (2026) 235502 (based on Chapter 4).

3. A. Bhattacharyya, S. Adhikari, Enhanced energy harvesting potential of inertially amplified nonlinear piezomagnetoelastic chains. International Journal of Engineering Science 226 (2026) 104573 (based on Chapter 5–intrawell regime).

4. A. Bhattacharyya, S. Adhikari, Localized energy harvesting in inertially amplified bi-stable piezomagnetoelastic chains. Physical Review E (minor revisions) (based on Chapter 5–interwell regime).

5. A. Bhattacharyya, S. Adhikari, Enhanced energy harvesting capacity of diatomic inertially amplified nonlinear piezomagnetoelastic chains. Nonlinear Dynamics (in peer review) (based on Chapter 6).

Funding Acknowledgements

Aneesh Bhattacharyya acknowledges the James Watt School of Engineering Ph.D. scholarship received from the University of Glasgow.

REFERENCES

[1] L. Brillouin, Wave Propagation in Periodic Structures, McGraw-Hill, 1946.

[2] D. J. Mead, Wave propagation in continuous periodic structures: research contributions from southampton, 1964–1974, Journal of Sound and Vibration 40 (1) (1975) 1–18.

[3] M. S. Kushwaha, P. Halevi, L. Dobrzynski, B. Djafari-Rouhani, Acoustic band structure of periodic elastic composites, Physical Review Letters 71 (1993) 2022–2025.

[4] P. A. Deymier (Ed.), Acoustic Metamaterials and Phononic Crystals, Springer, 2013.

[5] M. I. Hussein, M. J. Leamy, M. Ruzzene, Dynamics of phononic materials and structures: Historical origins, recent progress, and future outlook, Applied Mechanics Reviews 66 (4) (2014) 040802.

[6] S. A. Cummer, J. Christensen, A. Alù, Controlling sound with acoustic metamaterials, Nature Reviews Materials 1 (2016) 16001.

[7] K. Bertoldi, V. V. J. Christensen, M. van Hecke, Flexible mechanical metamaterials, Nature Reviews Materials 2 (2017) 17066.

[8] M. D. Fronk, L. Fang, P. Packo, M. J. Leamy, Elastic wave propagation in weakly nonlinear media and metamaterials: a review of recent developments, Nonlinear Dynamics 111 (12) (2023) 10709–10741.

[9] X. Fang, W. Lacarbonara, L. Cheng, Advances in nonlinear acoustic/elastic metamaterials and metastructures, Nonlinear Dynamics (2024) 1–28.

[10] S. Hajarolasvadi, Mechanical metamaterials for wave control: Effects of modularity and nonlinearity, Ph.D. thesis, University of Illinois at Urbana-Champaign (2021).

[11] N. Contreras, X. Zhang, H. Hao, F. Hernández, Application of elastic metamaterials/meta-structures in civil engineering: A review, Composite Structures 327 (2024) 117663.

[12] M. I. Hussein, M. J. Frazier, Metadamping: An emergent phenomenon in dissipative metamaterials, Journal of Sound and Vibration 332 (2013) 4767–4774.

[13] Z. Chen, W. Zhou, C. W. Lim, Active control for acoustic wave propagation in nonlinear diatomic acoustic metamaterials, International Journal of Non-Linear Mechanics 125 (2020) 103535.

[14] R. K. Narisetti, Wave propagation in nonlinear periodic structures, Georgia Institute of Technology, 2010.

[15] F. E. Udwadia, H. Mylapilli, Energy control of inhomogeneous nonlinear lattices, Proceedings of the Royal Society A: Mathematical, Physical and Engineering Sciences 471 (2176) (2015) 20140694.

[16] A. H. Nayfeh, Introduction to Perturbation Techniques, Wiley, 1993.

[17] A. H. Nayfeh, D. T. Mook, Nonlinear Oscillations, Wiley, 1979.

[18] K. L. Manktelow, Dispersion analysis of nonlinear periodic structures, Ph.D. thesis, Georgia Institute of Technology (2013).

[19] K. L. Manktelow, M. J. Leamy, M. Ruzzene, Weakly nonlinear wave interactions in multi-degree of freedom periodic structures, Wave Motion 51 (6) (2014) 886–904.

[20] K. L. Manktelow, M. Ruzzene, M. J. Leamy, Wave propagation in nonlinear lattice materials, Dynamics of Lattice Materials (2017) 107–137.

[21] M. D. Fronk, M. J. Leamy, Higher-order dispersion, stability, and waveform invariance in nonlinear monoatomic and diatomic systems, Journal of Vibration and Acoustics 139 (5) (2017) 051003.

[22] G. Kerschen, M. Peeters, J. C. Golinval, A. F. Vakakis, Nonlinear normal modes, part i: A useful framework for the structural dynamicist, Mechanical Systems and Signal Processing 23 (1) (2009) 170–194.

[23] G. Haller, S. Ponsioen, Nonlinear normal modes and spectral submanifolds: Existence, uniqueness and use in model reduction, Journal of Nonlinear Science 26 (4) (2016) 909–966.

[24] D. Wagg, S. Neild, Nonlinear Vibration with Control: For Flexible and Adaptive Structures, 2nd Edition, Vol. 218 of Solid Mechanics and Its Applications, Springer International Publishing, 2015.

[25] S. A. Neild, D. J. Wagg, Applying the method of normal forms to second-order nonlinear vibration problems, Proceedings of the Royal Society A: Mathematical, Physical and Engineering Sciences 467 (2128) (2011) 1141–1163.

[26] S. A. Neild, A. R. Champneys, D. J. Wagg, T. L. Hill, A. Cammarano, The use of normal forms for analysing nonlinear mechanical vibrations, Philosophical Transactions of the Royal Society A: Mathematical, Physical and Engineering Sciences 373 (2051) (2015) 20140404.

[27] T. L. Hill, A. Cammarano, S. A. Neild, D. J. Wagg, Interpreting the forced responses of a two-degree-of-freedom nonlinear oscillator using backbone curves, Journal of Sound and Vibration 349 (2015) 276–288.

[28] T. Breunung, G. Haller, Explicit backbone curves from spectral submanifolds of forced-damped nonlinear mechanical systems, Proceedings of the Royal Society A 474 (2213) (2018) 20180083.

[29] S. Ponsioen, T. Pedergnana, G. Haller, Model reduction to spectral submanifolds and forced-response calculation in high-dimensional mechanical systems, Journal of Sound and Vibration 488 (2020) 115640.

[30] C. M. Cheng, Z. K. Peng, W. M. Zhang, G. Meng, Analysis of locally nonlinear two dimensional periodic structures using nofrfs, in: Vibration Engineering and Technology of Machinery: Proceedings of VETOMAC X 2014, held at the University of Manchester, UK, September 9-11, 2014, 2014, pp. 811–823.

[31] C. M. Cheng, Z. K. Peng, X. J. Dong, W. M. Zhang, G. Meng, Locating non-linear components in two dimensional periodic structures based on nofrfs, International Journal of Non-Linear Mechanics 67 (2014) 198–208.

[32] M. P. Magalhães, et al., Análise da formação de band gaps em estruturas periódicas utilizando o método do elemento espectral (2023).

[33] X. Liu, G. Cai, K. W. Wang, Dispersion analysis of a two-dimensional metastable metastructure considering damping and nonlinear effects, Journal of Applied Physics 129 (11) (2021).

[34] H. Reda, K. Elnady, J. F. Ganghoffer, H. Lakiss, Wave propagation in pre-deformed periodic network materials based on large strains homogenization, Composite Structures 184 (2018) 860–871.

[35] A. Parsa, J. Bagrow, C. S. O'Hern, R. Kramer-Bottiglio, J. Bongard, Data-driven modeling of granular chains with modern koopman theory, arXiv preprint arXiv:2411.15142 (2024).

[36] R. Lin, L. Hou, Y. Chen, Y. Jin, N. Saeed, Y. Chen, A novel adaptive harmonic balance method with an asymptotic harmonic selection, Applied Mathematics and Mechanics 44 (11) (2023) 1887–1910.

[37] S. R. Panigrahi, Dynamics of nonlinear snap–through chains with application to energy harvesting and wave propagation, Michigan State University, 2014.

[38] N. Nadkarni, C. Daraio, D. M. Kochmann, Dynamics of periodic mechanical structures containing bistable elastic elements: From elastic to solitary wave propagation, Physical Review E 90 (2) (2014) 023204.

[39] J. G. Cui, M. Q. Niu, L. Q. Chen, T. Yang, Asymmetric propagation of acoustic waves in a conical granular chain, Communications in Nonlinear Science and Numerical Simulation 116 (2023) 106885.

[40] H. Jalali, P. Rizzo, A. Nasrollahi, Asymmetric propagation of low-frequency acoustic waves in a granular chain using asymmetric intruders, Journal of Applied Physics 126 (7) (2019).

[41] A. F. Arrieta, S. A. Neild, D. J. Wagg, Nonlinear dynamic response and modeling of a bi-stable composite plate for applications to adaptive structures, Nonlinear Dynamics 58 (1–2) (2009) 259–272.

[42] A. F. Arrieta, D. J. Wagg, S. A. Neild, Dynamic snap-through for morphing of bi-stable composite plates, Journal of Intelligent Material Systems and Structures 22 (2) (2011) 103–112.

[43] A. F. Arrieta, S. A. Neild, D. J. Wagg, On the cross-well dynamics of a bi-stable composite plate, Journal of Sound and Vibration 330 (14) (2011) 3424–3441.

[44] N. A. Saeed, Y. Ellabban, L. Hou, S. Zhong, F. Z. Duraihem, Geometric nonlinear dynamics of a quasi-zero stiffness isolator integrated with an energy harvester: monostable, perfect zero-linear stiffness, and bistable oscillation modes, Chaos, Solitons & Fractals 199 (2025) 116633.

[45] Q. Meng, L. Hou, R. Lin, Y. Chen, N. A. Saeed, A. Fouly, E. Awwad, On a quasi-zero stiffness vibration isolator with multiple zero stiffness points for mass load deviation, Applied Mathematical Modelling 145 (2025) 116112.

[46] Q. Meng, L. Hou, A. Wang, R. Lin, Z. Li, S. Zhong, Y. Chen, N. A. Saeed, A. Mohamed, E. Awwad, Subharmonic response suppression of a quasi-zero stiffness system, Journal of Sound and Vibration 594 (2025) 118674.

[47] N. Saeed, L. Hou, H. Yi, A. Shukur, S. Alamry, S. El-Shourbagy, On a broadband vibration isolator with tunable stiffness: from quasi-zero-stiffness to zero-stiffness behavior, Applied Mathematics and Mechanics 47 (2) (2026) 255–282.

[48] N. A. Saeed, Y. Ellabban, L. Hou, G. Moatimid, S. Zhong, F. Z. Duraihem, Nonlinear dynamics of a bio-inspired 2-dof low-frequency x-shaped vibration isolator with m-to-n layers driven harmonically under simultaneous primary and 1: 1 internal resonances, Chaos, Solitons & Fractals 190 (2025) 115786.

[49] N. A. Saeed, Y. Ellabban, G. Moatimid, L. Hou, A. Mohamed, Nonlinear interactions of an n-layer x-shape low-frequency vibration isolator equipped with a nonlinear vibration absorber at 1: 1 internal resonance: analytical and numerical investigations, Physica Scripta 99 (10) (2024) 105207.

[50] R. Yazbeck, S. El-Borgi, J. G. Boyd, M. Chen, D. C. Lagoudas, Non-dimensional linear analysis of one-dimensional wave propagation in tensegrity structures, Composite Structures 353 (2025) 118694.

[51] C. Yilmaz, G. M. Hulbert, N. Kikuchi, Phononic band gaps induced by inertial amplification in periodic media, Physical Review B 76 (2007) 054309.

[52] A. Banerjee, S. Adhikari, M. I. Hussein, Inertial amplification band-gap generation by coupling a levered mass with a locally resonant mass, International Journal of Mechanical Sciences 207 (2021) 106630.

[53] S. Chowdhury, A. Banerjee, S. Adhikari, The exact closed-form expressions for optimum inertial amplifier coupled nonlinear friction bearing isolators, in: International Conference on Nonlinear Dynamics and Applications, 2023, pp. 165–176.

[54] I. F. Lazar, S. A. Neild, D. J. Wagg, Using an inerter-based device for structural vibration suppression, Earthquake Engineering & Structural Dynamics 43 (8) (2014) 1129–1147.

[55] D. J. Wagg, A review of the mechanical inerter: historical context, physical realisations and nonlinear applications, Nonlinear Dynamics 104 (1) (2021) 13–34.

[56] S. Chowdhury, A. Banerjee, The nonlinear dynamic analysis of optimum nonlinear inertial amplifier base isolators for vibration isolation, Nonlinear Dynamics 111 (14) (2023) 12749–12786.

[57] S. Chowdhury, A. Banerjee, S. Adhikari, The nonlinear negative stiffness inertial amplifier base isolators for dynamic systems, Mechanics Based Design of Structures and Machines 52 (11) (2024) 8430–8469.

[58] S. Chowdhury, A. Banerjee, S. Adhikari, Enhancing seismic resilience of structures through optimally designed nonlinear negative stiffness base isolators: Exact closed-form expressions, Nonlinear Dynamics 112 (18) (2024) 15833–15856.

[59] D. R. Santo, E. Deckers, P. J. P. Goncalves, L. P. R. de Oliveira, Improving the vibration control performance of metamaterial structures by the inclusion of nonlinear local resonators, in: XLIV Ibero-Latin American Congress on Computational Methods in Engineering, Vol. 5, 2023.

[60] S. Flach, A. V. Gorbach, Discrete breathers—advances in theory and applications, Physics Reports 467 (1-3) (2008) 1–116.

[61] M. C. Smith, Synthesis of mechanical networks: The inerter, IEEE Transactions on Automatic Control 47 (10) (2002) 1648–1662.

[62] H. B. Al Ba'ba'a, X.-F. Zhu, Q. Wang, Enabling novel dispersion and topological characteristics in mechanical lattices via stable negative inertial coupling, Proceedings of the Royal Society A: Mathematical, Physical and Engineering Sciences 477 (2252) (2021) 20200820.

[63] H. B. Al Ba'ba'a, Z. Lin, S. Tol, Metadamping enhancement and tunability via scissor-like electromechanical metamaterials, Journal of Applied Physics 130 (18) (2021) 184901.

[64] S. Meninger, J. O. Mur-Miranda, R. Amirtharajah, A. Chandrakasan, J. H. Lang, Vibration-to-electric energy conversion, IEEE Transactions on Very Large Scale Integration (VLSI) Systems 9 (2001) 64–76.

[65] S. Roundy, P. K. Wright, J. Rabaey, A study of low level vibrations as a power source for wireless sensor nodes, Computer Communications 26 (2003) 1131–1144.

[66] P. D. Mitcheson, E. M. Yeatman, G. K. Rao, A. S. Holmes, T. C. Green, Energy harvesting from human and machine motion for wireless electronic devices, Proceedings of the IEEE 96 (2008) 1457–1486.

[67] H. A. Sodano, G. Park, D. J. Inman, Estimation of electric charge output for piezoelectric energy harvesting, Strain 40 (2004) 49–58.

[68] N. E. Dutoit, B. L. Wardle, S.-G. Kim, Design considerations for MEMS-scale piezoelectric mechanical vibration energy harvesters, Integrated Ferroelectrics 71 (2005) 121–160.

[69] C. Wei, X. Jing, A comprehensive review on vibration energy harvesting: modelling and realization, Renewable and Sustainable Energy Reviews 74 (2017) 1–18.

[70] C. B. Williams, R. B. Yates, Analysis of a micro-electric generator for microsystems, Sensors and Actuators A: Physical 52 (1996) 8–11.

[71] N. G. Stephen, On energy harvesting from ambient vibration, Journal of Sound and Vibration 293 (2006) 409–425.

[72] S. R. Anton, H. A. Sodano, A review of power harvesting using piezoelectric materials (2003–2006), Smart Materials and Structures 16 (3) (2007) R1–R21.

[73] P. J. Cornwell, J. Goethal, J. Kowko, M. Damianakis, Enhancing power harvesting using a tuned auxiliary structure, Journal of Intelligent Material Systems and Structures 16 (2005) 825–834.

[74] E. S. Leland, P. K. Wright, Resonance tuning of piezoelectric vibration energy scavenging generators using compressive axial preload, Smart Materials and Structures 15 (2006) 1413–1420.

[75] V. R. Challa, Y. Shi, F. T. Fisher, A vibration energy harvesting device with bidirectional resonance frequency tunability, Smart Materials and Structures 17 (2008) 015035.

[76] C. Peters, D. Maurath, W. Schock, F. Mezger, Y. Manoli, A closed-loop wide-range tunable mechanical resonator for energy harvesting systems, Journal of Micromechanics and Microengineering 19 (2009) 094004.

[77] A. Badel, E. Lefeuvre, Wideband piezoelectric energy harvester tuned through its electronic interface circuit, Journal of Physics: Conference Series 557 (2014) 012115.

[78] A. Morel, G. Pillonnet, P. Gasnier, E. Lefeuvre, A. Badel, Frequency tuning of piezoelectric energy harvesters thanks to a short-circuit synchronous electric charge extraction, Smart Materials and Structures 28 (2018) 025009.

[79] L.-Y. Wang, L.-W. Chen, C.-M. Liu, Acoustic energy harvesting using resonant cavity of a sonic crystal, Applied Physics Letters 95 (2009) 013506.

[80] K. Mikoshiba, J. M. Manimala, C. T. Sun, Energy harvesting using an array of multifunctional resonators, Journal of Intelligent Material Systems and Structures 24 (2) (2013) 168–179.

[81] M. Carrara, M. R. Cacan, M. J. Leamy, M. Ruzzene, A. Erturk, Dramatic enhancement of structure-borne wave energy harvesting using an elliptical acoustic mirror, Applied Physics Letters 100 (2012) 204105.

[82] M. Carrara, M. R. Cacan, J. Toussaint, M. J. Leamy, M. Ruzzene, A. Erturk, Metamaterial-inspired structures and concepts for elastoacoustic wave energy harvesting, Smart Materials and Structures 22 (2013) 065004.

[83] K. Li, P. Rizzo, Energy harvesting using arrays of granular chains and solid rods, Journal of Applied Physics 117 (2015) 215101.

[84] J. M. D. Ponti, A. Colombi, R. Ardito, F. Braghin, A. Corigliano, R. V. Craster, Graded elastic metasurface for enhanced energy harvesting, New Journal of Physics 22 (2020) 013013.

[85] H. Lv, X. Tian, M. Y. Wang, D. Li, Vibration energy harvesting using a phononic crystal with point defect states, Applied Physics Letters 102 (2013) 034103.

[86] M. Oudich, Y. Li, Tunable sub-wavelength acoustic energy harvesting with a metamaterial plate, Journal of Physics D: Applied Physics 50 (2017) 315104.

[87] Z. Lin, S. Tol, Elastic metasurfaces for full wavefront control and low-frequency energy harvesting, Journal of Vibration and Acoustics 143 (2021) 061005.

[88] A. Erturk, D. J. Inman, Piezoelectric Energy Harvesting, Wiley, 2011.

[89] M. F. Daqaq, R. Masana, A. Erturk, D. D. Quinn, On the role of nonlinearities in vibratory energy harvesting: A critical review and discussion, Applied Mechanics Reviews 66 (4) (2014) 040801.

[90] F. Cottone, H. Vocca, L. Gammaitoni, Nonlinear energy harvesting, Physical Review Letters 102 (2009) 080601.

[91] R. L. Harne, K.-W. Wang, A review of the recent research on vibration energy harvesting via bistable systems, Smart Materials and Structures 22 (2) (2013) 023001.

[92] H. Fu, E. M. Yeatman, Rotational energy harvesting using bi-stability and frequency up-conversion for low-power sensing applications: Theoretical modelling and experimental validation, Mechanical Systems and Signal Processing 125 (2019) 229–244.

[93] M. Rosso, S. Cuccurullo, F. P. Perli, F. Maspero, A. Corigliano, R. Ardito, A method to enhance the nonlinear magnetic plucking for vibration energy harvesters, Meccanica 59 (9) (2024) 1577–1592.

[94] A. Cammarano, S. A. Neild, S. G. Burrow, D. J. Wagg, D. J. Inman, Optimum resistive loads for vibration-based electromagnetic energy harvesters with a stiffening nonlinearity, Journal of Intelligent Material Systems and Structures 25 (14) (2014) 1757–1770.

[95] P. Kim, J. Seok, A multi-stable energy harvester: dynamic modeling and bifurcation analysis, Journal of Sound and Vibration 333 (2014) 5525–5547.

[96] G. Scarselli, F. Nicassio, F. Pinto, F. Ciampa, O. Iervolino, M. Meo, A novel bistable energy harvesting concept, Smart Materials and Structures 25 (2016) 055001.

[97] L. Xiong, L. Tang, K. Liu, B. R. Mace, Broadband piezoelectric vibration energy harvesting using a nonlinear energy sink, Journal of Physics D: Applied Physics 51 (18) (2018) 185502.

[98] Y. Cao, H. Huang, W. He, Energy harvesting characteristics of preloaded piezoelectric beams, Journal of Physics D: Applied Physics 53 (9) (2020) 095501.

[99] N. Saeed, Y. Ellabban, L. Hou, H. Yi, S. Zhong, F. Duraihem, O. Omara, Nonlinear vibration of quasi-zero stiffness structure with piezoelectric harvester and rl-load: intra-well and inter-well oscillation modes under 1: 1 internal resonance, Applied Mathematics and Mechanics 46 (8) (2025) 1451–1474.

[100] Z. Liu, X. Zhang, Y. Mao, Y. Y. Zhu, C. T. Chan, P. Sheng, Locally resonant sonic materials, Science 289 (2000) 1734–1736.

[101] Q. Geng, T. Wang, L. Wu, Y. Li, Defect coupling behavior and flexural wave energy harvesting of phononic crystal beams with double defects in thermal environments, Journal of Physics D: Applied Physics 54 (22) (2021) 225501.

[102] C. Sugino, A. Erturk, Analysis of multifunctional piezoelectric metastructures for low-frequency bandgap formation and energy harvesting, Journal of Physics D: Applied Physics 51 (2018) 215103.

[103] G. J. Chaplain, J. M. De Ponti, G. Aguzzi, A. Colombi, R. V. Craster, Topological rainbow trapping for elastic energy harvesting in graded Su–Schrieffer–Heeger systems, Physical Review Applied 14 (2020) 054035.

[104] S. Gonella, A. C. To, W. K. Liu, Interplay between phononic bandgaps and piezoelectric microstructures for energy harvesting, Journal of the Mechanics and Physics of Solids 57 (3) (2009) 621–633.

[105] K. J. Ma, T. Tan, F. R. Liu, L. C. Zhao, W. H. Liao, W. M. Zhang, Acoustic energy harvesting enhanced by locally resonant metamaterials, Smart Materials and Structures 29 (2020) 075025.

[106] F. C. Moon, P. J. Holmes., A magnetoelastic strange attractor, Journal of Sound and Vibration 65 (2) (1979) 275–296.

[107] M. Friswell, S. F. Ali, O. Bilgen, S. Adhikari, A. W. Lees, G. Litak., Non-linear piezoelectric vibration energy harvesting from a vertical cantilever beam with tip mass, Journal of Intelligent Material Systems and Structures 23 (13) (2012) 1505–1521.

[108] K. Aravind Kumar, S. F. Ali, A. Arockiarajan., Piezomagnetoelastic broadband energy harvester: Nonlinear modeling and characterization, The European Physical Journal Special Topics 224 (14) (2015) 2803–2822.

[109] B. Yan, H. Ma, B. Jian, K. Wang, C. Wu, Nonlinear dynamics analysis of a bi-state nonlinear vibration isolator with symmetric permanent magnets, Nonlinear Dynamics 97 (4) (2019) 2499–2519.

[110] E. Esmailzadeh, G. Nakhaie-Jazar., Periodic behavior of a cantilever beam with end mass subjected to harmonic base excitation, International Journal of Non-Linear Mechanics 33 (4) (1998) 567–577.

[111] J. A. Mosquera-Sánchez, C. D. M. Jr., Dynamics and wave propagation in nonlinear piezoelectric metastructures, Nonlinear Dynamics 105 (4) (2021) 2995–3023.

[112] R. Ramlan, M. Brennan, B. Mace, I. Kovacic, Potential benefits of a non-linear stiffness in an energy harvesting device, Nonlinear Dynamics 59 (2010) 545.

[113] S. C. Stanton, C. C. McGehee, B. P. Mann, Nonlinear dynamics for broadband energy harvesting: Investigation of a bistable piezoelectric inertial generator, Physica D: Nonlinear Phenomena 239 (10) (2010) 640–653.

[114] S. Zhou, M. Lallart, A. Erturk, Multistable vibration energy harvesters: Principle, progress, and perspectives, Journal of Sound and Vibration 528 (2022) 116886.

[115] S. Adhikari, A. Banerjee, Enhanced low-frequency vibration energy harvesting with inertial amplifiers, Journal of Intelligent Material Systems and Structures 33 (6) (2022) 822–838.

[116] A. F. Vakakis, Passive nonlinear targeted energy transfer, Philosophical Transactions of the Royal Society A: Mathematical, Physical and Engineering Sciences 376 (2127) (2018).

[117] A. F. Vakakis, O. V. Gendelman, L. A. Bergman, A. Mojahed, M. Gzal, Nonlinear targeted energy transfer: state of the art and new perspectives, Nonlinear Dynamics 108 (2) (2022) 711–741.

[118] M. Hwang, A. F. Arrieta, Input-independent energy harvesting in bistable lattices from transition waves, Scientific Reports 8 (2018) 3630.

[119] M. Hwang, A. F. Arrieta, Topological wave energy harvesting in bistable lattices, Smart Materials and Structures 31 (2022) 015021.

[120] D. K. Campbell, J. F. Schonfeld, C. A. Wingate, Resonance structure in kink-antikink interactions in ϕ^4 theory, Physica D: Nonlinear Phenomena 9 (1983) 1.

[121] I. B. Shiroky, O. V. Gendelman, Kinks in chains with on-site bistable nondegenerate potential: Beyond traveling waves, Physical Review E 98 (1) (2018) 012220.

[122] S. Katz, S. Givli, Solitary waves in a nonintegrable chain with double-well potentials, Physical Review E 100 (3) (2019) 032209.

[123] N. Nadkarni, A. F. Arrieta, C. Chong, D. M. Kochmann, C. Daraio, Unidirectional transition waves in bistable lattices, Physical review letters 116 (24) (2016) 244501.

[124] M. Hwang, A. F. Arrieta, Solitary waves in bistable lattices with stiffness grading: Augmenting propagation control, Physical Review E 98 (2018) 042205.

[125] J. R. Raney, N. Nadkarni, C. Daraio, D. M. Kochmann, J. A. Lewis, K. Bertoldi, Stable propagation of mechanical signals in soft media using stored elastic energy, Proceedings of the National Academy of Sciences 113 (35) (2016) 9722–9727.

[126] V. Ramakrishnan, M. J. Frazier, Transition waves in multi-stable metamaterials with space-time modulated potentials, Applied Physics Letters 117 (15) (2020) 151901.

[127] L. Jin, R. Khajehtourian, J. Mueller, A. Rafsanjani, V. Tournat, K. Bertoldi, D. M. Kochmann, Guided transition waves in multistable mechanical metamaterials, Proceedings of the National Academy of Sciences 117 (2020) 2319.

[128] H. Yasuda, L. M. Korpas, J. R. Raney, Transition waves and formation of domain walls in multistable mechanical metamaterials, Physical Review Applied 13 (5) (2020) 054067.

[129] S. P. Beeby, M. J. Tudor, N. M. White, Energy harvesting vibration sources for microsystems applications, Measurement Science and Technology 17 (12) (2006) R175–R195.

[130] H. A. Sodano, D. J. Inman, G. Park, A review of power harvesting from vibration using piezoelectric materials, The Shock and Vibration Digest 36 (3) (2004) 197–205.

[131] K. A. Cook-Chennault, N. Thambi, A. M. Sastry, Powering MEMS portable devices—a review of non-regenerative and regenerative power supply systems with special emphasis on piezoelectric energy harvesting systems, Smart Materials and Structures 17 (4) (2008) 043001.

[132] A. Khaligh, P. Zeng, C. Zheng, Kinetic energy harvesting using piezoelectric and electromagnetic technologies—state of the art, IEEE Transactions on Industrial Electronics 57 (3) (2010) 850–860.

[133] M. Safaei, H. A. Sodano, S. R. Anton, A review of energy harvesting using piezoelectric materials: state-of-the-art a decade later (2008–2018), Smart Materials and Structures 28 (11) (2019) 113001.

[134] S. Priya, Advances in energy harvesting using low profile piezoelectric transducers, Journal of Electroceramics 19 (1) (2007) 167–184.

[135] A. Erturk, D. J. Inman, A distributed parameter electromechanical model for cantilevered piezoelectric energy harvesters, Journal of Vibration and Acoustics 130 (4) (2008) 041002.

[136] A. Erturk, D. J. Inman, An experimentally validated bimorph cantilever model for piezoelectric energy harvesting from base excitations, Smart Materials and Structures 18 (2) (2009) 025009.

[137] Y. C. Shu, I. C. Lien, Analysis of power output for piezoelectric energy harvesting systems, Smart Materials and Structures 15 (6) (2006) 1499–1512.

[138] E. Lefeuvre, A. Badel, C. Richard, D. Guyomar, A comparison between several vibration-powered piezoelectric generators for standalone systems, Sensors and Actuators A: Physical 126 (2) (2006) 405–416.

[139] G. K. Ottman, H. F. Hofmann, A. C. Bhatt, G. A. Lesieutre, Adaptive piezoelectric energy harvesting circuit for wireless remote power supply, IEEE Transactions on Power Electronics 17 (5) (2002) 669–676.

[140] G. K. Ottman, H. F. Hofmann, G. A. Lesieutre, Optimized piezoelectric energy harvesting circuit using step-down converter in discontinuous conduction mode, IEEE Transactions on Power Electronics 18 (2) (2003) 696–703.

[141] D. Guyomar, A. Badel, E. Lefeuvre, C. Richard, Toward energy harvesting using active materials and conversion improvement by nonlinear processing, IEEE Transactions on Ultrasonics, Ferroelectrics, and Frequency Control 52 (4) (2005) 584–595.

[142] Y. Pennec, J. O. Vasseur, B. Djafari-Rouhani, L. Dobrzyński, P. A. Deymier, Two-dimensional phononic crystals: examples and applications, Surface Science Reports 65 (8) (2010) 229–291.

[143] M. Maldovan, Sound and heat revolutions in phononics, Nature 503 (7475) (2013) 209–217.

[144] M. I. Hussein, Theory of damped Bloch waves in elastic media, Physical Review B 80 (21) (2009) 212301.

[145] O. Thorp, M. Ruzzene, A. Baz, Attenuation and localization of wave propagation in rods with periodic shunted piezoelectric patches, Smart Materials and Structures 10 (5) (2001) 979–989.

[146] L. Airoldi, M. Ruzzene, Design of tunable acoustic metamaterials through periodic arrays of resonant shunted piezos, New Journal of Physics 13 (2011) 113010.

[147] F. Casadei, M. Ruzzene, L. Dozio, K. A. Cunefare, Broadband vibration control through periodic arrays of resonant shunts: experimental investigation on plates, Smart Materials and Structures 19 (1) (2010) 015002.

[148] S. Tol, F. L. Degertekin, A. Erturk, Phononic crystal Luneburg lens for omnidirectional elastic wave focusing and energy harvesting, Applied Physics Letters 111 (1) (2017) 013503.

[149] L. Gammaitoni, I. Neri, H. Vocca, Nonlinear oscillators for vibration energy harvesting, Applied Physics Letters 94 (16) (2009) 164102.

[150] M. F. Daqaq, Response of uni-modal Duffing-type harvesters to random forced excitations, Journal of Sound and Vibration 329 (18) (2010) 3621–3631.

[151] B. P. Mann, N. D. Sims, Energy harvesting from the nonlinear oscillations of magnetic levitation, Journal of Sound and Vibration 319 (1–2) (2009) 515–530.

[152] A. Erturk, J. Hoffmann, D. J. Inman, A piezomagnetoelastic structure for broadband vibration energy harvesting, Applied Physics Letters 94 (25) (2009) 254102.

[153] G. Litak, M. I. Friswell, S. Adhikari, Magnetopiezoelastic energy harvesting driven by random excitations, Applied Physics Letters 96 (21) (2010) 214103.

[154] S. C. Stanton, C. C. McGehee, B. P. Mann, Reversible hysteresis for broadband magnetopiezoelastic energy harvesting, Applied Physics Letters 95 (17) (2009) 174103.

[155] A. Erturk, D. J. Inman, Broadband piezoelectric power generation on high-energy orbits of the bistable Duffing oscillator with electromechanical coupling, Journal of Sound and Vibration 330 (10) (2011) 2339–2353.

[156] A. F. Arrieta, P. Hagedorn, A. Erturk, D. J. Inman, A piezoelectric bistable plate for nonlinear broadband energy harvesting, Applied Physics Letters 97 (10) (2010) 104102.

[157] L. Tang, Y. Yang, A nonlinear piezoelectric energy harvester with magnetic oscillator, Applied Physics Letters 101 (9) (2012) 094102.

[158] S. De Paula Pellegrini, N. Tolou, M. Schenk, J. L. Herder, Bistable vibration energy harvesters: a review, Journal of Intelligent Material Systems and Structures 24 (11) (2013) 1303–1312.

[159] G. Sebald, H. Kuwano, D. Guyomar, B. Ducharne, Simulation of a Duffing oscillator for broadband piezoelectric energy harvesting, Smart Materials and Structures 20 (10) (2011) 102001.

[160] H. Vocca, I. Neri, F. Travasso, L. Gammaitoni, Kinetic energy harvesting with bistable oscillators, Applied Energy 97 (2012) 771–776.

[161] A. F. Vakakis, Inducing passive nonlinear energy sinks in vibrating systems, Transactions-American society of mechanical engineers journal of vibration and acoustics 123 123 (3) (2001) 324–332.

[162] Y. S. Lee, G. Kerschen, A. F. Vakakis, P. Panagopoulos, L. Bergman, D. M. McFarland, Complicated dynamics of a linear oscillator with a light, essentially nonlinear attachment, Physica D:Nonlinear Phenomena 204 (1) (2005) 41–69.

[163] G. Kerschen, J. J. Kowtko, D. M. McFarland, L. A. Bergman, A. F. Vakakis, Theoretical and experimental study of multimodal targeted energy transfer in a system of coupled oscillators, Nonlinear Dynamics 47 (1–3) (2007) 285–309.

[164] A. F. Vakakis, O. V. Gendelman, L. A. Bergman, D. M. McFarland, G. Kerschen, Y. S. Lee, Nonlinear Targeted Energy Transfer in Mechanical and Structural Systems, Vol. 156 of Solid Mechanics and Its Applications, Springer, Dordrecht, 2008.

[165] A. F. Vakakis, L. I. Manevitch, O. Gendelman, L. Bergman, Dynamics of linear discrete systems connected to local, essentially non-linear attachments, Journal of Sound and Vibration 264 (3) (2003) 559–577.

[166] L. I. Manevitch, O. Gendelman, A. I. Musienko, A. F. Vakakis, L. Bergman, Dynamic interaction of a semi-infinite linear chain of coupled oscillators with a strongly nonlinear end attachment, Physica D: Nonlinear Phenomena 178 (1) (2003) 1–18.

[167] K. Remick, D. D. Quinn, D. M. McFarland, L. A. Bergman, A. F. Vakakis, High-frequency vibration energy harvesting from impulsive excitation utilizing intentional dynamic instability caused by strong nonlinearity, Journal of Sound and Vibration 370 (2016) 259–279.

[168] A. Mojahed, L. A. Bergman, A. F. Vakakis, Tunable-with-energy intense modal interactions induced by geometric nonlinearity, Proceedings of the Institution of Mechanical Engineers, Part C: Journal of Mechanical Engineering Science 235 (20) (2021) 4506–4525.

[169] Y. Liu, A. Mojahed, L. A. Bergman, A. F. Vakakis, A new way to introduce geometrically nonlinear stiffness and damping with an application to vibration suppression, Nonlinear Dynamics 96 (3) (2019) 1819–1845.

[170] A. Mojahed, Y. Liu, L. A. Bergman, A. F. Vakakis, Modal energy exchanges in an impulsively loaded beam with a geometrically nonlinear boundary condition: computation and experiment, Nonlinear Dynamics 103 (4) (2021) 3443–3463.

[171] A. Marathe, A. Chatterjee, Wave attenuation in nonlinear periodic structures using harmonic balance and multiple scales, Journal of Sound and Vibration 289 (4–5) (2006) 871–888.

[172] M. Peeters, R. Viguié, G. Sérandour, G. Kerschen, J.-C. Golinval, Nonlinear normal modes, part II: Toward a practical computation using numerical continuation techniques, Mechanical Systems and Signal Processing 23 (1) (2009) 195–216.

[173] G. Kerschen, K. Worden, A. F. Vakakis, J.-C. Golinval, Past, present and future of nonlinear system identification in structural dynamics, Mechanical Systems and Signal Processing 20 (3) (2006) 505–592.

[174] J. P. Noël, G. Kerschen, Nonlinear system identification in structural dynamics: 10 more years of progress, Mechanical Systems and Signal Processing 83 (2017) 2–35.

[175] S. Nacivet, C. Pierre, F. Thouverez, L. Jezequel, A dynamic lagrangian frequency-time method for the vibration of dry-friction-damped systems, Journal of Sound and Vibration 265 (1) (2003) 201–219.

[176] B. Cochelin, C. Vergez, A high order harmonic balance method for the calculation of periodic solutions of non-linear systems of differential equations, Journal of Sound and Vibration 324 (1–2) (2009) 243–262.

[177] T. Detroux, L. Renson, L. Masset, G. Kerschen, The harmonic balance method for bifurcation analysis of large-scale nonlinear mechanical systems, Computer Methods in Applied Mechanics and Engineering 296 (2015) 18–38.

[178] B. R. Mace, D. Duhamel, M. J. Brennan, L. Hinke, Finite element prediction of wave motion in structural waveguides, The Journal of the Acoustical Society of America 117 (5) (2005) 2835–2843.

[179] R. S. Langley, The response of two-dimensional periodic structures to point harmonic forcing, Journal of Sound and Vibration 197 (4) (1996) 447–469.

[180] D. J. Mead, Wave propagation in continuous periodic structures: research contributions from Southampton, 1964–1995, Journal of Sound and Vibration 190 (3) (1996) 495–524.

[181] M. C. Smith, Synthesis of mechanical networks: the inerter, IEEE Transactions on Automatic Control 47 (10) (2002) 1648–1662.

[182] C. Papageorgiou, N. E. Houghton, M. C. Smith, Experimental testing and analysis of inerter devices, Journal of Dynamic Systems, Measurement, and Control 131 (1) (2009) 011001.

[183] K. Ikago, K. Saito, N. Inoue, Seismic control of single-degree-of-freedom structure using tuned viscous mass damper, Earthquake Engineering & Structural Dynamics 41 (3) (2012) 453–474.

[184] L. Marian, A. Giaralis, Optimal design of a novel tuned mass-damper-inerter (TMDI) passive vibration control configuration for stochastically support-excited structural systems, Probabilistic Engineering Mechanics 38 (2014) 156–164.

[185] V. F. Nesterenko, Propagation of nonlinear compression pulses in granular media, Journal of Applied Mechanics and Technical Physics 24 (5) (1983) 733–743.

[186] N. Boechler, G. Theocharis, C. Daraio, Bifurcation-based acoustic switching and rectification, Nature Materials 10 (9) (2011) 665–668.

[187] M. A. Porter, P. G. Kevrekidis, C. Daraio, Granular crystals: nonlinear dynamics meets materials engineering, Physics Today 68 (11) (2015) 44–50.

[188] A. Chatterjee, Asymptotic solution for solitary waves in a chain of elastic spheres, Physical Review E 59 (5) (1999) 5912–5919.

[189] C. Daraio, V. F. Nesterenko, E. B. Herbold, S. Jin, Tunability of solitary wave properties in one-dimensional strongly nonlinear phononic crystals, Physical Review E 73 (2) (2006) 026610.

[190] F. Fraternali, G. Carpentieri, A. Amendola, R. E. Skelton, V. F. Nesterenko., Multiscale tunability of solitary wave dynamics in tensegrity metamaterials., Applied Physics Letters 105 (20) (2014) 201903.

[191] N. Boechler, G. Theocharis, S. Job, P. G. Kevrekidis, M. A. Porter, C. Daraio, Discrete breathers in one-dimensional diatomic granular crystals, Physical Review Letters 104 (24) (2010) 244302.

[192] V. F. Nesterenko, Dynamics of Heterogeneous Materials, Shock Wave and High Pressure Phenomena, Springer, New York, 2001.

[193] C. L. Kane, T. C. Lubensky, Topological boundary modes in isostatic lattices, Nature Physics 10 (1) (2014) 39–45.

[194] J. Paulose, B. G.-g. Chen, V. Vitelli, Topological modes bound to dislocations in mechanical metamaterials, Nature Physics 11 (2) (2015) 153–156.

[195] O. V. Gendelman, L. I. Manevitch., Reflection of short rectangular pulses in the ideal string attached to strongly nonlinear oscillator, Chaos, Solitons & Fractals 11 (15) (2000) 2473–2477.

[196] B. Yan, N. Yu, H. Ma, C. Wu, A theory for bistable vibration isolators, Mechanical Systems and Signal Processing 167 (2022) 108507.

[197] S. H. Strogatz, Nonlinear Dynamics and Chaos, Perseus Books Publishing, 1994.

[198] S. S. Rao, Vibration of continuous systems, John Wiley & Sons, 2019.

[199] M. A. Campana, M. Ouisse, E. Sadoulet-Reboul, M. Ruzzene, S. Neild, F. Scarpa, Impact of non-linear resonators in periodic structures using a perturbation approach, Mechanical Systems and Signal Processing 135 (2020) 106408.

[200] A. Bhattacharyya, S. Adhikari., Propagation characteristics of an elastic bar coupled with a discrete snap-through element, Nonlinear Dynamics 111 (4) (2022) 2961–2990.

[201] A. Bhattacharyya, S. Adhikari., Bandgap manipulation through a bi-stable inertially amplified strongly nonlinear periodic chain, International Journal of Non-Linear Mechanics 187 (2026) 105364.

[202] M. Lizunova, J. V. Wezel, An introduction to kinks in φ^4-theory, SciPost Physics Lecture Notes, 2021.

[203] M. Peyrard, M. D. Kruskal, Kink dynamics in the highly discrete sine-gordon system, Physica D: Nonlinear Phenomena 14 (1) (1984) 88–102.